

VARIATIONS IN THE LENGTH OF DAY  
OF THE EARTH DUE TO  
TOPOGRAPHIC CORE-MANTLE COUPLING  
IN A STRATIFIED LAYER

vorgelegt von  
Sebastian Glane, M.Sc.

an der Fakultät V – Verkehrs- und Maschinensysteme  
der Technischen Universität Berlin  
zur Erlangung des akademischen Grades

Doktor der Ingenieurwissenschaften  
– Dr.-Ing. –

genehmigte Dissertation

Promotionsausschuss:

Vorsitzender: Prof. Dr.-Ing. Utz von Wagner  
Gutachter: Prof. Dr. rer. nat. Wolfgang H. Müller  
Gutachter: Prof. Dr. Kolumban Hutter

Tag der wissenschaftlichen Aussprache: 09. Dezember 2020

Berlin 2021



## **Abstract**

There is evidence that a stably stratified layer of fluid, which is not penetrated by the convective flow of fluid in the bulk of the outer core, is located below the Core-Mantle Boundary (CMB). The question considered in this thesis is whether such a layer also affects the core-mantle coupling. If so, minute variations in the Length of Day (LOD) can be explained by a core-mantle coupling mechanism which accounts for the presence of stratification and deviations of the shape of the CMB from a perfect sphere. A first order perturbation analysis of the problem in CARTESIAN geometry predicts an average traction which is comparable to the value inferred from historical records of LOD variations. The dependence of this traction on the dimensionless parameters of the simplified problem is analyzed in detail. It is found that its dependence on the strength of the stratification, the velocity and the magnetic field is non-linear which yields a variation of the average traction by several orders of magnitude. Furthermore, a resulting torque which is acting on the CMB is obtained through the application of a synthetic model which combines the simplified CARTESIAN model with the results of numerical dynamo simulations. The LOD variations computed from the predicted torque are large in comparison to historical records. This is due to an inconsistent coupling of the numerical and the analytical model. If the predicted LOD variations are correct for the error due to the inconsistency, the validity of the proposed core-mantle coupling model cannot be confirmed by a comparison with historical records because the timescales of the predicted variations are too large in comparison to the available records. Nevertheless, the findings of this study suggest that topographic core-mantle coupling in a stratified layer could be confirmed as a possible candidate for a viable core-mantle coupling model.

---

## Zusammenfassung

Es gibt Hinweise darauf, dass sich unter der Kern-Mantel-Grenze ein stark stratifiziertes Fluid befindet, in welches die Konvektionsströmung im Inneren des äußeren Erdkern nicht eindringt. Die Fragestellung dieser Dissertationsschrift ist daher, ob und wie diese Fluidschicht die Kopplung zwischen dem Erdkern und dem Erdmantel beeinflusst. Winzige Änderungen in der Tageslänge könnten durch ein Kopplungsmodell zwischen Erdkern und Erdmantel erklärt werden, welches die Dichteschichtung und eine Abweichung der Gestalt der Kern-Mantel-Grenze von einer perfekten Kugel berücksichtigt. Eine Störungsrechnung erster Ordnung eines CARTESischen Modellproblems ergibt eine gemittelte Spannung, deren Wert mit demjenigen vergleichbar ist, der aus den Variationen der Tageslänge abgeleitet werden kann. Eine Analyse der dimensionslosen Parameterabhängigkeiten des Problems zeigt, dass die gemittelte Spannung nicht-linear vom Grad der Dichteschichtung, der Fluidgeschwindigkeit und dem Magnetfeld abhängt. Des weiteren wurde ein synthetisches Modell entwickelt, welches das auf den Mantel wirkende Drehmoment aus dem vereinfachten CARTESischen Modell und den Ergebnissen einer numerischen Dynamosimulation berechnet. Die durch das Drehmoment vorhergesagten Variationen der Tageslänge sind im Vergleich zu historischen Messdaten groß. Diese Tatsache ist auf eine inkonsistente Kopplung zwischen dem numerischen und analytischen Modell zurückzuführen. Wenn die vorhergesagten Variationen um diesen Fehler bereinigt werden, kann das untersuchte Kopplungsmodell nicht durch einen Vergleich mit historischen Messdaten endgültig bestätigt werden, da die Zeitskalen der vorhergesagten Variationen stark von jenen der verfügbaren Messdaten abweichen. Nichtsdestotrotz geben die Ergebnisse dieser Arbeit Hinweise darauf, dass Kombination von Dichteschichtung des Fluids und Topographie der Kern-Mantel-Grenze ein Kopplungsmodell zwischen Kern und Mantel darstellen, das in der Realität tatsächlich existieren könnte.

---

## Preface

The research presented in this thesis was conducted while I occupied the position of a research assistant at the chair of Continuum Mechanics and Material Theory at the Technische Universität Berlin and during my visit at the Department of Earth and Planetary Sciences at the University of California, Berkeley. I am grateful for the many opportunities and the supportive environment this position has entailed. Moreover, I am pleased especially by the experiences made and insights gained during my visit at Berkeley. Many conversations, scientific exchanges and cooperation in both groups made a positive contribution to the research presented in this work .

First of all, I would like to thank Professor W. MÜLLER for his supervision, kind support and the guidance which he offered over the past years. He created a research environment that encourages critical and free thinking in which the work of this thesis was able to evolve. His interest in a variety of different scientific fields greatly enriched my professional perspective. His will and willpower to rigorously understand physical problems at depth impressed me the most over the years.

Furthermore, I would like to express my gratitude to Professor K. HUTTER at the Eidgenössische Technische Hochschule Zürich for his acceptance of being a referee of this thesis. I am very grateful to him, not only for being patient with me until I finally completed the thesis, but also for reading the provisional version of my manuscript. His corrections, comments and remarks have not only significantly improved the quality of the thesis. They have, in fact, motivated me to finally complete it during the time of the COVID-19 pandemic.

Furthermore, I would like to sincerely thank Professor B. BUFFETT for hosting me at the University of California, Berkeley. I feel incredibly lucky for the many individual perspectives and nuances on the field of geosciences which he imparted to me. Moreover, it was his idea to consider the hybrid topographic core-mantle coupling model presented in this thesis. Without his support—especially regarding the question of funding—my stay at Berkeley would not have been possible at all. For this, I am truly grateful to him. I am impressed by his supportive, welcoming and cordial attitude and feel very grateful for the many enthusiastic discussions on the core of the Earth.

I also would like to thank Professor U. VON WAGNER for being the chairman of the thesis committee.

In our working group, there are many people I would like to express my thanks. Over the years, I valued the sincere and productive scientific cooperations with Dr. Felix Reich and Wilhelm Rickert. Furthermore, I am also grateful for many pleasant encounters and discussions with my other colleagues, Dr. Emek Abali,

---

Dr. Rolf Jungickel, Dr. Anton Köllner, Dr. Christian Liebold, Dr. Paul Lofink, Dr. Oliver Stahn, Dr. Ralf Wille, Gregor Ganzosch, Alexei Sokolov, Alexander Morozov Hua Yang, Guido Harneit, Arion Juritza, Peter Sahlmann, and Miriam Ziert.

I also would like to thank the members of the working group of Professor B. BUFFETT at the University of California, Berkeley. During my stay there, I shared and enjoyed very much many discussions in the weekly group meetings with Margaret Avery, Hiro Matsui, Tushar Mittal, Rodrgio Chi, and William Davis.

Last but not least, I thank my family for their support.

---

# Contents

<b>List of Symbols</b>	<b>XI</b>
<b>1 Introduction</b>	<b>1</b>
1.1 Motivation . . . . .	1
1.2 Objectives of the thesis . . . . .	2
1.3 Outline of the thesis . . . . .	3
<b>2 Physical modeling of the outer core of the Earth</b>	<b>7</b>
2.1 Internal structure of the Earth . . . . .	8
2.2 Rotational dynamics of the Earth . . . . .	15
2.3 Local balance equations of continuum thermomechanics . . . . .	21
2.4 Maxwell's equations and the magnetohydrodynamic approximation	24
2.4.1 OHM's law and the pointwise LORENTZ transformation . . . . .	26
2.4.2 Magnetohydrodynamic approximation . . . . .	31
2.5 Constitutive equations for a viscous electrically conducting and heat conducting fluid . . . . .	33
2.5.1 Caloric equation of state . . . . .	35
2.5.2 Thermal equation of state and thermodynamic linearization	38
2.6 Rotating systems and changes of observers . . . . .	40
2.7 The anelastic and BOUSSINESQ approximation . . . . .	45
2.7.1 The reference state . . . . .	46
2.7.2 The anelastic approximation . . . . .	52
2.7.3 The BOUSSINESQ approximation . . . . .	56
2.8 Summary . . . . .	58
<b>3 Linear analysis of a stratified layer with boundary topography</b>	<b>61</b>
3.1 Problem statement . . . . .	62
3.1.1 Dimensionless formulation . . . . .	64
3.2 Perturbation analysis for a 1D topography . . . . .	67
3.2.1 The role of the viscosity . . . . .	68
3.2.2 Discussion of the density perturbation . . . . .	70
3.2.3 Solution procedure . . . . .	72
3.2.4 Traction and torque on the Core-Mantle Boundary . . . . .	80
3.3 Analysis of the results . . . . .	82
3.3.1 Non-magnetic case . . . . .	83
3.3.2 Non-inertial magnetic case . . . . .	85
3.3.3 Unstratified magnetic case . . . . .	106

3.3.4	Inertial magnetic case . . . . .	107
3.4	Extension for a 2D topography . . . . .	124
3.5	Summary . . . . .	132
<b>4</b>	<b>Aspects of the numerical modeling of a dynamo process</b>	<b>135</b>
4.1	Problem statement . . . . .	136
4.2	Discretization based on the toroidal-poloidal decomposition . . .	141
4.2.1	Toroidal-poloidal decomposition . . . . .	141
4.2.2	Radial and temporal discretization . . . . .	151
4.2.3	Pseudo-spectral treatment . . . . .	152
4.3	Results . . . . .	153
4.4	Discussion . . . . .	159
<b>5</b>	<b>Signatures of a core-mantle coupling model including topography and stratification</b>	<b>163</b>
5.1	Core-mantle coupling models . . . . .	164
5.2	Model description . . . . .	167
5.2.1	Interpolation of the average traction . . . . .	175
5.2.2	Procedure of the computation of the resulting torque . . .	179
5.3	Resulting core-mantle boundary torque . . . . .	181
5.3.1	Spatial features of the traction and the torque density . .	181
5.3.2	Temporal features of the resulting core-mantle boundary torque . . . . .	186
5.4	Implications for the Length of Day . . . . .	189
5.4.1	Observational data for changes in the Length of Day . . .	190
5.4.2	Predicted variations in the Length of Day by the core-mantle coupling model . . . . .	194
5.4.3	Comparison of the predicted changes in the Length of Day with observations . . . . .	197
5.5	Summary . . . . .	203
<b>6</b>	<b>Conclusion</b>	<b>205</b>
6.1	Contributions of the thesis . . . . .	207
6.2	Outlook . . . . .	207
	<b>List of Figures</b>	<b>XVII</b>
	<b>List of Tables</b>	<b>XXI</b>
	<b>Bibliography</b>	<b>XXIII</b>
<b>A</b>	<b>Static stability and the buoyancy frequency</b>	<b>i</b>
<b>B</b>	<b>The EULIDian transformation</b>	<b>v</b>
B.1	Representations of the velocity and the acceleration . . . . .	vi

B.2	Representations of spatial gradients . . . . .	viii
<b>C</b>	<b>Analysis of sequential rotations</b>	<b>xi</b>
C.1	Angular velocity and angular acceleration vector . . . . .	xi
C.2	The RODRIGUES formula . . . . .	xiii
C.3	The EULER angles . . . . .	xiv
<b>D</b>	<b>The LORENTZ transformation of the velocity</b>	<b>xix</b>
<b>E</b>	<b>Results of the Singular Spectrum Analysis of LOD variations</b>	<b>xxiii</b>



## List of Symbols

### *General quantities and symbols*

$c$	speed of light in vacuum, $c = 299\,792\,458\text{ m s}^{-1}$	$\text{m s}^{-1}$
$r$	radial coordinate	$\text{m}$
$t$	time	$\text{s}$
$w_{\perp}$	normal velocity of a singular surface	$\text{m s}^{-1}$
$N$	BRUNT-VÄISÄLÄ frequency or buoyancy frequency	$\text{s}^{-1}$
$R_{\text{CMB}}$	radius of the core-mantle boundary	$\text{m}$
$R_{\text{ICB}}$	radius of the inner core boundary	$\text{m}$
$O(\bullet)$	order of magnitude of the quantity ( $\bullet$ )	
$e_i$	CARTESIAN basis vectors, $i = 1, 2, 3$	1
$e_r$	radial basis vector	1
$e_{\theta}$	polar basis vector	1
$e_{\varphi}$	azimuthal basis vector	1
$\mathbf{n}$	normal vector of a surface	1
$\mathbf{v}$	velocity of a material particle	$\text{m s}^{-1}$
$\mathbf{w}_I$	velocity of a singular surface	$\text{m s}^{-1}$
$\mathbf{x}$	position vector	$\text{m}$
$\theta$	polar coordinate or angle of colatitude	1
$\varphi$	azimuthal coordinate or angle of longitude	1
$\Delta\text{LOD}$	variations in the length of day of the Earth	$\text{s}$
$\overset{\langle 3 \rangle}{\epsilon}$	LEVI-CIVITA tensor	1
$\boldsymbol{\Omega}$	angular velocity vector of the Earth	$\text{s}^{-1}$
$\nabla$	nabla operator	$\text{m}^{-1}$
$\mathbf{1}$	identity tensor of rank two	1
$(\bullet)_{\text{CMB}}$	quantity ( $\bullet$ ) on the core-mantle boundary	
$(\bullet)_{\text{IC}}$	quantity ( $\bullet$ ) in the inner core of the Earth	
$(\bullet)_{\text{ICB}}$	quantity ( $\bullet$ ) on the inner core boundary	
$(\bullet)_{\text{M}}$	quantity ( $\bullet$ ) in the mantle of the Earth	

### *Abbreviations*

CMB	Core Mantle Boundary
ICB	Inner Core Boundary
LOD	Length of Day
PREM	Preliminary Reference Earth Model
SSA	Singular Spectrum Analysis

*Continuum Thermomechanics*

$p$	pressure	$\text{N m}^{-2}$
$\hat{r}$	thermal power	$\text{J m}^{-3} \text{s}^{-1}$
$\hat{r}^{(\text{EM})}$	electromagnetic thermal power	$\text{J m}^{-3} \text{s}^{-1}$
$s$	entropy density	$\text{J m}^{-3} \text{K}^{-1}$
$u$	internal energy density	$\text{J m}^{-3}$
$T$	temperature	K
$\mathbf{f}$	specific body force	$\text{N kg}^{-1}$
$\mathbf{f}^{(\text{EM})}$	electromagnetic body force density	$\text{N m}^{-3}$
$\mathbf{t}$	traction vector	$\text{N m}^{-2}$
$\mathbf{q}$	heat flux vector	$\text{J m}^{-2} \text{s}^{-1}$
$\xi$	entropy production	J
$\rho$	mass density	$\text{kg m}^{-3}$
$\boldsymbol{\sigma}$	CAUCHY stress tensor	$\text{N m}^{-2}$

*Electrodynamics*

$q$	total electric charge density	$\text{A s m}^{-3}$
$q_{\text{f}}$	free electric charge density	$\text{A s m}^{-3}$
$\mathbf{j}_{\text{f}}$	free diffusive electric current density	$\text{A s m}^{-2}$
$\mathbf{B}$	magnetic flux density	T
$D$	potential of the total electric charge	$\text{A s m}^{-2}$
$\mathfrak{D}$	potential of the free electric charge	$\text{A s m}^{-2}$
$\mathbf{E}$	electric field	$\text{V m}^{-1}$
$H$	potential of total electric current	$\text{A m}^{-1}$
$\mathfrak{H}$	potential of the free electric current	$\text{A s m}^{-2}$
$\mathbf{J}$	total electric current density	$\text{A s m}^{-2}$
$\mathbf{J}_{\text{f}}$	total electric current density	$\text{A s m}^{-2}$
$\mathbf{M}$	magnetization	$\text{A m}^{-1}$
$\mathbf{P}$	polarization	$\text{A s m}^{-2}$
$\gamma$	LORENTZ factor	1
$\epsilon_0$	vacuum permittivity	$(\text{As})^2/\text{N/m}^2$
$\mu_0$	vacuum permeability, $\mu_0 = 4\pi \times 10^{-7} \text{N A}^{-2}$	$\text{N A}^{-2}$

*Dimensionless numbers*

$Al$	ALFVÉN number	1
$Ek$	EKMAN number	1
$Em$	magnetic EKMAN number	1
$Fr$	FROUDE number	1
$Ha$	HARTMANN number	1
$Pr$	PRANDTL number	1
$Pm$	magnetic PRANDTL number	1
$Re$	REYNOLDS number	1
$Rm$	magnetic REYNOLDS number	1

$Ro$	ROSSBY number	1
$St$	stratification number	1
$A$	ELSASSER number	1
<i>Symbols in context of Chap. 2</i>		
$c_p$	specific heat capacity at constant pressure	$\text{J m}^{-3} \text{K}^{-1}$
$g$	GIBBS free energy density	$\text{J m}^{-3}$
$g_{\text{CMB}}$	gravitational acceleration at the CMB	$\text{m s}^{-2}$
$u_T$	isothermal speed of sound	$\text{m s}^{-1}$
$u_s$	isentropic speed of sound	$\text{m s}^{-1}$
$D$	dissipation number	1
$T_0$	standard length of one day, $T_0 = 86\,400 \text{ s}$	s
$V_M$	magnetic scalar potential in the mantle	T m
$\mathbf{c}$	relative position of two observers	m
$\mathbf{d}$	symmetric velocity gradient	$\text{s}^{-1}$
$\mathbf{d}^{\text{dev}}$	deviatoric part of the symmetric velocity gradient	$\text{s}^{-1}$
$\mathbf{g}_a$	density of the potential forces in the adiabatic reference state	$\text{m s}^{-2}$
$\mathbf{i}_i$	basis vectors attached to the ecliptic, $i = 1, 2, 3$	1
$\mathbf{j}_i$	intermediate basis vectors, $i = 1, 2, 3$	1
$\mathbf{k}_i$	basis vectors attached to the equatorial plane, $i = 1, 2, 3$	1
$\mathbf{e}_i$	basis vectors attached to the Earth, $i = 1, 2, 3$	1
$\mathbf{w}$	relative velocity of two observers	$\text{m s}^{-1}$
$\mathbf{B}_M$	magnetic field in the mantle	T
$\mathbf{J}$	tensor of moment of inertia (only in Sect. 2.2)	$\text{kg m}^2$
$\mathbf{M}$	resulting external torque (only in Sect. 2.2)	N m
$\mathbf{Q}$	orthogonal tensor which relates the $\mathbf{i}$ -basis to the $\mathbf{e}$ -basis	1
$\mathbf{Q}_i$	orthogonal tensor of an elementary rotation, $i \in \{\varepsilon, \psi, \varphi\}$	1
$\mathcal{P}_{\parallel}$	parallel projector	1
$\alpha$	coefficient of thermal expansion	$\text{K}^{-1}$
$\alpha_s$	coefficient of entropy expansion	$\text{K m}^3 \text{J}^{-1}$
$\beta$	compressibility	$\text{m}^2 \text{N}^{-1}$
$\gamma_s$	GRÜNEISEN parameter	1
$\varepsilon$	angle of precession	1
$\eta$	magnetic diffusivity	$\text{m}^2 \text{s}^{-1}$
$\kappa$	thermal conductivity	$\text{W m}^{-1} \text{K}^{-1}$
$\lambda$	bulk viscosity	$\text{N s m}^{-2}$
$\mu$	shear viscosity	$\text{N s m}^{-2}$
$\nu$	kinematic viscosity	$\text{m}^2 \text{s}^{-1}$
$\sigma$	electrical conductivity	$\text{S m}^{-1}$
$\varphi$	angle of rotation	1

---

$\psi$	angle of nutation	1
$\boldsymbol{\omega}$	angular velocity vector of the Earth (only in Sect. 2.2)	$\text{s}^{-1}$
$\boldsymbol{\Omega}$	angular velocity tensor related to $\boldsymbol{Q}$ (only in Sect. 2.2)	$\text{s}^{-1}$
$\boldsymbol{\Omega}_i$	angular velocity tensor of the elementary rotation $\boldsymbol{Q}_i$	$\text{s}^{-1}$
$(\bullet)_a$	quantity $(\bullet)$ in the adiabatic reference state	
$(\bullet)_c$	convective perturbation of the quantity $(\bullet)$	
$(\bullet)_{\text{ref}}$	reference value of the quantity $(\bullet)$	
$(\bullet)_0$	quantity $(\bullet)$ in the constant homogeneous reference state	
$(\bullet)_I$	quantity $(\bullet)$ of a singular surface	
$(\bullet)'$	quantity $(\bullet)$ measured by the observer $\mathcal{O}'$	
$\langle \bullet \rangle$	quantity $(\bullet)$ measured by the observer $\tilde{\mathcal{O}}$	
<i>Symbols in context of Chap. 3</i>		
$h$	height of the boundary topography	m
$i$	imaginary unit, $i^2 = -1$	1
$P$	modified pressure	$\text{N m}^{-2}$
$\boldsymbol{b}'$	perturbation of the magnetic field	T
$\boldsymbol{k}_T$	wave number vector of the boundary topography	$\text{m}^{-1}$
$\boldsymbol{k}_T$	wave number vector of the perturbations	$\text{m}^{-1}$
$\boldsymbol{n}$	normal vector of the boundary topography	1
$\boldsymbol{n}'$	normal vector of the perturbed boundary topography	1
$\boldsymbol{B}$	background magnetic field	T
$\boldsymbol{N}$	normal vector of the flat boundary topography	1
$\bar{\boldsymbol{V}}$	background velocity field	$\text{m s}^{-1}$
$\boldsymbol{A}$	matrix occurring in the eigenvalue problem	1
$\boldsymbol{B}$	skew-symmetric matrix occurring in the eigenvalue problem	1
$\boldsymbol{C}$	matrix occurring in the eigenvalue problem	1
$\boldsymbol{M}$	matrix of the eigenvalue problem	1
$\alpha_i$	coefficients of the perturbations	1
$\lambda_x$	wave length of the boundary topography in the $x$ -direction	m
$\chi$	switch for neglecting or incorporating the inertial term	
$\bar{H}$	dimensionless height of the boundary topography	1
$(\bullet)$	quantity $(\bullet)$ in the background state	
$(\bullet)'$	perturbation of the quantity $(\bullet)$	
$\hat{(\bullet)}_i$	amplitude of the quantity $(\bullet)$ , $i = 1, 2, 3$	
$\langle \bullet \rangle$	average of the quantity $(\bullet)$ on the boundary topography	
$(\bullet)^*$	complex conjugate of the quantity $(\bullet)$	

---

*Symbols in context of Chap. 4*

$a$	aspect ratio of the outer core of the Earth	1
$\mathbf{t}_l^m$	toroidal component of degree $l$ and order $m$	1
$\mathbf{p}_l^m$	poloidal component of degree $l$ and order $m$	1
$\mathbf{t}_l^m$	toroidal projector of degree $l$ and order $m$	1
$\mathbf{p}_l^m$	poloidal projector of degree $l$ and order $m$	1
$P$	poloidal scalar	1
$T$	toroidal scalar	1
$T_k$	CHEBYSHEV polynomials	1
$Y_l^m$	spherical harmonic of degree $l$ and order $m$	1
$\mathbf{T}$	toroidal vector field	1
$\mathbf{P}$	poloidal vector field	1
$\Gamma_{\text{CMB}}$	domain of the core-mantle boundary	
$\Gamma_{\text{ICB}}$	domain of the inner core boundary	
$\nabla_{\theta,\varphi}$	surface nabla operator	1
$\mathcal{D}_{\theta,\varphi}$	auxiliary differential operator	1
$(\bullet)_{\text{ref}}$	reference value of the quantity $(\bullet)$	
$\langle \bullet \rangle$	volumetric mean value of the quantity $(\bullet)$	
$\langle \bullet \rangle_{\text{rms}}$	volumetric root mean square of the quantity $(\bullet)$	

*Symbols in context of Chap. 5*

$\mathbf{M}$	resulting torque on the mantle of the Earth	N m
$\delta$	“virtual” thickness of the stratified layer	m
$\langle \bullet \rangle_{\varphi}$	azimuthal average of the quantity $(\bullet)$	
$\langle \bullet \rangle_{\varphi,t}$	temporal mean value of the azimuthal average $\langle \bullet \rangle_{\varphi}$	
$c(\bullet, \star)$	correlation coefficient of the quantities $(\bullet)$ and $(\star)$	



# 1 Introduction

In this introductory chapter, the motivation for the work presented in this thesis is outlined and the objective of the thesis is stated. Finally, a brief outline of the thesis is given with a summary of each chapter.

## 1.1 Motivation

A wealth of knowledge about the internal structure of the Earth has been collected in the past. Various sciences such as mineral physics, seismology and geodesy contributed to understanding the structure of the Earth, its evolution and dynamics [Dziewonski and Romanowicz (2015); Price and Stixrude (2015)]. The stratified nature of the interior of the Earth consisting of an atmosphere, a crust, a mantle and an inner and outer core is well established today [Dziewonski and Romanowicz (2015)]. In comparison to 100 years ago, it is also widely accepted that the geomagnetic field is generated inside the outer core of the Earth by the buoyancy-driven magnetohydrodynamic flow of fluid [Olson (2015)]. Additionally, the advancement of the geosciences has also provided profound explanations for rather extreme events which directly affect human lives such as volcanic eruptions, Earthquakes and changes of the climate. The manifestation of such events shows that the Earth is a complex and dynamic system.

Understanding the processes inside the deep Earth is elementary for explaining extreme processes apparent to humans at its surface, *e.g.*, Earthquakes. All of the major knowledge on the internal structure of the Earth has been built up by the combination of physical models with actual observations. For example, the field of seismology combines the theory of elasticity with measurements of oscillations of the surface of the Earth, whose most extreme forms are Earthquakes. In particular, seismology draws inferences on the interior structure of the Earth. Due its remoteness, the core of the Earth does not cause such dramatic surface-near events. However, the magnetic field of the Earth is also an elementary prerequisite for human life. The variation of the geomagnetic field, *i.e.*, its secular variation, provides insight into the processes within the Earth and especially inside its outer core. It represents a *signal* from the core which can serve for an assessment of a related model. However, apart from the geomagnetic field, there are not many other distinct physical quantities which can be uniquely associated with the core and are also observable (by humans). Nevertheless, the rotation of the Earth or, more precisely, of its mantle and crust can be influenced by an exchange of angular momentum between both regions. Thus, variations of the rotation of the Earth

---

represent another *signal* to gain knowledge about the processes occurring inside its core.

The rotation of the Earth is governed by many in-part coupled physical processes; it is therefore very complex. There are gravitational interactions with neighboring celestial objects such as the Moon and the Sun. Furthermore, the mantle continuously exchanges angular momentum with the atmosphere and the oceans. Apart from the interactions of the mantle with other regions of the Earth and neighboring celestial objects, the mantle itself can yield changes of its rotation because of changes in the moment of inertia due to a re-distribution of mass. However, some changes of the rotation of the Earth can be associated with processes in its core, because components due to other interactions and especially those due to neighboring celestial objects can be determined very accurately. Variations of the apparent Length of Day (LOD) on decadal or larger timescales are particularly associated with the core.

Contrary to the common expectation, the length of day which is the rotational period of the Earth with respect to its principle axis is not constant and not equal to the anticipated value of 24 hours. Rather, minute fluctuations of this period on the order of milliseconds can be observed [Stephenson (2003)]. After removing components due to the interactions with the Sun and the Moon and due to atmospheric and oceanic couplings, variations on intra-decadal, decadal or larger timescales can be identified in the residual LOD time series [Hide and Dikes (1991)]. These are believed to be due to interactions of the core with the mantle. Thus, an explanation of these variations allows us to further constrain the structure of the core of the Earth and the processes occurring inside its interior.

Core-mantle coupling models are constructed in order to predict the torque which is responsible for the exchange of angular momentum between the core and the mantle. Several core-mantle coupling models have been proposed in the literature but none of them could be finally confirmed because, for example, the predicted torque is too small to account for the LOD variations [Buffett (2015)]. However, core angular momentum models which predict changes of total angular momentum of the outer core have successfully reconstructed the exchange of angular momentum between the core and the mantle from the record of the geomagnetic field [Jault, Gire, and Le Mouél (1988)]. Even though this is a success, the question of how the angular momentum is transferred exactly is still open. Apart from viscous and electromagnetic core-mantle coupling, topographic and gravitational coupling are regarded as the most likely mechanisms which are responsible for the transfer of angular momentum between the core and the mantle [Roberts and Aurnou (2012); Buffett (2015)].

## 1.2 Objectives of the thesis

There is evidence that a stably stratified layer of fluid, which is not penetrated by the convective flow of fluid in the bulk of the outer core, is located below

the CMB. The question considered in this thesis is whether such a layer also affects core-mantle coupling. If so, there is hope that not only LOD variations can be explained by the core-mantle coupling mechanism but the properties of the stratified layer could also be further constraint.

In this thesis, the implications of a hybrid topographic core-mantle coupling mechanism which takes the stratification of the fluid into account on the LOD variations are analyzed. It is hypothesized that the core-mantle boundary is perfectly spherical but rather has a topography below which the stratified layer of fluid is located. Moreover, it is assumed that the thickness of the stratified layer exceeds the amplitude of the boundary topography. In this framework, the problem can be analyzed using a first order perturbation technique.

The analysis of the considered problem in a spherical annulus would come along with several problems. The boundary topography deviates from a perfect sphere, which makes the analysis in spherical coordinates more difficult. Furthermore, due to curvature, the problem is non-linear with respect to the spherical coordinates. Lastly, the coupled nature of the problem probably only allows for a numerical solution. Because of these complications, a simplified CARTESIAN model is considered, which allows to analyze the principle properties of the proposed mechanism in detail. Furthermore, a resulting torque acting on the CMB is obtained through the application of a synthetic model, which combines the simplified CARTESIAN model with results of numerical dynamo simulations. Then, this predicted torque is used to derive associated LOD variations which are compared with historical records.

The approach of a treatment in a CARTESIAN geometry and the application of a synthetic model has the advantage that the problem can be analyzed analytically in great detail which would not be possible with a numerical model. Moreover, a resulting torque which is acting on the mantle can be predicted in a rather simple manner. However, the approach also entails several insufficiencies and limitations which prohibit the modeling of the true Earth. Therefore, the results of this thesis can only be regarded as a further step towards a final (if ever possible) clarification of the governing core-mantle coupling mechanism. It is hoped that the results of this thesis provide guidance and inspiration for future research on topographic core-mantle coupling in a stratified layer using more sophisticated models and methods.

### 1.3 Outline of the thesis

Subsequently to this introduction, the outline of this thesis is as follows.

**Chap. 2:** In this chapter, the principles of the physical modeling of the outer core of the Earth are discussed in detail. Following an summary of the internal structure of the Earth, a review related to properties and processes relevant for the outer core of the Earth is presented. Then, the rotational dynamics of the

Earth is discussed in the framework of rigid body dynamics with a focus on LOD variations. Following this, the principles of continuum thermomechanics and continuum electrodynamics are applied to derive the equations governing the fluid in the outer core of the Earth. In doing so, particular attention is paid to the magnetohydrodynamic approximation in a rotating frame of reference. Finally, the anelastic and the BOUSSINESQ approximation are considered and derived by means of a first order perturbation analysis from the so-called adiabatic reference state.

**Chap. 3:** The considered topographic core-mantle coupling model is presented and analyzed. A first order perturbation analysis of the problem is derived and related approximations and assumptions are discussed in detail. The problem is formulated and solved in a dimensionless form. The analysis presented in this chapter extends that of Glane and Buffett [2018]. Especially the analysis of the results which is considering the dependence of the average traction on the dimensionless parameters of the model for several simplified cases extends that of the aforementioned publication. Furthermore, the regularity of the solutions of the different cases is analyzed and it is shown that only the so-called inertial magnetic case possesses a regular solution if both the velocity and magnetic fields become vanishingly small. Furthermore, it is shown that in some of the simplified cases the results are dominated by non-physical fluctuations if certain dimensionless parameters are below a certain value and that these fluctuations are caused by numerical instabilities.

**Chap. 4:** In this chapter, the aspects of the numerical modeling of a buoyancy driven magnetohydrodynamic fluid flow, *i.e.*, a dynamo process, in the outer core of the Earth are discussed. The dynamo process is described using the BOUSSINESQ approximation and the related initial boundary value problem is formulated in a dimensionless form. Subsequently, the numerical solution based on the toroidal-poloidal decomposition is presented. Following this, the process of obtaining equilibrated numerical results is described and the results are presented subsequently. Finally, the results of the dynamo simulation are assessed as to whether they are representative for the outer core of the Earth.

**Chap. 5:** In this chapter, a synthetic forward model which combines the results of the analytical model presented in Chap. 3 with those of the numerical dynamo model discussed in Chap. 4 is considered. The object is to assess whether the combined model can predict LOD variations which are comparable to historical records. Following a brief review of existing core-mantle coupling models, the construction of the synthetic model is outlined. In doing so, related assumptions and deficiencies are extensively addressed. Subsequently, the results of the synthetic model are presented and analyzed in detail before, finally, a comparison with a historical LOD record is made.

**Chap. 6:** The thesis closes with a conclusion and a summary of the main results. The contribution of the thesis regarding existing core-mantle coupling models is addressed and an outlook for future investigations is given.



## 2 Physical modeling of the outer core of the Earth

This chapter covers the fundamental physical modeling of the outer core of the Earth. Following a brief summary of the internal structure of the Earth, a review related to properties and processes relevant for the outer core of the Earth is presented in Sect. 2.1 with an emphasis on the presence of stratified layers and their consequences for the convection fluid flow. In Sect. 2.2, the rotational dynamics of the Earth is discussed in the framework of rigid body dynamics with a focus on fluctuations in the length of day. Additionally, observational data related to the nutation, precession and spin of the Earth is presented and briefly discussed.

In Sections 2.3 and 2.4 the fundamental local equations of continuum thermo-mechanics and continuum electrodynamics are presented. In several subsequent steps, the fundamental equations are specialized for the outer core of the Earth and an emphasis is put on electromechanical coupling and magnetohydrodynamics. Although a derivation from first principles is presented in Sects. 2.3 and 2.4, necessary assumptions, approximations as well as limitations and deficiencies of the theory (and the presentation in this chapter) are addressed and discussed.

Following these two sections on field equations, Sect. 2.5 focuses on the constitutive equations for a viscous heat and electrically conducting fluid. Using the method of COLEMAN and NOLL, it is shown that the NAVIER–STOKES' law for the CAUCHY stress tensor, FOURIER's law for the heat flux and OHM's law for the current density comply with the second law of thermodynamics. Moreover, the thermal and caloric equations of state are derived and discussed.

Section 2.6 takes up on the local balance equations presented in Sect. 2.3 and formulates them for a rotating observer. Here, the role of the LORENTZ force and its representation in the rotating frame is discussed.

The anelastic and BOUSSINESQ approximations, which simplify the local balances of mass, momentum and internal energy, are discussed in Sect. 2.7. These approximations are fundamental for a description of the convection in the outer core of the Earth. The discussion and presentation is related to the heat transport in the outer core of the Earth outlined in Sect. 2.1, and based on the thermodynamics presented in Sect. 2.5. The anelastic and BOUSSINESQ approximations are derived by a first order perturbation expansion from a so-called adiabatic reference state and the BOUSSINESQ approximation is presented as a limit of the anelastic approximation.

Finally, Sect. 2.8 summarizes the fundamental equations of magnetohydrodynamic BOUSSINESQ convection flows in the form commonly used for the outer core

---

of the Earth. A dimensionless form of these equations will be used to solve a initial boundary value problem later in Chap. 4.

## 2.1 Internal structure of the Earth

It is well established today that the Earth is stratified and its internal structure is composed of a crust, a silicate mantle, an iron outer and inner core. However, a century ago this was not the understanding and large progress in describing the internal structure of the Earth has since been made by geophysicists. In the following a brief summary of the internal structure of the Earth is given including some historical remarks. Subsequently, the focus is drawn to the outer core of the Earth and its thermochemical boundary layers.

Seismology provides information about the structure of the Earth by analyzing the propagation of elastic waves in the interior of the Earth. The first earthquake was recorded in Potsdam in 1889 [Rebeur-Paschwitz (1889)] and the existence of a core was established by Gutenberg by identifying reflections of elastic waves from the core-mantle boundary [Gutenberg (1913); Dziewonski and Romanowicz (2015)]. In 1936, LEHMANN found a pressure wave in the shadow zone of the liquid core and interpreted this wave as a reflection from a solid inner core [Kölbl-Ebert (2001)]. Following this discovery, three major domains were identified in the interior of the Earth—the solid mantle, the liquid outer core and the solid inner core. The development of advanced seismological methods has led to the Preliminary References Earth Model (PREM), which provides the density and the velocities of pressure and shear waves as functions of the depth or radius, respectively [Dziewonski and Anderson (1981)]. In seismology, the pressure and shear waves, also called primary and secondary waves, are referred to as  $P$ -waves and  $S$ -waves. The one-dimensional PREM utilizes geodesic observations, normal mode oscillations and body waves to determine the profiles shown in Fig. 2.1. Nowadays, seismic tomography allows to construct high-resolution models of the interior of the Earth, which include lateral and azimuthal heterogeneities as well as anisotropies, see Romanowicz [2003] for a review. Despite these advances, the one-dimensional PREM is still widely used today, which the adjective “preliminary” does not suggest at “a first glance.”

Figure 2.1 shows the pressure and shear wave velocities as functions of the Earth’s radius  $r$ , *i.e.*, the distance to the center of the Earth. The jumps in the profiles allow to distinguish regions of different physical or chemical states. Furthermore, the jumps allow to identify the mean radius of the core-mantle boundary as 3480 km and the mean radius of the inner core boundary as 1220 km [Olson (2015)]. The region between these boundaries is the outer core. The shear wave velocity vanishes in the outer core. Hence, the material is a fluid in this region because a fluid cannot transfer elastic shear waves.

The density profile in Fig. 2.1 is similar to the profile of the pressure wave velocity especially in the inner and outer core. Although the density is an independent

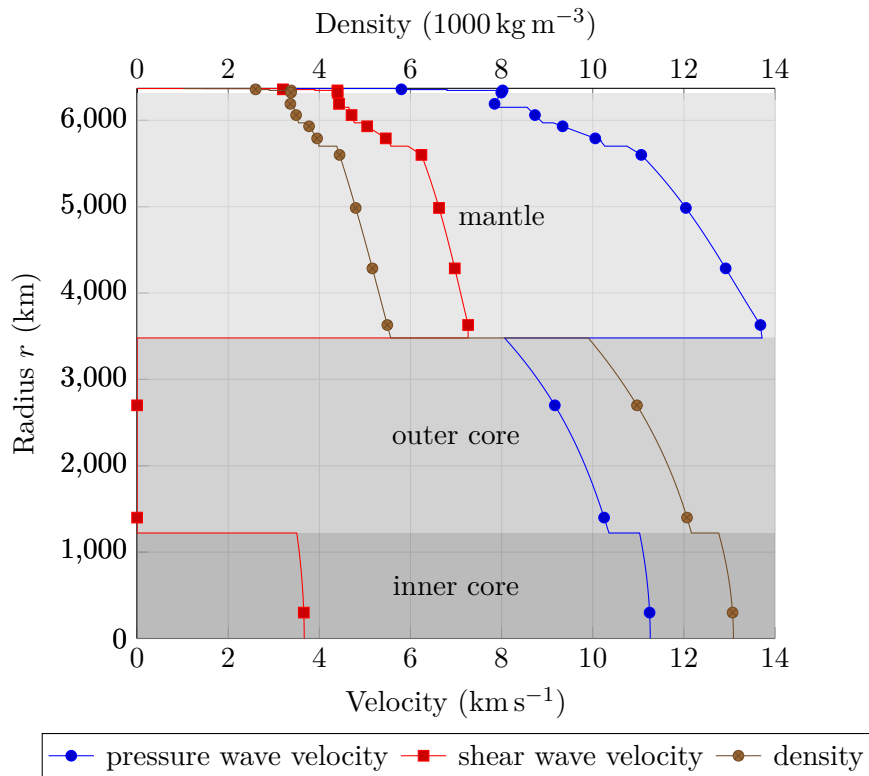


**Figure 2.1:** Density, pressure and shear wave velocities in the interior of the Earth according to the preliminary reference Earth model, Dziewonski and Anderson [1981]. Note that the axis referring to the density is located at the top of the chart and the axis referring to the velocities is located at the bottom. Data provided by Trabant et al. [2012].

model parameter in PREM, it can also be reconstructed from the pressure and the shear wave velocities by the ADAMS–WILLIAMSON equation [Williamson and Adams (1923)]. There is very good agreement of the analytical reconstruction and the density profile obtained by PREM in the lower mantle and the outer and inner core. Assuming a hydrostatic equilibrium, the density profile allows to determine the pressure in the interior of the Earth, which is important if chemical composition and material properties are considered in the deep interior of the Earth.

Regarding the chemical composition of the Earth, the mantle is composed of minerals, and the two main chemical components in the mantle are silicate ( $\text{SiO}_2$ ) with a bulk composition of approximately 45 % and magnesium oxide with a bulk composition of approximately 39 % [Fumagalli and Klemme (2015)]. As outlined by Vočadlo, the core of the Earth is mainly composed of iron but there is no general agreement in the literature on the exact chemical composition. There is evidence from cosmo- and geochemistry that nickel (Ni) is present in the core and that its mass fraction is approximately 10 % [Vočadlo (2015)]. Moreover, it is believed that several light elements such as hydrogen, oxygen, carbon, silicon, and sulfur could

**Table 2.1:** Comparison of temperatures at the inner core boundary,  $T_{\text{ICB}}$ , and the core-mantle boundary,  $T_{\text{CMB}}$ , assumed in five different studies. Temperatures are specified in Kelvin.

Reference	$T_{\text{ICB}}$	$T_{\text{CMB}}$
Buffett et al. [1996]	4668 K	3724 K
Roberts, Jones, and Calderwood [2003]	5100 K	3949 K
Labrosse [2003]	5600 K	4186 K
Pozzo et al. [2012]	5500 K	4039 K
Nimmo [2015]	5508 K	4180 K

also be present in the core [Vočadlo (2015)]. The density jump across the inner core boundary suggests that the fraction of light elements in the outer core is larger than in the inner core. According to Vočadlo, the mass fraction of light elements is 2% to 3% in the inner core and 5% to 10% in the outer core. The fact that the composition of the core is not very well known poses a major challenge concerning material modeling and the identification of material properties. Moreover, the material behavior determines the thermal and chemical evolution of the core on geological timescales and thereby also on its current state.

The phase change at the Inner Core Boundary (ICB) would allow to constrain the temperature at the ICB if the melting temperature of the material was known at the given pressure. As outlined above, there is an uncertainty about the core composition, which translates into an uncertainty regarding the temperature of the core. In Table 2.1 the temperatures at the inner core and the core-mantle boundary, which are assumed in five different studies, are specified. The references in Table 2.1 differ by approximately 1000 K for the temperature at the inner core boundary. For the temperature at the core-mantle boundary, the difference is approximately 475 K. This large span illustrates the challenges in constraining the thermal state of the core. Apart from the unknown composition, high pressures in the core, ranging from 136 GPa to 360 GPa, represent an additional challenge, because the material properties of the core's main constituent, iron, are far from being well established for the thermodynamic state of the inner and outer core [Olson (2015)].

Experimentalists try to reproduce the high pressure and high temperature state in the core using laser-heated diamond anvil cells [Mao and Mao (2015)]. This allows to determine, for example, phase transitions in solid iron at pressures up to 80 GPa [Mao et al. (1998)]. While experiments at ambient temperatures and high pressures or at high temperatures and ambient pressures are possible with solids, the experimental reproduction of core conditions with high temperatures and high pressures in the same experiment is very challenging or even impossible [Vočadlo (2015)]. Nevertheless, material properties of solid and liquid iron under core conditions are obtained from *ab initio* calculations, where SCHRÖDINGER's equation is solved for a collection of atomic nuclei and electrons. Various studies

apply density functional theories or a combination of *ab initio* calculations and molecular dynamics to determine material properties like, *e.g.*, melting curves, the viscosity, the electrical and thermal conductivity and the coefficient of thermal expansion at core conditions, see Silvestrelli, Alavi, and Parrinello [1997]; de Wijs et al. [1998]; Alfè, Gillan, and Price [1999]; Vočadlo et al. [2003]; Pozzo et al. [2012] among others.

The large span of the temperatures in Table 2.1 is not only related to an uncertainty regarding the thermodynamic properties and material parameters but also to a lack of information on the thermal and compositional evolution and the current state of the outer core. Especially, the thermal evolution of the core represents a problem, that is challenging geophysicists for more than 50 years. The processes in the outer core are divided usually into a slow adjustment to a configuration of equilibrium and fast fluctuations due to convective instabilities in the system. While the latter are modeled through thermal and compositional convection that is independent of the surrounding regions, the determination of the slow (thermal) evolution of the outer core is coupled to the inner core and the mantle. The release of latent heat through a growing inner core and a possible partial melting at the core-mantle boundary illustrate that the long-term evolution is a problem, where boundary effects play an important role. In fact, thermochemical boundary layers are believed to be present at the top and the bottom of the outer core and are the subject of recent research efforts, which are presented in the following.

As outlined above, boundary effects are important for the slowly evolving state. This in turn has consequences in relation to the convection of the core fluid. The convective motion of the fluid is mathematically described as a perturbation from a slowly evolving so-called “adiabatic reference state,” which is discussed in detail in Sect. 2.7. Therefore, a certain amount of information about this reference state is required for an accurate description of the convective motion. It is believed that, for example, the growth of the inner core by secular cooling not only releases latent heat, but also yields an increased concentration of light elements at the inner core boundary. It is therefore still under debate whether the convective motion is driven primarily by compositional buoyancy, stemming from an enrichment of light elements at the inner core boundary, or by thermal buoyancy due to a temperature gradient. Moreover, the role of radioactive heat is not constraint well. However, since convection drives the geodynamo, it should be possible to detect a thermochemical boundary layer at the core-mantle boundary in the geomagnetic field. A detection at the inner core boundary is only possible using seismic analyses because only the magnetic field at the core-mantle boundary is observable.

Regarding a boundary layer at the inner core boundary of the Earth, a so-called *F*-layer was already proposed in the 1950s and its existence was established by seismologists from anomalies in the *P*-wave velocity [Souriau and Poupinet (1991); Adam and Romanowicz (2015)]. The thickness of this layer is estimated to range from 150 km to 300 km. According to Gubbins, Masters, and Nimmo, the layer is a slurry, *i.e.*, a suspension of solid particles in the liquid, which they modeled by

constraining the temperature to the liquidus temperature of the mixture [Gubbins, Masters, and Nimmo (2008)]. This model is based on mixture theory for a binary FeO alloy, but it ignores convective motions of light element (oxygen) in the layer. Therefore, Wong, Davies, and Jones extended it by including melting and freezing of the material to allow frozen iron particles to fall under the influence of gravity [Wong, Davies, and Jones (2018)]. They find that their model for the  $F$ -layer is stably stratified and matches estimates for the temperatures and heat flux transferred across the layer.

Apart from the  $F$ -layer at the inner core boundary, a stably stratified thermochemical boundary layer is believed to be present at the core-mantle boundary. The existence of such a layer was first proposed in the late 1970s by Bullard and Gubbins [Bullard and Gubbins (1977)]. Later Braginsky argued that Magnetic ARCHIMEDEAN–CORIOLIS waves (MAC waves) could justify the existence of such a layer, because their period could match decadal variations in the secular variation of the magnetic field of the Earth [Braginsky (1993)]. He called this layer the “hidden ocean of core” and identified the thickness and the buoyancy frequency as the two parameters that govern the MAC wave solutions. The buoyancy frequency  $N$ , which is also referred to as the BRUNT–VÄISÄLÄ frequency, is a parameter that characterizes the strength of the stratification. Note that the underlying concept of static stability is discussed in Appendix A.

The existence and temporal evolution of the stratified layer was studied using a linear thermodynamic model for a binary mixture by Lister and Buffett. In this study, it was shown that a stratified layer at the core-mantle boundary might be present, if the heat flux across the core-mantle boundary is less than that of the so-called “adiabatic reference state” or if light mantle material is molten and dissolved in the core [Lister and Buffett (1998)]. Based on their model, the authors found that the thickness of a thermally stratified layer is approximately 100 km, whereas a compositionally stratified layer would be significantly thinner. However, the buoyancy frequency for the thin compositionally stratified layer is rather large compared to that of the thick thermally stratified layer. In subsequent studies, the formation of a stratified transition region by barodiffusion of oxygen and implications for the  $P$ -wave velocity in the core-mantle region were drawn [Braginsky (2006); Buffett and Seagle (2010)]. The role of barodiffusion was further investigated using models with different compositions of oxygen, sulfur and silicon by Gubbins and Davies [Gubbins and Davies (2013)]. They studied the diffusion of these elements in case of vanishing mass fluxes at the core-mantle boundary and obtained a stably stratified layer with thickness of approximately 100 km and a buoyancy frequency of  $N = 25\Omega$ , where  $\Omega$  denotes the standard rate of rotation of the Earth’s mantle [Gubbins and Davies (2013)]. Another mechanism that may yield a stratified layer at the core-mantle boundary is due to the precipitation of magnesium from the core [O’Rourke and Stevenson (2016)]. This chemical interaction mechanism occurs at the top of the core and is mainly regarded by O’Rourke and Stevenson as an additional source of energy for powering the geodynamo. Precipitated material is transported to the core-mantle boundary

because of the high density contrast between the precipitated magnesium and the core material. Therefore, a distinct chemically heterogeneous layer in form of a suspension likewise to the  $F$ -layer at the inner core boundary may form at the core-mantle boundary, which has a pronounced density variation in comparison to the remainder of the core.

Apart from theoretical work related to the formation of the stratified layer at the core-mantle boundary two studies make use of observational data in order to confirm its existence. In a first study by Buffett the amplitudes of magnetic ARCHIMEDES-CORIOLIS wave modes in a stratified layer were reconstructed from core-flow models, that are based on geomagnetic observations. More precisely, only the azimuthal component of the velocity, *i.e.*,  $v_\varphi$ , was used to fit MAC waves. The velocity field resulting from the fitted MAC waves then also has both a radial and a polar component, *i.e.*,  $v_r$  and  $v_\theta$ , which means that the convective transport of the magnetic field towards the polar regions occurs. This polar flow can be quantified by fluctuations in the dipole field. Finally, it could be shown, that a reconstruction of the altered magnetic field matches the fluctuations in the dipole component fairly well [Buffett (2014)]. In a subsequent follow-up paper the results related to MAC waves were extended and it was shown that these waves may account partially for observed fluctuations in the length of day [Buffett, Knezek, and Holme (2016)]. Moreover, the authors argue that the electromagnetic torque on the core-mantle boundary that is generated by the MAC waves is sufficiently large in order to yield variations in the length of day.

In addition to these studies providing evidence for the stratified layer from observations, several numerical studies have also been conducted in the recent past. A stratified layer was mimicked in numerical dynamo models by adding an artificial term to the equation governing the temperature. Using this relatively simple approach, it was found that the geodynamo fails, *i.e.*, the magnetic field vanishes at large times, if the layer is too thick [Nakagawa (2015)]. In two studies, Olson, Landeau, and Reynolds investigated the influence of stratification and a heterogeneous core-mantle boundary heat flux and compared the resulting magnetic field from their simulations to one of geomagnetic field models [Olson, Landeau, and Reynolds (2017); Olson, Landeau, and Reynolds (2018)]. They find that a stratified layer with a thickness of less than 400 km and a buoyancy frequency of  $N = 2\Omega$  is plausible if reversed flux patches of the magnetic field close to the poles are considered.

In contrast to the previous studies, a non-magnetic numerical model was used by Bouffard et al. to study the possible formation of a stratified layer at the core-mantle boundary. This model is entirely based on chemical convection and uses a particle method to avoid the solution of a hyperbolic transport equation, which results for a vanishing diffusion coefficient [Bouffard et al. (2019)]. However, due to the non-realistic parameters in their numerical model when compared to estimates for the Earth, a direct comparison of numerical with observational results regarding the thickness of the stratified layer and the strength of the stratification is challenging. A second study that is based on non-magnetic thermal convection

**Table 2.2:** Geometric and physical properties of the outer core of the Earth, values taken from [Olson (2015)]. The subscripts CMB and ICB refer to the core-mantle boundary and the inner core boundary, respectively.

Property	symbol	Value/range
core-mantle boundary radius	$R_{\text{CMB}}$	3480 km
inner core boundary radius	$R_{\text{ICB}}$	1220 km
core-mantle boundary gravity	$g_{\text{CMB}}$	$10.68 \text{ m s}^{-2}$
core-mantle boundary pressure	$p_{\text{CMB}}$	136 GPa
density	$\rho$	$1.09 \times 10^4 \text{ kg m}^{-3}$
kinematic viscosity	$\nu$	$(0.01 \text{ to } 100) \times 10^{-5} \text{ m}^2 \text{ s}^{-1}$
thermal expansion coefficient	$\alpha$	$(1.1 \text{ to } 1.9) \times 10^{-5} \text{ K}^{-1}$
thermal diffusivity	$\kappa$	$(2 \text{ to } 8) \times 10^{-6} \text{ m}^2 \text{ s}^{-1}$
electrical conductivity	$\sigma$	$(3 \text{ to } 7) \times 10^5 \text{ S m}^{-1}$

uses a heterogeneous core-mantle boundary heat flux that is derived from seismic observations [Mound et al. (2019)]. This model predicts the formation of regional stratified layers with buoyancy frequencies that are comparable to those of other studies [Mound et al. (2019)].

In summary, seismology and geodesy allow to constrain the geometry, the density, the pressure, and the gravity field of the outer core of the Earth. There is an agreement that the material in the outer core is a liquid, whose main constituent is iron. The magnetic field of the Earth is generated by a dynamo process in the outer core. This process is driven by vigorous convection of the core fluid resulting in a turbulent small-scale flow, which induces electric currents and generates a magnetic field. The source that drives the convection is still under debate. However, thermal buoyancy stemming from primordial heating, *i.e.*, internal energy generated during the formation of the Earth, and compositional buoyancy arising from inner core solidification, which releases (latent) heat and light elements, represent two primary components that power the convective process [Jones (2007)]. A third source for convection might be the presence of radioactive potassium ( $^{40}\text{K}$ ) and heat generated by its radioactive decay [Jones (2007)].

As outlined in this section, there are several uncertainties related to the outer core and its properties. However, the unique feature, that the core is generating the magnetic field of the Earth, allows to estimate the core flow, which in turn allows to infer some properties of the core fluid [Jault and Le Mouél (1989)]. In Table 2.2 some geometric and material properties of the outer core are listed, which will be used in the context of this manuscript.

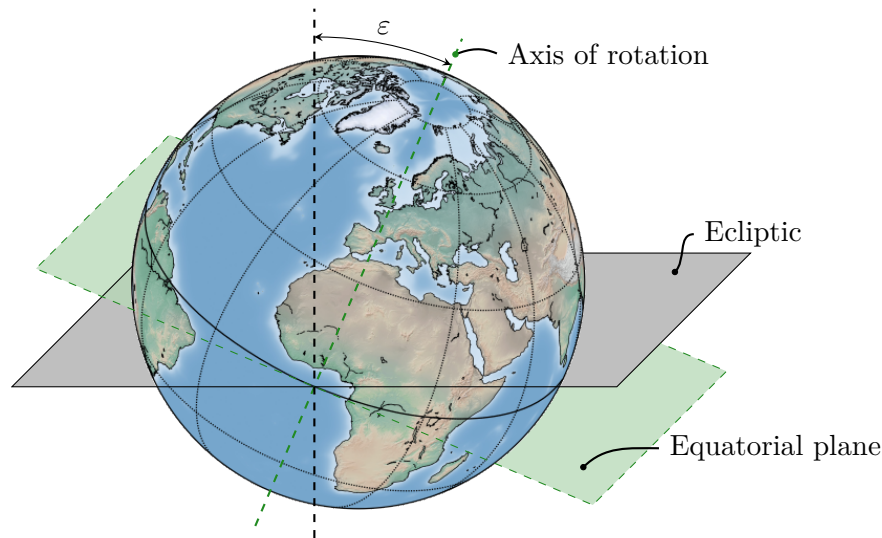


**Figure 2.2:** Reference planes and obliquity  $\epsilon$  of the Earth. Note that the axis of rotation is perpendicular to the equatorial plane.

## 2.2 Rotational dynamics of the Earth

The dynamics of the Earth as an entity is commonly described in the framework of rigid body mechanics. This motion of the Earth consists of the motion of its center of mass relative to the Sun and of its rotational motion, which changes the orientation of the Earth with respect to the Sun. Regarding its orientation, the obliquity of the Earth is the most prominent feature. As shown in Fig. 2.2, the obliquity  $\epsilon$  is the angle between the axis of rotation and the normal of the ecliptic. The ecliptic is the orbital plane of the Earth, *i.e.*, the plane, in which the center of mass of the Earth is moving around the Sun. The obliquity of the Earth is approximately  $23^\circ$  [Munk and MacDonald (1975)].

The orientation of the Earth with respect to the Sun is not fixed, but it is changing over time. This manifests itself in a precession and a nutation of the Earth-related axis of rotation with respect to the normal of the ecliptic. On the Earth, the precession can be observed, for example, as an earlier occurrence of equinoxes and solstices compared to previous years. A mathematical description of the orientation requires an exact definition of a frame of reference. There are several frames of reference in use like the International Terrestrial Reference Frame (ITRF) or the World Geodetic System (WGS84), whose definitions are exactly specified in standards, see Petit and Luzum [2010] and IERS [2014]. A detailed discussion of these frames of reference is out of the scope of this section, but a qualitative description of commonly used frames is given in the following.

Three types of reference frames are widely used in geodesy: an ecliptic celestial, a geocentric celestial and a terrestrial frame of reference [Dehant and Mathews (2015)]. All of these frames share the center of mass of the Earth as their origin.

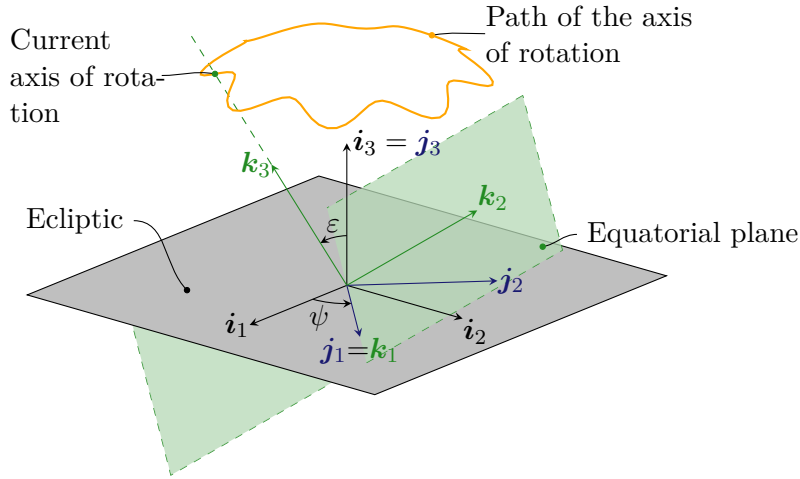


**Figure 2.3:** Precession and nutation of the Earth and related frames of reference. Note that the path of the axis of rotation does not correspond to the that of the Earth. The amplitude of the nutation oscillations is exaggerated.

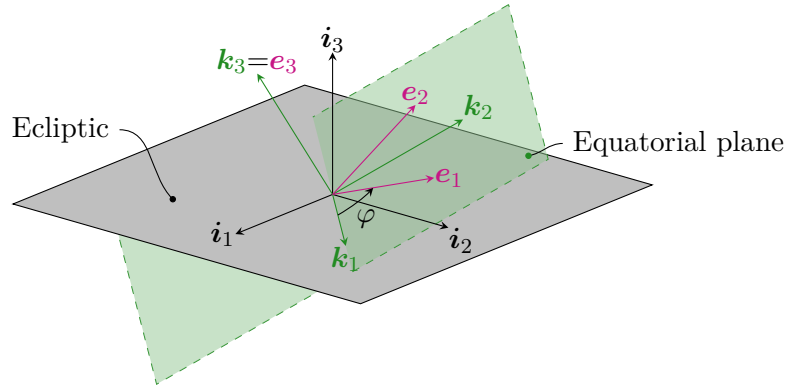


**Figure 2.4:** Rotation of the Earth and related frames of reference. Note that  $\mathbf{k}_3$  and  $\mathbf{e}_3$  are parallel to the current axis of rotation of the Earth.

The basis vectors of the ecliptic celestial frame of reference shall be denoted by  $\mathbf{i}_m$ ,  $m = 1, 2, 3$ , where  $\mathbf{i}_1$  and  $\mathbf{i}_2$  lie in the ecliptic and  $\mathbf{i}_3$  is parallel to a normal vector of the ecliptic, see Fig. 2.3. The basis vectors of an intermediate frame of reference are denoted by  $\mathbf{k}_m$ , where  $\mathbf{k}_1$  and  $\mathbf{k}_2$  lie in the equatorial plane and  $\mathbf{k}_3$  is perpendicular to this plane. As shown in Fig. 2.3, the ecliptic and the intermediate frame are related by two subsequent elementary rotations. First, a rotation around the axis  $\mathbf{i}_3$  is performed and then a second rotation about the newly obtained axis  $\mathbf{j}_1$  follows, see Fig. 2.3. The reference plane of the intermediate frame is the instantaneous equatorial plane. The intermediate frame coincides almost with the geocentric celestial frame of reference, which uses the equatorial plane of January 1, 2000 at 12:00 UT as a reference [Dehant and Mathews (2015)].

The rotational dynamics of the Earth is described by the balance of moment of

momentum in the terrestrial frame. While the framework of rigid body dynamics is sufficient to describe the dynamics of the Earth up to first order, an enhanced framework considering, *e.g.*, a deformable Earth, is required to explain the observed dynamics. Broadly speaking this enhanced framework would be given by continuum mechanics, which in contrast to rigid body dynamics can describe, for example, the redistribution of mass due to a deformation. However, a continuum model of the Earth including its ocean and atmosphere is complex. Ocean and atmosphere are dynamical systems, which are coupled to the mantle and also have their own angular momentum. Tides, for example, perturb the gravity field and there is a reciprocal coupling of these perturbations with the ocean and the mantle. Besides the generated net torque, the tensor of moment of inertia is also perturbed. The interplay of these effects is complex and instead of using a continuum model it is customary to use the framework of rigid body dynamics and to describe deformations as perturbations from the reference state. These perturbations then manifest themselves as additional torques.

As mentioned above, the components of the tensor of moment of inertia,  $J_{ij}$ , are constant in the co-moving terrestrial frame for a rigid body and the equations governing the rotational dynamics are the EULER equations. They read

$$\mathbf{J} \cdot \dot{\boldsymbol{\omega}} + \boldsymbol{\omega} \times \mathbf{J} \cdot \boldsymbol{\omega} = \mathbf{M}, \quad (2.1)$$

where  $\boldsymbol{\omega}$  is the angular velocity vector and  $\mathbf{M}$  the resulting external torque with respect to the center of mass.

The EULER equations stated in Eq. (2.1) require a specification of the angular velocity in order to describe the rotational motion of the Earth. To this end, the angles  $\psi$ ,  $\varepsilon$  and  $\varphi$  related to the three successive transformations from the ecliptic celestial to the terrestrial reference frame are used, see Figs. 2.3 and 2.4. These angles are referred to as the EULER angles.

The composition of the three elementary rotations related to the angles  $\psi, \varepsilon$  and  $\varphi$  is also a EUCLIDIAN transformation and the orthogonal tensor,  $\mathbf{Q}$ , which relates the basis vectors of the  $\mathbf{i}$ -basis to those of the  $\mathbf{e}$ -basis, is given by

$$\mathbf{Q} = \mathbf{Q}_\varphi \cdot \mathbf{Q}_\varepsilon \cdot \mathbf{Q}_\psi, \quad (2.2)$$

where the elementary transformations  $\mathbf{Q}_\psi$ ,  $\mathbf{Q}_\varepsilon$  and  $\mathbf{Q}_\varphi$  are specified in Appendix B. As detailed there, the angular velocity tensor  $\boldsymbol{\Omega}$  may be obtained from the tensor  $\mathbf{Q}$  and is given by

$$\boldsymbol{\Omega} = \boldsymbol{\Omega}_\varphi + \mathbf{Q}_\varphi \star \boldsymbol{\Omega}_\varepsilon + (\mathbf{Q}_\varphi \cdot \mathbf{Q}_\varepsilon) \star \boldsymbol{\Omega}_\psi. \quad (2.3)$$

Here  $\boldsymbol{\Omega}_\psi$ ,  $\boldsymbol{\Omega}_\varepsilon$ ,  $\boldsymbol{\Omega}_\varphi$  denote the angular velocity tensors of the elementary transformations and the symbol  $\star$  denotes the RAYLEIGH product as defined Appendix B. The angular velocity vector  $\boldsymbol{\omega}$  is defined as the axial vector of the angular velocity tensor  $\boldsymbol{\Omega}$  and it can be shown that the RAYLEIGH product with a (proper) orthogonal tensor alters the axial vector of a tensor. Therefore, the angular velocity

vector can be expressed as

$$\boldsymbol{\omega} = \boldsymbol{\omega}_\psi + \mathbf{Q}_\varphi \cdot \boldsymbol{\omega}_\varepsilon + (\mathbf{Q}_\varphi \cdot \mathbf{Q}_\varepsilon) \cdot \boldsymbol{\omega}_\varphi, \quad (2.4)$$

where  $\boldsymbol{\omega}_\psi$ ,  $\boldsymbol{\omega}_\varepsilon$  and  $\boldsymbol{\omega}_\varphi$  denote the axial vectors of the angular velocity tensors  $\boldsymbol{\Omega}_\psi$ ,  $\boldsymbol{\Omega}_\varepsilon$  and  $\boldsymbol{\Omega}_\varphi$ , respectively. Note that a representation of the angular velocity vector in a common basis, *e.g.*, in the  $\mathbf{e}$ -basis, yields components, which are non-linear expressions with respect to the EULER angles, yet linear with respect to their time derivatives. However, with regards to Eq. (2.1) the components of the tensor of moment of inertia are known and constant in time with respect to the  $\mathbf{e}$ -basis, and therefore it is convenient to use this basis. If the angular velocity vector is expressed as  $\boldsymbol{\omega} = \omega_i \mathbf{e}_i$ , the components of Eq. (2.1) read

$$J_1 \dot{\omega}_1 + (J_3 - J_2) \omega_2 \omega_3 = M_1, \quad (2.5a)$$

$$J_2 \dot{\omega}_2 + (J_1 - J_3) \omega_1 \omega_3 = M_2, \quad (2.5b)$$

$$J_3 \dot{\omega}_3 + (J_2 - J_1) \omega_1 \omega_2 = M_3. \quad (2.5c)$$

These equations describe the rotational dynamics of the Earth in the rigid body framework. The EULER angles may be recovered from the time evolutions of  $\omega_1$ ,  $\omega_2$  and  $\omega_3$  by using Eq. (2.4) and consulting Appendix C. Keeping this in mind, terms like wobble, polar motion or true polar wander, see, *e.g.*, Dehant and Mathews [2015] and Munk and MacDonald [1975], are nothing else than changes in the orientation of the Earth, which are either reflected in the EULER angles or may also be expressed in terms of  $\omega_1$ ,  $\omega_2$  and  $\omega_3$ .

In Fig. 2.5 the temporal evolution of the orientation of the equatorial plane is shown from 1973 onwards. This orientation is represented in terms of deviations of the angles  $\psi$  and  $\varepsilon$  from their reference values, and the deviations are denoted by  $\Delta\psi$  and  $\Delta\varepsilon$ , respectively, see the caption of Fig. 2.5 for details. These angles describe the precession and nutation of the Earth. Note that in the geodesic literature  $\psi$  and  $\varepsilon$  are referred to as longitude and obliquity, respectively. The temporal evolution of both angles has a rich spectrum containing several frequencies. The evolution of  $\Delta\psi$  has a clear linear trend, which means that there is a constant precession with a period of approximately 26 000 years—the so-called precession of the equinox [Munk and MacDonald (1975)]. There may be a linear trend in the obliquity as well, but the slope would be much less than that related to the longitude. Note that several annual and sub-annual frequencies are present, both in the longitude and obliquity.

While Fig. 2.5 presents the orientation of the Earth, Fig. 2.6 shows the difference of the Length of Day (LOD) from the reference value of 86 400 s from 1973 onwards. Additionally, LOD time series of a longer period are presented and analyzed in Chap. 5. The LOD variation is the excess of the length of day with respect to the

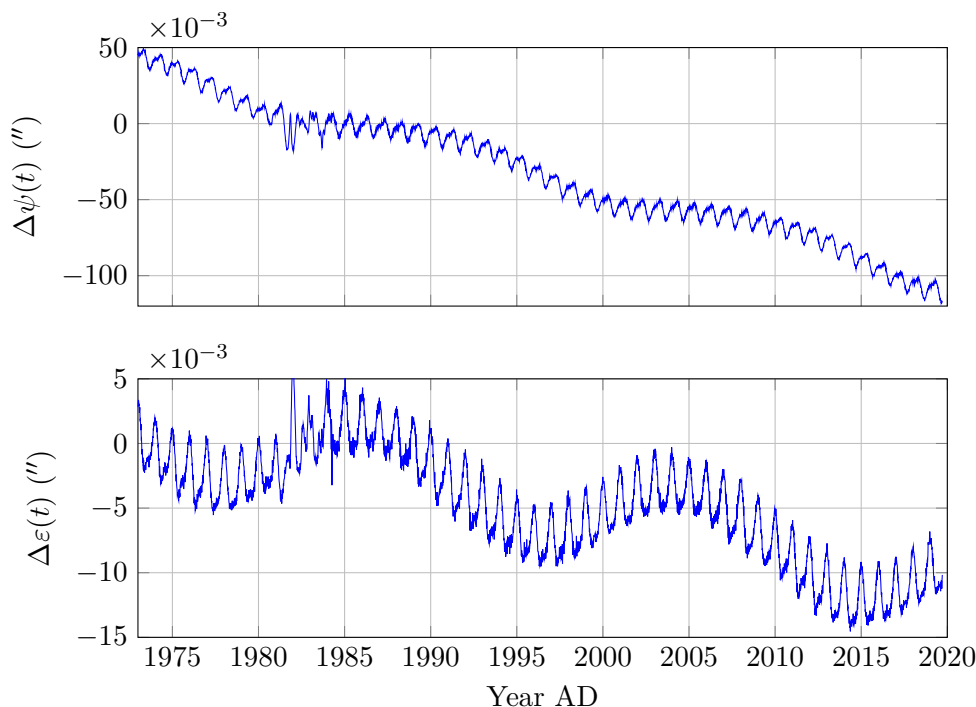


**Figure 2.5:** Orientation of the Earth in terms of a deviation of the angles related to precession and nutation (obliquity), *i.e.*,  $\Delta\psi(t) = \psi(t) - \psi_0$  and  $\Delta\varepsilon(t) = \varepsilon - \varepsilon_0$ , from their reference values,  $\psi_0$  and  $\varepsilon_0$ , respectively. The reference angle  $\psi_0$  is specified in the IAU 1976 System of Astronomical Constants [Duncombe, Sinclair, and Tucker (1977)]. The reference angle  $\varepsilon_0$  is specified in the IAU 1980 Theory of Nutation [Seidelmann (1982)]. The deviations are measured in milliarc seconds. The data is provided online by IERS [2019].

standard value and its relation to the spin angle  $\varphi$  is given by

$$\Delta\text{LOD} = \frac{2\pi}{\dot{\varphi}} - T_0 \quad \Leftrightarrow \quad \dot{\varphi} = \frac{2\pi}{T_0 + \Delta\text{LOD}}, \quad (2.6)$$

where  $\Delta\text{LOD}$  denotes the variations in the length of day and  $T_0 = 86\,400\text{ s}$  is the standard length of one day. The LOD variations are of the order of microseconds and frequencies with periods of, *e.g.*, a day, a month, one half of a year and a year are present. These short-period frequencies mainly stem from a tidal coupling to the Moon and from changes of the angular momentum of the atmosphere and the ocean [Hide and Dickes (1991)]. Approximately 90% of power of the short-period fluctuations amounts to the atmosphere and is associated to atmospheric waves [Volland (1996)]. Furthermore, by making use of harmonic analysis, LOD fluctuations due to tides can be accurately associated with distinct frequencies [Yoder, Williams, and Parke (1981)].

The apparent LOD fluctuations after removing the tidal and atmospheric com-

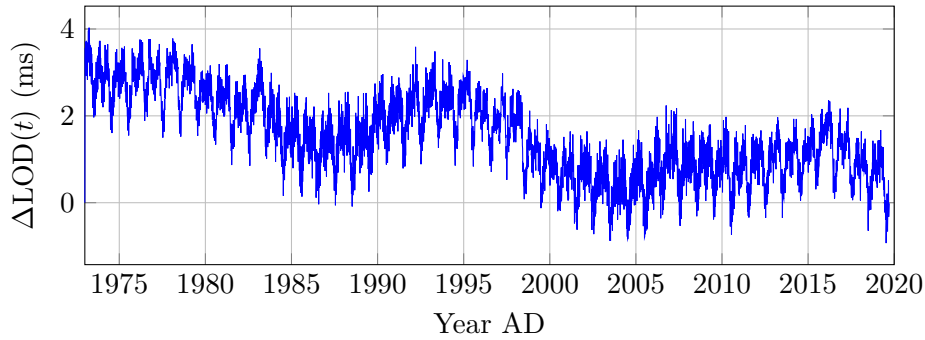


**Figure 2.6:** Variations in the Length of Day from 1973 onwards with respect to the reference value of 86 400 s. The data is provided online by IERS [2019].

ponents are commonly associated to a redistribution of mass or a net torque acting inside the Earth [Hide and Dickes (1991)]. Note that the Earth is not regarded as a rigid body when discussing processes in its interior and the LOD fluctuations are actually fluctuations in the rotation rate of the mantle. Regarding the redistribution of mass, tectonic motion of plates, melting of ice or mantle convection changes the moment of inertia of the mantle and the lithosphere on geological timescales. Moreover, Hide and Dickes mention that a deflection of the Core-Mantle Boundary (CMB) by the underlying fluid flow in the core which could also contribute to LOD variations [Hide and Dickes (1991)]. The review paper of Roberts and Aurnou states four principal processes contributing to the aforementioned net torque acting on the mantle: viscous, topographic, gravitational and magnetic coupling [Roberts and Aurnou (2012)]. The first one refers to a torque generated by stresses acting on the equipotential surface of the CMB. The second coupling mechanism considers a deviation of the CMB from an equipotential spherical surface and argues that a torque is generated by the pressure acting on the non-spherical surface. Gravitational coupling of the inner core and the mantle is the third mechanism. Regarding this mechanism, it is proposed that a torque is acting on the mantle because of anomalies in the gravity field, which are caused by an aspherical inner core. This coupling mechanism is supported by a super-rotation of the inner core, which can be inferred from seismology and excites harmonic oscillations between the inner core and the mantle [Song and Richards (1996); Buffett et al. (1996)]. Magnetic coupling is referred to as a torque generated by LORENTZ forces acting on the CMB if the mantle is electrically conducting. In 1970, Braginski proposed a relation between LOD fluctuations and oscillations of these forces due to torsional waves in the outer core [Braginski (1970)].

LOD fluctuations allow to draw inferences about processes in the core of the Earth. However, the treatment of the EULER equations (2.1) is simplified in this context. First, the dominant component of the angular velocity vector (of the mantle) is given by  $\dot{\varphi}$ . The magnitudes of the derivatives  $\dot{\psi}$  and  $\dot{\varepsilon}$  may be estimated roughly from Fig. 2.5 as  $10^{-8} \text{ d}^{-1}$ , if an amplitude of  $5 \times 10^{-3}''$  and a period of 1 d

are used. Hence, the rotation about the first principal axis is much faster than precession and nutation. This allows to approximate  $\boldsymbol{\omega}$  as  $\boldsymbol{\omega} \approx \dot{\varphi} \mathbf{e}_3$ . Apart from this, the Earth is an almost oblate spheroid, which means that the two smaller principal moments of inertia,  $J_1$  and  $J_2$ , are almost equal. According to Gross, their relative difference, *i.e.*,  $(J_2 - J_1)/J_1$ , is less than  $2 \times 10^{-5}$  for the whole Earth [Gross (2015)]. An estimation of this value for the mantle is not provided by Gross but it is very likely that the approximation  $J_1 \approx J_2$  may be applied for the whole Earth as well as for its mantle. Therefore, Eq. (2.5c) may be simplified to  $J_3 \ddot{\varphi} = M_3$ . Note that this equation describes the rotation of a rigid body about a fixed axis. Using a first order series expansion for the rate of the spin angle specified in Eq. (2.6) gives  $\omega_3 \approx \omega_0(1 - \Delta\text{LOD}/T_0)$ , where  $\omega_0 = 2\pi/T_0$ . Consequently, an approximation of Eq. (2.5c) up to first order with respect to LOD fluctuations reads

$$-J_3 \frac{\omega_0}{T_0} \frac{d}{dt}(\Delta\text{LOD}) = M_3. \quad (2.7)$$

This equation describes how LOD fluctuations are related to a net torque acting on the mantle. Note that this form of the law of moment of momentum should be interpreted as that for the mantle. Moreover, regarding long period LOD fluctuations, the torque is thought to be stemming either from a stress acting on the CMB or from a gravitational coupling of the mantle with the inner core. Therefore, this simplistic description of the rotation of the Earth is sufficient in order to draw conclusions from observable LOD fluctuations on processes occurring in the deep interior of the Earth.

## 2.3 Local balance equations of continuum thermomechanics

Continuum thermomechanics describes physical processes in a material on the continuum scale. For a material which does not possess internal rotational degrees of freedom, the fields of density,  $\rho$ , velocity,  $\mathbf{v}$ , and temperature,  $T$ , are commonly used to determine the state of the material during physical processes. These fields shall be piecewise continuous and differentiable inside regions, which are occupied by a material. However, at interfaces between two materials surface effects can become important and large gradients may occur, which cannot be resolved on a continuum scale. In order to resolve this loss of regularity, a so-called singular surface  $I$  is introduced. These surfaces may possess intrinsic physical properties and the (volumetric) fields may jump across them. In order to distinguish these two different regions, the term regular point is used to denote a point, where the fields are continuously differentiable, and the term singular point is used to denote a point, where a discontinuity occurs.

In the following the local balances of mass, linear momentum, and internal energy in regular and singular points are presented. In the course of this, intrinsic surface properties are neglected when balances in singular points are considered.

The local balances govern the temporal evolution of the involved fields and may be derived from global balances by applying REYNOLDS' transport theorem and the divergence theorem, see Müller [1985]; Liu [2002]; Hutter and Jöhnk [2004]; Müller [2014]; Dreyer [2015] and the seminal handbook article of Truesdell and Toupin for details.

In regular and singular points the local balance of mass reads

$$\frac{\partial \rho}{\partial t} + \nabla \cdot (\rho \mathbf{v}) = 0, \quad \mathbf{n} \cdot \llbracket \rho(\mathbf{v} - \mathbf{w}_I) \rrbracket = 0. \quad (2.8)$$

In the latter equation,  $\mathbf{n}$  denotes the outward unit normal vector of the interface  $I$  and  $\mathbf{w}_I$  its velocity. Furthermore,  $\llbracket \bullet \rrbracket$  represents the jump operator, which describes the difference of the limit values of a quantity from two opposite sides of the interface.

The local balance law of linear momentum is given by

$$\frac{\partial(\rho \mathbf{v})}{\partial t} + \nabla \cdot (\mathbf{v} \otimes \rho \mathbf{v}) = \nabla \cdot \boldsymbol{\sigma} + \rho \mathbf{f} + \mathbf{f}^{(\text{EM})}, \quad (2.9)$$

$$\mathbf{n} \cdot \llbracket (\mathbf{v} - \mathbf{w}_I) \otimes \rho \mathbf{v} - \boldsymbol{\sigma} \rrbracket = \mathbf{f}_I^{(\text{EM})}, \quad (2.10)$$

where  $\boldsymbol{\sigma}$  denotes the CAUCHY stress tensor. The body force (density) is decomposed into a part  $\mathbf{f}^{(\text{EM})}$ , which is acting in the presence of electromagnetic fields, and a part  $\mathbf{f}$ , which is independent of electromagnetic fields. The former is included to model electromechanical coupling. Equation (2.10) is the balance of linear momentum in singular points and  $\mathbf{f}_I^{(\text{EM})}$  denotes the electromagnetic surface force density.

As discussed by Hutter, van de Ven, and Ursescu, electromechanical coupling is controversially discussed in the literature for several reasons [Hutter, van de Ven, and Ursescu (2006)]: First, the transformations, which are used to transform the equations governing mechanics and electrodynamics, are the EUCLID and the LORENTZ transformation, respectively. These are fundamentally different. Second, electromagnetic fields and hence electromagnetic body forces may be separated into near and far fields and into forces acting on a short and a long range. In the balance of linear momentum, these two contributions are represented by a stress tensor and force densities. However, the decomposition of the electromagnetic force is not unique because parts of the electromagnetic force may be expressed as the divergence of a stress and added to the stress tensor. This conundrum is referred to as the ABRAHAM–MINKOWSKI controversy. Third, there is a large variation of formulations of the MAXWELL equations for polarizable and magnetizable materials in the literature and each formulation entails its own set of variables [Hutter, van de Ven, and Ursescu (2006)].

In this work, electromechanical coupling shall not be addressed in greater detail but the coupling model shall be presented and discussed. One way to approach electromechanical coupling is to postulate an electromagnetic momentum density in a first step and to derive a balance for the electromagnetic momentum density

by manipulating the MAXWELL equations algebraically in a second step. The third and last step is to require that the sum of electromagnetic and mechanical momentum is conserved, which results in an expression for the electromagnetic force density [Müller (1985); Reich, Rickert, and Müller (2017)]. As a consequence the CAUCHY stress tensor does not contain electromagnetic contributions. In this work, the LORENTZ force model is applied, *i.e.*,  $\mathbf{f}^{(\text{EM})} = q_f \mathbf{E} + \mathbf{J}_f \times \mathbf{B}$ . The LORENTZ force model does not imply severe restrictions in the context with the outer core of the Earth, because the material in this region is a fluid consisting of liquid iron and, in general, a fluid is considered to be neither polarizable nor magnetizable. In this case, all commonly used electromagnetic force models reduce to the LORENTZ model if magnetization and polarization vanish [Reich (2017)].

A last comment regarding Eq. (2.9) concerns the CAUCHY stress tensor, which shall be symmetric, *i.e.*,  $\boldsymbol{\sigma} = \boldsymbol{\sigma}^T$ . If the spin, the couple stresses and the volume couples vanish, the balance of moment of momentum and the balance of moment of linear momentum are equivalent [Müller (2014)]. In this case, a subtraction of both balances yields  $\overset{(3)}{\boldsymbol{\epsilon}} \cdot \boldsymbol{\sigma} = \mathbf{0}$  and hence the CAUCHY stress tensor is symmetric. Regarding the electromechanic coupling problem discussed above, it should be noted that the balance of moment of momentum presented by Müller could be supplemented by an electromagnetic volume couple. In this case, the line of argument to obtain a symmetric CAUCHY stress tensor fails. However, the discussion of electromechanical coupling with respect to moment of momentum would require an additional electromagnetic moment of momentum and is beyond the scope of this work. Therefore, the symmetry of the CAUCHY stress tensor is strictly speaking an assumption.

Considering thermodynamics, the first law of thermodynamics is expressed in terms of the balance of internal energy

$$\frac{\partial(\rho u)}{\partial t} + \nabla \cdot (\rho u \mathbf{v}) = -\nabla \cdot \mathbf{q} + \boldsymbol{\sigma} \cdot \mathbf{d} + \rho \hat{r} + \hat{r}^{(\text{EM})}, \quad (2.11)$$

$$\mathbf{n} \cdot \llbracket \rho u (\mathbf{v} - \mathbf{w}_I) + \mathbf{q} \rrbracket = \hat{r}_I^{(\text{EM})}, \quad (2.12)$$

where  $u$  denotes the internal energy and  $\mathbf{q}$  the heat flux and  $\mathbf{d}$  the symmetrized velocity gradient. The symmetry of  $\mathbf{d}$  is due to the symmetry of the stress tensor. The thermal power was also decomposed into a part,  $\hat{r}^{(\text{EM})}$ , which is the power due to presence of electromagnetic fields, and a part,  $\hat{r}$ , which is independent of them. Furthermore,  $\hat{r}_I^{(\text{EM})}$  is the electromagnetic surface power.

This decomposition is analogous to that for the balance of linear momentum and also involves similar problems for the electromechanical coupling as discussed above. In the same manner as for the electromagnetic force density an electromagnetic energy density can be postulated and a related balance equation may be derived from the MAXWELL equations. Then the electromagnetic thermal power can be derived by postulating that the total energy, *i.e.*, the sum of electromagnetic, mechanical and internal energy, is conserved [Reich and Müller (2018)]. In this work, the JOULE heating  $\hat{r}^{(\text{EM})} = \mathbf{j}_f \cdot (\mathbf{E} + \mathbf{v} \times \mathbf{B})$  is used, which is obtained if

POYNTING's theorem serves as the balance of electromagnetic energy and if the LORENTZ force model is applied [Reich and Müller (2018)]. Note that  $\mathbf{j}_f$  refers only to the diffusive part of the free current.

Hitherto, the local balance equations of continuum thermodynamics have been expressed in the form as they emerge from global balances—the so-called conservative form. However, the introduction of the material derivative and the substitution of the balance of mass in Eqs. (2.9) and (2.11) allow to recast these equations as

$$\frac{d\rho}{dt} = -\rho(\nabla \cdot \mathbf{v}), \quad (2.13)$$

$$\rho \frac{d\mathbf{v}}{dt} = \nabla \cdot \boldsymbol{\sigma} + \rho \mathbf{f} + q_f \mathbf{E} + \mathbf{J}_f \times \mathbf{B}, \quad (2.14)$$

$$\rho \frac{du}{dt} = -\nabla \cdot \mathbf{q} + \boldsymbol{\sigma} \cdot \mathbf{d} + \rho \hat{r} + \mathbf{j}_f \cdot (\mathbf{E} + \mathbf{v} \times \mathbf{B}). \quad (2.15)$$

In these equations, the explicit forms for the electromagnetic force and power were used. Here,  $q_f$  denotes the free electric charge density and  $\mathbf{j}_f$  the diffusive part of the free current density.

## 2.4 Maxwell's equations and the magnetohydrodynamic approximation

The MAXWELL equations are a set of equations, which describe the time evolution of the electromagnetic fields, *i.e.*, the electric field  $\mathbf{E}$  and the magnetic flux density  $\mathbf{B}$ . These equations result from FARADAY's law, which may also be interpreted as a conservation principle for the magnetic flux, GAUSS's or COULOMB's law and AMPÈRE's law with MAXWELL's addition. Jointly, GAUSS's and AMPÈRE's law describe the conservation of electric charge [Jackson (1975); Müller (2014)].

While there is a general agreement in the literature on the MAXWELL equations for the case of a vacuum, several formulations exist for the description of the evolution of the electromagnetic fields in continuous media. The different formulations for macroscopic media stem from the treatment of the balance of charge, see also the discussion in Sect. 2.3.

The MAXWELL equations for macroscopic media may be derived from their microscopic counterparts. The latter describe electromagnetic phenomena on a subatomic scale, where matter is modeled as an ensemble of molecules composed of nuclei and electrons. Jackson derives the macroscopic form of the MAXWELL equations by spatial averaging [Jackson (1975)]. He shows that the additional macroscopic fields of polarization and magnetization arise as the dipole components of the molecular charges and related currents in the averaging process. Hence, the polarization  $\mathbf{P}$  and the magnetization  $\mathbf{M}$  describe intrinsic electromagnetic properties of the material and are material functions in the macroscopic framework. Assuming that there are free charges in addition to the molecular charges and that the net charge of the molecules vanishes, Jackson shows that the macroscopic free

charge equals the spatially averaged microscopic charge [Jackson (1975)]. Moreover, by applying mixture theory, Dreyer shows that the balance of free charge can be obtained as a direct consequence of the balance of mass [Dreyer (2015)]. Therefore, the balance of charge may be formulated for free, intrinsic or total charges and three macroscopic variants of the MAXWELL equations are possible.

As suggested by spatial averaging, electric charges and currents are additively decomposed in the macroscopic framework into free and (virtual) intrinsic charges and currents.<sup>1</sup> Due to this additive decomposition, the potentials of total charge and total current,  $\mathbf{D}$  and  $\mathbf{H}$ , are additively decomposed as well. Hence,

$$\mathbf{D} = \mathfrak{D} - \mathbf{P}, \quad \mathbf{H} = \mathfrak{H} + \mathbf{M}, \quad (2.16)$$

where  $\mathfrak{D}$  and  $\mathfrak{H}$  are the potentials of free charge and free current. The potentials of total charge and total current are related to the electromagnetic fields by the MAXWELL–LORENTZ æther relations, which read

$$\mathbf{D} = \varepsilon_0 \mathbf{E}, \quad \mathbf{H} = \frac{1}{\mu_0} \mathbf{B}, \quad (2.17)$$

where the speed of light in vacuum is related to the vacuum permittivity,  $\varepsilon_0$ , and vacuum permeability,  $\mu_0$ , by  $c^2 = (\varepsilon_0 \mu_0)^{-1}$ . If the balance of total charge is applied, the macroscopic form of the MAXWELL equations reads [Jackson (1975); Kovetz (2000)]

$$\nabla \cdot \mathbf{B} = 0, \quad \frac{\partial \mathbf{B}}{\partial t} + \nabla \times \mathbf{E} = \mathbf{0}, \quad \nabla \cdot \mathbf{D} = q, \quad \frac{\partial \mathbf{D}}{\partial t} - \nabla \times \mathbf{H} = -\mathbf{J}, \quad (2.18)$$

where  $q$  is the total charge density and  $\mathbf{J}$  is the total electric current density.

The material in the outer core of the Earth is an electrically conducting fluid, which is neither polarizable nor magnetizable. Hence,  $\mathbf{P} \equiv \mathbf{0}$  and  $\mathbf{M} \equiv \mathbf{0}$ . Therefore, the last two equations of Eqs. (2.18) can be expressed as

$$\varepsilon_0 \nabla \cdot \mathbf{E} = q_f, \quad \varepsilon_0 \frac{\partial \mathbf{E}}{\partial t} - \frac{1}{\mu_0} \nabla \times \mathbf{B} = -\mathbf{J}_f, \quad (2.19)$$

where  $q_f$  denotes the free charge density and  $\mathbf{J}_f$  the free current density. Jump conditions describe the discontinuous transitions of the electromagnetic fields across interfaces, for example, at the core-mantle boundary. If the jump conditions corresponding to Eqs. (2.18) are simplified for  $\mathbf{P} \equiv \mathbf{0}$  and  $\mathbf{M} \equiv \mathbf{0}$ , one obtains

$$\begin{aligned} \mathbf{n} \cdot \llbracket \mathbf{B} \rrbracket &= 0, & w_\perp \llbracket \mathbf{B} \rrbracket + \mathbf{n} \times \llbracket \mathbf{E} \rrbracket &= \mathbf{0}, \\ \mathbf{n} \cdot \varepsilon_0 \llbracket \mathbf{E} \rrbracket &= q_f^f, & w_\perp \varepsilon_0 \llbracket \mathbf{E} \rrbracket - \mathbf{n} \times \frac{1}{\mu_0} \llbracket \mathbf{B} \rrbracket &= \mathbf{J}_f^f, \end{aligned} \quad (2.20)$$

---

<sup>1</sup>Note that this decomposition assumes that higher-order magnetic and electric multipole moments, *e.g.*, quadrupole, sextupole and octopole moments, may be neglected in the macroscopic framework.

where  $q_I^f$  and  $\mathbf{J}_I^f$  denote the interface charge and current densities. In summary, Eqs. (2.18)<sub>1,2</sub>, (2.19) and (2.20) constitute the basis for solving electrodynamic problems for materials with both, a vanishing polarization and magnetization.

### 2.4.1 OHM's law and the pointwise LORENTZ transformation

In order to actually determine the electromagnetic field, Eqs. (2.19) need to be supplemented with constitutive relations for the free charge density and the free current density. OHM's law is the constitutive equation for the free current density that is used in magnetohydrodynamics. In this section, OHM's law is discussed and derived for a moving conductor. In doing so, the LORENTZ transformation<sup>2</sup> is applied and the concept of sequential pointwise LORENTZ transformations is presented.

For an observer,  $\mathcal{O}'$ , for whom the material velocity  $\mathbf{v}'$  vanishes at the considered instance of time, OHM's law is given by

$$\mathbf{j}'_f = \sigma' \mathbf{E}' \quad \text{with} \quad \mathbf{j}'_f = \mathbf{J}'_f - q'_f \mathbf{v}'. \quad (2.21)$$

Note that this form of OHM's law only takes the diffusive part of the free current density into account. For an observer  $\mathcal{O}'$  the diffusive and total free current density are the same regardless of the free charge density, *i.e.*,  $\mathbf{j}'_f = \mathbf{J}'_f$ , because  $\mathbf{v}' = \mathbf{0}$ .

In order to describe the free charge density and the free current density for an observer,  $\mathcal{O}$ , who is moving relative to the observer  $\mathcal{O}'$ , a LORENTZ transformation is applied. For this special form of a LORENTZ transformation, charge and current densities transform as [Kovetz (2000)]

$$q_f = \gamma(q'_f - \frac{1}{c^2} \mathbf{w}' \cdot \mathbf{J}'_f), \quad \mathbf{J}_f = \mathbf{J}'_f - \gamma q'_f \mathbf{w}' + (\gamma - 1) \mathcal{P}'_{\parallel} \cdot \mathbf{J}'_f, \quad (2.22)$$

where  $\gamma = (1 - w'^2/c^2)^{-1/2}$  is the LORENTZ factor,  $\mathbf{w}'$  denotes the relative velocity between the two observers  $\mathcal{O}'$  and  $\mathcal{O}$  as observed by  $\mathcal{O}'$  and

$$\mathcal{P}'_{\parallel} = \frac{1}{w'^2} \mathbf{w}' \otimes \mathbf{w}' \quad (2.23)$$

is the tensor of the parallel projection.

The relative velocity is assumed to be small compared to the speed of light in vacuum, *i.e.*,  $w'^2 \ll c^2$ . This assumption allows to approximate the LORENTZ factor by  $\gamma \approx 1$  because  $\gamma = 1 + \mathcal{O}(w'^2/c^2)$ . Therefore, the last term in the

<sup>2</sup> The LORENTZ transformation between two observers with their respective space-time coordinates  $(t, \mathbf{x})$  and  $(t', \mathbf{x}')$  is given by [Scheck (2010)]

$$t' = \gamma(t - \frac{1}{c^2} \mathbf{w} \cdot \mathbf{x}), \quad \mathbf{x}' = \mathbf{x} - \gamma \mathbf{w} t + (\gamma - 1) \mathcal{P}_{\parallel} \cdot \mathbf{x}.$$

Here,  $\gamma = (1 - w^2/c^2)^{-1/2}$  is the LORENTZ factor and  $\mathbf{w}$  denotes the relative velocity between the two observers  $\mathcal{O}$  and  $\mathcal{O}'$ . Moreover, the parallel projector  $\mathcal{P}_{\parallel}$  is specified in Eq. (2.23) but here  $\mathbf{w}$  is used instead of  $\mathbf{w}'$ . This transformation is also referred to as a LORENTZ boost transformation.

second equation of Eqs. (2.22) can equally be neglected. Using the low velocity approximation and the constitutive relation in Eq. (2.21), the transformations in Eqs. (2.22) simplify to:

$$q_f = q'_f - \frac{\sigma'}{\epsilon_0^2} \mathbf{w}' \cdot \mathbf{E}', \quad \mathbf{J}_f = \sigma' \mathbf{E}' - q'_f \mathbf{w}'. \quad (2.24)$$

In order to determine the free charge density and the free current density for the observer  $\mathcal{O}$  it is required to specify the free charge density for the observer  $\mathcal{O}'$ . In electrostatics, the electromagnetic fields are stationary and the free current vanishes, *i.e.*,  $\mathbf{J}_f = \mathbf{0}$ . For this case, it can be shown that the free charge density vanishes inside the volume occupied by a conducting material and any excess charge is located on the surface of the volume [Jackson (1975); Kovetz (2000)]. This result does not generalize for the dynamic case; however, the subsequent scale analysis of the MAXWELL equations shows that the free charge density may be neglected under certain conditions.

In the following, a scale analysis is performed in order to obtain an estimate for the free charge density  $q'_f$ . Suppose the MAXWELL equations for the observer  $\mathcal{O}'$  are

$$\begin{aligned} \nabla' \cdot \mathbf{B}' &= 0, & \frac{\partial \mathbf{B}'}{\partial t'} + \nabla' \times \mathbf{E}' &= \mathbf{0}, \\ \epsilon_0 \nabla' \cdot \mathbf{E}' &= q'_f, & \epsilon_0 \frac{\partial \mathbf{E}'}{\partial t'} - \frac{1}{\mu_0} \nabla' \times \mathbf{B}' &= -\sigma' \mathbf{E}'. \end{aligned} \quad (2.25)$$

The second equation (FARADAY'S law) implies that the order of magnitude of the temporal variation of the magnetic flux density is equal to that of the spatial variation of the electric field. Hence,

$$\mathcal{O}\left(\frac{\partial \mathbf{B}'}{\partial t'}\right) = \mathcal{O}(\nabla' \times \mathbf{E}') \quad \Rightarrow \quad E'_{\text{ref}} = \frac{\ell'_{\text{ref}}}{t'_{\text{ref}}} B'_{\text{ref}}, \quad (2.26)$$

where  $B'_{\text{ref}}$  and  $E'_{\text{ref}}$  represent characteristic values for the strength of the magnetic flux density and the electric field. Furthermore,  $\ell'_{\text{ref}}$  and  $t'_{\text{ref}}$  refer to characteristic length scales and timescales, on which the electromagnetic field varies. The ratio of these two scales define a characteristic velocity, *i.e.*,  $c'_{\text{ref}} = \ell'_{\text{ref}}/t'_{\text{ref}}$ , which is assumed to be small compared to the speed of light, *i.e.*,  $c'^2_{\text{ref}} \ll c^2$ . This assumption on  $c'_{\text{ref}}$  allows to approximate the left-hand side of the last equation in Eqs. (2.25)

**Table 2.3:** Order of magnitude of the free charge density according to Eq. (2.29) for different values of the characteristic length scale and strength of the magnetic flux density. The conductivity is assumed as  $\sigma' = 10^6 \text{ S m}^{-1}$ .

$\mathcal{O}(q'_f) \text{ (A s m}^{-3}\text{)}$		$B'_{\text{ref}} \text{ (T)}$			
		$10^{-6}$	$10^{-3}$	1	$10^3$
$\ell'_{\text{ref}} \text{ (m)}$	$10^{-6}$	$10^{-6}$	$10^{-3}$	1	$10^3$
	$10^{-3}$	$10^{-12}$	$10^{-9}$	$10^{-6}$	$10^{-3}$
	1	$10^{-18}$	$10^{-15}$	$10^{-12}$	$10^{-9}$
	$10^3$	$10^{-24}$	$10^{-21}$	$10^{-18}$	$10^{-15}$

as

$$\begin{aligned}
\mathcal{O}\left(\varepsilon_0 \frac{\partial \mathbf{E}'}{\partial t'} - \frac{1}{\mu_0} \nabla' \times \mathbf{B}'\right) &= \mathcal{O}\left(\varepsilon_0 \frac{\partial \mathbf{E}'}{\partial t'}\right) + \mathcal{O}\left(\frac{1}{\mu_0} \nabla' \times \mathbf{B}'\right) \\
&= \varepsilon_0 \frac{E'_{\text{ref}}}{\ell'_{\text{ref}}} + \frac{1}{\mu_0} \frac{B'_{\text{ref}}}{\ell'_{\text{ref}}} \stackrel{(2.26)}{=} \varepsilon_0 \frac{\ell'_{\text{ref}} B'_{\text{ref}}}{\ell'^2_{\text{ref}}} + \frac{1}{\mu_0} \frac{B'_{\text{ref}}}{\ell'_{\text{ref}}} \\
&\stackrel{(\varepsilon_0 = \mu_0^{-1} c^{-2})}{=} \frac{1}{\mu_0} \frac{B'_{\text{ref}}}{\ell'_{\text{ref}}} \left(1 + \frac{c'^2_{\text{ref}}}{c^2}\right) \approx \frac{1}{\mu_0} \frac{B'_{\text{ref}}}{\ell'_{\text{ref}}}. \quad (2.27)
\end{aligned}$$

This result and the right-hand side of the last equation in Eqs. (2.25) allow to express the characteristic velocity as

$$\mathcal{O}\left(\varepsilon_0 \frac{\partial \mathbf{E}'}{\partial t'} - \frac{1}{\mu_0} \nabla' \times \mathbf{B}'\right) = \mathcal{O}(\sigma' \mathbf{E}') \quad \Rightarrow \quad c'_{\text{ref}} = \frac{1}{\mu_0 \sigma' \ell'_{\text{ref}}}. \quad (2.28)$$

Finally, the order of magnitude of the free charge density may be obtained from the third equation in Eqs. (2.25) by going through the following steps

$$\mathcal{O}(q'_f) = \mathcal{O}(\varepsilon_0 \nabla' \cdot \mathbf{E}') = \varepsilon_0 \frac{E'_{\text{ref}}}{\ell'_{\text{ref}}} = \varepsilon_0 \frac{B'_{\text{ref}}}{\ell'_{\text{ref}}} c'_{\text{ref}} \stackrel{(2.28)}{=} \frac{\varepsilon_0}{\mu_0} \frac{B'_{\text{ref}}}{\sigma' \ell'^2_{\text{ref}}}. \quad (2.29)$$

Table 2.3 shows that the order of magnitude of the free charge density according to Eq. (2.29) is not negligible if the characteristic length scale is of micrometer scale and if the magnitude of the magnetic flux density is larger than or equal to 1 T. However, for the outer core of the Earth, the magnetic field is not larger than 1 mT and the characteristic length scale is not less than 1 m. Therefore, the free charge density can be neglected in the co-moving system, *i.e.*,  $q'_f \approx 0$ . Note that the order of magnitude of the ratio of the characteristic velocity  $c'_{\text{ref}}$  to the speed of light in vacuum ranges from  $10^{-3}$  to  $10^{-15}$  for the characteristic length scales specified in Table 2.3. Hence, the assumption that  $c'^2_{\text{ref}} \ll c^2$  is not violated for the considered length scales.

The preceding discussion has shown that the observer  $\mathcal{O}'$  may neglect the free

charge density. As a consequence, Eqs. (2.22) simplify to

$$q_f = -\frac{\sigma'}{c^2} \mathbf{w}' \cdot \mathbf{E}' = \frac{\sigma'}{c^2} \mathbf{w} \cdot \mathbf{E}, \quad \mathbf{J}_f = \sigma' \mathbf{E}' = \sigma' (\mathbf{E} + \mathbf{w} \times \mathbf{B}), \quad (2.30)$$

where the transformation of the electric field was used and approximated according to [Kovetz (2000)]

$$\mathbf{E}' = \gamma (\mathbf{E} + \mathbf{w} \times \mathbf{B}) - (\gamma - 1) \mathcal{P}_{\parallel} \cdot \mathbf{E} \stackrel{(\gamma=1)}{\approx} \mathbf{E} + \mathbf{w} \times \mathbf{B}. \quad (2.31)$$

This transformation of the electric field implies that  $\mathcal{O}(\mathbf{E}) = (c'_{\text{ref}} + w') B'_{\text{ref}}$  and hence

$$\mathcal{O}(q_f) = \sigma' \left( \frac{c'_{\text{ref}} w'}{c^2} + \frac{w'^2}{c^2} \right) B'_{\text{ref}} \approx 0, \quad (2.32)$$

because the velocities,  $c'_{\text{ref}}$  and  $w'$ , are assumed to be much smaller than the speed of light. In conclusion, the free charge density observed by  $\mathcal{O}$  can also be neglected.

In the preceding discussion, the LORENTZ transformation was applied to transform the electromagnetic fields and the MAXWELL equations are invariant under all LORENTZ transformations. Therefore, using  $\sigma' = \sigma$  and the approximations  $q'_f \approx 0$  and  $q_f \approx 0$ , the MAXWELL equations for the observer  $\mathcal{O}$  take the form

$$\begin{aligned} \nabla \cdot \mathbf{B} &= 0, & \frac{\partial \mathbf{B}}{\partial t} + \nabla \times \mathbf{E} &= \mathbf{0}, \\ \nabla \cdot \mathbf{E} &= 0, & \varepsilon_0 \frac{\partial \mathbf{E}}{\partial t} - \frac{1}{\mu_0} \nabla \times \mathbf{B} &= \sigma (\mathbf{E} + \mathbf{w} \times \mathbf{B}). \end{aligned} \quad (2.33)$$

Note that the relative velocity of the two observers  $\mathbf{w}$  is still present in these equations and not the material velocity. This is due to the LORENTZ transformation, which relates the two observers, one of whom has  $\mathbf{v}' = \mathbf{0}$ .

Under a LORENTZ transformation the velocity transforms as

$$\mathbf{v} = \frac{\gamma_{\mathbf{v}'\mathbf{w}}^2}{\gamma} (\mathbf{v}' + (\gamma - 1) \mathcal{P}'_{\parallel} \cdot \mathbf{v}' - \gamma \mathbf{w}') \stackrel{(\gamma=1)}{\approx} \mathbf{v}' - \mathbf{w}', \quad (2.34)$$

where  $\gamma_{\mathbf{v}'\mathbf{w}}^{-1} = \sqrt{1 - \mathbf{v}' \cdot \mathbf{w}' / c^2}$ . As indicated, the low velocity approximation leads to the same transformation of the velocity as for a GALILEI transformation. Moreover,  $\mathbf{w} = -\mathbf{w}'$  holds and with  $\mathbf{v}' = \mathbf{0}$  the velocity  $\mathbf{w}$  is obtained as  $\mathbf{w} \approx \mathbf{v}$  and a simple substitution yields the usual form of the MAXWELL equations for a moving conductor. However, there are subtle problems with this simple substitution.

First,  $\mathcal{O}'$  observes a vanishing material velocity for one material point P at one instance of time  $t$ , *i.e.*,  $\mathbf{v}'(\mathbf{x}^{\text{P}}(t), t) = \mathbf{0}$ . At time  $t + \Delta t$  the material point P has a different velocity. If the observer  $\mathcal{O}'$  shall also observe a vanishing material velocity at time  $t + \Delta t$  it is accelerated. In this case, the simple LORENTZ transformation can no longer be applied because of the relative acceleration. Instead, the LORENTZ transformation becomes a linear integro-algebraic equation for an accelerated,

rotating frame of reference [Nelson (1987)]. In order to avoid this integro-algebraic transformation, it is customary to study a sequence of LORENTZ transformations between the three observers  $\mathcal{O}$ ,  $\mathcal{O}'$  and  $\mathcal{O}''$ , where the relative velocity between  $\mathcal{O}$  and  $\mathcal{O}''$  is given by  $\mathbf{w}'' = \mathbf{w}' + \Delta\mathbf{w}$  [Jackson (1975); Nelson (1987)]. In his textbook, Jackson assumes that the observers  $\mathcal{O}'$  and  $\mathcal{O}''$  are related by a linear relation, which is called an infinitesimal LORENTZ transformation, and shows that up to first order this transformation is given by the identity and terms, which are proportional to  $\gamma$  and  $\Delta\mathbf{w}/c$ . Applying the low velocity approximation the additional terms vanish and the infinitesimal LORENTZ transformation becomes the identity. Note that the assumption of a linear transformation between  $\mathcal{O}'$  and  $\mathcal{O}''$  is referred to as the concept of a “sequence of comoving inertial frames” [Nelson (1987)].

Second, applying the concept of differential LORENTZ transformations is contested for observers related by a rotation in the literature, see the discussion in the papers Pellegrini and Swift [1995]; Weber [1997]; Klauber [1998]; Klauber [1999]; Weber [1997] and Weber [1999]. However, a main part of the discussion is related to the question whether the theory of special relativity is applicable in a rotating frame and their effect is interpretable as the SAGNAC effect.<sup>3</sup> This is out of the scope of this work. In his comment regarding how to relativistically describe a rotating frame, Klauber argues:

“Only with use of the rotating frame itself (and associated transformations and metric) can one obtain internally consistent results that agree with all experiments. However, for the purposes of time dilation, mass-energy, and momentum calculations . . . , and Maxwell’s equations . . . , one can get away with using traditional special relativity and local Minkowski co-moving frames. That is, in these cases Nature conspires to make both the rotating (non-traditional) and co-moving (traditional) frame solutions produce the same result for lab observers. When it comes to matters of time synchronization, simultaneity, space (curvature), and Michelson-Morley/Sagnac-type experiments, however, then analysis must be confined to the rotating frame itself, otherwise the above-delineated inconsistencies and inexplicable ‘spurious’ experimental signals inevitably arise.” Klauber [1999]

Following these lines and applying the low-velocity LORENTZ transformation in the framework of sequentially co-moving reference frames allows to substitute the

---

<sup>3</sup>The SAGNAC effect refers to a phase shift of two light beams that travel in a rotating laser interferometer, where one of the beams travels clockwise and the other one counterclockwise with respect to the rotation of the interferometer. The effect is not observed in a non-rotating interferometer.

velocity  $\mathbf{w}$  by the material velocity  $\mathbf{v}$ . Hence,

$$\begin{aligned}\nabla \cdot \mathbf{B} &= 0, & \frac{\partial \mathbf{B}}{\partial t} + \nabla \times \mathbf{E} &= \mathbf{0}, \\ \nabla \cdot \mathbf{E} &= 0, & \varepsilon_0 \frac{\partial \mathbf{E}}{\partial t} - \frac{1}{\mu_0} \nabla \times \mathbf{B} &= \sigma(\mathbf{E} + \mathbf{v} \times \mathbf{B}).\end{aligned}\tag{2.35}$$

These equations describe the electrodynamics of moving conductors.

### 2.4.2 Magnetohydrodynamic approximation

Next, the magnetohydrodynamic approximation is applied to Eqs. (2.35). By the same line of arguments as those related to Eqs. (2.26), the relation  $E_{\text{ref}} = \ell_{\text{ref}} B_{\text{ref}} / t_{\text{ref}}$  may be established. Therefore, one has

$$\mathcal{O}\left(\varepsilon_0 \frac{\partial \mathbf{E}}{\partial t}\right) = \varepsilon_0 \frac{\ell_{\text{ref}}}{t_{\text{ref}}^2} B_{\text{ref}} = \frac{1}{\mu_0} \frac{c_{\text{ref}}^2}{c^2} \frac{B_{\text{ref}}}{\ell_{\text{ref}}},\tag{2.36}$$

where as usual  $c_{\text{ref}} = \ell_{\text{ref}} / t_{\text{ref}}$ . This result allows to neglect the temporal variation of the electric field relative to the spatial variation of the magnetic flux density, *i.e.*,

$$\mathcal{O}\left(\varepsilon_0 \frac{\partial \mathbf{E}}{\partial t}\right) \ll \mathcal{O}\left(\frac{1}{\mu_0} \nabla \times \mathbf{B}\right).\tag{2.37}$$

Applying this approximation to Eq. (2.35) results in

$$\begin{aligned}\nabla \cdot \mathbf{B} &= 0, & \frac{\partial \mathbf{B}}{\partial t} + \nabla \times \mathbf{E} &= \mathbf{0}, \\ \nabla \cdot \mathbf{E} &= 0, & -\frac{1}{\mu_0} \nabla \times \mathbf{B} &= \sigma(\mathbf{E} + \mathbf{v} \times \mathbf{B}).\end{aligned}\tag{2.38}$$

Furthermore, a substitution of the electric field in the second equation gives rise to the magnetic induction equation, which is the fundamental equation of magnetohydrodynamics

$$\frac{\partial \mathbf{B}}{\partial t} = \nabla \times (\mathbf{v} \times \mathbf{B}) + \nabla \times (\eta \nabla \times \mathbf{B}),\tag{2.39}$$

where  $\eta = (\mu_0 \sigma)^{-1}$  is the magnetic diffusivity. This equation describes the time evolution of the magnetic field in the core of the Earth and needs to be solved in combination with the constraint  $\nabla \cdot \mathbf{B} = 0$ .<sup>4</sup> The induction term, *viz.*, the first term on the right-hand side of Eq. (2.39), vanishes in the absence of a fluid motion. In this case, a parabolic equation results, which causes an initial magnetic seed field to simply decay in time.

---

<sup>4</sup>Note that the constraint  $\nabla \cdot \mathbf{B} = 0$  is naturally fulfilled if the right-hand side of Eq. (2.39) is evolved analytically. However, in a numerical framework this constraint requires special attention and its treatment is delicate.

Principal mechanisms related to the induction term may be interpreted by using a kinematic analogy. This analogy describes the stretching, twisting and folding of magnetic flux tubes and its effects on the magnetic field, see Childress and Gilbert [1995] and Roberts [2015] for further details. In this kinematic framework, for example, the helicity  $\mathbf{v} \cdot (\nabla \times \mathbf{v})$  has been identified as a parameter to quantify whether a flow can generate a dynamo. This indicates that a small-scale flow has the ability to generate a magnetic field. Nevertheless, solutions to the full magnetohydrodynamic problem with a self-sustaining dynamo were also found numerically for large-scale flows [Christensen et al. (2001)]. In the outer core of the Earth, the fluid flow has a multitude of scales and features that depend on the considered region. For example, due to the rotation of the Earth, the fluid motion inside an imaginary cylinder, that is aligned with the axis of rotation and has the radius of the inner core, is very different from the motion outside of this region. Therefore, it is challenging to exactly determine which type of flow is affecting what type of feature in the geomagnetic field.

Finally, the magnetic field in the mantle of the Earth and its transition at the core-mantle boundary are discussed. The conductivity of the lower mantle of the Earth is estimated by extrapolation from laboratory experiments to span several orders of magnitude [Shankland, Peyronneau, and Poirier (1993)]. Recent studies, which take the radial inhomogeneities related to mineral composition, pressure and temperature into account, state that the material with the highest conductivity is located at the core-mantle boundary and has a maximum conductivity of  $10 \text{ S m}^{-1}$  [Xu et al. (1998); Xu, Shankland, and Poe (2000)]. This value is at least four orders of magnitude smaller than that for the outer core, see Table 2.2. Therefore, the mantle is modeled as an insulator with a vanishing conductivity if the outer core of the Earth is considered. In this case, Eqs. (2.38) imply that the magnetic field in the mantle is a potential field. Hence,

$$\mathbf{B}_M = \nabla V_M, \quad \nabla^2 V_M = 0, \quad (2.40)$$

where  $V_M$  and  $\mathbf{B}_M$  denotes the magnetic scalar potential and the magnetic field in the mantle, respectively.

The transition of the magnetic field from the outer core to the mantle of the Earth is continuous, which means that the magnetic field of the core is coupled to a potential field in the mantle. This is a consequence of the jump conditions in Eqs. (2.20), because the normal component of the interface velocity vanishes, *i.e.*,  $w_\perp = 0$ , and an interface current density is neglected, *i.e.*,  $\mathbf{J}_I^f = \mathbf{0}$ . Moreover, the potential field due to the geodynamo decreases the larger the distance to the Earth becomes, which means that  $V_M \rightarrow 0$  for  $\|\mathbf{x}\| \rightarrow \infty$ . Consequently, the continuous transition of the magnetic field at the core-mantle boundary and the constraint for the magnetic potential in the mantle read

$$\mathbf{B}(\mathbf{x}) = \nabla V_M(\mathbf{x}), \quad \mathbf{x} \in \Gamma_{\text{CMB}} \quad \text{and} \quad \lim_{\|\mathbf{x}\| \rightarrow \infty} V_M(\mathbf{x}) = 0, \quad (2.41)$$

where  $\Gamma_{\text{CMB}}$  denotes the core-mantle boundary. In summary, the simultaneous solution of Eqs. (2.39), (2.40) and (2.41) would be required in order to describe the evolution of the magnetic field of the Earth. Note that the inner core of the Earth is treated as an insulator as well. However, some studies model instead the inner core as a conductor.

## 2.5 Constitutive equations for a viscous electrically conducting and heat conducting fluid

This section motivates the constitutive equations for a viscous electrically conducting and heat conducting fluid, which is experiencing thermal expansion and may be compressible. The objective is to derive thermodynamically consistent material functions for the CAUCHY stress  $\boldsymbol{\sigma}$ , the heat flux  $\mathbf{q}$ , the internal energy  $u$  and the (diffusive) free current density  $\mathbf{j}_f$  by applying the principles of material theory. While the necessary and sufficient set of principles is still under debate in the literature, commonly used principles are the principles of local action, determinism, material objectivity, and admissibility [Hütter (2017)]. Although the verbalization of these principles is similar in the literature, significant subtle differences arise regarding their mathematical formulation, especially for the principle of material objectivity [Glüge (2018)].

The principle of admissibility requires that the second law of thermodynamics is fulfilled by the governing (evolution) equations and material functions for all thermodynamic processes. In order to fulfill this principle, the procedure introduced by COLEMAN and NOLL is applied, which is based on the following entropy balance [Coleman and Noll (1963)]

$$\rho \frac{ds}{dt} = -\nabla \cdot \left( \frac{\mathbf{q}}{T} \right) + \frac{\rho \hat{r}}{T} + \xi. \quad (2.42)$$

Here,  $s$  denotes the entropy density,  $T$  the thermodynamic temperature, and  $\xi$  the entropy production. The second law of thermodynamics requires that the entropy production is non-negative, *i.e.*,  $\xi \geq 0$ . The characteristic feature of the COLEMAN-NOLL method is that the entropy flux and the entropy supply are assumed *a priori* as  $\mathbf{q}/T$  and  $\rho \hat{r}/T$ , respectively. This is more restrictive compared to, *e.g.*, the procedure of MÜLLER and LIU, in which the constraints regarding the entropy flux and supply are determined as well [Hutter and Jöhnk (2004)].

At this point, it is assumed that the coupling of thermomechanics and electrodynamics does not occur with respect to the material functions. This means that the thermomechanical material functions  $\hat{\boldsymbol{\sigma}}$ ,  $\hat{\mathbf{q}}$ ,  $\hat{u}$  and  $\hat{s}$  depend on thermomechanical variables only and the electrodynamic material function  $\hat{\mathbf{j}}_f$  depends on electrodynamic variables only. This separation of the variables of the material functions into thermomechanical and electromagnetic parts is very restrictive but simplifies the procedure. Kovetz presents an alternative approach to the entropy inequality for electrically conducting viscous fluids. His procedure follows that of

COLEMAN and NOLL, but the momentum density is considered as a material function and the balance of total energy is used to eliminate the thermal power [Kovetz (2000)]. This approach to electromechanical coupling is quite different in contrast to that presented in Müller [1985] and used in Sect. 2.3, because the question of electromechanical coupling is considered as one of material theory. Furthermore, note that OHM's law was used already in Sect. 2.4 and is not obtained as a result of an evaluation of the entropy inequality. However, it will be demonstrated that OHM's law complies with the entropy principle.

By substituting the thermal power,  $\hat{r}$ , from Eq. (2.15) into Eq. (2.42), the following relation can be established:

$$-\rho \left( \frac{dg}{dt} + s \frac{dT}{dt} \right) + \dot{p} - \frac{p}{\rho} \dot{\rho} + \boldsymbol{\sigma} \cdot \mathbf{d} - \frac{1}{T} \mathbf{q} \cdot \nabla T + \mathbf{j}_f \cdot (\mathbf{E} + \mathbf{v} \times \mathbf{B}) = \xi T \geq 0. \quad (2.43)$$

In this equation, the GIBBS free energy density,  $g = u - Ts + p/\rho$ , was introduced as a thermodynamic potential. However, other thermodynamic potentials like the HELMHOLTZ free energy,  $\psi = \hat{\psi}(\rho, T, \dots)$ , may also be used in the exploitation of the entropy inequality instead of the GIBBS free energy,  $g = \hat{g}(p, T, \dots)$ . In case of thermal expansion, the latter is more convenient, because the thermal equation of state is written as  $\rho = \hat{\rho}(p, T)$  or  $\rho = \hat{\rho}(T)$ . Hence, the density is not a state variable but instead the pressure is an element of the state space.

Next, the variables of the thermomechanical material functions are restricted to those for a simple viscous heat conducting fluid with thermal expansion and without a memory. Additionally, the variables are restricted according to the principle of material objectivity [Hutter and Jöhnik (2004)]. Then, the thermomechanical material functions have the following functional dependencies

$$\begin{aligned} \boldsymbol{\sigma} &= \hat{\boldsymbol{\sigma}}(p, \mathbf{d}, T, \nabla T), & \mathbf{q} &= \hat{\mathbf{q}}(p, \mathbf{d}, T, \nabla T), \\ u &= \hat{u}(p, \mathbf{d}, T, \nabla T), & s &= \hat{s}(p, \mathbf{d}, T, \nabla T). \end{aligned} \quad (2.44)$$

The GIBBS free energy density also has the same functional form, *i.e.*,  $g = \hat{g}(p, \mathbf{d}, T, \nabla T)$ , and its material time derivative is given by

$$\dot{g} = \frac{\partial \hat{g}}{\partial p} \dot{p} + \frac{\partial \hat{g}}{\partial \mathbf{d}} \cdot \dot{\mathbf{d}} + \frac{\partial \hat{g}}{\partial T} \dot{T} + \frac{\partial \hat{g}}{\partial \nabla T} \cdot (\nabla T) \cdot. \quad (2.45)$$

Using the mass balance, *i.e.*,  $\dot{\rho} = -\rho(\nabla \cdot \mathbf{v})$ , and the previous equation, Eq. (2.43) can be rewritten as

$$\begin{aligned} \left( 1 - \rho \frac{\partial \hat{g}}{\partial p} \right) \dot{p} - \rho \frac{\partial \hat{g}}{\partial \mathbf{d}} \cdot \dot{\mathbf{d}} - \rho \left( \frac{\partial \hat{g}}{\partial T} + s \right) \dot{T} - \rho \frac{\partial \hat{g}}{\partial \nabla T} \cdot (\nabla T) \cdot + \\ + (\boldsymbol{\sigma} + p\mathbf{1}) \cdot \mathbf{d} - \frac{1}{T} \mathbf{q} \cdot \nabla T + \mathbf{j}_f \cdot (\mathbf{E} + \mathbf{v} \times \mathbf{B}) = \xi T \geq 0. \end{aligned} \quad (2.46)$$

The inequality above is linear with respect to the material time derivatives of  $p$ ,  $\mathbf{d}$ ,  $T$ , and  $\nabla T$ . The fact that these time derivatives can have arbitrary values allows

to conclude that the factors preceding the material time derivatives of  $p$ ,  $\mathbf{d}$ ,  $T$ , and  $\nabla T$  vanish [Hutter and Jöhnik (2004)]. Hence,

$$\frac{1}{\rho} = \frac{\partial \hat{g}}{\partial p}, \quad s = -\frac{\partial \hat{g}}{\partial T}, \quad \frac{\partial \hat{g}}{\partial \mathbf{d}} = \mathbf{0}, \quad \frac{\partial \hat{g}}{\partial \nabla T} = \mathbf{0}. \quad (2.47)$$

Differentiating the first two equations with respect to  $\mathbf{d}$  and  $\nabla T$  and the last two equations with respect to  $p$  and  $T$  and using the symmetry of the second mixed derivatives of the function  $\hat{g}$ , yields

$$\frac{\partial \hat{\rho}}{\partial \mathbf{d}} = \mathbf{0}, \quad \frac{\partial \hat{\rho}}{\partial \nabla T} = \mathbf{0}, \quad \frac{\partial \hat{s}}{\partial \mathbf{d}} = \mathbf{0}, \quad \frac{\partial \hat{s}}{\partial \nabla T} = \mathbf{0}. \quad (2.48)$$

These relations imply  $\rho = \hat{\rho}(p, T)$ ,  $s = \hat{s}(p, T)$ ,  $u = \hat{u}(p, T)$ , which are a result of the entropy inequality. Due to the restrictions of functional dependencies above, the residual inequality reads

$$(\boldsymbol{\sigma} + p\mathbf{1}) \cdot \mathbf{d} - \frac{1}{T} \mathbf{q} \cdot \nabla T + \mathbf{j}_f \cdot (\mathbf{E} + \mathbf{v} \times \mathbf{B}) \geq 0. \quad (2.49)$$

The simple linear constitutive equations for the CAUCHY stress tensor, the heat flux, and the free current density for a fluid are given by NAVIER-STOKES' law, FOURIER's law and OHM's law as follows:

$$\boldsymbol{\sigma} = (-p + \lambda \operatorname{tr}(\mathbf{d}))\mathbf{1} + 2\mu \mathbf{d}^{\text{dev}}, \quad \mathbf{q} = -\kappa \nabla T, \quad \mathbf{j}_f = \sigma(\mathbf{E} + \mathbf{v} \times \mathbf{B}), \quad (2.50)$$

where  $\lambda$ ,  $\mu$ ,  $\kappa$  and  $\sigma$  are material functions to be specified and  $\mathbf{d}^{\text{dev}}$  denotes the deviatoric part of the symmetric velocity gradient. Substituting these linear relations into the residual inequality (2.49) yields:

$$\lambda \operatorname{tr}(\mathbf{d})^2 + 2\mu \mathbf{d}^{\text{dev}} \cdot \mathbf{d}^{\text{dev}} + \frac{1}{T} \kappa (\nabla T)^2 + \sigma(\mathbf{E} + \mathbf{v} \times \mathbf{B})^2 \geq 0. \quad (2.51)$$

Note that in this relation all summands are positive functions with respect to  $\mathbf{d}$ ,  $\nabla T$ , or  $\mathbf{E} + \mathbf{v} \times \mathbf{B}$ . Therefore the inequality is satisfied if the scalars  $\lambda$ ,  $\mu$ , and  $\kappa$  are positive functions of the thermomechanical variables and if  $\sigma$  is a positive function of the electromagnetic variables.

In summary, it was shown that the NAVIER-STOKES law, FOURIER law and OHM law are admissible material laws. What is missing is to supplement these laws by a thermal equation of state,  $\rho = \hat{\rho}(p, T)$ , and a caloric equation of state,  $u = \hat{u}(p, T)$  or  $s = \hat{s}(p, T)$ .

### 2.5.1 Caloric equation of state

In the following, the caloric equation of state is derived for a thermodynamically non-linear material response. In doing so, it turns out that the functions  $\hat{\rho}$ ,  $\hat{u}$  and  $\hat{s}$  are not independent and have to obey three constraints. The first two of these constraints are due to the definition of GIBBS free energy density, *i.e.*,

$g = u - Ts + p/\rho$ . A differentiation of this equation for the GIBBS free energy density with respect to the pressure and the temperature yields

$$\frac{\partial \hat{g}}{\partial p} = \frac{\partial \hat{u}}{\partial p} - T \frac{\partial \hat{s}}{\partial p} + \frac{1}{\rho} - \frac{p}{\rho^2} \frac{\partial \hat{\rho}}{\partial p}, \quad \frac{\partial \hat{g}}{\partial T} = \frac{\partial \hat{u}}{\partial T} - s - T \frac{\partial \hat{s}}{\partial T} - \frac{p}{\rho^2} \frac{\partial \hat{\rho}}{\partial T}. \quad (2.52)$$

Using Eq. (2.47), the left-hand sides of both equations can be replaced by  $1/\rho$  and  $-s$ , respectively. Then, a rearrangement of the resulting equations yields the following two GIBBS relations

$$T \frac{\partial \hat{s}}{\partial p} = \frac{\partial \hat{u}}{\partial p} - \frac{p}{\rho^2} \frac{\partial \hat{\rho}}{\partial p}, \quad T \frac{\partial \hat{s}}{\partial T} = \frac{\partial \hat{u}}{\partial T} - \frac{p}{\rho^2} \frac{\partial \hat{\rho}}{\partial T}. \quad (2.53)$$

These show that, *e.g.*, the internal energy is not independent of the entropy and the density. The third constraint is a MAXWELL relation, which is obtained by differentiating Eq. (2.47)<sub>1</sub> with respect to the temperature and Eq. (2.47)<sub>2</sub> with respect to the pressure. The resulting MAXWELL relation reads

$$\frac{\partial \hat{s}}{\partial p} = - \frac{\partial}{\partial T} \left( \frac{1}{\rho} \right) = \frac{1}{\rho^2} \frac{\partial \hat{\rho}}{\partial T}, \quad (2.54)$$

which means that the caloric equation of state is not independent of the thermal equation of state.

Suppose that a thermal equation of state,  $\rho = \hat{\rho}(p, T)$ , is given. Equation (2.54) is differentiated once more with respect to the temperature and subsequently integrated with respect to the pressure in order to derive a compatible caloric equation of state

$$\frac{\partial^2 \hat{s}}{\partial T \partial p} = \frac{\partial}{\partial T} \left( \frac{1}{\rho^2} \frac{\partial \hat{\rho}}{\partial T} \right) \Leftrightarrow \frac{\partial \hat{s}}{\partial T} = \int_{p_0}^p \frac{\partial}{\partial T} \left( \frac{1}{\rho^2} \frac{\partial \hat{\rho}}{\partial T} \right) \Big|_{\tilde{p}, T} d\tilde{p} + \hat{f}_1(T), \quad (2.55)$$

where the function  $\hat{f}_1$  does not depend on the pressure and is a “constant of integration.” Integrating this equation once more with respect to the temperature yields

$$\hat{s}(p, T) = \int_{p_0}^p \left( \frac{1}{\rho^2} \frac{\partial \hat{\rho}}{\partial T} \Big|_{\tilde{p}, T} - \frac{1}{\rho^2} \frac{\partial \hat{\rho}}{\partial T} \Big|_{\tilde{p}, T_0} \right) d\tilde{p} + \int_{T_0}^T \hat{f}_1(\tilde{T}) d\tilde{T} + \hat{f}_2(p). \quad (2.56)$$

The function  $\hat{f}_2$  does not depend on the temperature and is another “constant of integration.” The two functions  $\hat{f}_1$  and  $\hat{f}_2$  need to be determined in order to obtain the final expression for the entropy. The function  $\hat{f}_2$  can be determined from the MAXWELL relation in Eq. (2.54). Substituting the derivative of Eq. (2.56)

with respect to the pressure into the MAXWELL relation yields

$$\frac{\partial \hat{f}_2}{\partial p} = \frac{1}{\rho^2} \frac{\partial \hat{\rho}}{\partial T} \Big|_{p, T_0} \Rightarrow \hat{f}_2(p) = \int_{p_0}^p \frac{1}{\rho^2} \frac{\partial \hat{\rho}}{\partial T} \Big|_{\tilde{p}, T_0} d\tilde{p} + s(p_0, T_0), \quad (2.57)$$

where  $s(p_0, T_0)$  is the specific entropy at a reference state. Hence,

$$\hat{s}(p, T) = \int_{p_0}^p \frac{1}{\rho^2} \frac{\partial \hat{\rho}}{\partial T} \Big|_{\tilde{p}, T} d\tilde{p} + \int_{T_0}^T \hat{f}_1(\tilde{T}) d\tilde{T} + s(p_0, T_0). \quad (2.58)$$

This equation formally constitutes the caloric equation of state if the function  $\hat{f}_1(T)$  and the thermal equation of state are specified. However, it will be shown below that the function  $\hat{f}_1(T)$  can be implicitly related to the specific heat capacity and the coefficient of thermal expansion, which is present in the thermal equation of state.

In order to proceed and to simplify the analysis, the coefficient of thermal expansion,  $\alpha = \hat{\alpha}(p, T)$ , and the compressibility,  $\beta = \hat{\beta}(p, T)$  and the specific heat capacity at constant pressure,  $c_p = \hat{c}_p(p, T)$ , are introduced as:

$$\alpha = -\frac{1}{\rho} \frac{\partial \hat{\rho}}{\partial T}, \quad \beta = \frac{1}{\rho} \frac{\partial \hat{\rho}}{\partial p}, \quad c_p = T \frac{\partial \hat{s}}{\partial T}. \quad (2.59)$$

Rearranging the terms in Eq. (2.53) and substituting the MAXWELL relation in Eq. (2.54) and the coefficients above leads to the following GIBBS relations:

$$\frac{\partial \hat{u}}{\partial T} = T \frac{\partial \hat{s}}{\partial T} + \frac{p}{\rho^2} \frac{\partial \hat{\rho}}{\partial T} = c_p - \frac{\alpha}{\rho} p, \quad (2.60a)$$

$$\frac{\partial \hat{u}}{\partial p} = \frac{T}{\rho^2} \frac{\partial \hat{\rho}}{\partial T} + \frac{p}{\rho^2} \frac{\partial \hat{\rho}}{\partial p} = -\frac{\alpha}{\rho} T + \frac{\beta}{\rho} p. \quad (2.60b)$$

This equation shows that it is sufficient to specify the specific heat capacity  $c_p$ , the coefficient of thermal expansion  $\alpha$ , the compressibility  $\beta$ , and a thermal equation of state, *i.e.*,  $\rho = \hat{\rho}(p, T)$ , in order to obtain the internal energy. The function,  $\hat{f}_1$ , is only required if the entropy is considered. By differentiating Eq. (2.58) with respect to the temperature the function  $\hat{f}_1$  may be related to the specific heat capacity as follows

$$\hat{c}_p(p, T) = T \int_{p_0}^p \frac{\partial}{\partial T} \left( \frac{1}{\rho^2} \frac{\partial \hat{\rho}}{\partial T} \right) \Big|_{\tilde{p}, T} d\tilde{p} + \hat{f}_1(T) T. \quad (2.61)$$

The first term on the right-hand side and the specific heat capacity are functions of pressure and temperature. Therefore, the second term on right-hand side, *i.e.*,

$\hat{f}_1(T)T$ , is interpreted as a part of the specific heat capacity that does not depend on the pressure.

The two relations in Eq. (2.60) can be combined to obtain the material time derivative of the internal energy, which is required in the balance of the internal energy. The material time derivative of the internal energy reads

$$\rho \dot{u} = (\rho c_p - \alpha p) \dot{T} + (\beta p - \alpha T) \dot{p}. \quad (2.62)$$

Using the mass balance, the pressure-dependent stress power may be shown to be expressible as

$$-p \mathbf{1} \cdot \mathbf{d} = -p \nabla \cdot \mathbf{v} = \frac{p}{\rho} \dot{\rho} = p \left( \frac{1}{\rho} \frac{\partial \hat{\rho}}{\partial T} \dot{T} + \frac{1}{\rho} \frac{\partial \hat{\rho}}{\partial p} \dot{p} \right) = p(-\alpha \dot{T} + \beta \dot{p}), \quad (2.63)$$

where the coefficient of thermal expansion and the compressibility were introduced in the last step. Substituting Eqs. (2.62) and (2.63) in the balance of the internal energy yields

$$\rho c_p \dot{T} - \alpha T \dot{p} = -\nabla \cdot \mathbf{q} + (\boldsymbol{\sigma} - p \mathbf{1}) \cdot \mathbf{d} + \rho \hat{r} + \mathbf{j}_f \cdot (\mathbf{E} + \mathbf{v} \times \mathbf{B}). \quad (2.64)$$

This is the balance of internal energy for a compressible fluid with thermal expansion. It can be interpreted as an evolution equation for either the temperature or the pressure. A second evolution equation is obtained from the mass balance which takes the form

$$-\alpha \dot{T} + \beta \dot{p} + \nabla \cdot \mathbf{v} = 0. \quad (2.65)$$

Hitherto, an explicit thermal equation of state was not specified. This means that the functional dependencies of the specific heat capacity, the coefficient of thermal expansion and the compressibility were not restricted and may still be non-linear. As a consequence, the equations presented above describe the most general case for compressible fluids with thermal expansion and do not imply a specific thermal equation of state.

## 2.5.2 Thermal equation of state and thermodynamic linearization

In the following, a *linear thermal equation of state is used* and thermodynamic linearization is performed. Subsequently, the dependence of the density on pressure and temperature is described by the thermal equation of state

$$\rho = \hat{\rho}(p, T) = \rho_0 \left( 1 - \alpha_0(T - T_0) + \beta_0(p - p_0) \right), \quad (2.66)$$

where  $\alpha_0$  and  $\beta_0$  are constants. For the coefficient of thermal expansion and the compressibility given in Eq. (2.59) this equation of state implies

$$\alpha = \frac{\alpha_0}{\left(1 - \alpha_0(T - T_0) + \beta_0(p - p_0)\right)} = \alpha_0 + \mathcal{O}(\alpha_0\beta_0), \quad (2.67)$$

$$\beta = \frac{\beta_0}{\left(1 - \alpha_0(T - T_0) + \beta_0(p - p_0)\right)} = \beta_0 + \mathcal{O}(\alpha_0\beta_0). \quad (2.68)$$

In order to obtain an explicit expression for the entropy, Eq. (2.61) is considered and the integrand is analyzed. This integrand is the derivative of the ratio of the coefficient of thermal expansion to the density, and this derivative is given by

$$\frac{\partial}{\partial T} \left( \frac{1}{\rho^2} \frac{\partial \hat{\rho}}{\partial T} \right) = \frac{1}{\rho^2} \frac{\partial^2 \hat{\rho}}{\partial T^2} - \frac{2}{\rho^3} \left( \frac{\partial \hat{\rho}}{\partial T} \right)^2 \stackrel{(2.59)}{=} \frac{1}{\rho^2} \frac{\partial^2 \hat{\rho}}{\partial T^2} - \frac{2\alpha^2}{\rho}. \quad (2.69)$$

The first term on the right-hand side vanishes because the thermal equation of state is linear with respect to the temperature. The second term is at least quadratic in  $\alpha_0$ , *i.e.*,  $2\alpha^2/\rho = 2\alpha_0^2/\rho_0 + \mathcal{O}(\alpha_0^2\beta_0)$ . According to Nimmo, the coefficient of thermal expansion varies in the outer core of the Earth from approximately  $0.9 \times 10^{-5} \text{ K}^{-1}$  to  $1.8 \times 10^{-5} \text{ K}^{-1}$  [Nimmo (2015)]. This justifies the assumption that  $\alpha_0$  is small and the second order term may therefore be neglected. Thus, Eq. (2.61) simplifies to

$$c_p = \hat{c}_p(T) = \hat{f}_1(T)T, \quad (2.70)$$

which means that the neglect of second order terms implies that the specific heat capacity does not depend on the pressure. Therefore, the entropy is given by

$$s(p, T) = c_{p,0} \ln \left( \frac{T}{T_0} \right) - \frac{\alpha_0}{\rho_0} (p - p_0), \quad (2.71)$$

where the specific heat capacity was assumed to be constant. Furthermore, in order to obtain the thermodynamically linearized entropy function above, the integrand  $\rho^{-2} \partial \hat{\rho} / \partial T$  in Eq. (2.58) was also linearized with respect to  $\alpha_0$  and  $\beta_0$ .

In conclusion, for the given thermal equation of state and the thermodynamic linearization, the balances of mass and internal energy reduce to the forms

$$-\alpha_0 \dot{T} + \beta_0 \dot{p} = -\nabla \cdot \mathbf{v}, \quad (2.72)$$

$$\begin{aligned} \rho c_{p,0} \dot{T} - \alpha_0 T \dot{p} &= \kappa \nabla^2 T + \lambda \text{tr}(\mathbf{d})^2 + 2\mu \mathbf{d}^{\text{dev}} \cdot \mathbf{d}^{\text{dev}} + \rho \hat{r} + \\ &+ \sigma (\mathbf{E} + \mathbf{v} \times \mathbf{B})^2. \end{aligned} \quad (2.73)$$

These equations show that even in case of a thermodynamic linearization the balance laws of mass and internal energy are coupled evolution equations for the temperature and the pressure.

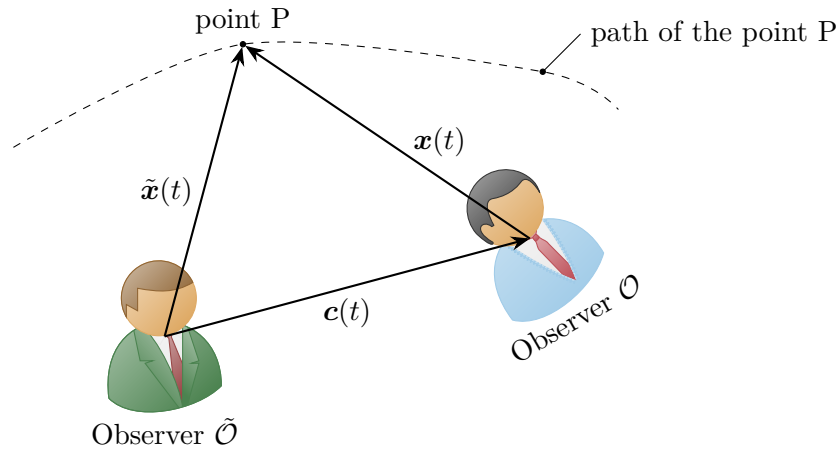


**Figure 2.7:** Two observers denoted by the symbols  $\mathcal{O}$  and  $\tilde{\mathcal{O}}$  are describing, for example, the motion of a point P. The motion of the point P in space is indicated by a dashed line. The relative orientation of the two observers is indicated by a rotation of observer  $\mathcal{O}$ .

## 2.6 Rotating systems and changes of observers

In Sect. 2.3, the fundamental equations of continuum mechanics have been formulated for an inertial observer, which is often also referred to as an inertial frame or system. However, the Earth is a rotating system. While this rotation is often ignored if processes in the mantle or the inner core are considered, it is especially important for the fluid flows in the outer core of the Earth, because here an accountancy of the inertial terms become important. Therefore, this section formulates the balance of momentum for an observer, who is co-rotating with the mantle of the Earth.

Suppose there are two observers  $\mathcal{O}$  and  $\tilde{\mathcal{O}}$ , which are characterized by their relative positions and orientations. Both observers shall describe the same physical processes occurring at an arbitrary point P, see Fig. 2.7. In relation to the Earth, one can imagine the two observers such that the observer  $\tilde{\mathcal{O}}$  is attached to the center of the Earth and that the observer  $\mathcal{O}$  is also attached to the center of the Earth but is co-rotating with the solid mantle of the Earth. Regarding Sect. 2.2, the observers  $\tilde{\mathcal{O}}$  and  $\mathcal{O}$  are associated with the ecliptic celestial and the terrestrial frame of reference, respectively.

The position vectors of the point P measured by both observers are denoted by  $\tilde{\boldsymbol{x}}$  and  $\boldsymbol{x}$ , respectively. The relative position of the two observers is described mathematically by the distance vector  $\boldsymbol{c}$ , which connects the two observers, see Fig. 2.7. Note that this vector vanishes for the case that both observers are located at the center of the Earth. The relative orientation of the two observers shall be described mathematically by

$$\tilde{Q}_{ij}(t) = (\tilde{\boldsymbol{e}}_i \cdot \boldsymbol{e}_j)(t), \quad (2.74)$$

in which  $\tilde{\mathbf{e}}_i$  and  $\mathbf{e}_i$  are the basis vectors used by the observers  $\tilde{\mathcal{O}}$  and  $\mathcal{O}$ , respectively, and  $\tilde{Q}_{ij}$  is an orthogonal matrix. This equation states that the relative orientation is described by the angles between the two sets of basis vectors used by the two observers. These angles depend on time because the relative position and orientation may change in time.

As shown in Fig. 2.7, the position vectors of the point P measured by the two observers are related by

$$\tilde{\mathbf{x}}(t) = \mathbf{x}(t) + \mathbf{c}(t). \quad (2.75)$$

Consequently, Eqs. (2.74) and (2.75) imply the following component equation:

$$\tilde{x}_i(t) = \tilde{Q}_{ij}(t)(x_j(t) + c_j(t)), \quad (2.76)$$

which is obtained by a scalar multiplication of Eq. (2.75) with the basis vector  $\tilde{\mathbf{e}}_i$ . This equation describes a EUCLIDIAN transformation. As outlined in Appendix B, the representations of the velocity and the acceleration may be shown to take the forms

$$\tilde{\mathbf{v}} = \mathbf{v} + \tilde{\boldsymbol{\omega}} \times \mathbf{x} + \frac{d\tilde{\mathbf{c}}}{dt}, \quad \frac{d\tilde{\mathbf{v}}}{dt} = \frac{d\mathbf{v}}{dt} + 2\tilde{\boldsymbol{\omega}} \times \mathbf{v} + \frac{d\tilde{\boldsymbol{\omega}}}{dt} \times \mathbf{x} + \tilde{\boldsymbol{\omega}} \times (\tilde{\boldsymbol{\omega}} \times \mathbf{x}) + \frac{d^2\tilde{\mathbf{c}}}{dt^2}, \quad (2.77)$$

where  $\tilde{\boldsymbol{\omega}}$  is the angular velocity vector describing the temporal change of the relative orientation of the two observers. Moreover, the relative velocity and acceleration are denoted by  $d\tilde{\mathbf{c}}/dt$  and  $d^2\tilde{\mathbf{c}}/dt^2$ , respectively. The symbol  $\mathbf{v}$  denotes the velocity of the point P measured by the observer  $\mathcal{O}$ . Note that the time dependence of the quantities is not stated explicitly in the equation above, and it will also be omitted, but accounted for, in the subsequent analysis.

Suppose that the observer  $\tilde{\mathcal{O}}$  is an inertial observer and that the linear momentum balance for this observer is given by that used in Sect. 2.3

$$\tilde{\rho} \frac{d\tilde{\mathbf{v}}}{dt} = \tilde{\nabla} \cdot \tilde{\boldsymbol{\sigma}} + \tilde{\rho} \tilde{\mathbf{f}} + \tilde{\mathbf{f}}^{(\text{EM})}, \quad (2.78)$$

where the tildes indicate that the quantities are measured by the observer  $\tilde{\mathcal{O}}$ . In order to formulate this equation for the observer  $\mathcal{O}$ , which is co-rotating with the Earth, the transformations of the non-kinematic quantities, *i.e.*,  $\tilde{\rho}$ ,  $\tilde{\boldsymbol{\sigma}}$ ,  $\tilde{\mathbf{f}}$  and  $\tilde{\mathbf{f}}^{(\text{EM})}$ , need to be specified. The density is a scalar and therefore transforms as  $\tilde{\rho} = \rho$ . Moreover, the stress is objective, *i.e.*,  $\tilde{\boldsymbol{\sigma}} = \boldsymbol{\sigma}$  [Müller (2014)]. Using  $\tilde{\nabla} = \nabla$  (which is derived in Appendix B) and the representation of the acceleration in Eq. (2.77)<sub>2</sub> Eq. (2.78) may be expressed as

$$\rho \frac{d\mathbf{v}}{dt} + 2\tilde{\boldsymbol{\omega}} \times \mathbf{v} + \dot{\tilde{\boldsymbol{\omega}}} \times \mathbf{x} + \tilde{\boldsymbol{\omega}} \times (\tilde{\boldsymbol{\omega}} \times \mathbf{x}) + \ddot{\tilde{\mathbf{c}}} = \nabla \cdot \boldsymbol{\sigma} + \rho \tilde{\mathbf{f}} + \tilde{\mathbf{f}}^{(\text{EM})}. \quad (2.79)$$

What remains to be specified is the transformation of the two force densities  $\tilde{\mathbf{f}}$  and  $\tilde{\mathbf{f}}^{(\text{EM})}$ . While the role of the former is usually addressed in connection with the EUCLID transformations, the LORENTZ force and its transformation is not widely

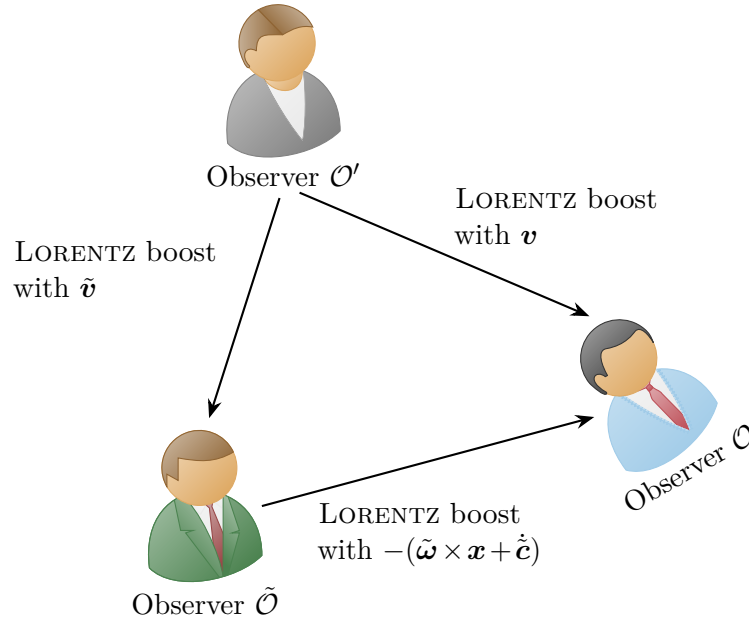


**Figure 2.8:** LORENTZ transformations between the observers  $\mathcal{O}$ ,  $\mathcal{O}'$  and  $\tilde{\mathcal{O}}$ . Likewise the observer  $\mathcal{O}'$  is co-moving with the (material) point P.

discussed in the literature. Recall that a LORENTZ transformation was used in Sect. 2.4 in order to transform the electromagnetic fields from an observer  $\mathcal{O}'$ , which is co-moving with the material to the co-rotating observer  $\mathcal{O}$ . The problem in relation to the balance of linear momentum is that the EUCLIDIAN transformation is applied in order to transform mechanical quantities like, *e.g.*, the acceleration and the stress tensor but the LORENTZ transformation is applied in relation to the MAXWELL equations to transform the electromagnetic fields. A unified treatment of both mechanics and electromagnetism would require a relativistic formulation of the balance of linear momentum and the application of the LORENTZ transformation to both electromagnetism and mechanics. In his textbook, Scheck discusses relativistic mechanics of particles and a relativistic version of NEWTON's second law. In this context, the LORENTZ transformation of a force (acting on a particle), *viz.*, the right-hand side of NEWTON's second law, is presented, which simplifies to  $\boldsymbol{F}' = \boldsymbol{F}$  in the low-velocity limit [Scheck (2010)]. However, the fully relativistic treatment of mechanics is beyond the subject and intention of this section, because a low-velocity approximation is applied anyway. Therefore, it seems reasonable to use  $\tilde{\boldsymbol{f}}^{(\text{EM})} = \boldsymbol{f}^{(\text{EM})}$ , when transforming the electromagnetic force density.

If the transformation of the electromagnetic force density is supposed to be given by  $\tilde{\boldsymbol{f}}^{(\text{EM})} = \boldsymbol{f}^{(\text{EM})}$ , the question arises how this force is represented in terms of the electromagnetic fields  $\boldsymbol{E}$  and  $\boldsymbol{B}$  or  $\tilde{\boldsymbol{E}}$  and  $\tilde{\boldsymbol{B}}$  measured either by the observer  $\mathcal{O}$  or  $\tilde{\mathcal{O}}$ , respectively. For the fixed inertial observer  $\tilde{\mathcal{O}}$ , the electromagnetic force density

is the LORENTZ force density and it is given by the classical formula

$$\tilde{\mathbf{f}}^{(\text{EM})} = \tilde{q}_f \tilde{\mathbf{E}} + \tilde{\mathbf{J}}_f \times \tilde{\mathbf{B}}. \quad (2.80)$$

The free charge density  $\tilde{q}_f$  and the free current density  $\tilde{\mathbf{J}}_f$  can be obtained by making use of the constitutive equations formulated for the observer  $\mathcal{O}'$  in Sect. 2.4, which is co-moving with the material. Under the assumption of the magnetohydrodynamic approximation, an application of a LORENTZ transformation from the observer  $\mathcal{O}'$  to the observer  $\tilde{\mathcal{O}}$  shows that the free charge density  $\tilde{q}_f$  is negligible in comparison to the free electric current density  $\tilde{\mathbf{J}}_f$ , see Eqs. (2.30) and (2.22). This also generalizes for the two terms present in Eq. (2.80). The contribution attributed to the free charge density, *i.e.*,  $\tilde{q}_f \tilde{\mathbf{E}}$ , is also negligible in comparison to that of the free current density, because the proportionality of the electric field to the magnetic field in the magnetohydrodynamic approximation does not introduce a factor that outweighs the negligibility of the free charge density. Hence,

$$\tilde{\mathbf{f}}^{(\text{EM})} = \tilde{\mathbf{J}}_f \times \tilde{\mathbf{B}} = \sigma(\tilde{\mathbf{E}} + \tilde{\mathbf{v}} \times \tilde{\mathbf{B}}) \times \tilde{\mathbf{B}}. \quad (2.81)$$

Here, OHM's law for the free current density was applied.

In the following, the electromagnetic variables on the right-hand side of the last equation are expressed in terms of those measured by the observer  $\mathcal{O}$ . In order to do so, a LORENTZ transformation from the observer  $\tilde{\mathcal{O}}$  to the observer  $\mathcal{O}$  is applied. From Fig. 2.8 it is clear that the relative velocities for the instantaneous LORENTZ transformations from the observer  $\mathcal{O}'$  to either  $\mathcal{O}$  and or  $\tilde{\mathcal{O}}$  are given by  $\mathbf{v}$  or  $\tilde{\mathbf{v}}$ , respectively. However, the correct relative velocity for the transformation from observer  $\tilde{\mathcal{O}}$  to  $\mathcal{O}$  is not obvious. Yet, the sequential transformation  $\mathcal{O}' \rightarrow \tilde{\mathcal{O}} \rightarrow \mathcal{O}$  is also a LORENTZ transformation, because each LORENTZ transformation is linear with respect to time and spatial coordinates. Therefore, the representations of, *e.g.*, the electric field  $\mathbf{E}$  in terms of the fields  $\mathbf{B}'$  and  $\mathbf{E}'$ , which are obtained from the transformations  $\mathcal{O}' \rightarrow \tilde{\mathcal{O}} \rightarrow \mathcal{O}$  or  $\mathcal{O}' \rightarrow \mathcal{O}$ , must coincide. Since this argument holds true, the relative velocity between the observers  $\tilde{\mathcal{O}}$  and  $\mathcal{O}$  can be identified as  $\mathbf{v} - \tilde{\mathbf{v}} = -(\tilde{\boldsymbol{\omega}} \times \mathbf{x} + \dot{\tilde{\mathbf{c}}})$ , where the difference of the two velocities was expressed by using Eq. (2.77)<sub>1</sub>.

When  $\dot{\tilde{\mathbf{c}}} = \mathbf{0}$ , the relative velocity reduces to  $-\tilde{\boldsymbol{\omega}} \times \mathbf{x}$  and the point-wise LORENTZ transformations of the electric and magnetic fields from the observer  $\mathcal{O}$  to  $\tilde{\mathcal{O}}$  are given by

$$\tilde{\mathbf{E}} = \mathbf{E} - (\tilde{\boldsymbol{\omega}} \times \mathbf{x}) \times \mathbf{B}, \quad \tilde{\mathbf{B}} = \mathbf{B} + \frac{1}{c^2}(\tilde{\boldsymbol{\omega}} \times \mathbf{x}) \times \mathbf{E}. \quad (2.82)$$

Substituting these relations into Eq. (2.80) yields

$$\begin{aligned}
\tilde{\mathbf{f}}^{(\text{EM})} &= \sigma \left( \mathbf{E} - (\tilde{\boldsymbol{\omega}} \times \mathbf{x}) \times \mathbf{B} + \tilde{\mathbf{v}} \times \left( \mathbf{B} + \frac{1}{c^2} (\tilde{\boldsymbol{\omega}} \times \mathbf{x}) \times \mathbf{E} \right) \right) \times \\
&\quad \times \left( \mathbf{B} + \frac{1}{c^2} (\tilde{\boldsymbol{\omega}} \times \mathbf{x}) \times \mathbf{E} \right) \\
&= \sigma \left( \left[ \left( 1 - \frac{\tilde{\mathbf{v}} \cdot (\tilde{\boldsymbol{\omega}} \times \mathbf{x})}{c^2} \right) \mathbf{1} + \frac{1}{c^2} \tilde{\mathbf{v}} \otimes (\tilde{\boldsymbol{\omega}} \times \mathbf{x}) \right] \cdot \mathbf{E} + \right. \\
&\quad \left. + [\tilde{\mathbf{v}} - \tilde{\boldsymbol{\omega}} \times \mathbf{x}] \times \mathbf{B} \right) \times \\
&\quad \times \left( \mathbf{B} + \frac{1}{c^2} (\tilde{\boldsymbol{\omega}} \times \mathbf{x}) \times \mathbf{E} \right). \tag{2.83}
\end{aligned}$$

In the last equation, there are terms with a factor, that includes  $\tilde{\mathbf{v}}$ ,  $\tilde{\boldsymbol{\omega}} \times \mathbf{x}$  and  $c^{-2}$ . In the low velocity limit these terms can be neglected because the two velocities are small compared to the speed of light. This assumes that the extension of the domain is not very large, such that the velocity  $\tilde{\boldsymbol{\omega}} \times \mathbf{x}$  does not get excessively large. Using the low velocity approximation and  $\mathbf{v} = \tilde{\mathbf{v}} - \tilde{\boldsymbol{\omega}} \times \mathbf{x}$ , the electromagnetic force density reads

$$\tilde{\mathbf{f}}^{(\text{EM})} \approx \sigma (\mathbf{E} + \mathbf{v} \times \mathbf{B}) \times \left( \mathbf{B} + \frac{1}{c^2} (\tilde{\boldsymbol{\omega}} \times \mathbf{x}) \times \mathbf{E} \right). \tag{2.84}$$

This representation of the electromagnetic force density is already very similar to that found, for example, in Roberts [2015]. However, the representation above differs from that found in Roberts [2015] by the presence of the term  $c^{-2} (\tilde{\boldsymbol{\omega}} \times \mathbf{x}) \times \mathbf{E}$ . This term may be neglected in comparison to the magnetic field  $\mathbf{B}$ . Recall from Sect. 2.4 that  $\mathcal{O}(\mathbf{E}) = c_{\text{ref}} \mathcal{O}(\mathbf{B})$ , where  $c_{\text{ref}}$  is a characteristic velocity, which is assumed to be much smaller than the speed of light. As a consequence, the term  $c^{-2} (\tilde{\boldsymbol{\omega}} \times \mathbf{x}) \times \mathbf{E}$  is proportional to the magnetic field and has a leading factor that is the ratio of the product of the two velocities  $\tilde{\boldsymbol{\omega}} \times \mathbf{x}$  and  $c_{\text{ref}}$  to the square of the speed of light. It can therefore be neglected in the low-velocity approximation:  $(\tilde{\boldsymbol{\omega}} \times \mathbf{x}) c_{\text{ref}} / c^2$ . Hence, the ‘‘traditional form’’ of the electromagnetic force density in magnetohydrodynamics is obtained,

$$\tilde{\mathbf{f}}^{(\text{EM})} \approx \sigma (\mathbf{E} + \mathbf{v} \times \mathbf{B}) \times \mathbf{B}. \tag{2.85}$$

To finalize the discussion related to the balance of linear momentum, the resulting equation for the observer  $\mathcal{O}$  is given by

$$\rho \frac{d\mathbf{v}}{dt} + 2\tilde{\boldsymbol{\omega}} \times \mathbf{v} + \dot{\tilde{\boldsymbol{\omega}}} \times \mathbf{x} + \tilde{\boldsymbol{\omega}} \times \tilde{\boldsymbol{\omega}} \times \mathbf{x} = \nabla \cdot \boldsymbol{\sigma} + \rho \mathbf{f} + \sigma (\mathbf{E} + \mathbf{v} \times \mathbf{B}) \times \mathbf{B}, \tag{2.86}$$

where  $\dot{\tilde{\mathbf{c}}} = \mathbf{0}$  and  $\tilde{\mathbf{f}} = \mathbf{f}$  were applied. Together with the NAVIER-STOKES law for the CAUCHY stress tensor, this equation constitutes the basis for the description of the magnetohydrodynamic fluid flow. For the outer core of the Earth, this fluid flow is driven by buoyancy forces, which requires to consider the balance of internal energy as well. It is shown in Müller [2014] that the classical balance of internal energy is not altered by the EUCLIDIAN transformation. This is also the case if the

electromagnetic thermal power is included, because OHM's law and the application of the low-velocity approximation allow the simplification of the electromagnetic thermal power in the same manner as the electromagnetic force density.

## 2.7 The anelastic and BOUSSINESQ approximation

This section considers approximations of the balance of mass, momentum balance and balance of internal energy for the cases of buoyancy-driven flows. Regarding these, two principal approximations exist in the literature: the *anelastic approximation* and the *BOUSSINESQ approximation*. These approximations both result from a perturbation analysis and are widely used in atmospheric and ocean dynamics as well as for studying convection in stars and planetary interiors. The anelastic approximation is suitable for liquids and gases. The BOUSSINESQ approximation is a special case of the anelastic approximation, which is only applicable either if the convective region is small or if the material is weakly compressible, *e.g.*, if it is a nearly density preserving liquid. The perturbation analysis requires the specification of a reference state, which in the literature is often referred to as a “well-mixed adiabatic state.” However, as outlined below the term “adiabatic” is misleading, because neither the heat flux vanishes in this state nor is the system in a thermodynamic equilibrium.

The common reason for approximating the basic equations is that the considered convective velocities are slow if compared to the speed of sound waves. This assumption is based on the fact that the reference state of the system is stable. The sound waves traveling through the domain do not significantly change temperature, pressure and density such that they can play a role in a large-scale convective motion in, for instance, the outer core of the Earth. The neglect or filtering of sound waves also significantly simplifies the numerical solution of the governing equations, which was already noted by Ogura and Phillips in 1962. This also applies to the outer core of the Earth, because the time it takes for a sound wave to travel through the core is approximately 300 s, which is negligible if compared to estimates for the convective overturn time of several thousand years.

Several papers have analyzed approximations of buoyancy-driven flows with different emphasis. The papers of Batchelor as well as Spiegel and Veronis discuss atmospheric convection using the state equation of an ideal gas [Batchelor (1953); Spiegel and Veronis (1960)]. The former author was among the first to depart from the classical BOUSSINESQ approximation and introduced the anelastic approximation of the balance of mass. On the contrary, the latter authors obtained the BOUSSINESQ approximation, because they were considering a layer, which is thin compared to the characteristic length scale of the reference state [Spiegel and Veronis (1960)]. The two papers mentioned above have in common that they require a small perturbation from the reference state. On the other hand, the analysis of Ogura and Phillips showed that the additional assumption, that the frequencies associated to the timescale of convection must be small if compared

to the buoyancy frequency, is required [Ogura and Phillips (1962)]. In fact, this paper is the first using the term anelastic. Following these papers, several specializations were considered, for example, a time-varying reference state [Gough (1969)], convection in stars [Spiegel and Weiss (1982)] and a pseudo-incompressible limit [Durrant (1989)]. The seminal work of Braginsky and Roberts and the paper by Anufriev, Jones, and Soward discuss the anelastic and the BOUSSINESQ approximation in relation to the outer core of the Earth [Braginsky and Roberts (1995); Anufriev, Jones, and Soward (2005)]. The authors of the two papers argue in favor of an anelastic model for several reasons. *First*, there are no working terms in the heat transport equation in a BOUSSINESQ model. This neglects, for example, ohmic dissipation, which is thought to have the strongest influence in the heat transport equation [Anufriev, Jones, and Soward (2005); Jones (2007)]. *Second*, the temperature profile of the Earth departs significantly from the adiabatic profile at the core-mantle boundary, where heat conduction is dominated by convective transport rather than conduction [Anufriev, Jones, and Soward (2005)]. As a consequence, the energy budget of a BOUSSINESQ model does not reflect the true energy budget of the core of the Earth. This is a problem if the temperature profile of a BOUSSINESQ model is compared to the true profile of the core of the Earth. *Third*, BOUSSINESQ models are usually applied to laboratory experiments, where the adiabatic temperature gradient is small [Braginsky and Roberts (1995)]. This is not the case in the outer core of the Earth, where the reference state varies greatly with depth, for example a relative temperature variation of at least 25% is obtained from Table 2.1. In spite of these deficiencies, the BOUSSINESQ model is still the most commonly used model when it comes to numerical modeling of convection in the outer core of the Earth, see Christensen et al. [2001] and Matsui et al. [2016].

In the following, the anelastic approximation is presented and subsequently the BOUSSINESQ approximation is obtained as a special case of the anelastic approximation. The presentation follows the papers of Braginsky and Roberts and Anufriev, Jones, and Soward but compositional effects are not taken into account in the discussion presented below [Braginsky and Roberts (1995); Anufriev, Jones, and Soward (2005)]. However, it should be remarked that especially the derivation of the reference state presented by Anufriev, Jones, and Soward makes use of some questionable thermodynamic arguments and simplifications, which are not repeated in the following.

### 2.7.1 The reference state

The first step to obtain the anelastic approximation is to define the reference state denoted by  $\rho_a$ ,  $p_a$ ,  $T_a$ . In this state, temporal fluctuations of all fields vanish and the velocity vanishes in the rotating frame, *i.e.*, the material is only performing a constant rigid body motion. In this case, the mass balance is trivially fulfilled and

the momentum balance reduces to the hydrostatic balance

$$-\nabla p_a + \rho_a \mathbf{g}_a = \mathbf{0} \quad \text{with} \quad \mathbf{g}_a = -\nabla(\varphi_a + \frac{1}{2}(\boldsymbol{\Omega} \times \mathbf{x})^2), \quad (2.87)$$

where  $\mathbf{g}_a$  denotes the density of the potential forces, which are given by the gravitational and the centripetal acceleration, and  $\varphi_a$  denotes the gravitational potential. Furthermore, note that here and in the following,  $\boldsymbol{\Omega}$  denotes the stationary angular velocity vector of the mantle and is used instead of the symbol  $\tilde{\boldsymbol{\omega}}$ . Additionally, it is also assumed that the LORENTZ force term also vanishes. This is so, because Eq. (2.38) yields an electro- and magnetostatic problem in the stationary case, which implies that the electric field is a potential field. In fact, there are no sources of the electric field, neither in the interior nor in the exterior of the liquid outer core of the Earth. Therefore, this field vanishes and so does also the electric current. As a consequence, the magnetic field is also a potential field.

Regarding the balance of the internal energy for the reference state, the production terms due to viscous heating as well as the electromagnetic thermal power, *i.e.*, the JOULE heating term, vanish. Therefore, the balance of internal energy is given by

$$\nabla \cdot (\kappa \nabla T_a) + \rho_a \hat{r}_a = 0. \quad (2.88)$$

Equations (2.87) and (2.88) do not allow a determination of a unique reference state and need to be supplemented by an additional relation. This additional relation is given by the thermal equation of state, see, for example, Eq. (2.66). However, a specification of the internal thermal power  $\hat{r}_a$  is also required in order to solve Eq. (2.88). Yet, the internal thermal power or internal heating is not well known in the core of the Earth, which is an additional weakness. In order to circumvent a specification, it is either neglected, which corresponds to a purely conducting state, or the assumption of a homogeneous entropy is applied [Braginsky and Roberts (1995); Jones (2007)]. The latter case is commonly chosen and referred to as the adiabatic reference state.

In view of Eq. (2.88) this designation is not correct, because there is a non-zero heat flux in the system, which neither will vanish on the boundaries. Furthermore, the associated entropy production is given by  $\xi = \kappa(\nabla T)^2/T^2 \neq 0$  and the designation of the reference state by the term thermodynamic equilibrium also does neither apply. Nevertheless, the term “adiabatic” is widely used in the literature on the thermal evolution of the outer core of the Earth, *cf.* Buffett et al. [1996], Gubbins et al. [2003] and Roberts, Jones, and Calderwood [2003] among others. This term is frequently used because it is adapted from atmospheric science and meteorology. The reference state of a stable atmosphere is determined by using the ideal gas law, and, additionally, adiabaticity is assumed, because the thermal conductivity of air is rather small. A consequence of the assumption of an adiabatic atmosphere is that the entropy is constant.<sup>5</sup> Moreover, the adiabatic atmosphere is always stable with respect to density perturbations, *i.e.*,  $N^2 > 0$ ,

<sup>5</sup> This may be shown by considering the thermal and caloric equations of state for an ideal gas,

see Appendix A for a discussion of the concept of static stability.<sup>6</sup> The reference state of the outer core of the Earth is also characterized by stable stratification, because otherwise compositional and thermal buoyancy forces would lead to a rapid adjustment to such a state. Moreover, the property that the atmosphere has a constant entropy, which is a consequence of the adiabaticity and the equations of state, is also assumed for the outer core of the Earth. This similarity between the stable atmosphere and the outer core of the Earth probably led to a transfer of the terminology from atmospheric sciences to sciences related to the Earth's deep interior, although the term adiabatic does not apply and is misleading.

In the following, the assumption of a homogeneous entropy is made for the reference state in order to resolve the lack of information on the internal heating in the outer core of the Earth. Hence,

$$\nabla s_a = \mathbf{0} \quad \Leftrightarrow \quad \frac{\partial \hat{s}}{\partial T} \nabla T_a + \frac{\partial \hat{s}}{\partial p} \nabla p_a = \mathbf{0}. \quad (2.89)$$

---

which are given by

$$\frac{p}{\rho} = R_s T \quad \text{and} \quad u(T) = c_v(T - T_0) + u_0,$$

where  $R_s$  denotes the specific gas constant and  $c_v$  the specific isochoric heat capacity. Furthermore, for an ideal gas the entropy may be expressed as

$$s(p, T) = c_p \left[ \ln \left( \frac{T}{T_0} \right) - \frac{\gamma - 1}{\gamma} \ln \left( \frac{p}{p_0} \right) \right] + s_0,$$

where  $\gamma = c_p/c_v$  is the adiabatic exponent and  $c_p$  the specific isobaric heat capacity. Using the assumption of an adiabatic atmosphere and the balance of internal energy the following relation may be found, for example,

$$\frac{p}{p_0} = \left( \frac{T}{T_0} \right)^{\frac{\gamma}{\gamma-1}}.$$

If this relation is substituted in the formula for the entropy to eliminate the pressure, it is found that the entropy is a constant, *viz.*,  $s = s_0$ .

<sup>6</sup>The stability, see Appendix A, may be shown by noting the following equivalence for an ideal gas

$$N^2 = -\frac{g}{\rho} \frac{\partial \rho}{\partial z} > 0 \quad \Leftrightarrow \quad \frac{1}{\rho} \frac{\partial \rho}{\partial z} = \frac{1}{p} \frac{\partial p}{\partial z} - \frac{1}{T} \frac{\partial T}{\partial z} < 0.$$

Here it is assumed that the  $z$ -coordinate is aligned with the gravity field. From the hydrostatic balance of momentum and the adiabatic relation in Footnote 5 the following relations for the vertical pressure and temperature gradient are obtained

$$\frac{\partial T}{\partial z} = -\frac{\gamma - 1}{\gamma} \frac{g}{R_s}, \quad \frac{1}{p} \frac{\partial p}{\partial z} = \frac{\gamma}{\gamma - 1} \frac{1}{T} \frac{\partial T}{\partial z}.$$

Hence,

$$\frac{1}{\rho} \frac{\partial \rho}{\partial z} = \left( \frac{\gamma}{\gamma - 1} - 1 \right) \frac{1}{T} \frac{\partial T}{\partial z} = -\frac{1}{\gamma} \frac{1}{R_s T} < 0,$$

which confirms the stability of the adiabatic atmosphere.

The thermodynamic relations, see Sect. 2.5,

$$\frac{\partial \hat{s}}{\partial T} = \frac{c_p}{T} \quad \text{and} \quad \frac{\partial \hat{s}}{\partial p} = \frac{1}{\rho^2} \frac{\partial \hat{\rho}}{\partial T} = -\frac{1}{\rho} \alpha$$

allow to obtain the following relation between the temperature and the gravity field  $\mathbf{g}_a$ , from Eq. (2.89) and Eq. (2.87)<sub>1</sub>,

$$\frac{c_p}{T_a} \nabla T_a = \frac{\alpha}{\rho_a} \nabla p_a = \alpha \mathbf{g}_a. \quad (2.90)$$

A similar relation can be derived from the thermal equation of state, *i.e.*,  $\rho = \hat{\rho}(p, T)$ . Taking the gradient of this equation and using the definitions of the coefficient of thermal expansion  $\alpha$  and of the compressibility  $\beta$  specified in Eq. (2.59) yields

$$\frac{1}{\rho_a} \nabla \rho_a = -\alpha \nabla T_a + \beta \nabla p_a = \left( \rho_a \beta - \frac{\alpha^2 T_a}{c_p} \right) \mathbf{g}_a = \left( \frac{1}{u_T^2} - \frac{\alpha^2 T_a}{c_p} \right) \mathbf{g}_a. \quad (2.91)$$

In the last step, the compressibility  $\beta$  was replaced by the isothermal speed of sound  $u_T$ , *viz.*,  $\beta = 1/(\rho u_T^2)$ .

In the following, the assumption of a constant entropy is used to determine the reference state. This allows to identify two combinations of material parameters as dimensionless numbers, which govern the spatial dependence of the reference state. These dimensionless numbers arise if the thermodynamic state space variables are chosen as entropy and pressure. In Sect. 2.5 the GIBBS free energy was used as a thermodynamic potential, *i.e.*,  $g = u - Ts + p/\rho$ , and the thermodynamic state variables were accordingly chosen as temperature and pressure, *i.e.*,  $g = \hat{g}(p, T)$ . If entropy and pressure are used as the state variables, the enthalpy is a suitable thermodynamic potential to formulate constitutive relations and thermodynamic constraints. However, relations between material parameters arising from the two different state spaces can be found without reiterating the procedure presented in Sect. 2.5. A relation between the speed of sound, the coefficient of thermal expansion and the coefficient of entropy expansion can be derived by introducing the following three functions  $\rho = \hat{\rho}(p, T) = \tilde{\rho}(p, s)$  and  $s = \hat{s}(p, T)$ . Using  $\hat{\rho}(p, T) = \tilde{\rho}(p, \hat{s}(p, T))$  and applying the chain rule of differentiation the relation between the two coefficients of thermal expansion reads

$$\alpha = -\frac{1}{\rho} \frac{\partial \hat{\rho}}{\partial T} = -\frac{1}{\rho} \underbrace{\frac{\partial \tilde{\rho}}{\partial s}}_{=\alpha_s} \frac{\partial \hat{s}}{\partial T} = \frac{\alpha_s c_p}{T}, \quad (2.92a)$$

where  $\alpha_s$  is the coefficient of entropy expansion. The relation for the isothermal and isentropic compressibilities or the respective two speeds of sound is found in a

similar manner and it is given by

$$\beta = \frac{1}{\rho c_T^2} = \frac{1}{\rho} \frac{\partial \hat{\rho}}{\partial p} = \frac{1}{\rho} \frac{\partial \tilde{\rho}}{\partial p} + \frac{1}{\rho} \frac{\partial \tilde{\rho}}{\partial s} \frac{\partial \hat{s}}{\partial p} = \beta_s + \frac{\alpha_s \alpha}{\rho} = \frac{1}{\rho u_s^2} + \frac{\alpha^2 T}{\rho c_p}, \quad (2.92b)$$

where  $u_s = 1/\sqrt{\rho \beta_s}$  denotes the isentropic speed of sound and  $\beta_s$  the respective compressibility. With this result for the relation for the two speeds of sound the expression in the parenthesis on the right-hand side of Eq. (2.91) can be identified as the reciprocal of the speed of sound at constant entropy  $u_s$ . Furthermore, Eq. (2.90) can be recast in such a way that the coefficient of entropy expansion  $\alpha_s$  occurs. In summary, Eqs. (2.90) and (2.91) can be expressed as

$$\frac{1}{\rho_a} \nabla \rho_a = \frac{1}{u_s^2} \mathbf{g}_a, \quad \nabla T_a = \alpha_s \mathbf{g}_a. \quad (2.93)$$

It is convenient to recast these equations in a dimensionless form. In order to do so, two non-dimensional numbers are introduced: the dissipation number  $D$  and the GRÜNEISEN parameter  $\gamma_s$  at constant entropy. The former is given by the ratio

$$D = \frac{\alpha g d}{c_p}, \quad (2.94a)$$

where  $d$  is the shell thickness of the outer core of the Earth and  $g$  a characteristic magnitude of the gravitational acceleration. For the dissipation number in the outer core of the Earth, a value of  $D = 0.3$  is usually assumed in the literature [Jones (2007)]. The isentropic GRÜNEISEN parameter can be defined in various ways, and it can be expressed in terms of various material parameters. For the material parameters introduced in the context of this section, the GRÜNEISEN parameter is obtained by going through the following steps

$$\gamma_s := \frac{\rho}{T} \frac{\partial \check{T}}{\partial \rho} = \frac{\rho}{T} \frac{\partial \check{T}}{\partial p} \frac{\partial \check{p}}{\partial \rho} = \frac{\rho}{T} \left( \underbrace{-\frac{1}{\rho^2} \frac{\partial \tilde{\rho}}{\partial s}}_{=\alpha_s/\rho} \right) \underbrace{\frac{\partial \check{p}}{\partial \rho}}_{=u_s^2} = \frac{\alpha_s u_s^2}{T} = \frac{\alpha u_s^2}{c_p}, \quad (2.94b)$$

where the functions  $T = \check{T}(\rho, s) = \check{T}(p, s)$ ,  $p = \check{p}(\rho, s)$  and  $\rho = \tilde{\rho}(p, s)$  were used to indicate the different functional dependencies of the thermodynamic state variables. Additionally, a MAXWELL relation was used to replace the derivative of the temperature function  $\check{T}$  with respect to the pressure by the derivative of the density function  $\tilde{\rho}$  with respect to the entropy. Regarding the outer core of the Earth, from *ab initio* calculations the GRÜNEISEN parameter is obtained to range from 1.51 to 1.52 if the pressure varies between 280 GPa and 340 GPa [Alfè, Price, and Gillan (2002)]. Moreover, Alfè, Price, and Gillan argue that the GRÜNEISEN parameter is constant for pressures varying between 280 GPa and 340 GPa and temperatures varying between 4000 K and 6000 K [Alfè, Price, and Gillan (2002)].

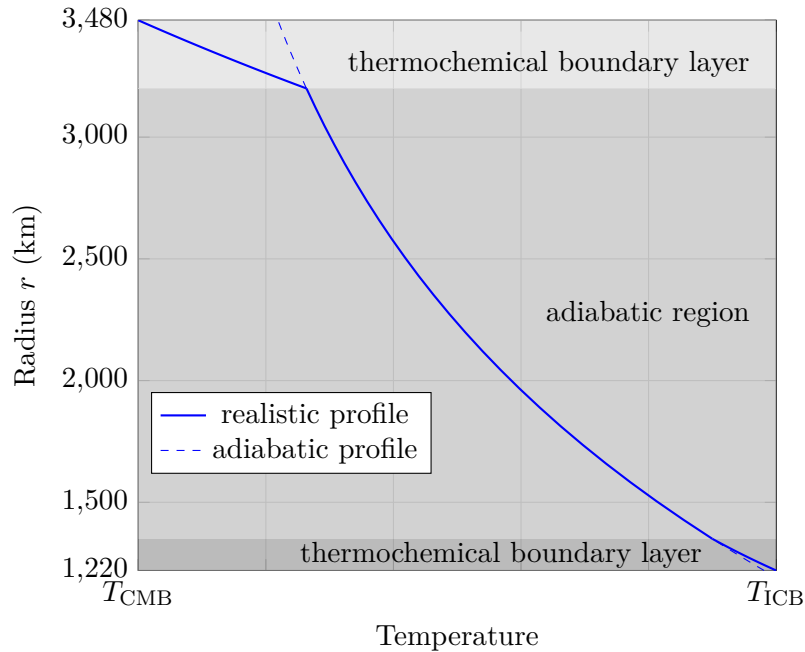


**Figure 2.9:** Qualitative temperature profile in the outer core of the Earth. At the inner core and the core-mantle boundary, thermal boundary layers are present, which leads to a deviation of the temperature profile from the adiabatic counterpart. At the top and bottom of the core the realistic temperature profile has a super-adiabatic heat flux. Illustration adopted from Gubbins, Masters, and Jacobs [1979].

Using the expression for the GRÜNEISEN parameter above, a multiplication of Eqs. (2.90) and (2.91) by the shell thickness and a rearrangement of the right-hand sides leads to

$$\frac{d}{\rho_a} \nabla \rho_a = \frac{D}{\gamma_s} \frac{\mathbf{g}_a}{g}, \quad \frac{d}{T_a} \nabla T_a = D \frac{\mathbf{g}_a}{g}. \quad (2.95)$$

Together with Eq. (2.87), these equations constitute the field equations for the reference density, temperature and pressure. The gravitational forces are computed from the reference potential  $\varphi_a$  and this potential is obtained from NEWTON's law of gravity, whose continuous version is given by  $\nabla^2 \varphi_a = 4\pi G \rho_a$  [Müller and Weiss (2016)]. In conclusion, NEWTON's law of gravity is an additional equation, which needs to be solved in order to obtain the so-called adiabatic reference state.

In summary, Eqs. (2.87), (2.95) and NEWTON's law of gravity form a coupled non-linear system of partial differential equations, which is usually solved using the assumption of the spherical symmetry, which neglects the non-spherical centripetal accelerations. This system can be significantly simplified if a constant gravitational acceleration is assumed. If the dissipation number  $D$  and the GRÜNEISEN parameter  $\gamma_s$  are also assumed as constants, the density and the temperature have an exponential dependence on the radius. This exponential dependence shows a suboptimal feature of the assumption of constant entropy. Regarding,

*e.g.*, the temperature profile can only match the boundary condition either at the core-mantle boundary and at the solid inner core, because the differential equation is first order with respect to the spatial derivatives. This means that the solution for the reference temperature, in general, does not reflect the true temperature profile in the outer core of the Earth. The assumption of a constant entropy simply fails in the boundary layers, where the temperature profile departs significantly from that obtained by solving the differential equations. An illustration of the temperature profile in the outer core of the Earth in contrast to the adiabatic profile is shown in Fig. 2.9.<sup>7</sup>

### 2.7.2 The anelastic approximation

In the following, a perturbation of the reference state is considered. Hence,

$$\rho = \rho_a + \rho_c, \quad p = p_a + p_c, \quad T = T_a + T_c, \quad \varphi = \varphi_a + \varphi_c, \quad \mathbf{g} = \mathbf{g}_a + \mathbf{g}_c, \quad (2.96)$$

where the subscript c refers to the perturbations due to a convective motion of the fluid and the subscript a refers to the reference state. Note that the same perturbation expansion is also applied for the velocity and the magnetic field, but these fields vanish in the reference state. The velocity perturbation is denoted by  $\mathbf{v}_c$  in order to indicate that this perturbation is associated with convective motion. The magnetic field is perturbed by the convective fluid motion, but electromagnetic waves entering the core may also be present and therefore the perturbation of the magnetic field is simply denoted by  $\mathbf{B}$ . More precisely, all thermomechanical quantities are expanded in the following form  $\rho = \rho_0 + \varepsilon_c \rho_1 + \varepsilon_c^2 \rho_2 + \dots$ , where  $\varepsilon_c$  is a small dimensionless parameter that quantifies the size of perturbation in relation to the reference state.

In the following, the parameter expansion is truncated at first order in  $\varepsilon_c$  and the non-linear terms are neglected, which corresponds to a thermomechanical linearization with respect to the reference state. Then, the momentum equation has the following form

$$\begin{aligned} \rho_a \frac{d\mathbf{v}_c}{dt} + 2\rho_a \boldsymbol{\Omega} \times \mathbf{v}_c = & -\nabla p_c + \rho_a \mathbf{g}_c + \rho_c \mathbf{g}_a + \\ & + \nabla \cdot [(\lambda - \frac{2}{3}\mu)(\nabla \cdot \mathbf{v}_c)\mathbf{1} + \mu(\mathbf{v}_c \otimes \nabla + \nabla \otimes \mathbf{v}_c)] + \mathbf{J}_f \times \mathbf{B}. \end{aligned} \quad (2.97)$$

Here, the inertial terms  $\rho_c(d\mathbf{v}_c/dt)$  as well as the CORIOLIS term  $2\rho_c \boldsymbol{\Omega} \times \mathbf{v}_c$  and the body force term  $\rho_c \mathbf{g}_c$  were neglected, because these are terms of second order. Note that due to Eq. (2.87), the centripetal acceleration  $\rho_c \boldsymbol{\Omega} \times (\boldsymbol{\Omega} \times \mathbf{x})$  is contained in the term  $\rho_c \mathbf{g}_a$ . In order to simplify this momentum equation, a pressure shift is

<sup>7</sup>The realistic profile in Fig. 2.9 has two discontinuities at the boundaries of the adiabatic region with the two thermochemical boundary layers. These discontinuities are due to the continuity of the radial component of the heat flux vector  $\mathbf{q}$ . Since the thermal conductivities are assumed to jump at the interfaces, a jump is also presented in the temperature profile.

applied. It reads

$$\bar{p} = p_c + \rho_a \varphi_c. \quad (2.98)$$

This modified pressure may now be introduced in Eq. (2.97) by using the following relation

$$\begin{aligned} -\nabla p_c + \rho_a \mathbf{g}_c + \rho_c \mathbf{g}_a &= -\nabla p_c - \rho_a \nabla \varphi_c + \rho_c \mathbf{g}_a \\ &= -\nabla(p_c + \rho_a \varphi_c) + \varphi_c \nabla \rho_a + \rho_c \mathbf{g}_a = -\nabla \bar{p} + \varphi_c \nabla \rho_a + \rho_c \mathbf{g}_a. \end{aligned} \quad (2.99a)$$

Inserting Eq. (2.93) for the gradient of the reference density yields

$$-\nabla p_c + \rho_a \mathbf{g}_c + \rho_c \mathbf{g}_a = -\nabla \bar{p} + \rho_a \left( \frac{\rho_c}{\rho_a} + \frac{\varphi_c}{u_{s,a}^2} \right) \mathbf{g}_a. \quad (2.99b)$$

The last two steps have replaced the perturbation of the gravity field by the perturbation of the gravitational potential, which now occurs in a product with the reference density and the reference gravitational acceleration. In order to eliminate the perturbation of the gravitational potential completely, the right-hand side of the last equation is divided by the reference density. This yields

$$-\frac{1}{\rho_a} \nabla \bar{p} + \left( \frac{\rho_c}{\rho_a} + \frac{\varphi_c}{u_{s,a}^2} \right) \mathbf{g}_a = -\nabla \left( \frac{\bar{p}}{\rho_a} \right) + \left( \frac{\rho_c}{\rho_a} - \frac{p_c}{\rho_a u_{s,a}^2} \right) \mathbf{g}_a, \quad (2.99c)$$

where the product rule for the gradient of the modified pressure and Eq. (2.93) were applied to obtain the expression on the right-hand side.

Note that the factor in front of the reference gravity field on the right-hand side of the last equation is governed by the perturbations of the density and the pressure. The density may be replaced through the following linearization of the thermal equation of state with respect to the reference state

$$\begin{aligned} \rho &= \tilde{\rho}(s, p) = \rho_a (1 - \alpha_{s,a}(s - s_a) + \beta_{s,a}(p - p_a)) \\ &= \rho_a (1 - \alpha_{s,a} s_c + \beta_{s,a} p_c), \end{aligned} \quad (2.100a)$$

where the subscripts added to the coefficient of thermal expansion and the compressibility shall indicate that these material parameters are evaluated in the reference state. Furthermore, the symbol  $s_c$  denotes the entropy perturbation. With this relation the factor in front of the reference gravity field in Eq. (2.99c) can be expressed as

$$\frac{\rho_c}{\rho_a} - \frac{p_c}{\rho_a u_{s,a}^2} = \frac{\rho_c}{\rho_a} - \beta_{s,a} p_c = -\alpha_{s,a} s_c. \quad (2.100b)$$

Substituting Eqs. (2.99) in junction with the last equation leads to the following

formulation of the momentum equation in Eq. (2.97)

$$\begin{aligned} \frac{d\mathbf{v}_c}{dt} + 2\boldsymbol{\Omega} \times \mathbf{v}_c = & -\nabla\left(\frac{\bar{p}}{\rho_a}\right) - \alpha_{s,a}s_c\mathbf{g}_a + \\ & + \frac{1}{\rho_a}\nabla \cdot [(\lambda - \frac{2}{3}\mu)(\nabla \cdot \mathbf{v}_c)\mathbf{1} + \mu(\mathbf{v}_c \otimes \nabla + \nabla \otimes \mathbf{v}_c)] + \frac{1}{\rho_a}\mathbf{J}^f \times \mathbf{B}. \end{aligned} \quad (2.101)$$

This formulation of the momentum is commonly found in the literature dealing with the anelastic approximation. It includes a buoyancy term  $\alpha_{s,a}s_c\mathbf{g}_a$ , that is governed by the entropy and not by the temperature perturbation. Moreover, the density perturbation in this equation has a spatial dependence as well as the coefficient of entropy expansion.

The above momentum equation is complemented by the balance of mass. More precisely, the perturbation expansion is applied and the balance of mass is also linearized with respect to these perturbations. The resulting equation reads

$$\frac{\partial \rho_c}{\partial t} + \nabla \cdot (\rho_a \mathbf{v}_c) = 0. \quad (2.102)$$

Here, the time derivative of the density perturbation is still present, and, as a consequence, the resulting system allows, *e.g.*, pressure waves, as possible solutions. The speed of these (elastic) waves is extremely large in comparison to the velocity of the fluid resulting from the convective motion. The timescale of interest in the context of the outer core of the Earth is the timescale of convection and therefore waves related to density fluctuations are filtered from the system by neglecting the partial time derivative in the equation above. The neglect of this term is referred to as the anelastic approximation and the associated simplified balance of mass is given by

$$\nabla \cdot (\rho_a \mathbf{v}_c) = 0. \quad (2.103)$$

In order to obtain a closed system, the momentum equation in Eq. (2.101) and the anelastic balance of mass in Eq. (2.103) need to be supplemented by an appropriate form of the balance of internal energy. There are two common ways to formulate the anelastic balance of internal energy. The first version contains only a material time derivative of the entropy whereas the second version contains material time derivatives of the temperature and the pressure.

From a practical point of view, it is desirable that a material derivative of only one field is present in the anelastic balance of internal energy. Therefore, the former version including the entropy is often used in the literature dealing with the anelastic approximation. However, this only seems easier at a first glance, because it is not possible to express the temperature, that is present in the heat conduction term, as a sole function of the entropy. Therefore, an approximation is made that neglects the dependence of the temperature on the pressure. More precisely, this approximation is equivalent to the assumption that the isentropic and isothermal speed of sound do not differ much.

Regarding the second version of the anelastic balance of internal energy, where material time derivatives of both temperature and pressure are present, an equivalent simplification related to the two material time derivatives of the temperature and the pressure can be derived. This corresponds to the assumption that the pressure dependence of the internal energy is negligible. This negligibility is justified by considering the following expression in terms of perturbed quantities

$$\rho_a \dot{u}_c + p_a \nabla \cdot \mathbf{v}_c = \rho_a \dot{u}_c - p_a \frac{\dot{\rho}_c}{\rho_a + \rho_c} \approx \rho_a \dot{u}_c - p_a \frac{\dot{\rho}_c}{\rho_a}. \quad (2.104a)$$

The time derivatives of the linearizations of the perturbations of the internal energy and the density with respect to the reference state may be obtained by first noting that  $p(\mathbf{x}, t) = p_a(\mathbf{x}) + p_c(\mathbf{x}, t)$  and  $T(\mathbf{x}, t) = T_a(\mathbf{x}) + T_c(\mathbf{x}, t)$ . Hence,  $\dot{p} = \dot{p}_c$  and  $\dot{T} = \dot{T}_c$ . Therefore, a linearization of the caloric equation of state specified in Eq. (2.62) with respect to the adiabatic reference state yields

$$\rho_a \dot{u}_c = \rho_a c_{p,a} \dot{T}_c - \alpha_a p_a \dot{T}_c + \beta_a p_a \dot{p}_c - \alpha_a T_a \dot{p}_c. \quad (2.104b)$$

If the same linearization procedure is applied for the thermal equation of state in Eq. (2.66), one obtains

$$\frac{\dot{\rho}_c}{\rho_a} = -\alpha_a \dot{T}_c + \beta_a \dot{p}_c. \quad (2.104c)$$

A summation of the latter two equations yields the following expression for the right-hand side of Eq. (2.104a)

$$\rho_a \dot{u}_c + p_a \nabla \cdot \mathbf{v}_c \approx \rho_a c_{p,a} \dot{T}_c - \alpha_a T_a \dot{p}_c. \quad (2.104d)$$

The coefficient of the second term on the right-hand side can now be related to the isentropic and isothermal speed of sound using Eqs. (2.92a) and (2.92b)

$$\alpha_a T_a \stackrel{(2.92a)}{=} \alpha_{s,a} c_{p,a} \stackrel{(2.92b)}{=} \frac{\rho_a c_{p,a}}{\alpha_a} (\beta_a - \beta_{s,a}) = \frac{c_{p,a}}{\alpha_a} \frac{u_{s,a}^2 - u_{T,a}^2}{u_{T,a}^2 u_{s,a}^2}, \quad (2.104e)$$

where the relations  $\beta_a = 1/(\rho_a u_{T,a}^2)$  and  $\beta_{s,a} = 1/(\rho_a u_{s,a}^2)$  were substituted in the last step. If the difference of the two speeds of sound  $u_{T,a}$  and  $u_{s,a}$  is small, the second term on the right-hand side of Eq. (2.104d) can be neglected. Note that the approximations made to simplify the first version of the anelastic balance of internal energy, where the entropy is used the desired thermodynamic variable, are equivalent to those made in the second version. Therefore, the two versions are equivalent. In summary, the anelastic balance of internal energy reduces to the following heat conduction equation

$$\rho_a c_{p,a} \dot{T}_c = \nabla \cdot (\kappa \nabla T_c) + \nabla \cdot (\kappa \nabla T_a) + (\rho_a + \rho_c) \hat{r}_a. \quad (2.105)$$

Note that the heat flux of the reference state, *i.e.*,  $\mathbf{q}_a = -\kappa \nabla T_a$ , does not neces-

sarily balance the internal heating in the reference state, *i.e.*,  $\rho_a \hat{r}_a$ , because the temperature profile is obtained, for example, from Eq. (2.95), which was derived based on the assumption of a homogeneous entropy. For this reason, these two terms are still present in Eq. (2.105). However, most discussions of convection in the outer core and the geodynamo are based on the BOUSSINESQ approximation, in which these terms are not present.

### 2.7.3 The BOUSSINESQ approximation

The anelastic approximation presented in the previous section represents an accurate description of convection in the core of the Earth. Due to the turbulent nature of this convection the related equations need to be solved numerically. In most numerical codes spectral methods are used as a numerical scheme. In general, these methods either cannot treat terms with spatially dependent coefficients like, *e.g.*, viscosity or thermal conductivity, or the spatial dependence of the coefficients is limited to simple functional relations like power laws. Therefore, the BOUSSINESQ approximation is often applied in order to ease the numerical solution of the equations. Moreover, Jones argues that a wealth of knowledge has been accumulated on BOUSSINESQ convection and that all laboratory experiments lie in a regime where the BOUSSINESQ approximation is appropriate [Jones (2007)]. According to Braginsky and Roberts, there is not much difference between the anelastic and the BOUSSINESQ approximation in laboratory experiments. However, for the core of the Earth the situation is significantly different [Braginsky and Roberts (1995)].

The BOUSSINESQ approximation is obtained formally by taking the limit  $D \rightarrow 0$  for the dissipation number, which, according to Eq. (2.95), corresponds to a homogeneous reference state. However, for the core of the Earth this does not apply, because the reference variables vary substantially with depth. Nevertheless, the convective fluctuations are rather small compared to the gradients of the reference state variables in the core of the Earth, whereas the situation is reversed in case of a laboratory experiment [Braginsky and Roberts (1995)]. The dissipation number  $D$  is estimated to vary considerably from approximately 0.3 to 0.5 [Anufriev, Jones, and Soward (2005)]. Rather than taking the limit  $D \rightarrow 0$ , this range implies that the relative density and temperature difference over the outer core of the Earth is small, *viz.*,  $(\rho_{\text{ICB}} - \rho_{\text{CMB}})/\rho_{\text{ICB}} < 1$  and  $(T_{\text{ICB}} - T_{\text{CMB}})/T_{\text{ICB}} < 1$ . Nevertheless, the limit  $D \rightarrow 0$  is commonly applied for the core of the Earth. Then, the reference density  $\rho_a$  is replaced by a reference density  $\rho_0$  and Eq. (2.101) and (2.103) are given by

$$\nabla \cdot \mathbf{v}_c = 0, \quad (2.106)$$

$$\frac{d\mathbf{v}_c}{dt} + 2\boldsymbol{\Omega} \times \mathbf{v}_c = -\frac{1}{\rho_0} \nabla \bar{p} - \alpha_{s,0} s_c \mathbf{g}_a + \frac{\mu}{\rho_0} \nabla^2 \mathbf{v}_c + \frac{1}{\rho_0} \mathbf{J}^f \times \mathbf{B}, \quad (2.107)$$

where the coefficient of the entropy expansion is denoted by  $\alpha_{s,0}$  in order to indicate that it corresponds to a constant reference state. Note that the balance of mass

simplifies to the so-called incompressibility condition and that this condition was already used to simplify the momentum equation above. Moreover, the shear viscosity was also assumed to be constant.

In this formulation of the momentum equation, the buoyancy term  $\alpha_{s,a}s_c\mathbf{g}_a$  is still governed by the entropy perturbation and not by the temperature perturbation. The temperature may be incorporated in the buoyancy term by a linearization of the caloric equation of state, *i.e.*, Eq. (2.58), with respect to the now constant reference state. This linearization yields

$$s_c = \frac{c_{p,0}}{T_a}T_c - \frac{\alpha_0}{\rho_0}p_c. \quad (2.108a)$$

Considering the product of the latter term with the coefficient of entropy expansion  $\alpha_{s,0}$ , that occurs in the buoyancy term, results in

$$\frac{\alpha_{s,0}\alpha_0}{\rho_0}p_c = \frac{\alpha_0^2T_0}{\rho_0c_{p,0}}p_c = \frac{1}{\rho_0}\left(\frac{1}{u_{T,0}^2} - \frac{1}{u_{s,0}^2}\right)p_c = \frac{1}{\rho_0}\frac{u_{s,0}^2 - u_{T,0}^2}{u_{T,0}^2u_{s,0}^2}p_c, \quad (2.108b)$$

where Eqs. (2.92a) and (2.92b) were used to obtain the relation between the two speeds of sound. If the difference between the speed of sound at a constant temperature and a constant entropy is small, then the dependence of the buoyancy term on the pressure can be neglected. In this case, the buoyancy term is solely dependent on the temperature

$$\alpha_{s,0}s_c \approx \frac{\alpha_{s,0}c_{p,0}}{T_0}T_c = \alpha_0T_c. \quad (2.108c)$$

With this approximation for the two speeds of sound the momentum equation may be expressed as

$$\frac{d\mathbf{v}_c}{dt} + 2\boldsymbol{\Omega} \times \mathbf{v}_c = -\frac{1}{\rho_0}\nabla\bar{p} - \alpha_0T_c\mathbf{g}_a + \nu\nabla^2\mathbf{v}_c + \frac{1}{\rho_0}\mathbf{J}^f \times \mathbf{B}, \quad (2.109)$$

where  $\nu = \mu/\rho_0$  is the kinematic viscosity.

The BOUSSINESQ approximation also modifies the anelastic balance of internal energy in Eq. (2.105). According to Eq. (2.95), the limit  $D \rightarrow 0$  implies that the temperature gradient of the reference state vanishes. This simplifies the right-hand side of Eq. (2.105), but the internal heating would be present. Recall that the internal heating, if included at all, requires additional modeling and knowledge about this term. This is rare for the core of the Earth. Therefore, it is often neglected in contexts of BOUSSINESQ convection. Moreover, the assumption of a vanishing dissipation number and the constant reference temperature, that would result, are not only inconsistent with the balance of internal energy for the reference state in Eq. (2.88), which would read  $\nabla \cdot (\kappa\nabla T_a) = 0$  for a vanishing internal heating, but also with the boundary conditions—a constant temperature profile cannot meet the two boundary conditions at the core-mantle and inner

core boundary. These inconsistencies in relation to the energy balance and the temperature profile originate from the assumption of a homogeneous entropy, which is associated with the so-called adiabatic reference state. In summary, using  $\nabla \cdot (\kappa \nabla T_a) = 0$  and  $\hat{r}_a = 0$  the simplified balance of internal energy of the BOUSSINESQ approximation is given by

$$\rho_0 c_{p,0} \dot{T}_c = \kappa \nabla^2 T_c, \quad (2.110)$$

where the thermal conductivity was also assumed to be constant.

## 2.8 Summary

The fundamental field equations and constitutive laws of magnetohydrodynamics were presented in Sects. 2.3, 2.4, 2.5. Based on these and the formulation for a rotating observer in Sect. 2.6, the previous section derived the equations governing the convective fluid motion in the outer core of the Earth as a first order perturbation from a steady reference state. This section summarizes the equations for the BOUSSINESQ approximation. These equations serve as a basis for Sect. 3 and will also be solved in a dimensionless form in Sect. 4.

In order to simplify the notation, the subscripts referring to the adiabatic reference state and the convective perturbation are subsequently dropped. According to Eq. (2.38)<sub>4</sub>, the free current density  $\mathbf{J}_f = \sigma(\mathbf{E} + \mathbf{v} \times \mathbf{B})$  can be expressed in terms of the curl of the magnetic field, *i.e.*,  $\mathbf{J}_f = \mu_0^{-1} \nabla \times \mathbf{B}$ . This fact is acknowledged and the electric field is removed completely from the system, such that the LORENTZ force density is given by  $\mu_0^{-1} (\nabla \times \mathbf{B}) \times \mathbf{B}$ . Then, the system describing the magnetohydrodynamic BOUSSINESQ convection in the outer core of the Earth is given by

$$\begin{aligned} \nabla \cdot \mathbf{v} &= 0, & \nabla \cdot \mathbf{B} &= 0, & \rho_0 c_p \dot{T} &= \kappa \nabla^2 T, \\ \frac{d\mathbf{v}}{dt} + 2\boldsymbol{\Omega} \times \mathbf{v} &= -\frac{1}{\rho_0} \nabla \bar{p} - \alpha T \mathbf{g}_0 + \nu \nabla^2 \mathbf{v} + \frac{1}{\rho_0 \mu_0} (\nabla \times \mathbf{B}) \times \mathbf{B}, \\ \frac{\partial \mathbf{B}}{\partial t} &= \nabla \times (\mathbf{v} \times \mathbf{B}) + \eta \nabla \times \nabla \times \mathbf{B}. \end{aligned} \quad (2.111)$$

Here, all material parameters, *viz.*, the coefficient of thermal expansion  $\alpha$ , the kinematic viscosity  $\nu$ , the isobaric specified heat capacity  $c_p$  and the magnetic diffusivity  $\eta$ , are for simplicity assumed to be constants. The quantities originating from the reference state are given by the reference gravitational acceleration  $\mathbf{g}_0$  and the reference density  $\rho_0$ , which is assumed to be homogeneous.

Finally, recall that the derivation of the anelastic approximation involved the pressure shift specified in Eq. (2.99) and that this pressure shift is only applied to the pressure perturbation due to the convective motion. Therefore, it should be kept in mind that the pressure  $\bar{p}$ , which is subsequently used, does not correspond to the thermodynamic pressure or its perturbation. Moreover, the volumetric body

force density  $\mathbf{g}_0$  does not only consist of a gravitational part but also contains a part reflecting the centripetal acceleration. Note that the latter part causes a slightly aspheric body force, which is often neglected in the literature, see Matsui et al. [2016], and also in this work.



### 3 Linear analysis of a stratified layer with boundary topography

In this chapter, an analysis of a stratified layer of an electrically conducting viscous fluid is performed in a rotating system. At the top of this stratified layer, a solid boundary with a sinusoidal topography is present. This model mimics the stratified layer below the Core-Mantle Boundary (CMB) of the Earth and only represents a simplified approximation of the actual situation, because the alteration of the CMB from a perfectly spherical shape is modeled using a simple sinusoidal function. Furthermore, the stratified layer is modeled having an infinite extension which is of course also not the case in the outer core of the Earth.

The question is whether a fluid flow at the bottom of this layer may induce a perturbation of the pressure field which yields a net torque on the CMB. Therefore, the problem is formulated in terms of a linear stability analysis, which considers perturbation from the reference state corresponding to a flat CMB. The fluid flow at the bottom of the stratified layer mimics the fluid, which is convecting in the deeper parts of the outer core of the Earth. This convecting flow is also generating a magnetic field, which is traversing the stratified layer.

The presence of a stably stratified layer at the CMB was discussed in the review in Sect. 2.1. It was discussed that a stratified layer may form due to compositional (chemical) and thermal effects. These thermochemical processes, which occur on geological timescales, are widely addressed in the literature, but related studies entirely neglect the influence of a fluid flow in the stratified layer. This work focuses on the net torque that may occur if there is a fluid flow in a stratified layer. Therefore, the thermochemical processes are neglected and the stratified layer is simply modeled by a linear density profile.

In the following, a local two-dimensional model neglecting curvature is presented, see Fig. 3.1. The neglect of the curvature of the CMB is justified by the fact that the wavelength characterizing the topography is assumed to be small compared to the radius of the CMB. Moreover, the thickness of the stratified layer is also small compared to this radius. This local approximation is referred to as the  $\beta$ -plane approximation in the literature on geophysical fluid mechanics [Pedlosky (1987)]. Consequently, the angular velocity vector used in the following analysis only represents the local radial component of the angular velocity vector of the Earth.

The analysis in this chapter and related results were partly presented in Glane and Buffett [2018]. However, this chapter discusses the problem, associated assumptions and solutions in much greater detail and extent. This includes the dimensionless

---

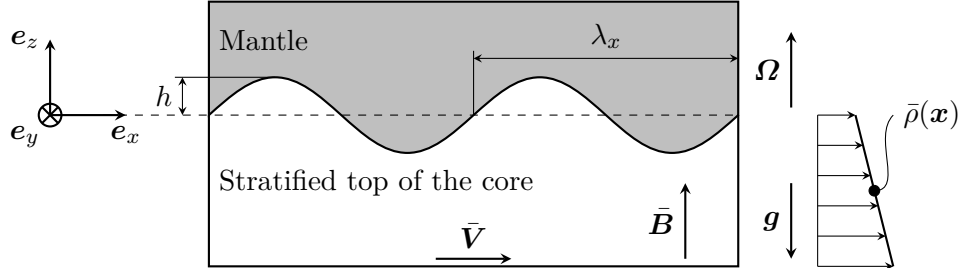


**Figure 3.1:** Sketch of a two-dimensional Core-Mantle Boundary with a sinusoidal topography with amplitude  $h$  and wavelength  $\lambda_x$ . As indicated by the density profile on the right-hand side the fluid is stratified in the core of the Earth. The reference directions of the velocity and magnetic fields are indicated at the bottom of the sketch.

formulation in Sect. 3.1.1, which was not used in the context of the referenced paper. Moreover, the perturbation analysis, which was only briefly discussed in the appendix of that paper, is presented and discussed in greater detail in Sect. 3.2. Additionally, only one of the cases which are analyzed in Sect. 3.3, were incorporated in the paper by Glane and Buffett.

### 3.1 Problem statement

The basic equations describing the problem are given by the NAVIER-STOKES equations and the magnetic induction equation. Moreover, the BOUSSINESQ approximation is applied, which neglects density gradients in all terms except for the body force term. The system is considered in a rotating frame with a constant angular velocity,  $\boldsymbol{\Omega} = \Omega(\theta)\mathbf{e}_z$ , whose magnitude is proportional to the angular velocity of the mantle of the Earth and depends on the colatitude  $\theta$  because of the  $\beta$ -plane approximation. Furthermore, the gravitational acceleration is homogeneous and given by  $\mathbf{g} = -g\mathbf{e}_z$ . The equations governing the system are

$$\nabla \cdot \mathbf{v} = 0, \quad \nabla \cdot \mathbf{B} = 0, \quad (3.1a)$$

$$\rho_0 \frac{d\mathbf{v}}{dt} + 2\rho_0 \boldsymbol{\Omega} \times \mathbf{v} = -\nabla P + \mu \nabla^2 \mathbf{v} + \rho \mathbf{g} + \frac{1}{\mu_0} \mathbf{B} \cdot \nabla \otimes \mathbf{B}, \quad (3.1b)$$

$$\frac{\partial \mathbf{B}}{\partial t} = \nabla \times (\mathbf{v} \times \mathbf{B}) + \eta \nabla^2 \mathbf{B}. \quad (3.1c)$$

In the momentum equation,  $P$  refers to a modified pressure, which consists of the pressure  $\bar{p}$ , see Sect. 2.7.2, and a component due to the LORENTZ force, *i.e.*,

$$P = \bar{p} + \frac{\mathbf{B}^2}{2\mu_0}. \quad (3.2)$$

The topography of the CMB can be imagined as a rippled surface. In the following, this surface is modeled as a plane wave with an arbitrary direction in the

$x$ - $y$ -plane, see Fig. 3.1. Later, Sect. 3.4 extends the results of the one-dimensional case to a truly two-dimensional topography. This plane wave description of the topography is given by

$$f(\mathbf{x}) = z - h(\mathbf{x}) = 0 \quad \text{with} \quad h(\mathbf{x}) = \hat{h} \exp(i\mathbf{k}_T \cdot \mathbf{x}), \quad (3.3)$$

where the wave number vector of the topography,  $\mathbf{k}_T$ , is given by  $\mathbf{k}_T = k_x \mathbf{e}_x + k_y \mathbf{e}_y$ . The two wave numbers may be related to the two wavelengths of the topography by  $k_x = 2\pi/\lambda_x$  and  $k_y = 2\pi/\lambda_y$ .

The stratification is modeled in terms of a linear profile of the reference density. The mathematical description of this profile is given by

$$\bar{\rho}(\mathbf{x}) = \rho_0 (1 + az) \quad \text{with} \quad a = \frac{1}{\rho_0} \frac{\partial \bar{\rho}}{\partial z} = -\frac{N^2}{g} < 0, \quad (3.4)$$

where  $a$  describes the relative density variation and may be expressed in terms of the buoyancy or BRUNT-VÄISÄLÄ frequency  $N$ .

In order to obtain a well-posed problem, boundary conditions for the velocity and the magnetic field need to be specified. Because of the assumption of a sinusoidal topography, a periodicity constraint is enforced on all fields in the  $x$ - and  $y$ -direction. At the bottom of the stratified layer, the velocity and the magnetic field shall match the background fields  $\bar{\mathbf{V}}$  and  $\bar{\mathbf{B}}$ , respectively, which originate from the deeper convecting region of the outer core of the Earth. The thickness of the stratified layer is not well known and shall not be introduced as an additional parameter. Therefore, the boundary conditions at the bottom of the stratified layer are formulated in an asymptotic manner, *i.e.*,

$$\lim_{z \rightarrow -\infty} \mathbf{v}(x, y, z) = \bar{\mathbf{V}}(x, y), \quad \lim_{z \rightarrow -\infty} \mathbf{B}(x, y, z) = \bar{\mathbf{B}}(x, y). \quad (3.5)$$

This asymptotic formulation corresponds to an infinitely thick stratified layer, which, of course, does not occur in reality. Nevertheless, the usage of the limit  $z \rightarrow -\infty$  simplifies the subsequent analysis. The rate, at which the solutions approach the background fields, can be associated with a certain length scale. This length scale may later be estimated by analyzing the solutions. For the subsequent analysis to hold true, it is necessary that this length scale is smaller than the thickness of the stratified layer.

Two types of velocity boundary conditions are possible at the CMB. Either a slip boundary condition,  $\mathbf{n} \cdot \mathbf{v} = 0$ , or a no-slip boundary condition,  $\mathbf{v} = \mathbf{0}$ , could be used. The answer to the question as to which is applicable depends upon the material model. The no-slip boundary condition is not applicable for an inviscid fluid, because the traction vector is only normal to the boundary. For a viscous fluid, both boundary conditions are applicable in theory. The magnetic field must comply with a continuity condition. This condition describes the continuous transition of the magnetic field from the outer core to the mantle. The mantle is typically modeled as an electric insulator. Therefore, the magnetic field in the

**Table 3.1:** Dimensions of the parameters of the boundary topography problem.  $[M]$ ,  $[L]$ ,  $[T]$  and  $[I]$  refer to the base dimensions of mass, length, time and electric current. The numbers are the exponents of the dimensions of the parameters in terms of the base dimensions.

	$[\lambda_x]$	$[h]$	$[\boldsymbol{\Omega}]$	$[\bar{\mathbf{V}}]$	$[\rho_0]$	$[\nabla\rho_0]$	$[\mathbf{g}]$	$[\mu]$	$[\bar{\mathbf{B}}]$	$[\eta]$	$[\mu_0]$
$[M]$	0	0	0	0	1	1	0	1	1	-1	1
$[L]$	1	1	0	1	-3	-4	1	-1	0	-3	1
$[T]$	0	0	-1	-1	0	0	-2	-1	-2	3	-2
$[I]$	0	0	0	0	0	0	0	0	-1	2	-2

mantle can be described by a scalar potential. Using the slip boundary condition for the velocity field, the boundary conditions at the top of the stratified layer are given by

$$\mathbf{n}(\mathbf{x}) \cdot \mathbf{v}(\mathbf{x}) = 0, \quad \mathbf{B}(\mathbf{x}) = \nabla V_M(\mathbf{x}), \quad \mathbf{x} \in \Gamma_{\text{CMB}}, \quad (3.6)$$

where  $\Gamma_{\text{CMB}}$  denotes the CMB,  $\mathbf{n}$  its unit normal vector and  $V_M$  the scalar potential of the magnetic field in the mantle. The application of the slip boundary condition is justified by the discussion on the role of the viscosity in Sect. 3.2.1. It is pointed out in Sect. 3.2.1 that the viscosity is negligible and hence the slip boundary condition is appropriate.

### 3.1.1 Dimensionless formulation

It is convenient to formulate the problem in a dimensionless form. In order to do so, it is necessary to identify the parameters that may have an influence on the solution of the problem. These parameters are the magnitude of the background velocity and magnetic background field at the bottom of the stratified layer, *i.e.*, the magnitudes of  $\bar{\mathbf{V}}$  and  $\bar{\mathbf{B}}$ , respectively, the angular velocity  $\boldsymbol{\Omega}$  and the gravity field  $\mathbf{g}$ . The material-dependent quantities are given by the reference density  $\rho_0$  and its gradient, the viscosity  $\mu$ , the magnetic diffusivity  $\eta$ , and the magnetic permeability  $\mu_0$ . There are also geometric parameters: the wavelength  $\lambda_x$  and the height  $h$  of the topography. Note that for simplicity, the wavelength  $\lambda_y$  is not considered in this analysis and that  $\lambda_x$  is used as a characteristic length scale. Instead of  $\lambda_x$ , the wave length corresponding to the magnitude of the wave number vector of the boundary topography  $|\mathbf{k}_T|$  could also be used.

The set of independent dimensionless parameters is identified by dimensional analysis. This analysis is based on BUCKINGHAM's  $\Pi$ -theorem, which allows to determine the number of independent dimensionless numbers from the rank of the so-called dimensional matrix, see Hutter and Jöhnk [2004] for a detailed discussion. Table 3.1 is used to construct the dimensional matrix of the problem. The numbers in Table 3.1 represent the exponents of the dimensions of the relevant parameters and these numbers form the dimensional matrix. There are  $n = 11$

relevant parameters and the dimensional matrix in Table 3.1 has full (row) rank, *i.e.*,  $r = 4$ . Hence, there are  $p = n - r = 7$  independent dimensionless parameters. The choice of these parameters is not unique. However, it can be shown that the following set of parameters is independent:

$$\begin{aligned} \Pi &= \frac{h}{\lambda_x}, & Ro &= \frac{V_0}{\Omega_0 \lambda_x}, & Re &= \frac{\rho_0 V_0 \lambda_x}{\mu}, & Fr &= \frac{V_0}{\sqrt{g \lambda_x}} \\ Al &= \frac{B_0}{\sqrt{\rho_0 \mu_0} V_0}, & Rm &= \frac{V_0 \lambda_x}{\eta}, & St &= \frac{N}{\Omega_0}. \end{aligned} \quad (3.7)$$

Here,  $Ro$  denotes the ROSSBY number,  $Re$  the REYNOLDS number,  $Fr$  the FROUDE number,  $Al$  the ALFVÉN number and  $Rm$  the magnetic REYNOLDS number. The symbols  $St$  and  $\Pi$  represent dimensionless numbers, which characterize the strength of the stratification and height of the boundary topography, respectively. Note that the reference length is chosen as the wavelength of the topography and therefore this length scale occurs in some of the dimensionless parameters introduced above. Furthermore, the symbols  $B_0$  and  $V_0$  are the reference values of the background magnetic and velocity field, *i.e.*,  $B_0 = \|\bar{\mathbf{B}}\|$  and  $V_0 = \|\bar{\mathbf{V}}\|$ , respectively. Regarding the angular velocity,  $\Omega_0$  denotes the standard value for the angular velocity of the Earth's mantle and is used to characterize the stratification as well as in the ROSSBY number. However, the ROSSBY number used above is not identical to that of the  $\beta$ -plane approximation, because the corresponding local angular velocity depends on the colatitude angle  $\theta$ . Therefore, the factor  $\cos(\theta)$  will occur as a factor in front of the CORIOLIS term in the subsequent analysis.

Note that Table 3.1 does not contain all parameters which influence the solution of the problem, because the pressure is not present in this table. If the pressure is included in the table, another dimensionless number can be found. This number is, for example, given by the EULER number  $Eu = p_0 / (\rho_0 V_0^2)$ . However, the reference pressure is commonly chosen as  $p_0 = \rho_0 V_0^2$  such that the EULER number is equal to unity. Therefore, the EULER number does not occur in the dimensionless formulation. A timescale is neither introduced to the set of influential parameters, because it would introduce an additional dimensionless parameter. This parameter would be given by  $\lambda_x t_0 / V_0$ . The timescale  $t_0$  is chosen as that of the convective transport, such that this additional dimensionless parameter is also equal to unity. It can be noted that the scale of the pressure and of the time are not unique; other choices could be applied.

The density, gravitational acceleration, pressure, velocity, angular velocity and magnetic field are expressed in terms of dimensionless fields as follows:

$$\rho = \rho_0 \tilde{\rho}, \quad g = g_0 \tilde{g}, \quad P = \rho_0 V_0^2 \tilde{P}, \quad \mathbf{v} = V_0 \tilde{\mathbf{v}}, \quad \boldsymbol{\Omega} = \Omega_0 \tilde{\boldsymbol{\Omega}}, \quad \mathbf{B} = B_0 \tilde{\mathbf{B}},$$

where the quantities with a tilde are dimensionless. If the dimensional variables

are substituted by their dimensionless counterparts, Eqs. (3.1) reads

$$\tilde{\nabla} \cdot \tilde{\mathbf{v}} = 0, \quad \tilde{\nabla} \cdot \tilde{\mathbf{B}} = 0, \quad (3.8a)$$

$$\frac{d\tilde{\mathbf{v}}}{d\tilde{t}} + \frac{2}{Ro} \tilde{\boldsymbol{\Omega}} \times \tilde{\mathbf{v}} = -\tilde{\nabla} \tilde{P} + \frac{1}{Re} \tilde{\nabla}^2 \tilde{\mathbf{v}} + \frac{1}{Fr^2} \tilde{\rho} \tilde{\mathbf{g}} + Al^2 \tilde{\mathbf{B}} \cdot \tilde{\nabla} \otimes \tilde{\mathbf{B}}, \quad (3.8b)$$

$$\frac{\partial \tilde{\mathbf{B}}}{\partial \tilde{t}} = Rm \tilde{\nabla} \times (\tilde{\mathbf{v}} \times \tilde{\mathbf{B}}) + \tilde{\nabla}^2 \tilde{\mathbf{B}}, \quad (3.8c)$$

where  $\tilde{\nabla} = \nabla/\lambda_x$  is the dimensionless nabla operator. This system of differential equations is complemented by the dimensionless version of the boundary conditions in Eqs. (3.5) and (3.6), which are given by

$$\lim_{\tilde{z} \rightarrow -\infty} \tilde{\mathbf{v}}(\tilde{x}, \tilde{y}, \tilde{z}) = \tilde{\mathbf{V}}(\tilde{x}, \tilde{y}), \quad \lim_{\tilde{z} \rightarrow -\infty} \tilde{\mathbf{B}}(\tilde{x}, \tilde{y}, \tilde{z}) = \tilde{\mathbf{B}}(\tilde{x}, \tilde{y}), \quad (3.9)$$

$$\mathbf{n}(\tilde{\mathbf{x}}) \cdot \tilde{\mathbf{v}}(\tilde{\mathbf{x}}) = 0, \quad \tilde{\mathbf{B}}(\tilde{\mathbf{x}}) = \tilde{\nabla} \tilde{V}_M(\tilde{\mathbf{x}}), \quad \tilde{\mathbf{x}} \in \Gamma_{\text{CMB}}. \quad (3.10)$$

Note that the dimensionless parameters  $\Pi$  and  $St$  do not explicitly occur in Eqs. (3.8).

The parameter  $\Pi$ , which characterizes the relative height of the topography, enters the problem through the boundary conditions at the CMB. More precisely, the height of the topography occurs in the normal vector  $\mathbf{n}$ . The normal vector of the topography is computed from the implicit description of the surface of the topography in Eq. (3.3), whose dimensionless version reads:

$$\tilde{f}(\tilde{\mathbf{x}}) = \tilde{z} - \tilde{h}(\tilde{\mathbf{x}}) \quad \text{with} \quad \tilde{h}(\tilde{\mathbf{x}}) = \Pi \exp(i\tilde{\mathbf{k}}_T \cdot \tilde{\mathbf{x}}), \quad (3.11)$$

where  $\tilde{\mathbf{k}}_T = 2\pi\mathbf{e}_x$  is the dimensionless wavelength of the topography for the simplified case of  $k_y = 0$ . The normal vector of the topography may now be computed by taking the gradient of the function  $\tilde{f}$  and a subsequent normalization of the result, *i.e.*,

$$\mathbf{n} = \frac{\mathbf{e}_z - i\tilde{\mathbf{k}}_T \Pi \exp(i\tilde{\mathbf{k}}_T \cdot \tilde{\mathbf{x}})}{\|\mathbf{e}_z - i\tilde{\mathbf{k}}_T \Pi \exp(i\tilde{\mathbf{k}}_T \cdot \tilde{\mathbf{x}})\|}. \quad (3.12)$$

This result depends on the parameter  $\Pi$  and therefore it implicitly occurs in Eq. (3.10)<sub>1</sub>.

The stratification parameter  $St$  enters the problem through the reference density profile. If Eq. (3.4) is rewritten in a dimensionless form, ones obtains the following dimensionless reference density profile

$$\frac{1}{\rho_0} \tilde{\rho}(\tilde{\mathbf{x}}) = 1 + a\lambda_x \tilde{z} = 1 - \frac{N^2 \lambda_x}{g} \tilde{z} = 1 - \frac{St^2 Fr^2}{Ro^2} \tilde{z}. \quad (3.13)$$

Note that the dimensionless density  $\tilde{\rho}$  occurs in Eq. (3.8b) in front of the body force term rather than the dimensionless reference density  $\tilde{\rho}/\rho_0$  specified above. This is due to the fact that the flow of the fluid over the topography yields local deviations of the density from the reference state. For example, in regions where

the topography is low, fluid with a low density is flowing downwards the stratified layer and *vice versa*. How this process is modeled in terms of linear analysis is discussed in Sect. 3.2.2.

### 3.2 Perturbation analysis for a 1D topography

In this section, a first-order perturbation expansion of the system in Eqs. (3.1) from a reference state is performed. In order to avoid an overloaded notation, the tildes identifying dimensionless variables are dropped from this point onward and for the remainder of this chapter. As a consequence, all equations presented subsequently are dimensionless. Regarding the perturbation analysis, the reference state corresponds to a flat CMB and this state is perturbed by the topography. In this framework, the density, velocity, pressure and magnetic field are expressed as

$$\rho = \bar{\rho} + \rho', \quad \mathbf{v} = \bar{\mathbf{V}} + \mathbf{v}', \quad P = \bar{P} + p', \quad \mathbf{B} = \bar{\mathbf{B}} + \mathbf{b}', \quad (3.14)$$

where the fields corresponding to the reference state are indicated by a vertical bar and the perturbations are indicated by a dash. It is assumed that the reference velocity field is homogeneous, *i.e.*,  $\bar{\mathbf{V}} \neq \bar{\mathbf{V}}(\mathbf{x})$ . The same assumption is made regarding the reference magnetic field, *i.e.*,  $\bar{\mathbf{B}} \neq \bar{\mathbf{B}}(\mathbf{x})$ . As a consequence, gradients of these fields vanish.

The perturbation expansions in Eqs. (3.14) are substituted in Eqs. (3.8) and the non-linear terms are neglected in the following. Under the assumption of a stationary perturbation, the resulting equations are given by

$$\nabla \cdot \mathbf{v}' = 0, \quad \nabla \cdot \mathbf{b}' = 0, \quad (3.15a)$$

$$\bar{\mathbf{V}} \cdot (\nabla \otimes \mathbf{v}') + \frac{2}{Ro} \boldsymbol{\Omega} \times \mathbf{v}' = -\nabla p' + \frac{1}{Re} \nabla^2 \mathbf{v}' + \frac{1}{Fr^2} \rho' \mathbf{g} + \quad (3.15b)$$

$$+ Al^2 \bar{\mathbf{B}} \cdot (\nabla \otimes \mathbf{b}'),$$

$$Rm(\nabla \times (\mathbf{v}' \times \bar{\mathbf{B}}) + \nabla \times (\bar{\mathbf{V}} \times \mathbf{b}')) = -\nabla^2 \mathbf{b}'. \quad (3.15c)$$

Note that the reference pressure field  $\bar{P}$  has not been specified yet and neither does it occur in the momentum equation. This is due to the fact that the reference pressure field  $\bar{P}$  must be compatible with the reference state. The reference velocity and magnetic field are homogeneous and therefore the momentum equation governing the reference pressure and its solution are given by

$$\frac{2}{Ro} \boldsymbol{\Omega} \times \bar{\mathbf{V}} = -\nabla \bar{P} + \bar{\rho} \mathbf{g} \quad \Rightarrow \quad \bar{P} = - \int_0^z \bar{\rho}(z) g dz - \frac{2}{Ro} (\boldsymbol{\Omega} \times \bar{\mathbf{V}}) \cdot \mathbf{x} + C, \quad (3.16)$$

where the first term of the solution represents the hydrostatic pressure and  $C$  is a constant of integration.

### 3.2.1 The role of the viscosity

The reference velocity field is a solution of the problem for a fluid with a vanishing viscosity. It does not represent a solution of the system in Eqs. (3.1) for the case of a viscous fluid because the no-slip boundary condition at the CMB is violated by the simple choice of a constant velocity field. In order to fulfill this boundary condition, a variation of the velocity field in the  $z$ -direction is required, which is not the case for the simple reference state specified above.

For a viscous fluid, a solution can be found if the effects of a magnetic field are neglected. More precisely, a closed-form solution for the flow of an unstratified, viscous fluid over a flat surface in a rotating system was determined by EKMAN and therefore this problem is known as the EKMAN layer [Ekman (1905)]. The  $x$ - and  $y$ -components of the velocity of this EKMAN layer solution are proportional to  $\exp(z/\delta_E) \cos(z/\delta_E)$  and  $\exp(z/\delta_E) \sin(z/\delta_E)$ , respectively [Ekman (1905); Pedlosky (1987)]. Here the symbol  $\delta_E$  denotes the EKMAN layer thickness, *i.e.*, the characteristic length of the problem. The solution has a gradient with respect to the  $z$ -axis because of the no-slip boundary condition at the flat surface, *i.e.*, at the CMB. Due to the CORIOLIS term, the  $x$ -component of the velocity introduces a fluid flow in the  $y$ -direction.

The structure of the solution of the problem which includes viscous and magnetic effects is very similar to that of the EKMAN layer. It is presented in the appendix of the paper by Hide, see Hide [1969a]. The solution to this problem is governed by three dimensionless parameters: the EKMAN, the HARTMANN and the magnetic REYNOLDS number, where the former two are given by

$$Ek = RoRe, \quad Ha = \sqrt{\frac{Rm}{Re}} Al. \quad (3.17)$$

If the HARTMANN and the magnetic REYNOLDS number vanish, the EKMAN problem is recovered. If the EKMAN number tends to be very large, rotational effects can be neglected and the so-called HARTMANN problem is recovered [Hartmann (1937)]. The case of a vanishing EKMAN number corresponds to a problem which includes rotation and magnetic induction but neglects viscosity. This case is used as a reference state in this work, which was specified at the beginning of the Sect. 3.2.

In the following, only the problem for an inviscid fluid is considered for two reasons. First, the solution of the unperturbed viscous problem has gradients with respect to the  $z$ -axis. Thus, the (reference) fields  $\bar{\mathbf{B}}$  and  $\bar{\mathbf{V}}$  and gradients of these fields introduce terms in Eqs. (3.15), which depend on the  $z$ -coordinate. These terms yield a system of partial differential equations with non-constant coefficients, which, if it can be solved at all, cannot be solved using a solution, whose spatial dependence is described by the exponential function.

Second, for the outer core of the Earth, the EKMAN number is estimated to range from  $10^{-15}$  to  $5 \times 10^{-15}$  [Olson (2015)]. This indicates that the inviscid limit may be used as an approximation. For this order of magnitude of the EKMAN number, the EKMAN layer thickness, *i.e.*, the thickness of the viscous boundary layer, is

**Table 3.2:** Values of the EKMAN number  $Ek$ , REYNOLDS number  $Re$  and the ROSSBY number  $Ro$  for different wavelengths of the boundary topography. The values are based on the nominal value of angular velocity of the Earth's mantle of  $\Omega_0 = 7.27 \times 10^{-5} \text{ s}^{-1}$  and a kinematic viscosity of  $\nu = 1 \times 10^5 \text{ m}^2 \text{ s}^{-1}$ , which is the maximum value specified in Table 2.2. The reference velocity is given by  $5 \times 10^{-4} \text{ m s}^{-1}$ , which is characteristic for the flow in the outer core of the Earth.

$\lambda_x$	1 km	100 km
$Ek$	$1 \times 10^{-5}$	$1 \times 10^{-9}$
$Re$	$5 \times 10^4$	$5 \times 10^6$
$Ro$	$7 \times 10^{-3}$	$7 \times 10^{-5}$

approx. 0.1 m.<sup>1</sup> Even if the EKMAN number is increased to  $10^{-5}$ , the thickness only increases to 10 km, which is still relatively small compared to the thickness of the stratified region of 100 km. Hence, in the outer core of the Earth, the thickness of the region, where viscous effects become important, *i.e.*, the viscous boundary layer, is much smaller than the region, where stratification matters.

This argument may lead to a misleading conclusion if the boundary topography is introduced. The boundary topography introduces a length scale that is different from that used for the entire outer core of the Earth. The appropriate length scale for the bulk outer core is the shell thickness, but for the boundary topography it is either the wavelength or the height of the topography. Values of the EKMAN number and the REYNOLDS number for different wavelengths of the boundary are specified in Table 3.2. The EKMAN number, which quantifies the importance of viscous forces in comparison to the CORIOLIS term, is much less than unity, which allows to neglect the viscous forces in comparison to the inertial term. The REYNOLDS number, *i.e.*, ratio of the inertial term to viscous forces, is much larger than unity, which indicates that the viscous term can also be neglected in comparison to the inertial term if the considered length scales apply. The values of the ROSSBY number in Table 3.2 also suggest that the CORIOLIS term is much more important than the inertial term.

In summary, a hierarchy of the relevance of the CORIOLIS, the viscous and the inertial term can be established by comparing the EKMAN, the ROSSBY and the REYNOLDS numbers in Table 3.2. The CORIOLIS term dominates the other two terms and may never be neglected. Moreover, the inertial term also dominates the viscous term. Therefore, the viscous term may be neglected as long as the characteristic length scale of the solution does not become too small.

The importance of the inertial term in relation to the CORIOLIS term is characterized by the ROSSBY number. Considering the values in Table 3.2, the magnitude

<sup>1</sup>This result is obtained from the formula  $\delta_E = \sqrt{2\mu/(\rho_0\Omega_0)}$  and using a reference length of  $D = 2260 \text{ km}$ , which is the shell thickness of the outer core of the Earth. Another way to determine the thickness of the EKMAN layer directly from the EKMAN number is to use the dimensionless thickness  $\tilde{\delta}_E = \sqrt{2Ek}$  and  $\delta_E = \tilde{\delta}_E D$ .

of the exponent of the ROSSBY number is the smallest if compared to those of the REYNOLDS and EKMAN number. Therefore, the neglect of the inertial term in relation to the CORIOLIS term represents the strongest assumption compared to the other omissions discussed in this contexts. In order to study the influence of the inertial term, it is retained in the following analysis but the switch  $\chi \in \{0, 1\}$  is introduced in front of the inertial term. This allows an easy algebraic elimination of the inertial term. The omissions of the inertial term, *i.e.*,  $\chi = 0$ , corresponds to the so-called geostrophic approximation, which is widely used in geophysical fluid mechanics, see Pedlosky [1987] among others.

Based on these arguments, the viscous term is neglected and the momentum equation in Eq. (3.15b) simplifies to

$$\chi \bar{\mathbf{V}} \cdot (\nabla \otimes \mathbf{v}') + \frac{2}{Ro} \boldsymbol{\Omega} \times \mathbf{v}' = -\nabla p' + \frac{1}{Fr^2} \rho' \mathbf{g} + Al^2 \bar{\mathbf{B}} \cdot (\nabla \otimes \mathbf{b}'), \quad (3.18)$$

where the switch  $\chi$  was introduced as a factor in front of the inertial term.

### 3.2.2 Discussion of the density perturbation

As outlined above, the flow over the boundary topography transports fluid with a relatively large or small density upwards or downwards in the stratified layer. This perturbs the static equilibrium such that the fluid is no longer in a neutrally buoyant state. This view of the transport mechanism is based on the assumption that thermodynamic processes are irrelevant for the density perturbation. This is controversial regarding the discussion of the constitutive equations and the anelastic approximation in Sects. 2.5 and 2.7.3, where the thermal equation of state specifies the density as a function of temperature and pressure. Thus, a heat conduction process or the constraint of isentropy, for example, have direct consequences for the density. However, in this chapter, thermodynamic processes are not considered, which requires an alternative modeling approach for the density. This alternative approach is based on an approximation of the balance of mass and will be outlined below.

If only the hydrodynamic part of the problem is considered, the three perturbations  $\rho'$ ,  $p'$  and  $\mathbf{v}'$  need to be determined. However, the purely hydrodynamic problem only consists of the two equations specified in Eq. (3.15a) and, for example, in Eq. (3.18). Therefore, it is clear from an algebraic point of view that an additional equation is required. The constraint  $\nabla \cdot \mathbf{v}' = 0$  is used to solve for the pressure perturbation  $p'$  and the momentum equation is used to solve for the velocity perturbation  $\mathbf{v}'$ . As a consequence, there is no independent equation to determine the density perturbation  $\rho'$ . If a thermal equation of state is used, this problem does not occur. Yet, in this case, the balance of internal energy must be considered, which entails a coupling of temperature, pressure and velocity. Instead, the stationary form of the balance of mass  $\nabla \cdot (\rho \mathbf{v}) = 0$  is considered in the following in order to obtain an additional equation for the density perturbation.

If the perturbation expansions for the density and the velocity are substituted,

**Table 3.3:** Values of the parameter  $St^2 Fr^2 / Ro^2$ , which characterizes the density gradient for different wavelengths and stratification parameters. Note that  $St^2 Fr^2 / Ro^2 = N^2 \lambda_x / g$  and that  $g = 10 \text{ m s}^{-2}$  is applied for the gravitational acceleration.

	$\frac{St^2 Fr^2}{Ro^2}$	$St$		
		0.1	1	20
$\lambda_x$	0.1 km	$5 \times 10^{-10}$	$5 \times 10^{-8}$	$2 \times 10^{-5}$
	1 km	$5 \times 10^{-9}$	$5 \times 10^{-7}$	$2 \times 10^{-4}$
	10 km	$5 \times 10^{-8}$	$5 \times 10^{-6}$	$2 \times 10^{-3}$
	100 km	$5 \times 10^{-7}$	$5 \times 10^{-5}$	$2 \times 10^{-2}$

the linearized dimensionless stationary balance of mass reads

$$(\bar{\mathbf{V}} + \mathbf{v}') \cdot \nabla \bar{\rho} + \bar{\mathbf{V}} \cdot \nabla \rho' + \bar{\rho} (\nabla \cdot \mathbf{v}') = 0, \quad (3.19)$$

where the dimensionless reference density  $\bar{\rho}$  is specified in Eq. (3.13) and its gradient is given by

$$\nabla \bar{\rho} = -\frac{St^2 Fr^2}{Ro^2} \mathbf{e}_z. \quad (3.20)$$

The only non-vanishing component of the dimensionless background velocity is the  $x$ -component, *i.e.*,  $\bar{\mathbf{V}} \propto \mathbf{e}_x$ . Therefore,  $\bar{\mathbf{V}}$  and  $\nabla \bar{\rho}$  are orthogonal and their scalar product in Eq. (3.19) vanishes. As a consequence, a division of the linearized balance of mass by the reference density  $\bar{\rho}$  yields

$$\nabla \cdot \mathbf{v}' + \frac{1}{\bar{\rho}} (\mathbf{v}' \cdot \nabla \bar{\rho} + \bar{\mathbf{V}} \cdot \nabla \rho') = 0. \quad (3.21)$$

Next, the orders of magnitude of the three terms in Eq. (3.21) are analyzed. The dimensionless background velocity  $\bar{\mathbf{V}}$  has the magnitude of unity because of the normalization. The magnitude of the velocity perturbation  $\mathbf{v}'$  is characterized with respect to the background velocity by  $\varepsilon_{\mathbf{v}'} = \|\mathbf{v}'\| / \|\bar{\mathbf{V}}\|$ . The two density-related terms in Eq. (3.21) contain ratios of a density gradient to the reference density. These two ratios may be approximated as follows:

$$\frac{1}{\bar{\rho}} \nabla \bar{\rho} = \frac{-\frac{St^2 Fr^2}{Ro^2}}{1 - \frac{St^2 Fr^2}{Ro^2} z} \mathbf{e}_z \approx -\frac{St^2 Fr^2}{Ro^2} \mathbf{e}_z, \quad \frac{1}{\bar{\rho}} \nabla \rho' = \frac{1}{1 - \frac{St^2 Fr^2}{Ro^2} z} \nabla \rho' \approx \nabla \rho'. \quad (3.22)$$

In order to perform the two approximations above, the fact was used that the ratio  $St^2 Fr^2 / Ro^2$  is small, which is inferred from the values specified in Table 3.3. Moreover, the two approximations represent upper bounds of the respective terms in the stratified layer, because the interval of the  $z$ -coordinate is given by  $-\infty \leq z \leq 0$ . Using this approximation, the order of magnitude of the terms in Eq. (3.21) may

be expressed as

$$\mathcal{O}(\nabla \cdot \mathbf{v}') = \varepsilon_{\mathbf{v}'}, \quad (3.23a)$$

$$\mathcal{O}\left(\frac{1}{\bar{\rho}} \mathbf{v}' \cdot \nabla \bar{\rho}\right) = \varepsilon_{\mathbf{v}'} \frac{St^2 Fr^2}{Ro^2}, \quad (3.23b)$$

$$\mathcal{O}\left(\frac{1}{\bar{\rho}} \bar{\mathbf{V}} \cdot \nabla \rho'\right) = \mathcal{O}\left(\frac{1}{\bar{\rho}} \bar{\mathbf{V}} \cdot \|\nabla \bar{\rho}\| \frac{\nabla \rho'}{\|\nabla \bar{\rho}\|}\right) = \varepsilon_{\nabla \rho'} \frac{St^2 Fr^2}{Ro^2}, \quad (3.23c)$$

where the ratio of the gradient of the density perturbation to that of the reference density is introduced as  $\varepsilon_{\nabla \rho'}$ , *i.e.*,

$$\varepsilon_{\nabla \rho'} = \frac{\|\nabla \rho'\|}{\|\nabla \bar{\rho}\|}. \quad (3.23d)$$

If Eq. (3.21) is expressed in terms of orders of magnitude, one obtains

$$\varepsilon_{\mathbf{v}'} + \frac{St^2 Fr^2}{Ro^2} (\varepsilon_{\mathbf{v}'} + \varepsilon_{\nabla \rho'}) = 0 \quad \Leftrightarrow \quad 1 + \frac{St^2 Fr^2}{Ro^2} \left(1 + \frac{\varepsilon_{\nabla \rho'}}{\varepsilon_{\mathbf{v}'}}\right) = 0. \quad (3.24)$$

From the last equation and the range values for the factor  $St^2 Fr^2 / Ro^2$ , it may be concluded that the divergence term  $\nabla \cdot \mathbf{v}'$  dominates the balance of mass in terms of the orders of magnitude. This holds as long as the ratio  $\varepsilon_{\nabla \rho'} / \varepsilon_{\mathbf{v}'}$  does not become excessively large.

Based on the analysis regarding the orders of magnitude, the balance of mass in Eq. (3.21) is split into two equations, namely

$$\nabla \cdot \mathbf{v}' = 0 \quad \mathbf{v}' \cdot \nabla \bar{\rho} + \bar{\mathbf{V}} \cdot \nabla \rho' = 0. \quad (3.25)$$

The former equation contains the first order terms in the balance of mass and the latter the second order terms. The latter equation contains the density perturbation and shall serve as the equation, which is required to obtain a closed hydrodynamic problem. If Eq. (3.13) is substituted in the latter equation, the stratification parameter  $St$  occurs explicitly in the equation that contains the density perturbation, *i.e.*,

$$-\frac{St^2 Fr^2}{Ro^2} \mathbf{v}' \cdot \mathbf{e}_z + \bar{\mathbf{V}} \cdot \nabla \rho' = 0. \quad (3.26)$$

This form will be used in the subsequent analysis and is consistent with the expectation that the density perturbation vanishes for a vanishing stratification.

### 3.2.3 Solution procedure

In the following, the solution procedure for the boundary topography problem is presented and the problem is transformed to an eigenvalue problem. Then, a strategy how this eigenvalue problem is solved is outlined. Based on the discussion

in the two preceding sections, the viscosity is neglected and the problem is supplemented by Eq. (3.26) in order to have a closed system of equations. Then, the following set of coupled differential equations arises:

$$\nabla \cdot \mathbf{v}' = 0, \quad \nabla \cdot \mathbf{b}' = 0, \quad (3.27a)$$

$$-\frac{St^2 Fr^2}{Ro^2} \mathbf{v}' \cdot \mathbf{e}_z + \bar{\mathbf{V}} \cdot \nabla \rho' = 0, \quad (3.27b)$$

$$\chi \bar{\mathbf{V}} \cdot (\nabla \otimes \mathbf{v}') + \frac{2}{Ro} \boldsymbol{\Omega} \times \mathbf{v}' = -\nabla p' + \frac{1}{Fr^2} \rho' \mathbf{g} + Al^2 \bar{\mathbf{B}} \cdot (\nabla \otimes \mathbf{b}'), \quad (3.27c)$$

$$Rm(\bar{\mathbf{B}} \cdot \nabla \otimes \mathbf{v}' - \bar{\mathbf{V}} \cdot \nabla \otimes \mathbf{b}') = -\nabla^2 \mathbf{b}'. \quad (3.27d)$$

This system is coupled but it has constant coefficients, because the background fields  $\bar{\mathbf{B}}$  and  $\bar{\mathbf{V}}$  were assumed to be constant. This system is solved with the same wave *ansatz* for all fields, *i.e.*,  $\rho' = \hat{\rho} \exp(\mathbf{i}\mathbf{k} \cdot \mathbf{x})$ ,  $\mathbf{v}' = \hat{\mathbf{v}} \exp(\mathbf{i}\mathbf{k} \cdot \mathbf{x})$  and likewise for the pressure and the magnetic field. Here,  $\mathbf{k} = k_x \mathbf{e}_x + k_y \mathbf{e}_y + k_z \mathbf{e}_z$  denotes the wave number vector of the solution, whose  $x$ - and  $y$ -components are the same as those of the wave number vector of the boundary topography  $\mathbf{k}_T$ . The symbols with a circumflex denote the constant “amplitudes” of the respective fields and the spatial dependency is described by the complex exponential. This *ansatz* assumes the same spatial dependency for all fields, which is characterized by the unknown  $z$ -component of the wave number vector. A substitution of the wave *ansatz* in the system of Eqs. (3.27) gives rise to

$$\mathbf{i}\mathbf{k} \cdot \hat{\mathbf{v}} = 0, \quad \mathbf{i}\mathbf{k} \cdot \hat{\mathbf{b}} = 0, \quad (3.28a)$$

$$-\frac{St^2 Fr^2}{Ro^2} \hat{\mathbf{v}} \cdot \mathbf{e}_z + (\bar{\mathbf{V}} \cdot \mathbf{i}\mathbf{k}) \hat{\rho} = 0, \quad (3.28b)$$

$$\chi (\bar{\mathbf{V}} \cdot \mathbf{i}\mathbf{k}) \hat{\mathbf{v}} + \frac{2}{Ro} \boldsymbol{\Omega} \times \hat{\mathbf{v}} = -\mathbf{i}\mathbf{k} \hat{p} + \frac{1}{Fr^2} \hat{\rho} \mathbf{g} + Al^2 (\bar{\mathbf{B}} \cdot \mathbf{i}\mathbf{k}) \hat{\mathbf{b}}, \quad (3.28c)$$

$$Rm((\bar{\mathbf{B}} \cdot \mathbf{i}\mathbf{k}) \hat{\mathbf{v}} - (\bar{\mathbf{V}} \cdot \mathbf{i}\mathbf{k}) \hat{\mathbf{b}}) = \mathbf{k}^2 \hat{\mathbf{b}}. \quad (3.28d)$$

Furthermore, the spatial dependence of all fields was eliminated from the system by a simple division by  $\exp(\mathbf{i}\mathbf{k} \cdot \mathbf{x})$ ; a system of algebraic equations remains.

In the following, this system is algebraically reduced for the case that the magnetic field has only a  $z$ -component and the velocity field has only a  $x$ -component. In terms of the dimensionless formulation and related normalization, this implies  $\bar{\mathbf{B}} = \mathbf{e}_z$  and  $\bar{\mathbf{V}} = \mathbf{e}_x$ . Moreover, the boundary topography shall be aligned with the fluid flow, *i.e.*,  $k_y = 0$ . This specialization is not only made to simplify the subsequent algebraic manipulations, but it is also expected that the largest perturbation and thereby the largest torque occur in this case.

From this point onward, two ways of simplifying the algebraic system above are possible. Either the velocity amplitude  $\hat{\mathbf{v}}$  or the magnetic field amplitude  $\hat{\mathbf{b}}$  is chosen as the “primary variable.” In the first case, the velocity amplitude  $\hat{\mathbf{v}}$  is substituted in the magnetic induction equation, whereas in the latter case the

magnetic field amplitude  $\hat{\mathbf{b}}$  is substituted in the momentum equation. Although both ways are algebraically equivalent, the latter one is chosen, because it turns out that it allows for a simpler analysis of the purely hydrodynamic case by setting  $Al \rightarrow 0$ . This cannot be realized in this simple manner if the first alternative is chosen.

Using  $\bar{\mathbf{B}} = \mathbf{e}_x$  and  $\bar{\mathbf{V}} = \mathbf{e}_x$ , Eq. (3.28d) is solved for the magnetic field amplitude:

$$Rm(ik_z \hat{\mathbf{v}} - ik_x \hat{\mathbf{b}}) = \mathbf{k}^2 \hat{\mathbf{b}} \quad \Leftrightarrow \quad \hat{\mathbf{b}} = \frac{ik_z Rm}{\mathbf{k}^2 + ik_x Rm} \hat{\mathbf{v}}, \quad (3.29)$$

where  $\mathbf{k}^2 = k_x^2 + k_z^2$ . Furthermore, Eq. (3.26) is solved for the density perturbation

$$-\frac{St^2 Fr^2}{Ro^2} \hat{v}_z + ik_x \hat{\rho} = \quad \Leftrightarrow \quad \hat{\rho} = -\frac{i\hat{v}_z}{k_x} \frac{St^2 Fr^2}{Ro^2}. \quad (3.30)$$

Both the perturbations of the density and the magnetic field are now expressed in terms of the perturbation of the velocity field. These expressions are substituted in Eq. (3.28c), which yields

$$\chi(\bar{\mathbf{V}} \cdot \mathbf{i}\mathbf{k})\hat{\mathbf{v}} + \frac{2}{Ro} \boldsymbol{\Omega} \times \hat{\mathbf{v}} = -\mathbf{i}\mathbf{k}\hat{p} - \frac{i\hat{v}_z}{k_x} \frac{St^2}{Ro^2} \mathbf{g} - k_z^2 \frac{RmAl^2}{\mathbf{k}^2 + ik_x Rm} \hat{\mathbf{v}}. \quad (3.31)$$

This equation is now recast in terms of an eigenvalue for the yet unknown wave number  $k_z$  and velocity amplitude  $\hat{\mathbf{v}}$ . In doing so, it is convenient to eliminate the amplitude of the pressure perturbation  $\hat{p}$  by considering the  $z$ -component of the latter equation,

$$\begin{aligned} \chi ik_x \hat{v}_z &= -ik_z \hat{p} + \frac{St^2}{Ro^2} \frac{i\hat{v}_z}{k_x} - k_z^2 \frac{RmAl^2}{\mathbf{k}^2 + ik_x Rm} \hat{v}_z \\ \Leftrightarrow \hat{p} &= \left( -\chi \frac{k_x}{k_z} + \frac{1}{k_x k_z} \frac{St^2}{Ro^2} + ik_z \frac{RmAl^2}{\mathbf{k}^2 + ik_x Rm} \right) \hat{v}_z, \end{aligned} \quad (3.32)$$

where the fact that the dimensionless gravitational acceleration is given by  $\mathbf{g} = -\mathbf{e}_z$  was already incorporated. This expression ties the pressure perturbation only to the vertical component of the velocity perturbation. Before turning to the  $x$ - and  $y$ -components of the momentum, *i.e.*, the in-plane components, the divergence constraints in Eq.(3.28a) are considered. Because of the solution of the magnetic induction equation in Eq. (3.29), the amplitude of the magnetic field perturbation is proportional to that of the velocity perturbation. Therefore, the magnetic field is always solenoidal if Eq. (3.28a)<sub>1</sub> holds. Using the fact that  $k_y = 0$  for the first time in the analysis, Eq. (3.28a)<sub>1</sub> allows to express the vertical component of the velocity amplitude in terms of its horizontal counterpart, *i.e.*,

$$\hat{v}_z = -\frac{k_x}{k_z} \hat{v}_x. \quad (3.33)$$

Using Eq. (3.32) as well as Eq. (3.33) to eliminate  $\hat{p}$  and  $\hat{v}_z$ , the  $x$ -component of Eq. (3.31) can be expressed as

$$ik_x \chi \hat{v}_x - \frac{2}{Ro} \cos(\theta) \hat{v}_y = ik_x \left( -\chi \frac{k_x^2}{k_z^2} + \frac{1}{k_z^2} \frac{St^2}{Ro^2} \right) \hat{v}_x - k_z^2 \left( 1 + \frac{k_x^2}{k_z^2} \right) \frac{RmAl^2}{\mathbf{k}^2 + ik_x Rm} \hat{v}_x. \quad (3.34)$$

In this equation, the factor  $\cos(\theta)$  occurs, because the dimensionless local angular velocity is given by  $\boldsymbol{\Omega} = \cos(\theta) \mathbf{e}_z$ . For the  $y$ -component of Eq. (3.31), one obtains

$$ik_x \chi \hat{v}_y + \frac{2}{Ro} \cos(\theta) \hat{v}_y = -k_z^2 \frac{RmAl^2}{\mathbf{k}^2 + ik_x Rm} \hat{v}_y. \quad (3.35)$$

In the last two equations, only the horizontal amplitudes of the velocity perturbation  $\hat{v}_x$  and  $\hat{v}_y$  are present as well as the yet unknown wave number  $k_z$ . Therefore, these two equations are formulated in terms of a matrix-vector equation as follows:

$$\underbrace{\left( ik_x \mathbf{A} + \frac{2}{Ro} \cos(\theta) \mathbf{B} + k_z^2 \frac{RmAl^2}{\mathbf{k}^2 + ik_x Rm} \mathbf{C} \right)}_{=: \mathbf{M}} \cdot \begin{bmatrix} \hat{v}_x \\ \hat{v}_y \end{bmatrix} = \mathbf{0}, \quad (3.36a)$$

where the matrices  $\mathbf{A}$ ,  $\mathbf{B}$  and  $\mathbf{C}$  are given by

$$\mathbf{A} = \begin{bmatrix} \chi \left( 1 + \frac{k_x^2}{k_z^2} \right) - \frac{1}{k_z^2} \frac{St^2}{Ro^2} & 0 \\ 0 & \chi \end{bmatrix}, \quad \mathbf{B} = \begin{bmatrix} 0 & -1 \\ 1 & 0 \end{bmatrix}, \quad \mathbf{C} = \begin{bmatrix} 1 + \frac{k_x^2}{k_z^2} & 0 \\ 0 & 1 \end{bmatrix}. \quad (3.36b)$$

This matrix formulation constitutes a non-linear eigenvalue problem for the wave number  $k_z$  and the two velocity amplitudes  $\hat{v}_x$  and  $\hat{v}_y$ . In this formulation, the matrix  $\mathbf{A}$  contains the contributions due to the inertial terms and the stratification. If both  $\chi = 0$  and  $St = 0$ , this matrix vanishes and a geostrophic unstratified version of the problem is obtained. The skew-symmetric matrix  $\mathbf{B}$  represents the CORIOLIS term and it vanishes for  $\theta = \pi/2$ , which corresponds to the non-rotating problem. Regarding the  $\beta$ -plane approximation, the case of  $\theta = \pi/2$  corresponds to the equator. The matrix  $\mathbf{C}$  represents the magnetic part of the problem and is due to the LORENTZ force and the magnetic induction equation. It drops out for the non-magnetic case, *i.e.*,  $Al \rightarrow 0$ , but also for the case that  $Rm = 0$ , which corresponds either to a vanishing electrical conductivity or a vanishing velocity.

The characteristic equation corresponding to the eigenvalue problem determines the wave number  $k_z$  and is given by

$$\det \left( (\mathbf{k}^2 + ik_x Rm) \left( ik_x \mathbf{A} + \frac{2}{Ro} \cos(\theta) \mathbf{B} \right) + k_z^2 RmAl^2 \mathbf{C} \right) = 0, \quad (3.37)$$

where a multiplication by  $\mathbf{k}^2 + ik_x Rm = k_x^2 + k_z^2 + ik_x Rm$  was performed. If the

**Table 3.4:** Values of the dimensionless parameters of the boundary problem in the “standard case,” see text.

$k_x$	$Ro$	$St$	$Fr$	$Al$	$Rm$	$\Pi$
$2\pi$	$6.9 \times 10^{-5}$	20.0	$1.6 \times 10^{-6}$	11.6	62.5	$3.0 \times 10^{-4}$

determinant above is computed, a polynomial of degree six is obtained with respect to the sought-for wave number  $k_z$ , which, in general, has six roots. However, all odd powers of  $k_z$  vanish in this polynomial, *viz.*, it has the form  $a_6 k_z^6 + a_4 k_z^4 + a_2 k_z^2 + a_0$ . The coefficients  $a_i$  of the resulting polynomial are excessively large expressions of combinations of the parameters, which occur in Eq. (3.36), and are therefore not specified here. The same also applies to the roots themselves. However, the special structure of the polynomial allows to infer that the wave numbers occur in complex-conjugate pairs. The reason for this is that the characteristic equation can be interpreted as a cubic equation in terms of  $k_z^2$ , which has three roots. Taking the square root of these three roots results in three complex-conjugate pairs, whose numerical values need to be analyzed in order to obtain an admissible solution.

Apart from  $\chi$ ,  $\cos(\theta)$  and the dimensionless wave number  $k_x = 2\pi$ , the eigenvalue problem in Eq. (3.36) itself involves only four of the six dimensionless parameters that govern the non-viscous problem, see Eqs. (3.7). The dimensionless parameter  $\Pi$  enters in the problem through the boundary conditions. From Eqs. (3.30) and (3.32) it is clear that the FROUDE number occurs only in the solutions of the density and pressure amplitudes. The values of all of these parameters are specified in Table 3.4 for a “standard case”, which is characterized by a background velocity of  $5 \times 10^{-4} \text{ m s}^{-1}$ , a magnetic background field of 0.65 mT, a buoyancy frequency of  $N = 20 \times \Omega_0$ , a wave length of 100 km and a height of the topography of 30 m. The values of the dimensionless parameters in Table 3.4 differ by seven orders of magnitude. This makes a numerical solution of the problem challenging; due to finite machine precision round-off errors occur, which propagate in a manner that cannot be controlled *a priori*. Moreover, the polynomial coefficients  $a_i$  and all subsequent results contain non-linear combinations of the dimensionless numbers, which will introduce an even larger imbalance regarding the orders of magnitude of the different terms. Another way of introducing a wider span in the dimensionless parameters is to consider a de- or increase of the values of the background magnetic and velocity field, respectively. Therefore, the solution of the problem is computed symbolically using the computer algebra system *Mathematica* [Wolfram Research, Inc. (2015)]. In doing so, intermediate results are only evaluated numerically if necessary.

In the following, the symbolic solution procedure, which was implemented in *Mathematica*, will be described. First, the six wave numbers are determined symbolically and then their numerical values are computed for the given set of dimensionless parameters. Considering the numerical values, some of the wave numbers need to be discarded, because a decay of the solution is required in

order to fulfill the boundary conditions in Eqs. (3.9). Using the decomposition  $k_z = \Re(k_z) + i\Im(k_z)$ , where the operators  $\Re(\bullet)$  and  $\Im(\bullet)$  refer to the real and imaginary parts, respectively, and the fact that the spatial dependency of all perturbations is identical, Eq. (3.9) can be reduced to

$$\lim_{z \rightarrow -\infty} \exp(ik_z z) = \lim_{z \rightarrow -\infty} \exp(i\Re(k_z)z) \exp(-\Im(k_z)z) \stackrel{!}{=} 0 \quad \Rightarrow \quad \Im(k_z) < 0. \quad (3.38)$$

The wave numbers occur in complex-conjugate pairs and, based on the requirement of a negative imaginary part, one wave number is selected from each pair. This yields the admissible three wave numbers  $k_z^{(i)}$ ,  $i = 1, 2, 3$ , which are taken into account in the subsequent analysis.

In the next step, for each admissible wave number a corresponding non-trivial solution for the velocity amplitudes  $\hat{v}_x$  and  $\hat{v}_y$  is determined. This non-trivial solution is the eigenvector of the system matrix  $\mathbf{M}$  in Eq. (3.36). Due to the complex and excessive algebraic structure of the wave numbers, a non-trivial solution of the resulting linear system cannot be determined symbolically with the built-in methods of *Mathematica*. Therefore, the solution is constructed manually as follows:

$$\hat{v}_x^{(i)} = 1, \quad \hat{v}_y^{(i)} = -\frac{M_{21}^{(i)}}{M_{22}^{(i)}}, \quad \hat{v}_z^{(i)} = -\frac{k_x}{k_z^{(i)}}, \quad (3.39)$$

where  $M_{mn}^{(i)}$ ,  $(m, n) = 1, 2$  and  $i = 1, 2, 3$ , denote the components of the system matrix  $\mathbf{M}$  in Eq. (3.36) if the previously computed wave number  $k_z^{(i)}$  is substituted. Note that the last equation above is a consequence of Eq. (3.33). At this point, the wave number (eigenvalues) and related velocity amplitudes (eigenvectors) are determined. However, each velocity amplitude is only determined up to a constant. Thus, the constant coefficients  $\alpha_i$ ,  $i = 1, 2, 3$ , are introduced to scale each velocity amplitude. The coefficients  $\alpha_i$  are determined through boundary conditions and, in order to do so, the velocity perturbation is expressed as

$$\mathbf{v}' = \sum_{i=1}^3 \alpha_i \hat{\mathbf{v}}_i \exp(i(k_x x + k_z^{(i)} z)). \quad (3.40)$$

Note that the solutions of the other perturbations have a similar structure.

The boundary conditions in Eqs. (3.10) are used to determine the coefficients  $\alpha_i$  in the next step. While there are three unknown coefficients  $\alpha_i$ , the two equations in Eqs. (3.10) represent four linear independent scalar equations, which contain the yet unknown potential field in the mantle  $V_M$ . If the perturbation expansions are substituted in Eqs. (3.10), one obtains

$$(\bar{\mathbf{n}} + \mathbf{n}'(\mathbf{x})) \cdot (\bar{\mathbf{V}} + \mathbf{v}'(\mathbf{x})) = 0, \quad \mathbf{b}'(\mathbf{x}) = \nabla V_M'(\mathbf{x}), \quad \mathbf{x} \in \Gamma_{\text{CMB}}, \quad (3.41)$$

where  $V_M'$  denotes the perturbation of the scalar potential of the magnetic field in the mantle. Here, the normal vector  $\mathbf{n}$  was decomposed in a part  $\bar{\mathbf{n}} = \mathbf{e}_z$ , which

corresponds to a flat topography, and a part  $\mathbf{n}' = -i\mathbf{k}_T \Pi \exp(i\mathbf{k}_T \cdot \mathbf{x})$ , which is associated with a perturbation of the flat state. Note that these parts are already present in the numerator on the right-hand side of Eq. (3.12).

As indicated in Eqs. (3.41), the two boundary conditions are evaluated on the CMB, *i.e.*,  $z = \Pi \exp(ik_x x)$  for  $k_y = 0$ . Hence, the spatial dependency of all perturbations is characterized by

$$\begin{aligned} \exp(i\mathbf{k} \cdot \mathbf{x})|_{\mathbf{x} \in \Gamma_{\text{CMB}}} &= \exp(i(k_x x + k_z \Pi \exp(ik_x x))) \\ &= e^{ik_x x} + ik_z \Pi e^{2ik_x x} - \frac{1}{2} k_z^2 \Pi^2 e^{3ik_x x} + \mathcal{O}(\Pi^3), \end{aligned} \quad (3.42)$$

where a TAYLOR series expansion with respect to the parameter  $\Pi$  was performed in the second step. Keeping only terms that are linear with respect to the parameter  $\Pi$ , the slip boundary condition for the velocity reads

$$\sum_{i=1}^3 \left[ \underbrace{\alpha_i \hat{v}_z^{(i)} \left( e^{ik_x x} + ik_z^{(i)} \Pi e^{2ik_x x} \right)}_{\approx \hat{\mathbf{n}} \cdot \mathbf{v}'} - \underbrace{ik_x \Pi e^{ik_x x}}_{=\mathbf{n}' \cdot \bar{\mathbf{v}}} - \underbrace{\alpha_i ik_x \hat{v}_x^{(i)} \left( e^{2ik_x x} + ik_z^{(i)} \Pi e^{3ik_x x} \right)}_{\approx \mathbf{n}' \cdot \mathbf{v}'} \right] = 0. \quad (3.43)$$

In this equation, terms with the spatial dependencies  $\exp(ik_x x)$ ,  $\exp(2ik_x x)$  and  $\exp(3ik_x x)$  occur and these terms are mutually orthogonal on the interval  $(0, 1)$  with respect to the standard  $L^2$  inner product,<sup>2</sup> because the dimensionless wave number is given by  $k_x = 2\pi$ . In doing so, three linear independent equations are obtained from Eq. (3.41)<sub>1</sub>. In conclusion, this approach would generate three algebraic equations from the scalar boundary condition  $\mathbf{n} \cdot \mathbf{v}' = 0$ , which could be used to determine the coefficients  $\alpha_i$ .

However, the transition condition for the magnetic field is also present, which represents three additional algebraic equations, which can be used to determine the sought-for coefficients. Thus, the question arises how the equations, which are used to determine the coefficients  $\alpha_i$ , can be derived in a consistent way such that both boundary conditions are satisfied equally. It turns out that a consistent approach is to truncate the TAYLOR series expansion in Eq. (3.42) at the first term. This corresponds to a zeroth-order approximation with respect to  $\Pi$  and an evaluation of the boundary conditions on the reference surface, *i.e.*,  $z = 0$ . Applying this approximation, the only terms from Eq. (3.43), which are still present, are those with a spatial dependence that is characterized by  $\exp(ik_x x)$ . Hence, the boundary

<sup>2</sup>For the two complex-valued functions  $f$  and  $g$ , this inner product is given by

$$\langle f, g \rangle = \int_0^1 f(x) g^*(x) dx,$$

where  $(\bullet)^*$  denotes the complex conjugates of  $(\bullet)$ .

conditions in Eq. (3.41)<sub>1</sub> yield the following constraint for the coefficients  $\alpha_i$

$$\sum_{i=1}^3 \alpha_i \hat{v}_z^{(i)} - ik_x \Pi = 0. \quad (3.44)$$

Additional constraints are derived subsequently using Eq. (3.41)<sub>2</sub> for the transition of the magnetic field. For this, the perturbation of the scalar potential of the magnetic field in the mantle is required. This field is governed by the LAPLACE equation  $\nabla^2 V'_M = 0$ , whose solution is given by

$$V'_M(\mathbf{x}) = \hat{V}_M \exp(-k_x z) \exp(ik_x x), \quad (3.45)$$

where  $\hat{V}_M$  denotes an unknown constant ‘‘amplitude’’ and the fact that the topography is aligned with the fluid flow was used, *i.e.*,  $k_y = 0$ . The  $z$ -dependence of the perturbed scalar potential guarantees a decay for  $z \rightarrow \infty$ . Regarding Eq. (3.41)<sub>2</sub>, an application of the zeroth-order approximation of the TAYLOR series and a substitution of the gradient of the perturbed scalar potential of the magnetic field in the mantle yields

$$\sum_{i=1}^3 \alpha_i \hat{\mathbf{b}}_i = (ik_x \mathbf{e}_x - k_x \mathbf{e}_z) \hat{V}_M. \quad (3.46)$$

Combining this equation with Eq. (3.44) gives four equations for the three unknown coefficients  $\alpha_i$  and the constant  $\hat{V}_M$ , which characterizes the strength of the perturbation of the magnetic field in the mantle. In summary, the linear system, which is described by Eqs. (3.44) and (3.46), is given by

$$\begin{bmatrix} \hat{v}_z^{(1)} & \hat{v}_z^{(2)} & \hat{v}_z^{(3)} & 0 \\ \hat{b}_x^{(1)} & \hat{b}_x^{(2)} & \hat{b}_x^{(3)} & -ik_x \\ \hat{b}_y^{(1)} & \hat{b}_y^{(2)} & \hat{b}_y^{(3)} & 0 \\ \hat{b}_z^{(1)} & \hat{b}_z^{(2)} & \hat{b}_z^{(3)} & k_x \end{bmatrix} \begin{bmatrix} \alpha_1 \\ \alpha_2 \\ \alpha_3 \\ \hat{V}_M \end{bmatrix} = \begin{bmatrix} ik_x \Pi \\ 0 \\ 0 \\ 0 \end{bmatrix}. \quad (3.47)$$

Note that the entries of the system matrix above are constructed from the eigenvectors according to Eq. (3.39), where entries related to the magnetic field are constructed from Eq. (3.29). Due to the fact that the entries also depend on the wave numbers  $k_z^{(i)}$ , which are given by cumbersome expressions of combinations of the dimensionless parameters, the linear system above also contains these extensive expressions. Therefore, the system above is not solved with these complex expressions, but instead symbolic proxies are used. Finally, it should be noted that the right-hand side of the system is proportional to the parameter  $\Pi$ , which characterizes the relative height of the topography. Thus, all coefficients and thereby all perturbations are proportional to this parameter. Consequently, the parameter  $\Pi$  can be regarded as a small parameter, with respect to which the perturbation expansion of the solution is truncated. Moreover, for  $\Pi = 0$  the

right-hand side of the system vanishes, which implies that the coefficients  $\alpha_i$  and thus all perturbations also vanish.

If the system in Eq. (3.47) is solved, the solution to the problem is determined in principle. The solutions for the density, pressure, velocity and magnetic field perturbations can be computed once the wave numbers  $k_z^{(i)}$ , the velocity amplitudes  $\hat{v}^{(i)}$  and the coefficients  $\alpha_i$  are determined. For example, the solution for the pressure perturbation  $p'$  is given by

$$p'(\mathbf{x}) = \sum_{i=1}^3 \left[ \alpha_i \left( -\chi \frac{k_x}{k_z^{(i)}} + \frac{1}{k_x k_z^{(i)}} \frac{St^2}{Ro^2} + ik_z^{(i)} \frac{RmAl^2}{k_x^2 + (k_z^{(i)})^2 + ik_x Rm} \right) \times \right. \\ \left. \times \hat{v}_z^{(i)} \exp(i(k_x x + k_z^{(i)} z)) \right], \quad (3.48)$$

as obtained from Eq. (3.32). In this expression, the previously obtained symbolic solutions for the coefficients  $\alpha_i$ , the velocity amplitudes  $\hat{v}^{(i)}$  and the wave numbers need to be substituted. The coefficients  $\alpha_i$  are substituted first, because they depend on the velocity amplitudes  $\hat{v}^{(i)}$ , which are used as a symbolic proxy. Then, the velocity amplitudes  $\hat{v}^{(i)}$  are substituted themselves, the resulting expression is simplified if possible, and finally, the wave numbers  $k_z^{(i)}$  are substituted. The procedure of a sequential substitution allows for a partial simplification of the result, which is not possible in *Mathematica* if all substitutions are applied at the same time. Finally, a fully symbolic solution is obtained and the values of the dimensionless parameters are substituted in this fully symbolic expression in the very last step in order to obtain a numerical result.

### 3.2.4 Traction and torque on the Core-Mantle Boundary

Recall that the question posed at the beginning of this chapter was whether the pressure perturbation can cause an average traction on the CMB. Moreover, the size of the associated torque is of interest for an assessment of the plausibility of the model presented in this chapter in relation to fluctuations in the length of day. The traction or, more precisely, the perturbation of the traction vector is obtained using CAUCHY's argument with a spherical CAUCHY stress tensor, *i.e.*,  $\boldsymbol{\sigma}' = -p'\mathbf{1}$ . All results are, in general, complex valued, but for the traction and the subsequent computation of the net torque through an integration, only the real parts need to be taken into account. Therefore, the real parts of both the normal vector and the stress tensor are used in CAUCHY's formula, *i.e.*,

$$\mathbf{t}' = \Re(\mathbf{n}_M) \cdot \Re(\boldsymbol{\sigma}') = \Re(-\mathbf{n}) \cdot \Re(-p'\mathbf{1}) = \Re(p')\Re(\mathbf{n}), \quad (3.49)$$

where  $\mathbf{n}_M = -\mathbf{n}$  denotes the normal vector of the mantle, which points to the center of the core of the core of the Earth. This normal vector is used, because the traction on the mantle is considered.

The real parts on right-hand side can be expressed as follows:

$$\Re(p') = \frac{1}{2}(p' + p'^*), \quad \Re(\mathbf{n}) = \frac{1}{2}(\mathbf{n} + \mathbf{n}^*). \quad (3.50)$$

where  $(\bullet)^*$  denotes the complex conjugate of  $(\bullet)$ . Thus, the product  $\Re(p')\Re(\mathbf{n})$ , which occurs in Eq. (3.49), consists of the four terms  $p'\mathbf{n}$ ,  $p'^*\mathbf{n}$ ,  $p'\mathbf{n}^*$  and  $p'^*\mathbf{n}^*$ . For the normal vector  $\mathbf{n}$ , the following first order approximation of Eq. (3.12) with respect to  $\Pi$  is applied subsequently

$$\mathbf{n} = \frac{\mathbf{e}_z - ik_x \Pi \mathbf{e}_x \exp(ik_x x)}{\|\mathbf{e}_z - ik_x \Pi \mathbf{e}_x \exp(ik_x x)\|} \approx \mathbf{e}_z - ik_x \Pi \exp(ik_x x) \mathbf{e}_x. \quad (3.51)$$

For the four terms, which occur in the traction vector  $\mathbf{t}'$ , this yields

$$p'\mathbf{n} = \sum_{i=1}^3 \alpha_i \hat{p}_i e^{ik_z^{(i)} z} \left( e^{ik_x x} \mathbf{e}_z - ik_x \Pi e^{i2k_x x} \mathbf{e}_x \right), \quad (3.52a)$$

$$p'\mathbf{n}^* = \sum_{i=1}^3 \alpha_i \hat{p}_i e^{ik_z^{(i)} z} \left( e^{ik_x x} \mathbf{e}_z + ik_x \Pi \mathbf{e}_x \right), \quad (3.52b)$$

$$p'^*\mathbf{n} = \sum_{i=1}^3 \alpha_i^* \hat{p}_i^* \left( e^{ik_z^{(i)} z} \right)^* \left( e^{-ik_x x} \mathbf{e}_z - ik_x \Pi \mathbf{e}_x \right), \quad (3.52c)$$

$$p'^*\mathbf{n}^* = \sum_{i=1}^3 \alpha_i^* \hat{p}_i^* \left( e^{ik_z^{(i)} z} \right)^* \left( e^{-ik_x x} \mathbf{e}_z + ik_x \Pi e^{-i2k_x x} \mathbf{e}_x \right), \quad (3.52d)$$

where  $\hat{p}_i$  denotes the amplitude of the pressure perturbations corresponding to the wave numbers  $k_z^{(i)}$ . The average traction is computed by integrating the traction vector over one period of the wave, *i.e.*,

$$\langle \mathbf{t}' \rangle = \int_0^1 \mathbf{t}'(\mathbf{x})|_{\Gamma_{\text{CMB}}} dx, \quad (3.53)$$

where the fact was used that the wave length of the topography is unity in the dimensionless formulation. The integral in Eq. (3.53) needs to be evaluated at the CMB, *i.e.*, for  $z = \Pi \exp(ik_x x)$ . However, this evaluation introduces higher terms with respect to the parameter  $\Pi$ , which is related to the height of the topography. Considering, for example, the TAYLOR series expansion of the following expression for  $z = \Pi \exp(ik_x x)$  with respect to  $\Pi$ :

$$e^{ik_x x} e^{ik_z \Pi e^{ik_x x}} \approx e^{ik_x x} \left( 1 + ik_z \Pi e^{ik_x x} - \frac{1}{2} k_z^2 \Pi^2 e^{i2k_x x} + \mathcal{O}(\Pi^3) \right) \quad (3.54)$$

shows that the higher order terms do not contribute to the traction at all, because these terms are integrated over one period of the wave and therefore vanish. Thus, regarding Eq. (3.52), only terms, which do not possess an explicit dependence on

the  $x$ -coordinate, do not vanish when the integration is performed. These terms occur in the  $x$ -components of Eq. (3.52b) and (3.52c). Therefore, the expression for the average traction on the CMB is given by

$$\langle \mathbf{t}' \rangle = ik_x \Pi e_x \frac{1}{4} \sum_{i=1}^3 (\alpha_i \hat{p}_i - \alpha_i^* \hat{p}_i^*). \quad (3.55)$$

Furthermore, the  $z$ -component of the  $\mathbf{t}'$  vanishes.

This expression is subsequently used in order to assess the value of the resulting torque on the CMB. In general, the resulting torque  $\langle \mathbf{m}^{(\mathcal{O})} \rangle$  with respect to the center of the Earth  $\mathcal{O}$  is computed by

$$\langle \mathbf{m}^{(\mathcal{O})} \rangle = \int_0^1 \mathbf{x}_{\text{CMB}} \times \mathbf{t}'(\mathbf{x})|_{\Gamma_{\text{CMB}}} dx, \quad (3.56)$$

where  $\mathbf{x}_{\text{CMB}}$  denotes the distance vector from the center of the Earth to the CMB. For the coordinate system used in Fig. 3.1, the dimensionless form of this vector is given by

$$\mathbf{x}_{\text{CMB}} = x \mathbf{e}_x + \left( \frac{R_{\text{CMB}}}{\lambda_x} + \Pi \exp(ik_x x) \right) \mathbf{e}_z. \quad (3.57)$$

The ratio of  $R_{\text{CMB}}/\lambda_x$  clearly dominates all other terms in this expression. Therefore the dimensionless position  $\mathbf{x}_{\text{CMB}}$  is simply approximated by  $R_{\text{CMB}}/\lambda_x \mathbf{e}_z$ . Hence, the averaged torque is given by

$$\langle \mathbf{m}^{(\mathcal{O})} \rangle = \frac{R_{\text{CMB}}}{\lambda_x} \mathbf{e}_z \times \langle \mathbf{t}' \rangle = ik_x \Pi \frac{1}{4} \frac{R_{\text{CMB}}}{\lambda_x} \mathbf{e}_y \sum_{i=1}^3 (\alpha_i \hat{p}_i - \alpha_i^* \hat{p}_i^*), \quad (3.58)$$

where Eq. (3.55) was applied to obtain the final result. This expression for the averaged torque concludes the discussion related to the traction and the torque and also the analysis of the topography problem. The traction and torque of solutions, which are obtained by applying certain simplifications, will be analyzed and discussed in the next section.

### 3.3 Analysis of the results

The analysis in Sect. 3.2 was held in a rather general way and results have neither been presented nor analyzed. In this section, results for certain special cases are presented, evaluated and discussed. As already indicated in Sect. 3.1, the algebraic expressions, which occur if the problem is solved analytically, are complex and excessively large. However, if certain simplifications are applied, the expressions become tractable. These simplifications consist of the neglect of the magnetic field ( $Al = 0$ ), the inertial term ( $\chi = 0$ ), the stratification ( $St = 0$ ) and the CORIOLIS term ( $\theta = \pi/2$ ). In these cases, the algebraic structure of the wave numbers is

simplified significantly, because one of the matrices in Eq. (3.36) drops out of the problem. Moreover, the number of eigenvalues decreases, because the degree of the characteristic polynomial is lowered if certain terms are neglected. As a consequence, the number of coefficients  $\alpha_i$  also decreases and only a part of the linear system in Eq. (3.47) needs to be considered. For all of the simplifications, the resulting average traction on the CMB and its dependence on some of the dimensionless parameters will be discussed. Additionally, the dependence of the wave number and the average traction on the background velocity and magnetic field will be detailed. While the neglect of the magnetic field and the inertial term are addressed independently, the neglect of the CORIOLIS term is considered by simply setting the colatitude equal to  $\pi/2$  in each of the cases.

### 3.3.1 Non-magnetic case

In this section, the non-magnetic case is analyzed. Note that this case is also analyzed in the textbook by Gill in the context of internal gravity waves [Gill (1982)]. However, Gill's presentation and approach to the problem is different from that presented here, because it is not formulated in a dimensionless form and also neglects the CORIOLIS term. Therefore, a comparison with this work is deliberately kept short.

The non-magnetic case corresponds to a vanishing magnetic background field and hence  $Al = 0$ . Apart from the ALFVÉN number  $Al$ , the magnetic REYNOLDS number  $Rm$  also drops out of the problem. As a consequence of  $Al = 0$ , the matrix  $\mathbf{C}$  is no longer present in Eq. (3.36), which yields a single admissible wave number,

$$k_z^{(1)} = -ik_x \frac{\sqrt{\chi \frac{St^2}{Ro^2} - \chi^2 k_x^2}}{\sqrt{\frac{4 \cos^2(\theta)}{Ro^2} - \chi^2 k_x^2}}. \quad (3.59)$$

This expression was arranged in such a way that the two square roots in the numerator and denominator are real for typical values of  $St$  and  $Ro$  for the Earth. Note that if  $\chi = 0$  the wave number vanishes, which means that the perturbations do not decay with increasing distance from the topography. Thus, the non-inertial non-magnetic case is not considered further and the switch  $\chi$  is subsequently set to unity, *i.e.*,  $\chi \rightarrow 1$ .

For the "standard case" specified in Table 3.4, the value of the wave number is given by  $k_z^{(1)} = -62.832i$ , which indicates that the solution decays rapidly with respect to the  $z$ -coordinate. The dependence of the imaginary part of the wave number  $k_z^{(1)}$  in Eq. (3.59) on the ROSSBY number is shown in Fig. 3.2 for different values of the colatitude  $\theta$ . In Fig. 3.2, the stratification parameter has a value of  $St = 20$  for all curves, which corresponds to the value of the "standard case" specified in Table 3.4. For all curves in Fig. 3.2, the imaginary part is constant for a large range of values of the ROSSBY number. For larger ROSSBY numbers, a pole with a change of sign occurs and admissible solutions are no longer found, because

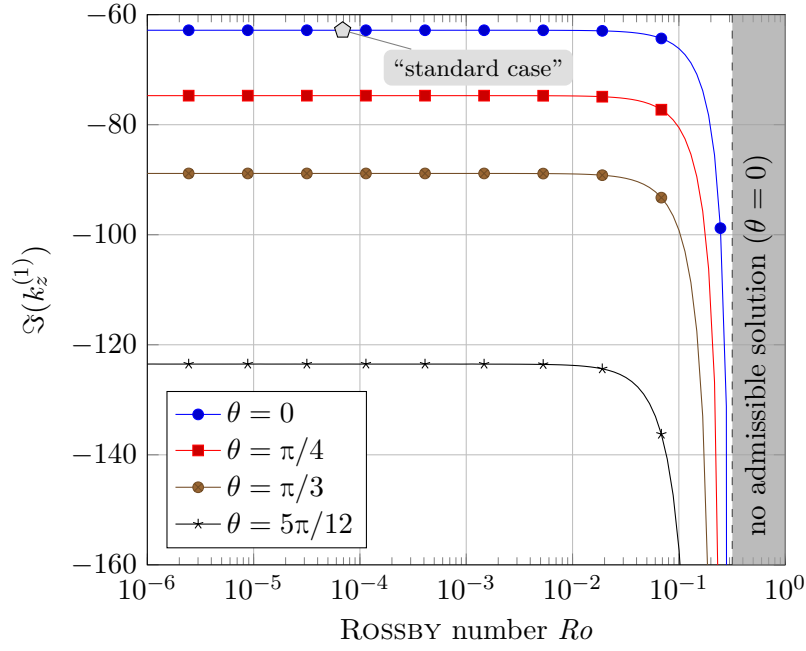


**Figure 3.2:** Imaginary part of the wave number  $k_z^{(1)}$  as function of the ROSSBY number  $Ro$  and different colatitudes  $\theta$ .

the imaginary part becomes positive. If the colatitude is increased, the ROSSBY numbers, at which the pole occurs, decreases.

For the limit case of a vanishing ROSSBY number and  $\theta < \pi/2$ , which corresponds to a vanishing background velocity or an infinite wavelength of the topography, the imaginary part of the wave number is negative as well, which indicates that the solution is regular for  $Ro \rightarrow 0$ . In the case of a vanishing rotation, *i.e.*, for  $\theta = \pi/2$ , an admissible root can be found if  $St^2/Ro^2 < k_x^2$ . This requires that the stratification parameter  $St$  becomes very small, *i.e.*,  $St < 10^{-4}$ . A corresponding requirement for the existence of waves is also formulated by Gill, see Gill [1982], p. 143. This requirement regarding the stratification parameter is far off from the range of values that is expected for the stratified layer at the top of the core of the Earth. Thus, the case of a vanishing rotation is not considered further and not shown in Fig. 3.2.

The eigenvector corresponding to the wave number in Eq. (3.59) is given by

$$\hat{\mathbf{v}}_1 = \mathbf{e}_x + \frac{2i}{k_x Ro} \cos(\theta) \mathbf{e}_y - \frac{k_x}{k_z^{(1)}} \mathbf{e}_z. \quad (3.60)$$

Using this eigenvector, the corresponding coefficient  $\alpha_1$  is determined from the no-slip boundary condition in Eq. (3.44) as  $\alpha_1 = -ik_z^{(1)} \Pi$ . This yields the following

pressure perturbation  $\hat{p}$ , which governs the average traction on the boundary,

$$\hat{p} = \alpha_1 \hat{p}_1 = -\frac{i\Pi}{k_z^{(1)}} \left( \frac{St^2}{Ro^2} + k_x^2 \right) = -\frac{\Pi}{k_x} \left( \frac{St^2}{Ro^2} + k_x^2 \right) \frac{\sqrt{\frac{4 \cos^2(\theta)}{Ro^2} - k_x^2}}{\sqrt{\frac{St^2}{Ro^2} - k_x^2}}. \quad (3.61)$$

This factor is purely real if the wave number is admissible and therefore the average traction vanishes according to Eq. (3.55). In summary, the non-magnetic case can never exert a net stress or a net torque on the boundary.

Finally, the sizes of the perturbations are analyzed and the validity of the approximations made in Sect. 3.2.2, where the balance of mass was simplified, are reviewed. In doing so, the “standard case” specified in Table 3.4 is used when numerical values are specified. The amplitudes of the velocity and the density perturbations are given by

$$\hat{\mathbf{v}} = -\Pi \left( ik_z^{(1)} \mathbf{e}_x + \frac{2}{Ro} \frac{k_z^{(1)}}{k_x} \cos(\theta) \mathbf{e}_y + ik_x \mathbf{e}_z \right), \quad \hat{\rho} = -\frac{Fr^2 St^2}{Ro^2} \Pi. \quad (3.62)$$

The magnitude of the velocity amplitude is dominated by the  $y$ -component because the small value of the ROSSBY number outweighs all other terms and factors. Taking the  $y$ -component into account yields a velocity magnitude of  $|\hat{\mathbf{v}}| \approx 87$ , which does not correspond to a small perturbation. However, the  $y$ -component is a component that is only present because of the rotation. Moreover, it is the component of the out-of-plane direction. The solution, the topography and the background fields do not possess any variations with respect to this direction. Therefore, there is no physical mechanism hindering a fluid flow in the  $y$ -direction. If only the in-plane components of the velocity are considered, the magnitude of the velocity amplitude is given by  $|\hat{v}_x \mathbf{e}_x + \hat{v}_z \mathbf{e}_z| = 1.9 \times 10^{-2}$ , which is less than unity and confirms that the velocity perturbation is still small.

The density perturbation is also small because its magnitude is given by  $|\rho'| = 6.3 \times 10^{-5}$ . In Sect. 3.2.2, the ratio of the gradient of the density perturbation to that of the reference density was introduced and it was pointed out that this ratio should be small such that the approximation is admissible. Its value is given by  $\varepsilon_{\nabla \rho'} = 1.9 \times 10^{-2}$ , which means that the ratio  $\varepsilon_{\nabla \rho'} / \varepsilon_{\mathbf{v}'}$  is of order unity. Thus, the approximations made in Sect. 3.2.2 regarding the orders of magnitude of the different terms in the balance of mass are not violated, see the discussion related to Eq. (3.24).

### 3.3.2 Non-inertial magnetic case

In the non-inertial magnetic case, the inertial term is neglected by applying  $\chi = 0$ . This neglect partially simplifies the solution and reduces the algebraic complexity of the problem. In general, the non-inertial magnetic case yields an eigenvalue problem with two admissible wave numbers, which inherits the complex algebraic expressions mentioned earlier. However, an additional simplification of the non-

inertial magnetic case results in a problem with a single wave number instead of two. This simplified case is obtained if an additional approximation regarding the wave numbers  $k_x$  and  $k_z$  is made and entails algebraic expressions, which are manageable without the help of a computer algebra system. Subsequently, the simplified case with one wave number will be discussed first and subsequently the results related to the general non-inertial magnetic case with two waves will be presented.

### Simplified non-inertial magnetic case

The simplified case with only one wave number is obtained if the assumption  $k_z^2 \gg k_x^2$  is made. Thus, approximations of the related terms in Eq. (3.36) are made as follows:

$$1 + \frac{k_x^2}{k_z^2} \approx 1, \quad k_z^2 \frac{RmAl^2}{\mathbf{k}^2 + ik_x Rm} = k_z^2 \frac{RmAl^2}{k_x^2 + k_z^2 + ik_x Rm} \approx k_z^2 \frac{RmAl^2}{k_z^2 + ik_x Rm}. \quad (3.63a)$$

These approximations still yield two admissible wave numbers. Yet, if the additional assumption  $k_z^2 \gg k_x Rm$  is made, the polynomial degree of the characteristic equation can be further reduced and a single admissible wave number is found. The magnetic REYNOLDS number has a value of 62.5 for the “standard case” and the dimensionless wave number of the topography is given by  $2\pi$ . Therefore, the assumption is justified as long as  $k_z \gg 20$ . In summary, the additional assumption  $k_z^2 \gg k_x Rm$  allows to further approximate the second term in the equation above as

$$k_z^2 \frac{RmAl^2}{\mathbf{k}^2 + ik_x Rm} \approx RmAl^2. \quad (3.63b)$$

The resulting wave number, which is obtained from the simplified characteristic equation, is given by

$$k_z^{(1)} = -\frac{1}{\sqrt{2}}(1+i) \frac{St}{Ro} \frac{\sqrt{k_x RmAl^2}}{\sqrt{(RmAl^2)^2 + \frac{4 \cos^2(\theta)}{Ro^2}}}. \quad (3.64)$$

For the “standard case” specified in Table 3.4, the numerical value of this wave number is given by  $k_z^{(1)} = -1561.13(1+i)$ . This confirms that the approximations discussed above are not violated, because the magnitude of the wave number is well within the permitted limit. Note that the magnitude of the wave number depends on the dimensionless parameters whereas the argument does not and is constant. The value of the argument is given by  $\arg(k_z^{(1)}) = -3\pi/4$ .

The dependence of the magnitude of this wave number on the dimensionless parameters cannot be inferred easily apart from the stratification parameter  $St$ . The linear dependence on  $St$  results in a vanishing wave number if the stratification vanishes. As a consequence, a stratified fluid is required in order to obtain an admissible wave number.

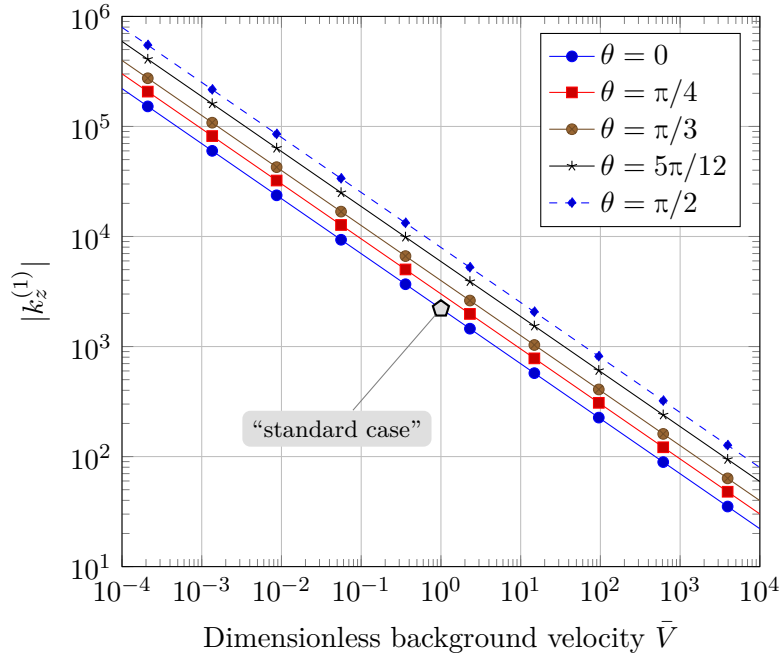


**Figure 3.3:** Dependence of the magnitude of the wave number  $k_z^{(1)}$  in Eq. (3.64) on the background velocity  $\bar{V}$  for different values of the colatitude  $\theta$ .

Furthermore, asymptotic limits such as  $Ro \rightarrow 0$  are considered. In doing so, the limit of an equivalent physical parameter of the boundary value problem needs to be kept in mind. Considering the example of  $Ro \rightarrow 0$  would either correspond to an infinite wave length of the boundary topography ( $\lambda_x \rightarrow \infty$ ) or a vanishing background velocity field ( $\bar{\mathbf{V}} \rightarrow \mathbf{0}$ ), of which only the latter is physically meaningful. Thus, instead of considering variations of the ALFVÉN, ROSSBY, and the magnetic REYNOLDS number, a variation of the background velocity field  $\bar{\mathbf{V}}$  is analyzed. The magnetic REYNOLDS and the ROSSBY numbers are proportional to the magnitude of the background velocity  $V_0 = |\bar{\mathbf{V}}|$  and the ALVÉN number is inversely proportional to it, see Eq. (3.7)<sub>5</sub>. Therefore, these three dimensionless parameters are substituted by their reference values for a velocity of  $V_0 = 5 \times 10^{-4} \text{ m s}^{-1}$  multiplied or divided by the dimensionless background velocity  $\bar{V}$ , *i.e.*,  $Rm \rightarrow Rm(V_0)\bar{V}$ ,  $Ro \rightarrow Ro(V_0)\bar{V}$  and  $Al \rightarrow Al(V_0)/\bar{V}$ , respectively. Additionally, the magnitude of the wave number is analyzed for a variation of the magnetic background field. This analysis can be achieved easily by considering a variation of the ALFVÉN number only, because it is the only dimensionless parameter of the problem that depends on the magnitude of the magnetic background field  $B_0$ , see Eq. (3.7). The influence of the rotation can be analyzed by a variation of the colatitude  $\theta$ .

The dependence of the magnitude of the wave number in Eq. (3.64) on the dimensionless background velocity  $\bar{V}$  is shown in Fig. 3.3 for different values of the colatitude  $\theta$ . From the set of curves in Fig. 3.3, it can clearly be seen that the

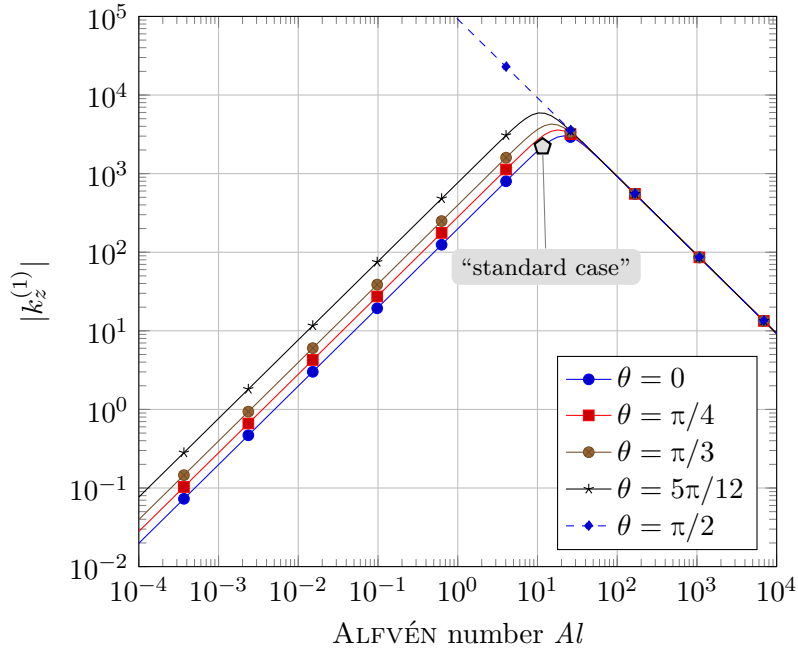


**Figure 3.4:** Dependence of the magnitude of the wave number  $k_z^{(1)}$  in Eq. (3.64) on the ALFVÉN  $Al$  number for different values of the colatitude  $\theta$ .

magnitude decreases if the background velocity increases. Moreover, the magnitude of the wave number is not very sensitive with respect to the value of the colatitude  $\theta$ , because the different curves are parallel. Recall that the approximations discussed above are only valid as long as  $|k_z| \gg 20$ . Considering the curves in Fig. 3.3, it can be argued that this requirement is fulfilled for a large range of values of the dimensionless background velocity and is violated only for very large values. Furthermore, the “standard case”, which is indicated in Fig. 3.3 by a gray filled pentagon, does not violate this requirement.

Next, the dependence of the wave number on the magnetic background field is analyzed by considering a variation of the ALFVÉN number for a fixed value of the background velocity. The dependence is shown in Fig. 3.4 for different values of the colatitude  $\theta$ . According to Fig. 3.4, the magnitude of the wave number increases with the ALFVÉN number as long as the ALFVÉN number is small. Then, the magnitude reaches a maximum for  $Al \approx 10$  and subsequently decreases if the ALFVÉN number is increased further. This holds as long as rotational effects are relevant, *i.e.*, if  $\theta \neq \pi/2$ . If the CORIOLIS term vanishes, which is the case if  $\theta = \pi/2$ , the wave number does not decrease if the magnetic background field decreases. Instead the wave number increases. Furthermore, the magnitude of the wave number does not depend on the value of the colatitude  $\theta$  for large values of the ALFVÉN number whereas the contrary holds for small values.

The decrease of the magnitude of the wave number for  $Al > 10$  can be ex-

plained by considering the square root in the denominator in Eq. (3.64). When  $Al^2 > 2 \cos(\theta)/(RmRo)$ , the square root in the denominator is dominated by the summand containing the ALFVÉN number; therefore, it is proportional to  $RmAl^2$ . This factor also occurs in the square root in the numerator in Eq. (3.64) and, as a consequence, the magnitude of the wave number is proportional to  $1/\sqrt{RmAl^2}$ . This inverse proportionality results in the decrease of the magnitude of the wave numbers in Fig. 3.4 if the ALFVÉN number is sufficiently large. In fact, the value of the ALFVÉN number predicted by the criterion  $Al > \sqrt{2 \cos(\theta)/(RmRo)}$  is given by  $Al > 21.6$ , if the magnetic REYNOLDS and the ROSSBY numbers have the values specified for the “standard case” and  $\theta = 0$ . This value of the ALFVÉN number complies very well with the value, where the slope of the corresponding curve in Fig. 3.8 changes from a positive slope to a negative one. The criterion  $Al > \sqrt{2 \cos(\theta)/(RmRo)}$  can be expressed in terms of the corresponding dimensional parameters of the problem as  $B_0^2 > 2\rho_0 \cos(\theta)\Omega_0\eta/\mu_0$ . This expression relates the magnetic background field to the CORIOLIS term (or rotational inertia) and the electrical conductivity. Furthermore, it is independent of the background velocity. In summary, this criterion can be interpreted as follows. Magnetic diffusion effects are governing the solution if the magnetic background field is small. However, if the magnetic background field is sufficiently large, this is no longer the case and induction effects become important as well.

The requirement  $k_z \gg 20$ , which needs to be satisfied for the approximations made above to hold true, is only fulfilled for a limited range of values of the ALFVÉN number. From Fig. 3.4 it can be seen that the requirement is violated if the ALFVÉN number is either less than  $10^{-1}$  or larger than  $10^3$ . The magnitude of the wave number corresponding to the “standard case,” which is indicated in Fig. 3.4 by a gray filled pentagon, is well within these limits. Additionally, its location is very close to the maximum of the respective curve.

In order to analyze the perturbations obtained in the simplified non-inertial case, the eigenvector corresponding to the wave number in Eq. (3.64) is required. It is given by

$$\hat{\mathbf{v}} = \alpha_1 \hat{\mathbf{v}}_1 = -i\Pi \left( k_z^{(1)} \mathbf{e}_x + \frac{2 \cos(\theta)}{RoRmAl^2} k_z^{(1)} \mathbf{e}_y - k_x \mathbf{e}_z \right). \quad (3.65)$$

Here,  $\alpha_1 = -ik_z^{(1)} \Pi$  was applied, which results from the no-slip boundary condition in Eq. (3.44). The magnitude of the velocity amplitude is given by  $|\hat{\mathbf{v}}| = 2.39$ . This value is much less than that of the non-magnetic case, because the out-of-plane component is significantly smaller. However, due to the small value of the ROSSBY number, the magnitude of the velocity is still dominated by the out-of-plane component. The same applies for the perturbation of the magnetic field and its magnitude, because it is proportional to the velocity perturbation. If only the in-plane components, *i.e.*, the  $x$ - and  $z$ -components, are considered, the magnitude of the corresponding in-plane velocity is given by  $|\hat{v}_x \mathbf{e}_x + \hat{v}_z \mathbf{e}_z| = 0.66$ . This value is less than unity but not very small, which challenges the linearization of the problem.

Apart from the velocity amplitude, it is also important to consider the density perturbation because of the approximation of the balance of mass, see Sect. 3.2.2. The magnitude of the density perturbation is given by  $|\rho'| = 6.3 \times 10^{-5}$ , which is the same as that of the non-magnetic case. Moreover, the ratio, which is relevant to judge whether the approximation of the balance of mass in Sect. 3.2.2 is valid, is given by  $\varepsilon_{\nabla\rho'} = 1.4 \times 10^{-1}$ . This value is an order of magnitude larger than that of the non-magnetic case but it is still within the range of values, such that the approximation in Sect. 3.2.2 is valid and applicable for this case.

The discussion of the simplified non-inertial case is continued by analyzing the pressure perturbation and the associated average traction. In the simplified non-inertial case, the approximation  $k_z^2 \gg k_x Rm$  was applied to simplify the problem. The factor that contains these quantities is also present in the pressure perturbation specified in Eq. (3.32). Thus, the same approximation as in Eq. (3.63) needs to be applied in Eq. (3.32) as well in order to obtain a consistent pressure perturbation, *viz.*,

$$\hat{p} = \frac{1}{k_x k_z} \left( \frac{St^2}{Ro^2} + ik_x RmAl^2 \right) \hat{v}_z. \quad (3.66)$$

According to Eq. (3.65),  $\hat{v}_z = ik_x \Pi$ . Thus, the resulting pressure perturbation is given by

$$\begin{aligned} \hat{p} &= \frac{i\Pi}{k_z^{(1)}} \left( \frac{St^2}{Ro^2} + ik_x RmAl^2 \right) \\ &= -\frac{1}{\sqrt{2}}(1+i)\Pi \left( \frac{St^2}{Ro^2} + ik_x RmAl^2 \right) \frac{Ro}{St} \frac{\sqrt{(RmAl^2)^2 + \frac{4\cos^2(\theta)}{Ro^2}}}{\sqrt{k_x RmAl^2}}, \end{aligned} \quad (3.67)$$

where the wave number according to Eq. (3.64) was substituted in the second step. The argument or phase of the pressure perturbation depends on the phase of the wave number and on the dimensionless parameters. For typical values in the outer core of the Earth, the factor  $St^2/Ro^2$  is six orders of magnitude larger than the factor  $k_x RmAl^2$ . Therefore, the phase of a wave number determines the phase of the pressure perturbation. As a consequence, the phase of the pressure perturbation is given by approximately  $-3\pi/4$ . Hence, the phase shift or offset between the topography and the pressure perturbation is given by  $\pi/4$  or  $45^\circ$ . The pressure perturbation vanishes where the topography is high or low. It is maximum or minimum where the topography vanishes.

The average of the perturbation of the traction vector according to Eq. (3.55), which results from the pressure perturbation specified above, is given by

$$\langle \mathbf{t}' \rangle = \frac{1}{2\sqrt{2}} k_x \Pi^2 \left( \frac{St^2}{Ro^2} + k_x RmAl^2 \right) \frac{Ro}{St} \frac{\sqrt{(RmAl^2)^2 + \frac{4\cos^2(\theta)}{Ro^2}}}{\sqrt{k_x RmAl^2}} \mathbf{e}_x. \quad (3.68)$$

For the ‘‘standard case,’’ this expression yields a dimensionless numerical value

of  $\langle \mathbf{t}' \rangle = 7.66 \mathbf{e}_x$ . If this dimensionless average traction value is converted to a dimensional physical quantity using the pressure scale factor  $\rho_0 V_0^2$ , an average traction of  $0.02 \text{ N m}^{-2}$  is obtained. Subsequently, the dependence of the average traction on the dimensionless parameters of the boundary topography problem is analyzed. From Eq. (3.68) it is clear that the dependence on the parameter  $\Pi$ , which characterizes the height of the topography, is quadratic. Moreover, vanishing stratification ( $St \rightarrow 0$ ) would yield an infinite average traction. However, this limit value is not admissible, because, according to Eq. (3.64), the wave number vanishes concurrently with the stratification parameter  $St$ .

In order to analyze the dependence of the average traction on the background velocity and magnetic fields, the same procedure is applied as for the analysis of the wave number in Eq. (3.64). The dependence on the dimensionless background velocity and the ALFVÉN number is considered. If the dependence of the average traction on the dimensionless background velocity is analyzed, special care is required, because the pressure scale factor  $\rho_0 V_0^2$  associated with the average traction also involves the magnitude of the background velocity. After a rescaling, the dimensional value of the average traction is given by  $\rho_0 V_0^2 \langle \mathbf{t}' \rangle$ . Therefore, the dimensional average traction is finite for  $V_0 \rightarrow 0$  if the dimensionless average traction obeys  $\langle \mathbf{t}' \rangle \propto V_0^p$  with  $p \geq -2$  for  $V_0 \rightarrow 0$ . It is found that  $\langle \mathbf{t}' \rangle \propto V_0^{-3/2}$  and thus  $\rho_0 V_0^2 \langle \mathbf{t}' \rangle \propto \sqrt{V_0}$ . Therefore, the dimensionless average traction  $\langle \mathbf{t}' \rangle$  is infinite for  $V_0 \rightarrow 0$ , although the dimensional average traction  $\rho_0 V_0^2 \langle \mathbf{t}' \rangle$  vanishes. This fact is taken into account if the dependence of the average traction on the dimensionless background velocity is analyzed. In order to avoid a misleading infinite average traction for  $V_0 \rightarrow 0$  or  $\bar{V} \rightarrow 0$ , respectively, the average traction is multiplied by  $\bar{V}^2$  if the dependence on the dimensionless background velocity is considered to account for a possible rescaling. In doing so, a true physical singularity of the solution can be identified.

If the substitutions corresponding to the analysis of the dependence on the background velocity are applied in Eq. (3.68), the set of curves shown in Fig. 3.5 results. Accordingly, the average traction increases in parallel with the dimensionless background velocity. The slope of all curves in the double-logarithmic chart is given by  $1/2$ , which means that the average traction is proportional to the square root of the dimensionless background velocity. Likewise to the wave number, the dependence of the average traction on the dimensionless background velocity is not significantly influenced by the CORIOLIS term, whose variation is performed by a variation of the colatitude  $\theta$ .

The dependence of the average traction on the ALFVÉN number is shown in Fig. 3.6 for different values of the colatitude  $\theta$ . The curves in Fig. 3.6 are clearly correlated to those for the magnitude of the wave number in Fig. 3.4. A small ALFVÉN number of, *e.g.*,  $Al < 1$  yields a small wave number and a large average traction. Likewise for a large ALFVÉN number of, say,  $Al > 50$ , the wave number is also small and the average traction is large as well. Moreover, there is no distinction between the curves of different colatitude if the ALFVÉN number becomes large.

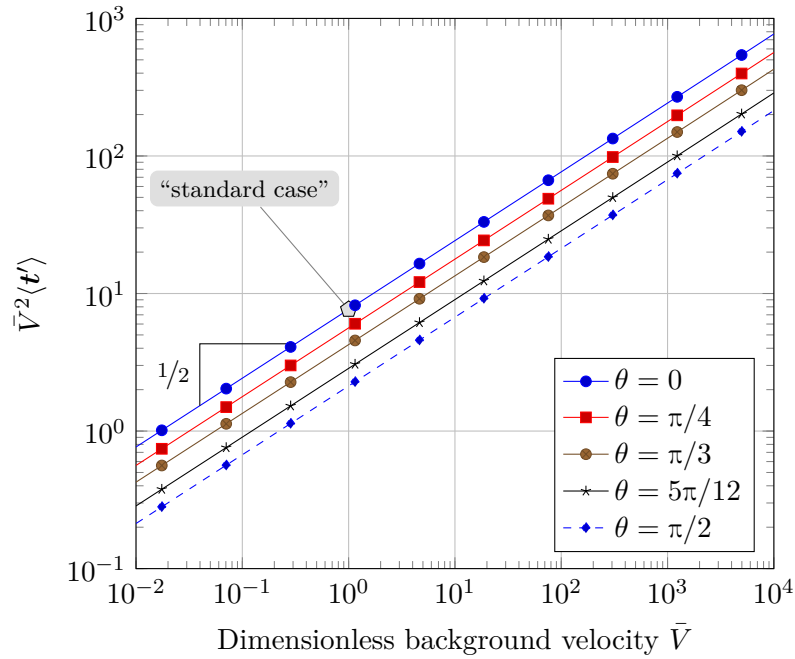


**Figure 3.5:** Dependence of the magnitude of the average traction in Eq. (3.68) on the background velocity  $\bar{V}$  for different values of the colatitude  $\theta$ . The slope of the curves for small values of the ALFVÉN number is indicated using a triangle close to the bottom-left corner.

For intermediate values of the ALFVÉN number, the traction becomes rather small and the corresponding magnitude of the wave number is large. These relations hold true as long as the rotation is taken into account, *i.e.*, for  $\theta < \pi/2$ . Considering the curve for  $\theta = \pi/2$ , which corresponds to a vanishing CORIOLIS term, the average traction decreases together with the ALFVÉN number. This is not the case if  $\theta < \pi/2$ . The value of the average traction corresponding to the “standard case” is indicated by a gray filled pentagon in Fig. 3.6; it is located closely to the minimum of the corresponding curve.

According to Fig. 3.6, an infinite average traction would result if the magnetic background field would become infinitely large or vanishingly small. This infinitely large average traction is contradictory, because at least a finite traction is expected if the magnetic background field becomes vanishingly small. While a large average traction is plausible for a strong magnetic background field, this is not the case if the magnetic background field is weak. The large average traction for a strong magnetic background field is caused predominantly by the in-plane components of the velocity perturbation. The  $x$ - and  $z$ -components of the velocity perturbation yield a distortion of the magnetic background field and thus induce a perturbation of the magnetic field, which causes LORENTZ forces to act on the fluid. According to Eq. (3.65), the out-of-plane component of the velocity perturbation is inversely

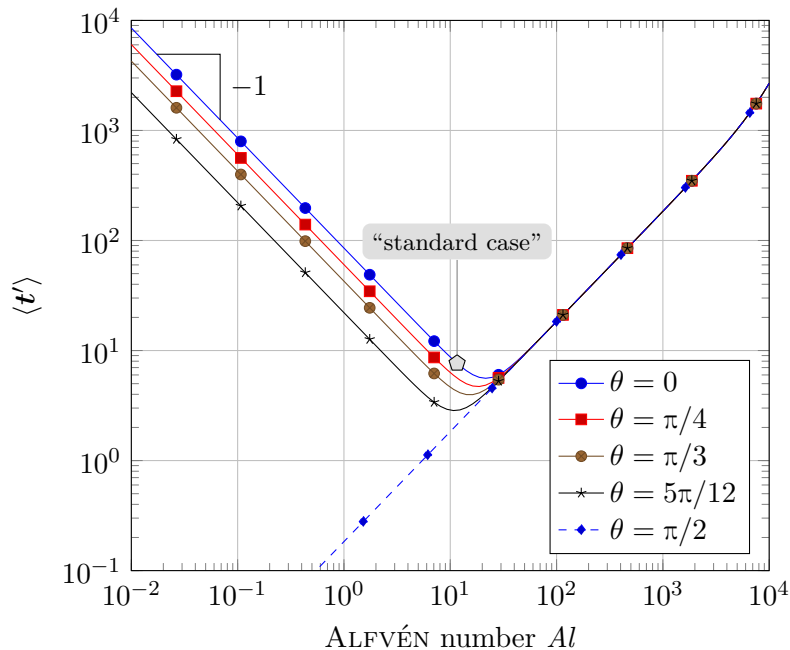


**Figure 3.6:** Dependence of the magnitude of the average traction in Eq. (3.68) on the ALFVÉN number  $Al$  for different values of the colatitude  $\theta$ . The slope of the curves is indicated using a triangle close to the top-left corner.

proportional to the square of the ALFVÉN number and thus inversely proportional to the square of the magnitude of the magnetic background field. As a consequence, there is virtually no fluid flow in the  $y$ -direction if the magnetic background field is sufficiently strong. Thus, only the in-plane components distort the magnetic field in the presence of a strong background field.

Keeping this in mind, the very large value of the average traction for a weak magnetic background field can be explained. According to Eq. (3.65) the out-of-plane component of the velocity perturbation becomes dominant in the weak regime as long as the CORIOLIS term does not vanish. Thus, the out-of-plane flow strongly distorts the magnetic background field and large LORENTZ forces occur, which result in a large average traction. If the CORIOLIS term vanishes ( $\theta = \pi/2$ ), the out-of-plane flow also does so, see Eq. (3.65). Therefore, an increase of the average traction for small values of the magnetic background field is not observed in Fig. 3.6 in this case.

The out-of-plane flow occurs because of the CORIOLIS term and it is rather large because the ROSSBY number is small. Apart from the LORENTZ force, there are no other forces which can prevent this flow, because the inertia and viscosity of the fluid are neglected. Moreover, the topography as well as the solutions themselves have a two-dimensional spatial structure. Therefore, there is neither a pressure gradient in the out-of-plane direction nor does the flow over the topography in

the out-of-plane direction introduce any buoyancy forces. Therefore, the inertial term should be taken into account to assess whether the solutions of the boundary topography problem still possess the singularity for a vanishing small magnetic background field. In a subsequent step, the two-dimensional problem could be studied to analyze whether the use of a two-dimensional topography regularizes the solution in this regard. Additionally, it should also be kept in mind that the non-inertial case was so far analyzed only in a simplified form, which requires that the magnitude of the wave number is sufficiently large. This requirement is violated in the presence of a weak magnetic background field, and the discussed behavior of the average traction may not occur in the general non-inertial magnetic case, which is considered subsequently.

### General non-inertial magnetic case

In the following, the general non-inertial case is considered. Apart from ignoring the inertial term, the results presented in the following do not require any further approximations or omissions. The characteristic equation for the general non-inertial case is a polynomial of degree four with respect to  $k_z$  and yields the following two admissible wave numbers:

$$k_z^{(1)} = \pm \frac{1}{\sqrt{(RmAl^2)^2 + \frac{4\cos^2(\theta)}{Ro^2}}} \sqrt{a + ib + k_x RmAl^2 \sqrt{c + ib}}, \quad (3.69a)$$

$$k_z^{(2)} = \pm \frac{1}{\sqrt{(RmAl^2)^2 + \frac{4\cos^2(\theta)}{Ro^2}}} \sqrt{a + ib - k_x RmAl^2 \sqrt{c + ib}}, \quad (3.69b)$$

where the coefficients  $a$ ,  $b$  and  $c$  are functions of the dimensionless parameters of the problem, *i.e.*,  $\{a, b, c\} = \{\hat{a}, \hat{b}, \hat{c}\}(k_x, Al, Rm, Ro, St, \theta)$ . These functions are given by

$$\hat{a}(k_x, Al, \dots) = -\frac{1}{2}(k_x RmAl^2)^2 - \frac{4\cos^2(\theta)}{Ro^2} k_x^2, \quad (3.70a)$$

$$\hat{b}(k_x, Al, \dots) = k_x Rm \left( \frac{1}{2} Al^2 \frac{St^2}{Ro^2} - \frac{4\cos^2(\theta)}{Ro^2} \right), \quad (3.70b)$$

$$\hat{c}(k_x, Al, \dots) = \frac{4\cos^2(\theta)}{Ro^2} Rm + \frac{1}{4} \left( k_x^2 (RmAl^2)^2 - \frac{St^4}{Ro^4} \right) - Rm^2 Al^2 \frac{St^2}{Ro^2}. \quad (3.70c)$$

The plus-minus sign occurs in both wave numbers in Eq. (3.69) because the imaginary part of both wave numbers changes its sign depending on the values of the dimensionless parameters. This fact needs to be taken into account in order to obtain an admissible wave number. In *Mathematica*, the argument or phase of a square root of a complex number is in the range from  $-\pi$  to  $\pi$  and it is positive if the complex number lies in the upper half of the complex plane and negative otherwise. A wave number is admissible if  $\Im(k_z) < 0$  and therefore the positive square root is an admissible wave number if the phase of the square root lies in

the range from  $-\pi/2$  to zero. Otherwise, the negative square root is admissible, because its phase is in the range from  $-\pi$  to  $-\pi/2$ .

It is clear from Eq. (3.69) that the location of the radicand, *i.e.*, the expression under the square root sign, in the complex plane depends on the values of the coefficients  $a$ ,  $b$  and  $c$ . The coefficient  $a$  is real and negative and the coefficients  $b$  and  $c$  are real but may change their sign depending on the values of the dimensionless parameters. The coefficient  $b$  plays an important role regarding the wave numbers, because it is the only coefficient in Eq. (3.69) which directly introduces an imaginary part. The coefficient  $b$  vanishes if

$$AlSt = 2\sqrt{2} \cos(\theta). \quad (3.71)$$

If the coefficient  $b$  vanishes, the question arises, whether the wave numbers are still complex and hence admissible. The answer depends only on the coefficient  $c$ , because this coefficient can change its sign whereas the coefficient  $a$  cannot. If Eq. (3.71) is solved for one of the dimensionless parameters and if this parameter is substituted in the expression for the coefficient  $c$ , then the coefficient  $c$  is negative for the values of the dimensionless parameters specified in Table 3.4. Thus, the wave numbers in Eq. (3.69) are still complex if  $b = 0$ , because the coefficient  $a$  is negative, the square root of the coefficient  $c$  is imaginary and thus  $a \pm k_x Rm Al^2 \sqrt{c}$  is still complex. This indicates that an admissible wave number can be found for typical values corresponding to the stratified layer at the top of the outer core even though  $b = 0$ . The role of the coefficient  $b$  and the case of  $b = 0$  will be addressed in greater detail when the dependence of the two wave numbers on the dimensionless parameters is analyzed.

For the values of the dimensionless parameters in the “standard case” specified in Table 3.4, the two wave numbers in Eq. (3.69) are given by

$$k_z^{(1)} = -1561.07 - 1561.09i, \quad k_z^{(2)} = 13.33 - 14.73i. \quad (3.72)$$

The first wave number, *i.e.*,  $k_z^{(1)}$ , is almost identical in its magnitude as well as its phase to the wave number which is obtained in the approximated case. Furthermore, the magnitude of the second wave number  $k_z^{(2)}$  is much smaller in comparison to the first and adds a long range component to the solution, which is decaying slowly with depth. Additionally, the phases of the first and second wave number are given by

$$\arg(k_z^{(1)}) = -3\pi/4, \quad \arg(k_z^{(2)}) \approx -\pi/4. \quad (3.73)$$

Thus the difference of the phases of the two wave numbers is given by  $\pi/2$ .

The presence of two wave numbers poses several questions regarding the mutual interaction of the two corresponding pressure perturbations  $\hat{p}_1$  and  $\hat{p}_2$ . These components are multiplied by the coefficients  $\alpha_1$  and  $\alpha_2$ , which are determined from the linear system in Eq. (3.47) and thus both depend on the two wave numbers  $k_z^{(1)}$

and  $k_z^{(2)}$ . In the simplified non-inertial magnetic case, a small wave number led to a large pressure perturbation and a large traction on the boundary topography. However, if two wave numbers are present, this may no longer necessarily be the case for several reasons. *First*, the coefficients  $\alpha_1$  and  $\alpha_2$  depend on both wave numbers and thus a small wave number does not necessarily result in a large coefficient. *Second*, the phases of the perturbations are important for the average traction as well. If, for example, the coefficient  $\alpha_1$  and the amplitude of the pressure perturbation  $\hat{p}_1$  both have a large magnitude, their product  $\alpha_1\hat{p}_1$  may result in a vanishing traction because of its phase.

A direct algebraic analysis of the coefficients  $\alpha_i$  and the amplitudes of the pressure perturbations  $\hat{p}_i$  with respect to their dependencies on the wave numbers is neither feasible nor useful, because the respective expressions are cumbersome. Instead, the dependence of the wave numbers and the average traction are analyzed in the same manner as for the simplified case above. In doing so, similarities and differences between the two cases become apparent. Additionally, the values of the coefficients  $\alpha_i$  and corresponding pressure perturbations  $\alpha_i\hat{p}_i$  will be specified below for the “standard case.”

First, the dependence of the wave numbers on the stratification parameter  $St$ , the dimensionless background velocity  $\bar{V}$  and the ALFVÉN number  $Al$  will be analyzed. The stratification parameter is added to the set of parameters whose dependence is studied, because it occurs in the coefficients  $b$  and  $c$  in a non-linear way. The dependence of the magnitude of the wave numbers  $k_z^{(1)}$  and  $k_z^{(2)}$  on the stratification parameter  $St$  is shown in Fig. 3.7. Regarding the wave number  $k_z^{(1)}$ , two regions can be clearly distinguished. In the first region, where the stratification parameter is small, say,  $St < 0.1$ , the magnitude of  $k_z^{(1)}$  is almost constant and independent of the colatitude  $\theta$ . In the second region, the magnitude of  $k_z^{(1)}$  increases with the stratification parameter and depends on the colatitude. For the case of  $St > 1$ , the slope of the curves in the double-logarithmic diagram is approximately unity, which indicates that the magnitude of  $k_z^{(1)}$  is proportional to the stratification parameter. This proportionality holds also true for the simplified case discussed above. Additionally, the magnitude corresponding to the “standard case” is indicated by a gray filled pentagon, which is located in the second region. The transition between the two aforementioned regions is also evident if the wave number  $k_z^{(2)}$  is considered. The magnitude of  $k_z^{(2)}$  is constant for a large range of values of the stratification parameter and almost independent of the colatitude  $\theta$ . However, its magnitude decreases and subsequently increases in exactly the same region where the first wave number changes its dependence on the stratification parameter. If only the curves for  $\theta = \pi/2$  are considered, which correspond to a vanishing CORIOLIS term, the two regions cannot be identified. This indicates that the presence of the CORIOLIS term is important in this regard.

In Fig. 3.7, four colored triangles are present in each panel. These triangles are located at the positions where the coefficient  $b$  vanishes, *i.e.*, where the stratification parameter has a value of  $St = 2\sqrt{2}\cos(\theta)/Al$ , see Eq. (3.71). The locations of the

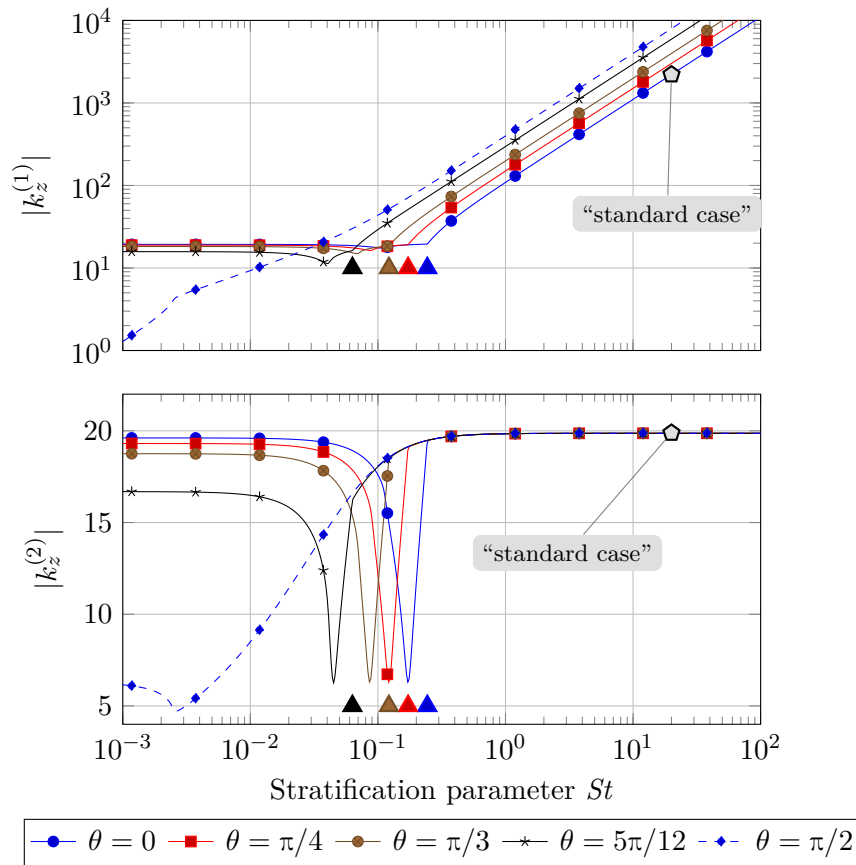


**Figure 3.7:** Dependence of the magnitude of the two wave numbers  $k_z^{(1)}$  and  $k_z^{(2)}$  in Eq. (3.69) on the stratification parameter  $St$  for different values of the colatitude  $\theta$ . The four colored triangles are located at the positions where the coefficient  $b$  vanishes, see Eq. (3.71) on page 95.

four triangles coincide with the individual point where the transition between the two regions occurs. This indicates that the coefficient  $b$  is in part responsible for the occurrence of the two regions. The curves in Fig. 3.7 are characterized by very abrupt changes in the transition regions, which may yield the conclusion that, for example, a kink or a pole might be present. However, in a further detailed inspection of the numerical values it is found that the coefficients  $b$  varies greatly in the vicinity of its zero-crossing. Its value changes by eighteen orders of magnitude if the stratification parameter is varied by a value of  $2 \times 10^{-3}$ . The primary cause of the step gradient of the coefficient  $b$  is the large ROSSBY number. This fact and the algebraic structures in Eqs. (3.69) and (3.70) are responsible for the abrupt but continuous transitions in the curves.

Apart from the magnitudes, the phases of the two wave numbers also experience a similar transition, which occurs for the same values of the stratification parameter.

When  $\theta = 0$ , the phase of the first wave number  $k_z^{(1)}$  changes from a value of approximately  $-\pi/5$  in the first region to  $-3\pi/4$  in the second region and is constant outside of the transition zone. The phase of the second wave number changes from a value of approximately  $-\pi/3$  to  $-\pi/4$  from the first to the second region, respectively, and it is also constant. The large change of the phase of the first wave number is due to the fact that the positive square root in Eq. (3.69) yields an admissible root in the first region whereas the negative square root does in the second region. Finally, it should be pointed out that the two wave numbers have a comparable magnitude and a similar phase in the first region, which is no longer the case in the second region, where the magnitudes as well as the phases are significantly different.

The physical reason for the transition behavior of the wave numbers can be explained by considering Eq. (3.71). This equation relates the buoyancy frequency  $N$  to the local angular velocity  $\Omega$ , the ALFVÉN velocity  $v_{Al}$  and the background fluid velocity  $V_0$  according to

$$N \propto \frac{V_0}{v_{Al}} \Omega, \quad (3.74)$$

where the ALFVÉN velocity is given by  $v_{Al} = B_0/\sqrt{\mu_0\rho_0}$  and  $B_0$  denotes the magnetic background field. If the buoyancy frequency is large, then the forces, which restore vertical perturbations of the fluid from the equilibrium, are large and, as a consequence, the rate at which they decay is large. The fluid flow over the topography causes a vertical velocity perturbation, which induces a perturbation of the magnetic field. Furthermore, the rather large out-of-plane component of the velocity perturbation, which is present due to the CORIOLIS term, additionally induces a perturbation of the magnetic field. The vertical propagation of the velocity perturbations is only hindered by the stratification of the fluid. Regarding the magnetic field, magnetic diffusion is included in the model, which hinders the propagation of a perturbation but, unlike the stratification, does not possess a preferred direction. Thus, if the stratification is rather small, it is not the dominant mechanism that yields a decaying solution with respect to the vertical coordinate; instead, magnetic diffusion dominates. However, if the stratification is sufficiently strong, it becomes dominant and a rapid decay of the solution results. Thus, the two regions discussed can be associated with a weakly and a strongly stratified regime, respectively.

The dependence of the magnitude of the two wave numbers in Eq. (3.69) on the dimensionless background velocity  $\bar{V}$  is shown in Fig. 3.8 for different values of the colatitude  $\theta$ . As in Fig. 3.7, the curves in Fig. 3.8 also show a clear transition between two regions. Here, the transition occurs at a dimensionless background velocity of approximately  $\bar{V} \approx 100$ . Below this value, the magnitude of the first wave number decreases with an increasing value of the dimensionless background velocity. This is also the case for the approximate non-inertial case discussed previously. If the transition between the two regions has occurred, the magnitude of the first wave number increases with an increasing background velocity. The

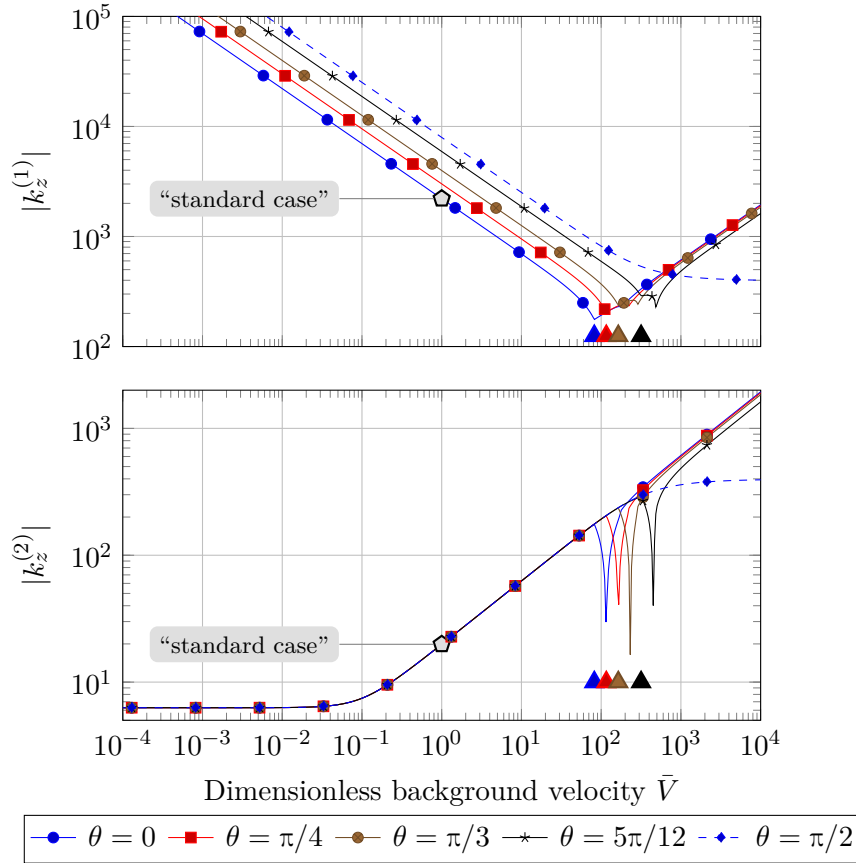


**Figure 3.8:** Dependence of the magnitude of the two wave numbers  $k_z^{(1)}$  and  $k_z^{(2)}$  in Eq. (3.69) on the dimensionless background velocity  $\bar{V}$  for different values of the colatitude  $\theta$ . The four colored triangles are located at the positions where the coefficient  $b$  vanishes, see Eq. (3.71) on page 95.

colored triangles, which indicate the positions where the coefficient  $b$  vanishes for the different values of the colatitude  $\theta$ , are located closely to the transition points. This confirms that the transitions in Fig. 3.8 also correspond to a transition from the strongly to the weakly stratified regime. The strongly stratified regime, which refers to the second region regarding Fig. 3.7, is located on the left of the transition zone and *vice versa* for the weakly stratified regime. This is due to Eq. (3.74), which states that a higher stratification is required, if the background velocity increases. Moreover, as in Fig. 3.7, the magnitudes and the phases of the wave numbers are comparable in the weakly stratified region and do not strongly depend on the colatitude  $\theta$ . In the strongly stratified region, this is not the case, which is also similar to Fig. 3.7.

The analysis of the wave numbers is finalized by considering the dependence of the magnitude of the two wave numbers in Eq. (3.69) on the ALFVÉN number  $Al$ . This dependence is shown in Fig. 3.9 for different values of the colatitude  $\theta$ . A variation

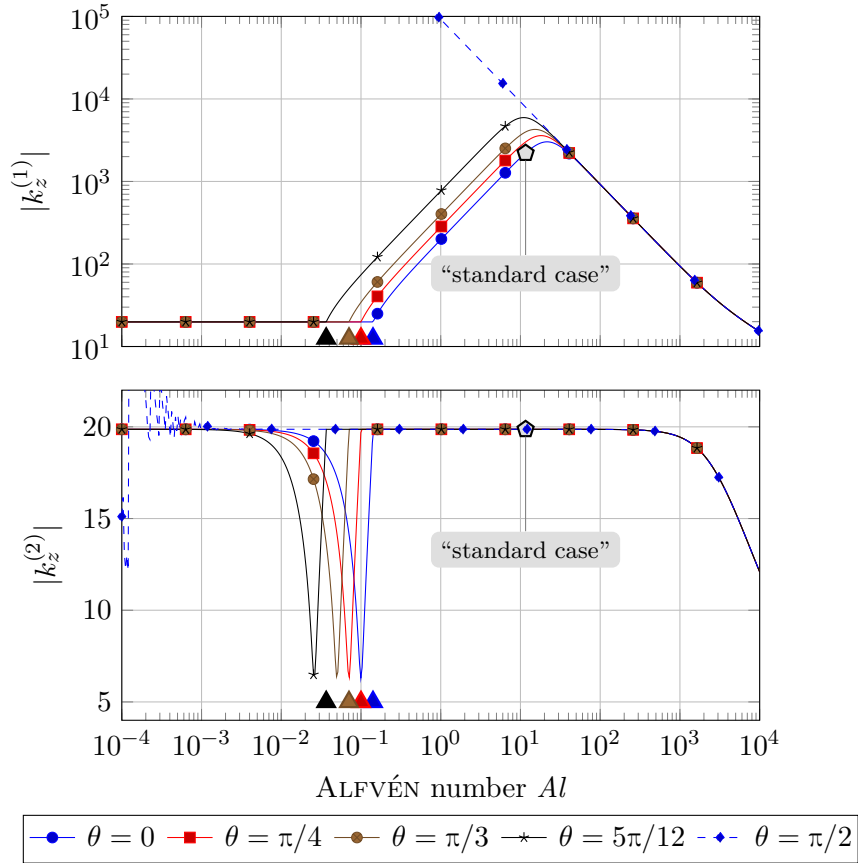


**Figure 3.9:** Dependence of the magnitude of the two wave numbers  $k_z^{(1)}$  and  $k_z^{(2)}$  in Eq. (3.69) on the ALFVÉN number  $Al$  for different values of the colatitude  $\theta$ . The four colored triangles are located at the positions where the coefficient  $b$  vanishes, see Eq. (3.71) on page 95.

of the ALFVÉN number corresponds to a variation of the magnetic background field. It is indicated by the set of curves in Fig. 3.9 that a transition between the weakly and the strongly stratified regime also occurs. This transition takes place at an ALFVÉN number of approximately equal to 0.1. As in Figs. 3.7 and 3.8, four differently colored triangles are located at an ALFVÉN number which is determined according to the condition for a transition in Eq. (3.71). In the strongly stratified regime, which is located to the right of the transition zone, the dependence of the magnitude of the first wave number  $k_z^{(1)}$  is similar to that in the simplified non-inertial case. For  $Al > 0.1$ , the magnitude of the first wave number is first increasing with an increasing value of the ALFVÉN number and then decreasing if the ALFVÉN number assumes values larger than 20. The magnitude decreases for the same reason as outlined for the simplified non-inertial case. Considering the second wave number  $k_z^{(2)}$ , the behavior in the transition zone with a decrease

and subsequent increase of the magnitude is similar to Figs. 3.7 and 3.8. However, for very large values of the ALFVÉN number, the magnitude of the second wave number is no longer constant but decreases slightly. Furthermore, when  $\theta = \pi/2$ , fluctuations occur in the second wave number for very small values of the ALFVÉN number, which are due to a term that is inversely proportional to the ALFVÉN number in the asymptotic case  $Al \rightarrow 0$ . This term makes the numerical evaluation of the related expressions challenging. This suggests that the fluctuations do not represent any additional physical phenomenon.

In order to obtain the pressure perturbations, the coefficients  $\alpha_1$  and  $\alpha_2$  corresponding to the two wave numbers need to be determined from the linear system in Eq. (3.47). Apart from these unknown coefficients, the unknown constant  $\hat{V}_M$  associated to the magnetic scalar potential in the mantle is also present. Thus, there are three unknowns but the linear system in Eq. (3.47) was formulated for the case that three waves exist and consists of four equations. Therefore, one equation needs to be omitted and it is clear that the omitted equation must originate from the transition conditions for the magnetic field, because otherwise the right-hand side of the linear system vanishes. The omitted equation is the continuity constraint on the magnetic field in the out-of-plane direction, *i.e.*, the  $y$ -direction, and a continuity of the magnetic field is enforced with respect to the components of the in-plane directions. As an alternative, the enforcement of a tangential continuity of the magnetic field, *viz.*, a continuity of the  $x$ - and  $y$ -components, was also considered but it was found that the linear system cannot be solved in this case. Therefore, this alternative is disregarded and instead the continuity of the  $x$ - and  $z$ -components of the magnetic field is enforced.

The numerical values of the coefficients  $\alpha_1$  and  $\alpha_2$ , which result from the solution of the linear system described in the previous paragraph, are given by

$$\alpha_1 = -0.47 + 0.47i, \quad \alpha_2 = (-1.82 - 2.33i) \times 10^{-8}. \quad (3.75)$$

Here, the values of the dimensionless parameters are those of the “standard case” specified in Table 3.4. The coefficient  $\alpha_1$  corresponding to the first wave number is much larger than that of the second wave number, which indicates that the pressure perturbation is dominated by the first wave number, at least in the strongly stratified regime. If the stratification parameter is changed to  $St = 0.01$  and all other parameters remain unchanged, this corresponds to the weakly stratified case. Then, the numerical values of the two coefficients are given by

$$\alpha_1 = (-1.831 - 2.366i) \times 10^{-3}, \quad \alpha_2 = (-2.419 - 1.503i) \times 10^{-3}. \quad (3.76)$$

These values suggest that both wave numbers now contribute to the pressure perturbation at the same level. The magnitude of the second coefficient  $\alpha_2$  increased but the magnitude of the first coefficient  $\alpha_1$  also decreased, compared to the strongly stratified case, which indicates that the size of the corresponding perturbations has also decreased. However, in order to judge whether the pressure

perturbations in the weakly stratified regime may really result in an average traction, which is not comparable to the strongly stratified regime, the phases and values of the pressure amplitudes  $\hat{p}_1$  and  $\hat{p}_2$  also need to be considered.

Subsequently, the average traction is considered. For the values of the dimensionless parameters of the “standard case,” the numerical value of the average traction is given by  $\langle \mathbf{t}' \rangle = 7.66 \mathbf{e}_x$ , which is the same as the value obtained in the simplified non-inertial case. This indicates that the first wave number dominates the average traction in the strongly stratified regime. The pressure amplitudes corresponding to the two wave numbers  $k_z^{(1)}$  and  $k_z^{(2)}$  are given by

$$\hat{p}_1 = 1.190 \times 10^{-1} - 1.736 \times 10^4 i, \quad \hat{p}_2 = -1.259 \times 10^2 - 2.155 \times 10^8 i. \quad (3.77)$$

Note that the imaginary parts of both pressure amplitudes are much larger than their respective real parts. Using these values of the pressure amplitudes and the values of the coefficients  $\alpha_1$  and  $\alpha_2$  specified above, the traction components corresponding to the two wave numbers are obtained as

$$\langle \mathbf{t}'_1 \rangle = 7.66 \mathbf{e}_x, \quad \langle \mathbf{t}'_2 \rangle = -3.70 \times 10^{-3} \mathbf{e}_x. \quad (3.78)$$

These values confirm the dominance of the component  $\langle \mathbf{t}_1 \rangle$  which is associated with the first wave number  $k_z^{(1)}$ . In fact, the contribution to the average traction of the second wave number is 0.05%. Although the magnitude of the second pressure amplitude  $\hat{p}_2$  exceeds the magnitude of the first one, *i.e.*,  $\hat{p}_1$ , by several orders of magnitude, this cannot overcome the very small value of the coefficient  $\alpha_2$ . Besides that, due to Eq. (3.55) the traction generated by the second wave number is negative, because the product  $\alpha_2 \hat{p}_2$  has a positive imaginary part.

In the weakly stratified regime, *i.e.*, when  $St = 0.01$ , the average traction is given by  $\langle \mathbf{t}' \rangle = -4.57 \times 10^{-4} \mathbf{e}_x$ , which is four orders of magnitude smaller than the value in the strongly stratified case. In this case, the two pressure amplitudes are given by

$$\hat{p}_1 = (-1.235 - 5.257 i) \times 10^2, \quad \hat{p}_2 = (-1.392 - 4.048 i) \times 10^2. \quad (3.79)$$

These two amplitudes have the same order of magnitude. Additionally, the two corresponding coefficients  $\alpha_1$  and  $\alpha_2$  have a comparable value, which suggests that both wave numbers contribute equally to the average traction. In fact, the contributions of the two components are given by

$$\langle \mathbf{t}'_1 \rangle = -1.18 \times 10^{-3} \mathbf{e}_x, \quad \langle \mathbf{t}'_2 \rangle = 7.26 \times 10^{-4} \mathbf{e}_x. \quad (3.80)$$

The average traction related to the first wave number is negative, whereas that related to the second wave number is positive. This is due to the opposite locations of the products  $\alpha_1 \hat{p}_1$  and  $\alpha_2 \hat{p}_2$  with respect to the real axis in the complex plane. The two components of the average traction have a comparable value. Therefore,

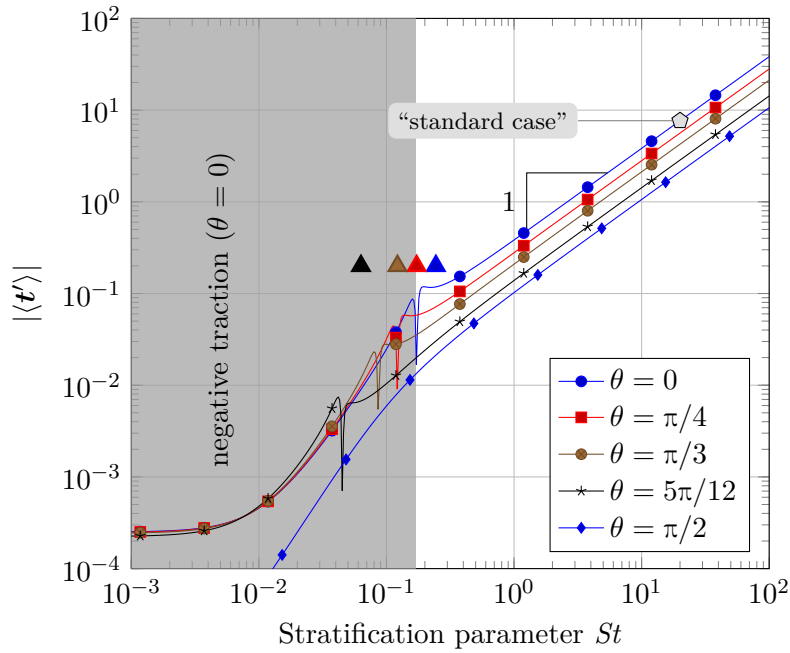


**Figure 3.10:** Dependence of the magnitude of the average traction in the non-inertial case on the stratification parameter  $St$  for different values of the colatitude  $\theta$ . The four colored triangles are located at the positions where the coefficient  $b$  vanishes, see Eq. (3.71) on page 95.

both contributions almost cancel each other and yield rather small values of the average traction, as specified above.

Comparing the weakly and the strongly stratified regime, the dimensional values corresponding to the average tractions are given by  $\langle t' \rangle = 1.10 \times 10^{-7} \text{ N m}^{-2}$  and  $\langle t' \rangle = 0.02 \text{ N m}^{-2}$ , respectively. Thus, the average traction and related torque on the CMB generated in the weakly stratified regime is negligibly small compared to that of the strongly stratified regime. In order to assess whether the average traction in the transition zone might be comparable to that in the strongly stratified regime, the dependence of the average traction on the stratification parameter, the dimensionless background velocity and the ALFVÉN number are subsequently considered.

First, the dependence of the average traction on the stratification parameter is shown in Fig. 3.10. In the strongly stratified regime, *i.e.*, for  $St > 0.2$ , the average traction is linearly proportional to the stratification parameter  $St$ , because the slope of the curves in the doubly logarithmic chart is unity in this region. If the transition to the weakly stratified regime occurs, the average traction decreases in magnitude but also becomes negative. When  $\theta = 0$ , the region where the average traction is negative is indicated by a gray shading in Fig. 3.10. The large decrease and subsequent increase of the magnitude in the transition zone is due to the zero

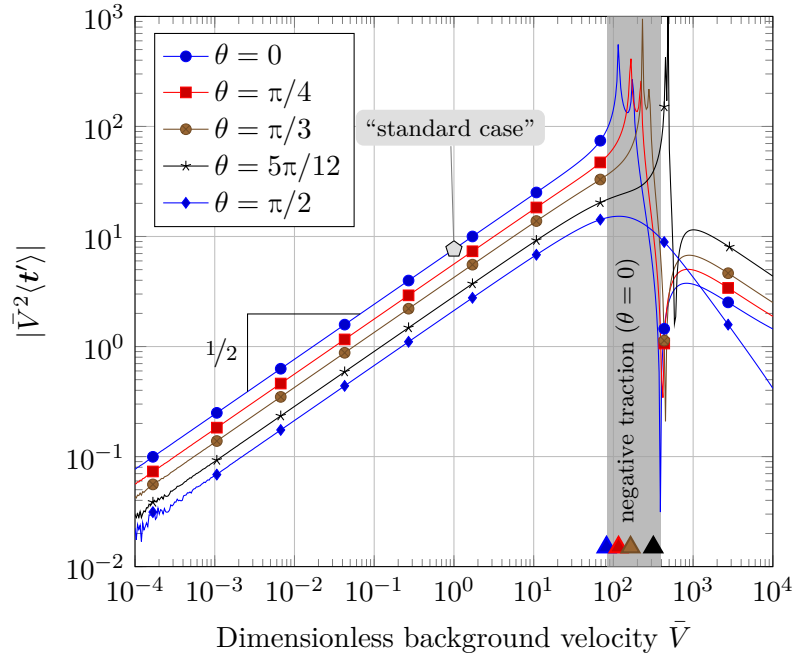


**Figure 3.11:** Dependence of the magnitude of the average traction in the non-inertial case on the dimensionless background velocity  $\bar{V}$  for different values of the colatitude  $\theta$ . The four colored triangles are located at the positions where the coefficient  $b$  vanishes, see Eq. (3.71) on page 95.

crossing from negative to positive values of the average traction. For the curves corresponding to other colatitudes, the location of the region of a negative traction can be inferred from the location of the rapid decrease and subsequent increase of the respective curve. For very low values of the stratification parameter  $St$ , the average traction is constant in magnitude. However, its value is more than four orders of magnitude less than that of the “standard case,” which is indicated by a gray filled pentagon. Furthermore, the dependence on the CORIOLIS term is only present in the strongly stratified regime, because there the curves corresponding to different values of the colatitude can be distinguished well.

The dependence of the average traction on the dimensionless background velocity  $\bar{V}$  is shown in Fig. 3.11. In the discussion of the simplified non-inertial case it was pointed out that the average traction needs to be rescaled, if the dependence of the average traction is considered. Therefore, the magnitude of the rescaled traction  $\bar{V}^2\langle t' \rangle$  is shown in Fig. 3.11. Its curves basically show the same behavior regarding the transition from the weakly to the strongly stratified regime as those in Fig. 3.10. However, in Fig. 3.11 the strongly stratified regime is located left of the transition zone. In this region, the average traction is proportional to the square root of the dimensionless background velocity, because the slope of the curves in the doubly logarithmic chart is given by  $1/2$ . This proportionality was also found when

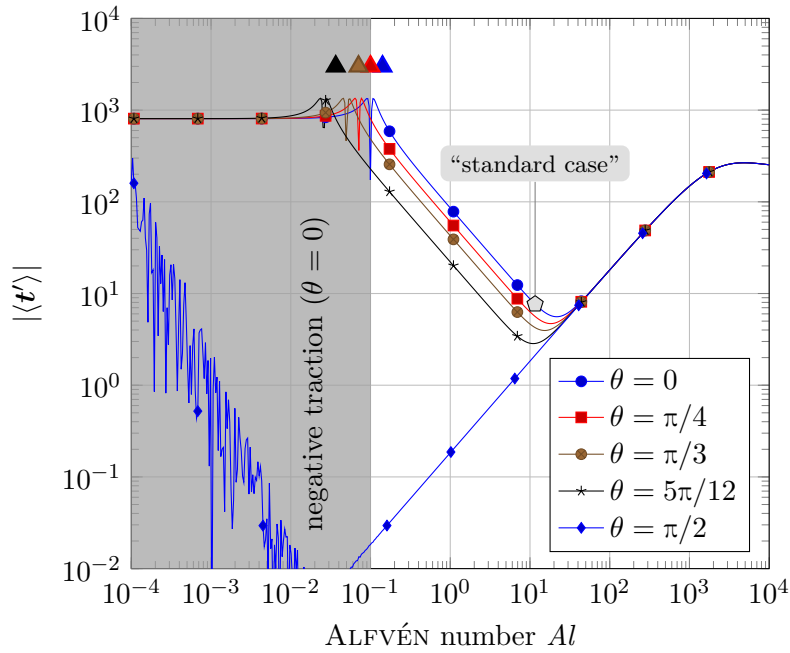


**Figure 3.12:** Dependence of the magnitude of the average traction in the non-inertial case on the ALFVÉN number  $Al$  for different values of the colatitude  $\theta$ . The four colored triangles are located at the positions where the coefficient  $b$  vanishes, see Eq. (3.71) on page 95.

the simplified non-inertial case was analyzed and thus both cases are very similar in this regime. As in Fig. 3.10, the gray shaded rectangle in Fig. 3.11 indicates the region where the traction becomes negative for  $\theta = 0$ . This rectangle is also located in the transition zone. However, here a zero crossing at the beginning of the region, where the average traction is negative, cannot be observed, which is probably due to a limited sampling of the curves in Fig. 3.11. Past the transition zones and for very large values of the dimensionless velocity, the average traction becomes positive but the slope of the curve is negative.

The analysis of the average traction is completed by considering its dependence on the ALFVÉN number  $Al$ , which is shown in Fig. 3.12. In this figure, the strongly stratified region is located to the right of the transition zone, *viz.*,  $Al > 0.1$ . In this region, the dependence of the average traction on the ALFVÉN number closely resembles that of the simplified non-inertial case in Fig. 3.6. Nevertheless, following the similar decrease and subsequent increase, if the ALFVÉN number varies from 0.1 to 10, a decline of the increase is observed in the general non-inertial case. Comparing Figs. 3.10 and 3.12 with respect to the transition zone and the behavior of the average traction, two major differences are apparent. *First*, the transition from the strongly to the weakly stratified regime yields an increase of the magnitude of the average traction rather than a decrease, whereas it is *vice versa* in Figs. 3.10 and 3.11. *Second*, for a vanishing rotation, which corresponds to a value of the

colatitude of  $\theta = \pi/2$ , strong fluctuations are present in the magnitude of the average traction if the value of the ALFVÉN number is less than  $2 \times 10^{-2}$ . These fluctuations are due to the inverse proportionality of the second wave number on the ALFVÉN number in the asymptotic limit of  $Al \rightarrow 0$ . This seems to challenge the numerical evaluation of the symbolic expressions in *Mathematica*.

The reason for the occurrence of a negative traction is that the phase as well as the magnitude of both wave numbers becomes very similar. As a consequence, the coefficient  $\alpha_1$  and the corresponding amplitude  $\hat{p}_1$  both become very small compared to  $\alpha_2$  and  $\hat{p}_2$  as the value of the ALFVÉN number is decreased. Thus, the pressure perturbation corresponding to the second wave number dominates the average traction, which is negative. Although the average traction  $\langle \mathbf{t}'_1 \rangle$ , which is associated with the first wave number, is positive, it cannot balance the negative component of the average traction associated to the second wave number. Thus, the total average traction is negative. Furthermore, it should be remarked that the average traction is bounded if the ALFVÉN number vanishes. This was not the case when the simplified non-inertial problem was considered. However, in the simplified non-inertial case, the traction was positive regardless of the value of the ALFVÉN number. Besides that, the limit of  $Al \rightarrow 0$  and a non-vanishing velocity is critical regarding the out-of-plane component of the velocity perturbation. The  $y$ -component is inversely proportional to  $k_z Rm Al^2 Ro$ . The ROSSBY number  $Ro$  is already very small in the “standard case” and yields a large out-of-plane component. If the ALFVÉN number becomes small, the magnitudes of both wave numbers do not increase but remain constant instead. Thus the inverse proportionality with respect to  $Al^2$  is contributing to an even smaller denominator and, as a consequence, the out-of-plane velocity becomes even larger. This large fluid flow in the out-of-plane direction in turn induces a significant magnetic field. This is somehow controversial because a small ALFVÉN number corresponds to a weak magnetic background field and hence magnetic effects should not be of a great relevance. As discussed previously regarding the simplified non-inertial case, this controversial aspect could be removed if either the inertial term is included in the problem or a two-dimensional topography is considered.

### 3.3.3 Unstratified magnetic case

A further case, which was analyzed, is the situation with a vanishing stratification. The case is obtained by letting  $St \rightarrow 0$ . Two or three admissible wave numbers are found if the inertial term is either neglected or taken into account. However, the magnitudes of these wave numbers are rather small compared to the stratified cases. Although these magnitudes are increased if the dimensionless background velocity is increased, the resulting average tractions are negligibly small. For example, if the values of the dimensionless parameters are those of the “standard case” specified in Table 3.4, the average traction is given by  $\langle \mathbf{t} \rangle = 1.82 \times 10^{-6} \mathbf{e}_x$ . If the dimensionless background velocity and the ALFVÉN number vary, the value of the average traction does not change significantly. Most importantly, it does

not reach the order of magnitude which is found for the cases when stratification is present. Thus, the presence of stratification is essential for the generation of a large average traction on the boundary topography. As a consequence, the analysis of the unstratified magnetic case is deliberately not investigated any further.

### 3.3.4 Inertial magnetic case

In the following, the inertial magnetic case is considered. This case does not entail any simplifications or approximations and contains all possible physical effects of the model described in Sect. 3.2, for which the switch  $\chi$  was introduced to either neglect or incorporate the inertial term. Therefore, the inertial magnetic case is obtained by setting the switch  $\chi$  to unity, *i.e.*,  $\chi = 1$ . As a consequence, the algebraic structure of the problem is such that the symbolic expressions of the wave numbers become excessively large. A direct analysis or discussion of the expression is neither feasible nor useful because of their algebraic complexity. Therefore, the dependence of the wave numbers and the average traction is analyzed as in the previous sections. In addition to the analysis of these dependences, the resulting fields of the perturbations of the density, pressure, velocity and magnetic field will be presented and briefly discussed at the end of this section.

The discussion of the inertial magnetic case starts with a consideration of the wave numbers and their dependences. As outlined in Sect. 3.2, the characteristic equation of the problem is a third order polynomial with respect to  $k_z^2$  and thus three admissible wave numbers are found. Regarding the “standard case” specified in Table 3.4, the numerical values of these three wave numbers are given by

$$k_z^{(1)} = -1560.58 - 1561.58 i \quad k_z^{(2)} = 13.32 - 14.73 i, \quad k_z^{(3)} = 0.54 - 0.02 i.$$

Comparing these numerical values with those obtained in the non-inertial magnetic case shows that the first two wave numbers  $k_z^{(1)}$  and  $k_z^{(2)}$  are the same in both cases. The magnitude of the third wave number is three orders of magnitude smaller than that of the second wave number. Thus, the three wave numbers can be clearly distinguished with respect to their spatial contributions to the solution. The first wave number corresponds to a short-range component of the solution and decays fast. The second and third wave numbers correspond to long-range components, whereas the component corresponding to the third wave number decays the slowest. Subsequently, the dependence of the magnitude of these three wave numbers on the stratification parameter, the dimensionless background velocity and the ALFVÉN number is analyzed as before.

The dependence on the stratification parameter  $St$ , which is shown in Fig. 3.13, will be discussed first. In the three panels in Fig. 3.13, the magnitudes of the three wave numbers corresponding to the “standard case,” which are specified above, are indicated by a gray filled pentagon. Furthermore, the four differently colored triangles indicate the transition points from the weakly to the strongly stratified region according to Eq. (3.71). In general, the dependence of the wave

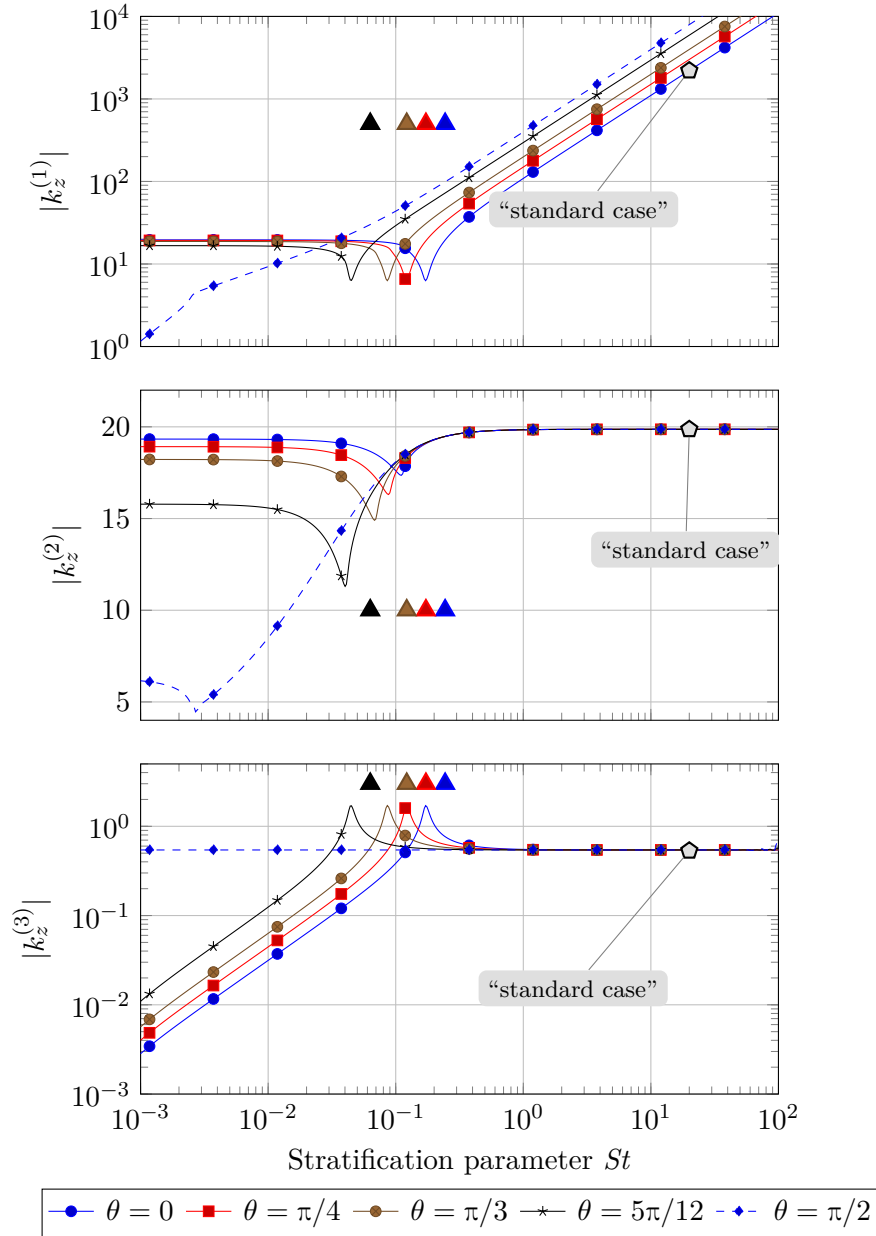


**Figure 3.13:** Dependence of the magnitude of the three wave numbers  $k_z^{(1)}$ ,  $k_z^{(2)}$  and  $k_z^{(3)}$  in the inertial magnetic case on the stratification parameter  $St$  for different values of the colatitude  $\theta$ . The four colored triangles are located at the positions where the coefficient  $b$  vanishes, see Eq. (3.71) on page 95.

numbers  $k_z^{(1)}$  and  $k_z^{(2)}$  is analogous to the non-inertial magnetic case discussed in Sect. 3.3.2, see also Fig. 3.7. The transition region is located in the vicinity of the differently colored triangles and the strongly stratified regime lies to the

right of this region. In the strongly stratified region, the magnitude of the first wave number  $k_z^{(1)}$ , which is shown in the top panel of Fig. 3.13, increases with an increasing value of the stratification parameter and depends on the value of the colatitude  $\theta$ . In the weakly stratified region, the magnitude of the first wave number  $k_z^{(1)}$  is constant and almost independent of the value of the colatitude  $\theta$ . The case of a vanishing rotation, *i.e.*,  $\theta = \pi/2$ , represents an exception in this regard because of its dependence in the weakly stratified region. Considering the second wave number  $k_z^{(2)}$ , the magnitude of the curves in the middle panel of Fig. 3.13 decreases and increases subsequently at the transition from the weakly to the stratified region. The magnitude is independent of the value of the colatitude in the strongly stratified regime. Furthermore, it is constant outside of the transition zone. However, as for the first wave number, the case of a vanishing rotation represents an exception in the weakly stratified region. The only difference between the inertial and the non-inertial case, which is recognizable to the eye, is that the transition is much smoother in the inertial than in the non-inertial case. While there were sharp kinks in the magnitude of the first wave number and almost a jump in the magnitude of the second wave number in the non-inertial case, these features are not present in the inertial case.

The magnitude of the additional third wave number  $k_z^{(3)}$  is shown in the bottom panel of Fig. 3.13. It also shows the same transition behavior as the other two wave numbers, which occur simultaneously. In the weakly stratified regime, the magnitude of the third wave number increases with an increasing value of the stratification parameter with the exception of the case of a vanishing rotation. In the strongly stratified region, it is constant. While a dependence of the magnitude of the third wave number on the value of the colatitude is visible in the weakly stratified region, this is not the case in the strongly stratified region.

In summary, the first and the second wave number show exactly the same qualitative dependence as in the non-inertial case discussed in Sect. 3.3.2, see Figs. 3.7, 3.8 and 3.9. Likewise, the third wave number also experiences a transition. Additionally, the transition from the weakly to the strongly stratified regime occurs for a value of the stratification parameter which is close to that obtained from Eq. (3.71) for all three wave numbers. In conclusion, these facts support the idea that the distinction of a weakly and a strongly stratified regime also transfers to the inertial case. In fact, the dependencies of the wave numbers on two other parameters pertinent to the problem, which will be presented subsequently, support this idea.

The dependence of the magnitude of the wave numbers on the dimensionless background velocity  $\bar{V}$  is shown in Fig. 3.14. In this figure, a transition is clearly visible in the curves of all wave numbers and this transition is also located in the vicinity of the four differently colored triangles. These are located at a velocity for which the transition according to Eq. (3.71) should occur. In contrast to Fig. 3.13, the strongly stratified region is located to the left of the respective triangle whereas the weakly stratified region is located to the right. The magnitude of the first

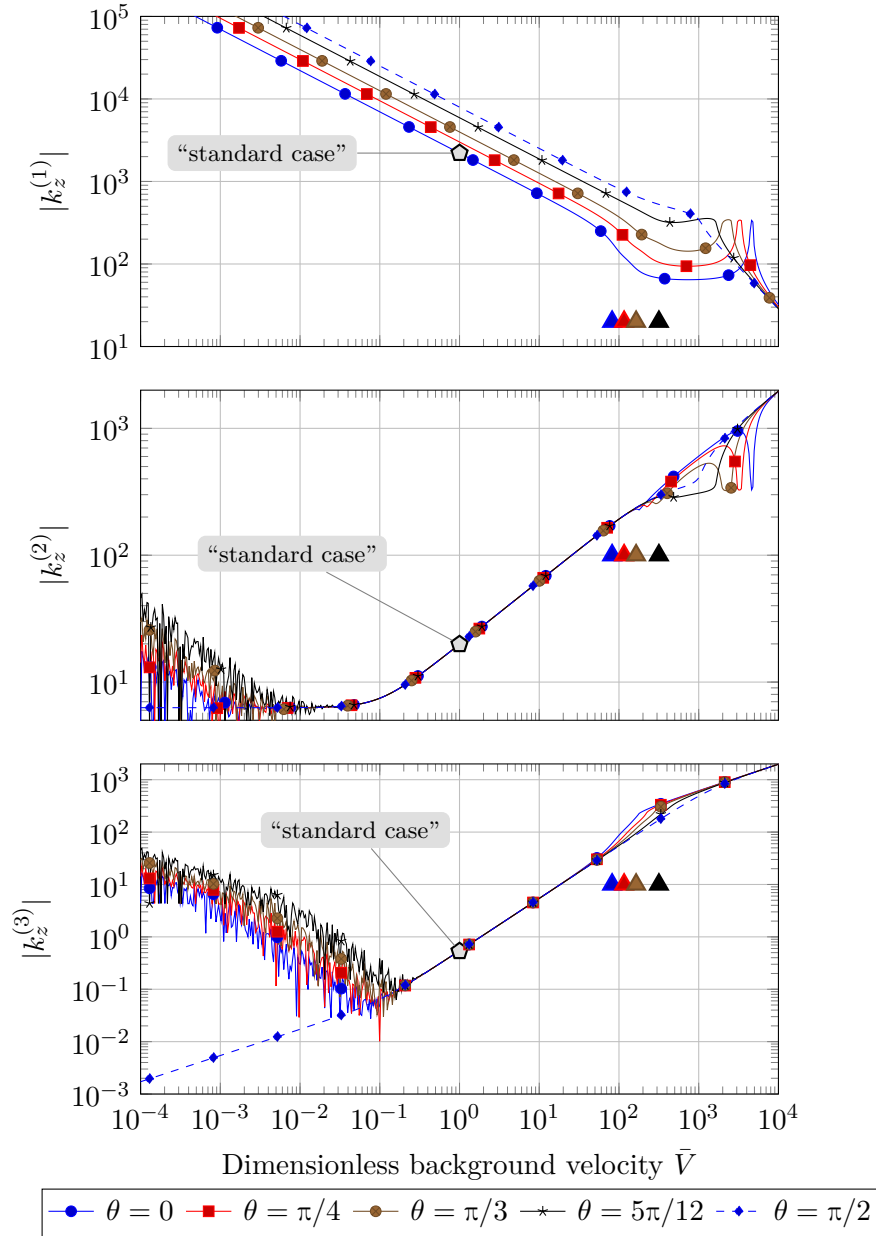


**Figure 3.14:** Dependence of the magnitude of the three wave numbers in the inertial magnetic case on the dimensionless background velocity  $\bar{V}$  for different values of the colatitude  $\theta$ . The four colored triangles are located at the positions where the coefficient  $b$  vanishes, see Eq. (3.71) on page 95.

wave number  $k_z^{(1)}$  is shown in the top panel of Fig. 3.14. In the strongly stratified region, which is ranging from  $\bar{V} = 10^{-4}$  to  $\bar{V} \approx 10^2$ , the magnitude of the first wave number decreases if the dimensionless background velocity increases. Moreover,

the magnitude of the first wave number depends on the colatitude  $\theta$  in this region. The decrease of the magnitude of the first wave number stops in the transition zone, where the magnitude is not changing significantly. Then, the magnitude increases slightly and is subsequently decreasing again. Comparing Fig. 3.14 with Fig. 3.8 in relation to the first wave number shows that there are distinct similarities in the strongly stratified region but significant differences in the weakly stratified region. In the non-inertial case shown in Fig. 3.8, an increase of the magnitudes of the wave numbers can be observed for a dimensionless background velocity of  $\bar{V} > 10^3$ . This is no longer the case in the inertial magnetic case shown in Fig. 3.14.

The dependence of the second wave number  $k_z^{(2)}$  is shown in the middle panel in Fig. 3.14. Considering the second wave number in the weakly stratified region, *i.e.*, in the case of values of the dimensionless background velocity of  $\bar{V} > 10^3$ , a decrease and subsequent increase of the magnitude is visible. Although this feature interrupts the increase of the magnitude in the region ranging from  $\bar{V} \approx 10^{-1}$  to  $\bar{V} \approx 10^2$ , there is a clear tendency that the magnitude returns to this trend if the dimensionless background velocity is further increased. Comparing Fig. 3.14 with Fig. 3.8 in relation to the second wave number for a dimensionless background velocity ranging from  $\bar{V} \approx 10^{-1}$  to  $\bar{V} \approx 10^4$ , there is a good agreement of the two cases if the transition zone is not considered. However, for very small dimensionless background velocities of, say,  $\bar{V} < 10^{-1}$ , large fluctuations are present in the magnitude of the second wave number in the inertial case in Fig. 3.14. These fluctuations do not occur in the non-inertial case where the magnitudes of all wave numbers are smooth and continuous. The fact that the fluctuations become stronger if the dimensionless background velocity decreases suggests that the fluctuations are due to limitations with respect to the numerical evaluation of the expressions and the machine precision. For example, for a dimensionless background velocity of  $\bar{V} = 10^{-2}$ , the ROSSBY number is given by  $Ro = 6.9 \times 10^{-7}$  and thus, for example, factors like  $St^4/Ro^4$ , which occur in Eq. (3.70), can easily exceed the machine precision. Nevertheless, the second wave number has the tendency to become constant before the fluctuations dominate. This tendency is similar to the dependence of the magnitude in the non-inertial case, see Fig. 3.8.

The dependence of the magnitude of the third wave number  $k_z^{(3)}$  is shown in the bottom panel of Fig. 3.14. It also experiences the same fluctuations as the second wave number. These fluctuations end at a dimensionless background velocity of  $\bar{V} \approx 2 \times 10^{-1}$ , which is an order of magnitude larger than the corresponding value of the second wave number. Apart from the fluctuations, the magnitude of the third wave number is a smooth function of the dimensionless background velocity. Hence, likewise to the second wave number, the fluctuations are also a consequence of the numerical evaluation. A transition zone is also visible if the third wave number is considered. However, this transition zone does not result in a variation of the magnitude which is comparable to that of the first and the second wave number. In general, outside of the region, where the fluctuations occur, the magnitude of the third wave number increases along with the dimensionless background velocity.

Although the validity of the results inside of the region, where the fluctuations occur, is questionable, the trend of an increasing magnitude with a decreasing dimensionless background velocity is visible.

In conclusion, the inertial term has a significant influence on the dependence of all three wave numbers on the dimensionless background velocity. The concept of a weakly and strongly stratified regime also applies in the inertial magnetic case. In the transition zone, a significant change of the dependence of the first wave number compared to the non-inertial case is found. The second and third wave numbers are not influenced by the transition as much as the first one, but they experience tremendous numerical fluctuations if the dimensionless background velocity becomes small. It is not possible to judge exactly why these fluctuations occur, but they are definitely associated to the incorporation of the inertial term. While the differences of the dependence on the stratification parameter  $St$  are marginal between the inertial and the non-inertial case, there are considerable differences if the dependence on the dimensionless background velocity is considered. This matches the expectations, because the incorporation of the inertial term yields a larger impact of the velocity.

In the following, the dependence of the magnitude of the three wave numbers on the ALFVÉN number  $Al$  is considered. The magnitude of the first wave number  $k_z^{(1)}$  is shown in the top panel of Fig. 3.15. This magnitude is constant for low values of the ALFVÉN number and experiences the transition from the weakly to the strongly stratified region at an ALFVÉN number of approximately 0.2. After the transition, it increases with an increasing value of the ALFVÉN number. Then the magnitude reaches a maximum at an ALFVÉN number of approximately 20 and subsequently decreases again. For a vanishing rotation, *i.e.*,  $\theta = 0$ , the magnitude has a different dependence for  $Al < 20$  but complies with the other curves if  $Al > 20$  holds. Comparing the characteristics of the first wave number in Fig. 3.15 with those of the non-inertial case in Fig. 3.9 shows that there is a good agreement between the two cases. The most prominent difference is that the transition from the weakly to the strongly stratified region is much smoother in the inertial than in the non-inertial case. Moreover, the transition occurs at an ALFVÉN number which is independent of the colatitude in the inertial case. Additionally, the ALFVÉN number at which the transition occurs is larger than values suggested by the condition in Eq. (3.71), which are indicated in Fig. 3.15 by differently colored triangles. Besides these differences related to the transition, the magnitude of the first wave number depends on the colatitude in the weakly stratified region, which is not the case in Fig. 3.9.

If the magnitude of the second wave number  $k_z^{(2)}$  in middle panel of Fig. 3.15 is considered, it is obvious that it is constant and independent for a large range of values of the ALFVÉN number. Only for very large values of the ALFVÉN number a decrease of the magnitude occurs. Additionally, a transition of the second wave number does not occur and a dependence on the colatitude is not present. If the curves related to the second wave number in Fig. 3.15 are compared with those of

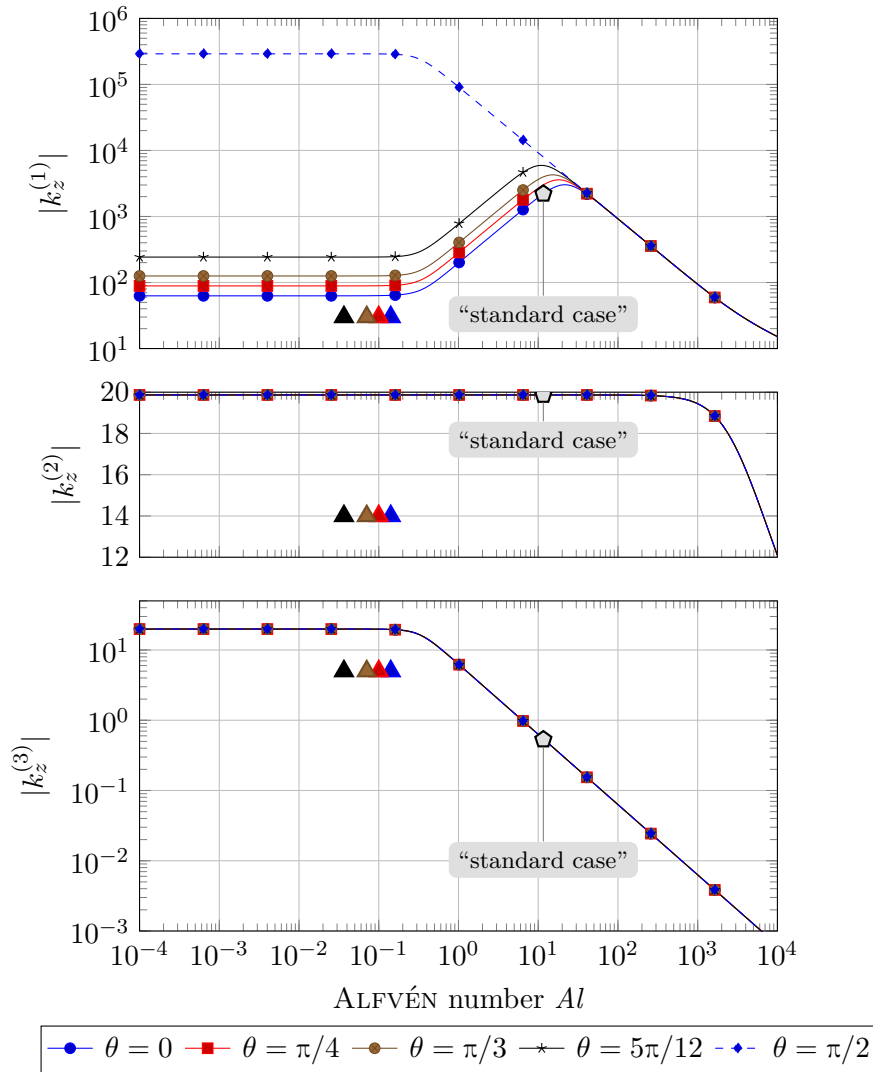


**Figure 3.15:** Dependence of the magnitude of the three wave numbers in the inertial magnetic case on the ALFVÉN number  $Al$  for different values of the colatitude  $\theta$ . The four colored triangles are located at the positions where the coefficient  $b$  vanishes, see Eq. (3.71) on page 95.

the non-inertial case in Fig. 3.9, the major difference is that a transition zone does not occur in the inertial case.

The magnitude of the third wave number  $k_z^{(3)}$  is shown in the bottom panel of Fig. 3.15 and is constant if the ALFVÉN number is smaller than 0.2. If the ALFVÉN number becomes larger than 0.2, the magnitude decreases with an increasing value of the ALFVÉN number and is independent of the colatitude.

In summary, the introduction of the inertial term has changed the dependence of the wave numbers  $k_z^{(1)}$  and  $k_z^{(2)}$  on the ALFVÉN number. The transition of the first

wave number  $k_z^{(1)}$  is much smoother in the non-inertial case and a transition of the second wave number  $k_z^{(2)}$  does no longer occur. However, the incorporation of the inertial term did not change the overall dependence of the wave numbers as much as when the dependence on the dimensionless background velocity is considered.

The analysis of the inertial case is continued by considering the average traction and its dependence on the stratification parameter, the dimensionless background velocity and the ALFVÉN number. Before the dependences are considered, the numerical value of the average traction is discussed for the values of the dimensionless parameters of the “standard case” specified in Table 3.4. In this case, the average traction is given by  $\langle \mathbf{t}' \rangle = 11.08 \mathbf{e}_x$ , which is considerably larger than the value obtained in the non-inertial case. After a rescaling of this result with the pressure scale factor  $\rho_0 V_0^2$ , a dimensional value of  $0.028 \text{ N m}^{-2}$  is obtained. The average traction is a linear superposition of three components  $\langle \mathbf{t}'_1 \rangle$ ,  $\langle \mathbf{t}'_2 \rangle$  and  $\langle \mathbf{t}'_3 \rangle$ , which are associated to the three different wave numbers. These three components of the average traction are given by

$$\langle \mathbf{t}'_1 \rangle = 7.661 \mathbf{e}_x, \quad \langle \mathbf{t}'_2 \rangle = -0.004 \mathbf{e}_x, \quad \langle \mathbf{t}'_3 \rangle = 3.423 \mathbf{e}_x. \quad (3.81)$$

These values show that the contributions of the first and the second wave numbers have not changed significantly compared to the non-inertial case. In fact, the sum of  $\langle \mathbf{t}'_1 \rangle$  and  $\langle \mathbf{t}'_2 \rangle$  results exactly in the value of the average traction obtained in the non-inertial case, see Eq. (3.78) on page 102. The component associated to the third wave number, which is present due to the incorporation of the inertial term, contributes approximately 30% of the average traction. The reason for the unexpectedly large contribution of the third wave number becomes clear if the numerical values of the related coefficient  $\alpha_3$  and pressure amplitude  $\hat{p}_3$  are specified

$$\alpha_3 = (38.475 + 1.234 \text{ i}) \times 10^{-8}, \quad \hat{p}_3 = (-28.532 - 2.891 \text{ i}) \times 10^{10}.$$

Although the coefficient  $\alpha_3$  and thus the relative contribution of the third wave number to the total perturbation is very small, the magnitude of the pressure amplitude  $\hat{p}_3$  is very large. This large pressure amplitude overcomes the smallness of the coefficient and yields a considerable pressure perturbation. Recall from the discussion of the non-inertial case that a large pressure amplitude and a small coefficient also occurs for the second wave number and does not result in a significant contribution to the average traction. However, the situation is different for the third wave number, because the phase  $\alpha_3 \hat{p}_3$  is such that the relative difference to the phase of the topography yields a significant average traction.

The analysis of the traction above considered the strongly stratified regime with a stratification parameter of  $St = 20$ . Subsequently, the average traction is analyzed in the weakly stratified regime, *i.e.*, for a stratification parameter of  $St = 10^{-2}$ . In this case, the average traction is given by  $\langle \mathbf{t}' \rangle = 3.32 \times 10^{-5} \mathbf{e}_x$ , which is comparable to the non-inertial case. The associated dimensional value of

the average traction is given by  $8.30 \times 10^{-8} \text{ N m}^{-2}$ . The contributions of the three different wave numbers to the average traction is given by:

$$\langle \mathbf{t}'_1 \rangle = 3.522 \times 10^{-6} \mathbf{e}_x, \quad \langle \mathbf{t}'_2 \rangle = -2.164 \times 10^{-6} \mathbf{e}_x, \quad \langle \mathbf{t}'_3 \rangle = 3.186 \times 10^{-5} \mathbf{e}_x.$$

The average traction associated to the first two wave numbers is an order of magnitude smaller than that associated to the third wave number. Comparing these values to those of the non-inertial case shows that the average tractions  $\langle \mathbf{t}'_1 \rangle$  and  $\langle \mathbf{t}'_2 \rangle$  still possess an opposite sign and comparable values, but they do no longer dominate the average traction. While the values of the pressure amplitudes  $\hat{p}_1$  and  $\hat{p}_2$  are comparable to those of the non-inertial case, the associated coefficients  $\alpha_1$  and  $\alpha_2$  are three orders of magnitude smaller than in the non-inertial case, but comparable to the value of the coefficient  $\alpha_3$ . The values of the coefficient  $\alpha_3$  and the corresponding pressure amplitude  $\hat{p}_3$  are given by

$$\alpha_3 = (-9.463 - 4.753 \times 10^{-3} \text{ i}) \times 10^{-6}, \quad \hat{p}_3 = (2.136 \times 10^4 - 7.158 \text{ i}) \times 10^3.$$

Note that the real parts of  $\alpha_3$  and  $\hat{p}_3$  are much larger than their respective imaginary parts. Although the product  $\alpha_3 \hat{p}$  has a magnitude which is substantially larger, its imaginary part is very small such that it can be regarded as a real number. Therefore, the phase shift of the associated pressure perturbation relative to the boundary topography becomes small and, as a consequence, the average traction becomes very small as well. Nevertheless, it is still positive, which is also the case if the non-inertial problem is considered.

In the following, the dependence of the average traction on the stratification parameter, the dimensionless background velocity and the ALFVÉN number is analyzed. First, the dependence on the stratification parameter  $St$  is considered, which is shown in Fig. 3.16 for different values of the colatitude. With an exception in the transition zone, the average traction is increasing with an increasing value of the stratification parameter. In the weakly stratified region, the average traction is several orders of magnitude smaller than in the strongly stratified region, but the increase is large. In the strongly stratified region, on the other hand, the average traction is comparably larger, but the increase is relatively small. If the stratification parameter  $St$  becomes larger than 10, fluctuations of the average traction occur. These fluctuations begin at a smaller value of the stratification parameter, the smaller the colatitude  $\theta$  is. Note that no fluctuations are present in the non-rotating case, *i.e.*, for  $\theta = \pi/2$ . The traction is a smooth function of the stratification parameter over a wide range of values and the dependence of the wave numbers on the stratification parameter shown in Fig. 3.13 neither possesses any fluctuations. Therefore, it is likely that the fluctuations are due to problems with the numerical evaluation of the symbolic expressions, which result for the coefficients  $\alpha_i$  and the corresponding pressure amplitudes  $\hat{p}_i$ . Moreover, in the non-inertial case the average traction is proportional to the stratification parameter  $St$  in the region where the fluctuations occur. This suggest that the

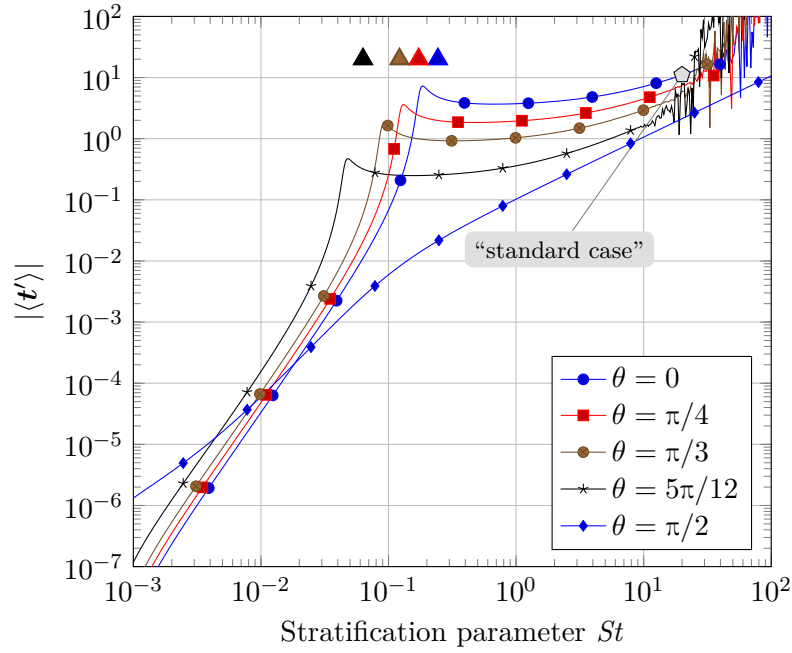


**Figure 3.16:** Dependence of the magnitude of the average traction in the inertial magnetic case on the stratification parameter  $St$  for different values of the colatitude  $\theta$ . The four colored triangles are located at the positions where the coefficient  $b$  vanishes, see Eq. (3.71) on page 95.

problems with the numerical evaluation of the symbolic expressions are related to the incorporation of the inertial term and the presence of the third wave number.

In order to analyze the reasons for the fluctuations, Figure 3.17 is considered in the following. This figure shows the dependence of the components of the average traction  $\langle t'_i \rangle$ , which are associated to the three wave numbers, on the stratification parameter  $St$  for a colatitude of  $\theta = 0$ . The curves in Fig. 3.17 show that the component  $\langle t'_1 \rangle$  associated to the wave number  $k_z^{(1)}$  does not exhibit any fluctuations. Likewise to the non-inertial case, it is proportional to the stratification parameter, *i.e.*,  $\langle t'_1 \rangle \propto St$ , if the stratification parameter is large. The components  $\langle t'_2 \rangle$  and  $\langle t'_3 \rangle$ , which correspond to the wave numbers  $k_z^{(2)}$  and  $k_z^{(3)}$ , respectively, experience the aforementioned fluctuations if the stratification parameter becomes large. Before the fluctuations occur, both components are constant and the corresponding wave numbers are constant as well, see Fig. 3.13. This suggests that the two components  $\langle t'_2 \rangle$  and  $\langle t'_3 \rangle$  would also remain constant if a reliable numerical evaluation of the related symbolic expressions would be possible for very large values of the stratification parameter.

In summary, the average traction can be reliably evaluated if the stratification parameter is less than 10 for all considered values of the colatitude. If the stratification parameter exceeds this values, the problems with the numerical evaluations

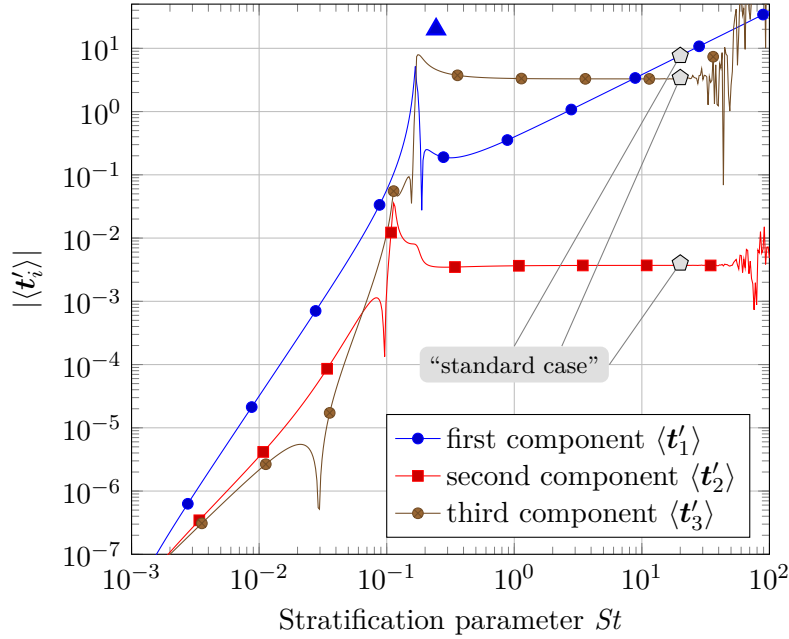


**Figure 3.17:** Dependence of the magnitude of the components of the average traction on the stratification parameter  $St$  for the colatitude  $\theta = 0$ . The blue colored triangle is located at the position where the coefficient  $b$  vanishes for  $\theta = 0$ , see Eq. (3.71) on page 95.

prevent a reliable computation of the average traction, because fluctuations occur in the components of the average traction, which are related to the second and third wave number. However, the analysis of the components in Fig. 3.17 suggests that the average traction is dominated by the component associated with the first wave number and that the other components remain constant. This allows to also compute a meaningful value of the average traction if the stratification parameter becomes large.

Next, the dependence of the average traction on the dimensionless background velocity  $\bar{V}$ , which is shown in Fig. 3.18, is discussed. As in Sect. 3.3.2, the rescaled average traction  $\bar{V}^2 \langle \mathbf{t}' \rangle$  is shown in Fig. 3.18, because otherwise misleading results are obtained regarding the dependence on the dimensionless background velocity  $\bar{V}$ . Although the average traction was computed in the interval  $10^{-4} \leq \bar{V} \leq 10^4$ , the results are only presented for the interval  $10^{-1} \leq \bar{V} \leq 10^4$ , because for smaller values of the dimensionless background velocity the results are dominated by fluctuations. These fluctuations are due to problems with the numerical evaluation of the symbolic expressions. These fluctuations begin once the dimensionless background is approximately less than unity and result in a very large increase of the average traction. This increase is definitely the result of the fluctuations, which occurred in the magnitudes of the second and third wave number in Fig. 3.14. If the dimensionless background velocity is larger than unity, the average traction increases with an increasing value of the dimensionless background velocity. In the

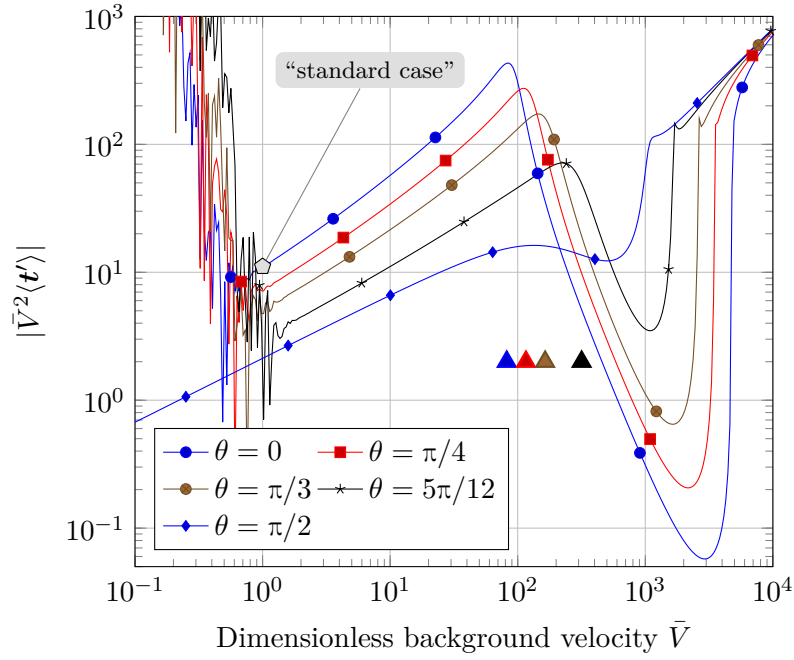


**Figure 3.18:** Dependence of the magnitude of the average traction (weighted by  $\bar{V}^2$ ) in the inertial magnetic case on the dimensionless background velocity  $\bar{V}$  for different values of the colatitude  $\theta$ . The four colored triangles are located at the positions where the coefficient  $b$  vanishes, see Eq. (3.71) on page 95.

transition zone, which is located close to the four differently colored triangles, the traction decreases. For very large values of the dimensionless background velocity, *i.e.*,  $\bar{V} > 10^3$ , the situation changes and the average traction increases again. This feature is related to the behavior of the wave numbers in Fig. 3.14 in this region.

In the following, Fig. 3.19 is considered, where the components of the average tractions  $\langle t'_1 \rangle$ ,  $\langle t'_2 \rangle$  and  $\langle t'_3 \rangle$  corresponding to the three wave numbers are shown. Here, a value of the colatitude of  $\theta = 0$  is applied again. The dependence of the different components on the dimensionless background velocity in Fig. 3.19 shows that large fluctuations only occur in the components  $\langle t'_2 \rangle$  and  $\langle t'_3 \rangle$ . The beginning of a fluctuation is also visible in the component  $\langle t'_1 \rangle$  close to a value of the dimensionless background velocity of  $\bar{V} = 10^{-1}$ . Thus fluctuations occur eventually in all three components if the value of the dimensionless background velocity becomes sufficiently small. Besides, the curves of all components of the average traction have constant slopes in the double-logarithmic chart before the fluctuations become dominant. If these are compared to the dashed black line with a slope of  $1/2$ , the slopes of the two components  $\langle t'_2 \rangle$  and  $\langle t'_3 \rangle$  are smaller than  $1/2$ . Additionally, the slope of the first component  $\langle t'_1 \rangle$  exactly matches the value of  $1/2$ . As a consequence, a finite average traction would result for a vanishing background velocity if the fluctuations would not occur. Furthermore, a continuation of the

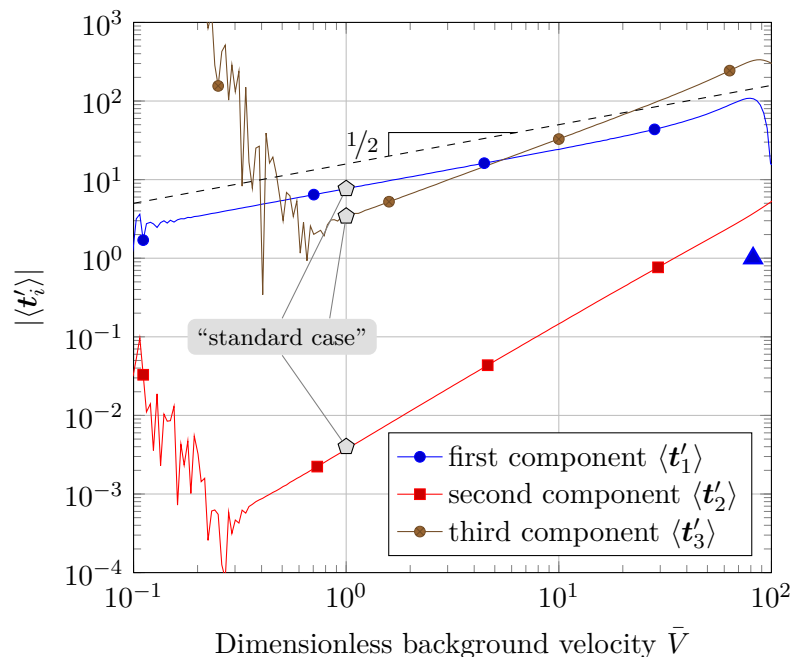


**Figure 3.19:** Dependence of the magnitude of the components of the average traction on the dimensionless background velocity  $\bar{V}$  for the colatitude  $\theta = 0$ . The blue colored triangle is located at the position where the coefficient  $b$  vanishes for  $\theta = 0$ , see Eq. (3.71) on page 95.

undisturbed curves with a constant slope to lower velocities suggests that the average traction is dominated by the first component.

In conclusion, the dependence of the average traction on the dimensionless background velocity can be reliably computed if the dimensionless background velocity is larger than unity and if the other dimensionless parameters have the same values as those specified for the “standard case.” If the dimensionless background velocity becomes less than unity, fluctuations due to the problems with the numerical evaluation of the symbolic expressions become dominant. However, the analysis of the three traction components associated to the three different wave numbers in Fig. 3.19 shows that the component associated to the wave number  $k_z^{(1)}$  not only dominates the average traction for low values of the dimensionless background velocity, but also experiences the smallest numerical fluctuations. Additionally, it resembles the behavior of the non-inertial case closely with a proportionality of  $\langle t'_1 \rangle \propto \sqrt{\bar{V}}$ . Thus, a reasonable value of the average traction for low values of the dimensionless background velocity can be obtained by applying this proportionality.

Finally, the dependence of the average traction on the ALFVÉN number is analyzed by considering Fig. 3.20, which shows this dependence for different values of the colatitude. For very low values of the ALFVÉN number, the average traction

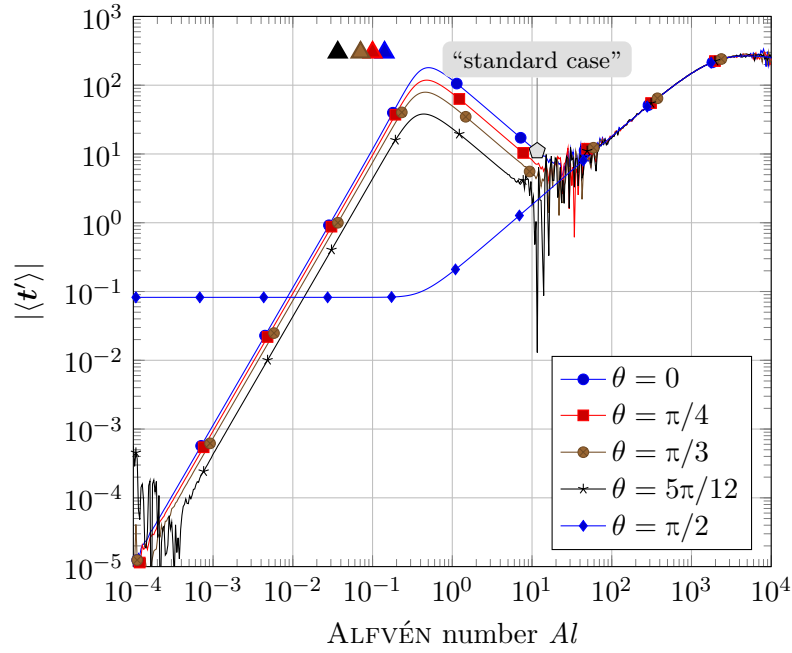


**Figure 3.20:** Dependence of the magnitude of the average traction in the inertial magnetic case on the ALFVÉN number  $Al$  for different values of the colatitude  $\theta$ . The four colored triangles are located at the positions where the coefficient  $b$  vanishes, see Eq. (3.71) on page 95.

is increasing with a growing value of the ALFVÉN number. Then at a value of  $Al = 0.2$ , a transition occurs and the average traction is decreasing if the ALFVÉN number is further increased. This transition is clearly related to that from the weakly to the strongly stratified regime. At a value of approximately  $Al = 10$ , the situation changes again and significant fluctuations occur. However, the strength of the fluctuations decreases if the ALFVÉN number is further increased and an increase of the average traction is visible. If the curves in Fig. 3.20 are compared to those of the non-inertial case in Fig. 3.12, the dependence of the average traction in Fig. 3.20 in the interval  $2 \times 10^{-1} \leq Al \leq 10^4$  is the same as in Fig. 3.12 with the exception of the fluctuations. However, the most evident difference between the two cases is that the average traction becomes very small in the inertial case if the ALFVÉN number becomes very small too. In this sense, the incorporation of the inertial term has regularized the solution for the case of a vanishingly small magnetic field, such that it is conforming with the result obtained in the non-magnetic case, where the average traction always vanishes, see Sect. 3.3.1.

The dependence of the components of the average traction  $\langle t'_i \rangle$  on the ALFVÉN number is shown in Fig. 3.21 for the colatitude  $\theta = 0$ . It is clear from the curves in Fig. 3.17 that the fluctuations can be attributed to the components associated with the second and third wave number  $k_z^{(2)}$  and  $k_z^{(3)}$ . The fluctuations at low values of

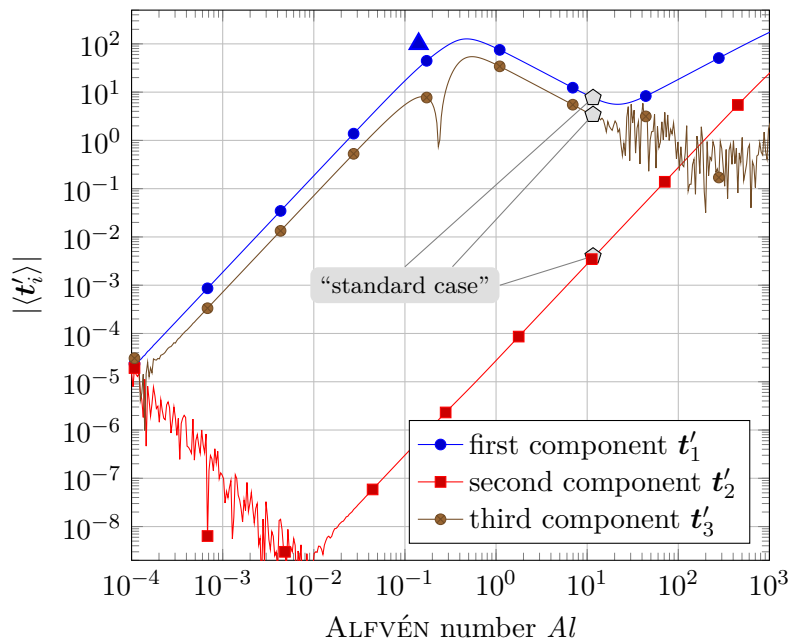


**Figure 3.21:** Dependence of the magnitude of the components of the average traction on the ALFVÉN number  $Al$  for the colatitude  $\theta = 0$ . The blue colored triangle is located at the position where the coefficient  $b$  vanishes for  $\theta = 0$ , see Eq. (3.71) on page 95.

the ALFVÉN number occur in the second component  $\langle t'_2 \rangle$ , whereas the fluctuations at large values occur in the third component  $\langle t'_3 \rangle$ . While the fluctuations in the third component begin where the dependence of the first component of the average traction changes from a decrease to an increase with the ALFVÉN number, there is no correlation of the fluctuations of the second component  $\langle t'_2 \rangle$  with other features in the curves of the traction components or wave numbers. Once the fluctuations become dominant, the second component changes its dependence from an increase to a decrease with an increasing value of the ALFVÉN number. As a consequence, this component becomes larger if the ALFVÉN number becomes smaller, which would result in an infinite traction in the limit as  $Al \rightarrow 0$ . Furthermore, the fluctuations of the second component begin at an ALFVÉN number of approximately 0.01. This value is not close to that related to the transition from the weakly to the strongly stratified region. Additionally, the wave numbers are constant if the ALFVÉN number is close to 0.01. This suggests that the increase of the second component with a decreasing value of the ALFVÉN number is purely due to the fluctuations. It is not a physical phenomenon which is superimposed by the fluctuations. The situation is similar to the dependence of the components of the average traction on the dimensionless background velocity, where a large increase and associated fluctuations also occur for small values. If the fluctuations of the second component are not considered, the continuous continuation of the respective curve yields a vanishing traction in the limit as  $Al \rightarrow 0$ .

In summary, the analysis of the dependence of the average traction on the ALFVÉN number showed that a reliable computation using all three components is possible in the interval  $2 \times 10^{-1} \leq Al \leq 10^1$ . Outside this interval, fluctuations due to the problems with the numerical evaluation of the symbolic expressions occur in the components associated with the second and third wave number. Although these fluctuations are bothersome, the analysis of the three components of the average traction showed that the average traction is dominated by the component associated to the first wave number, whose dependence is similar to the non-inertial case for  $2 \times 10^{-1} \leq Al \leq 10^1$ . Furthermore, this component does not experience any fluctuations for the considered range of values of the ALFVÉN number and thus a meaningful average traction can be determined by discarding the fluctuating components in the respective regions.

In order to finalize the discussion of dependencies of the average traction, it should be mentioned that the total average traction is always positive, insofar as no fluctuations occur. Even though certain components can also be negative, see, for example, Eq. (3.81), the total average traction is always positive. This is not the case if the inertial term is not taken into account, in which case the total traction becomes negative in certain regions, see Sect. 3.3.2. However, note that the magnitude of the average traction is shown in Figs. 3.16, 3.19 and 3.21, because the fluctuations result in arbitrarily alternating positive and negative values of the average traction. This fact additionally supports the hypothesis that the fluctuations do not represent any physical phenomenon but are simply numerical instabilities.

The solution of the inertial magnetic case is visualized in Figs. 3.22 and 3.23. In both figures, the dimensionless parameters of the problem are those of the “standard case” specified in Table 3.4 on page 76. The in-plane components of the velocity perturbation are shown in Fig. 3.22 and the pressure perturbation is shown in Fig. 3.23. In Fig. 3.22, the minimum of the velocity perturbation is located closely to the maximum of the boundary topography, which is indicated in the top panel of Fig. 3.22. Thus, the velocity perturbation is shifted relative to the boundary topography. In Fig. 3.22, the  $z$ -coordinate ranges from  $z = -0.001$  to  $z = 0$ , which corresponds to a vertical extension of 100 m if the horizontal wavelength of the boundary topography is given by  $\lambda_x = 100$  km. The velocity perturbation decays rapidly with respect to the  $z$ -coordinate, because at  $z = -0.001$  its magnitude almost vanishes. Hence, the perturbation is confined to a very thin layer below the boundary topography, where the character of the perturbation can be analyzed using Fig. 3.22. The presence of the boundary topography results in a vertical and horizontal motion of the fluid. While a downward motion of the fluid is expected if the boundary topography penetrates the stratified layer, this is not exactly the case in Fig. 3.22. The shift of the solution relative to the topography results, for example, in a downward motion in regions where the boundary topography is high. This motion can be seen in Fig. 3.22 by considering the vertical component of the velocity in the range  $0 \leq x \leq 0.3$ . However, apart from a small shift relative to the topography, the horizontal component of the velocity perturbation is negative

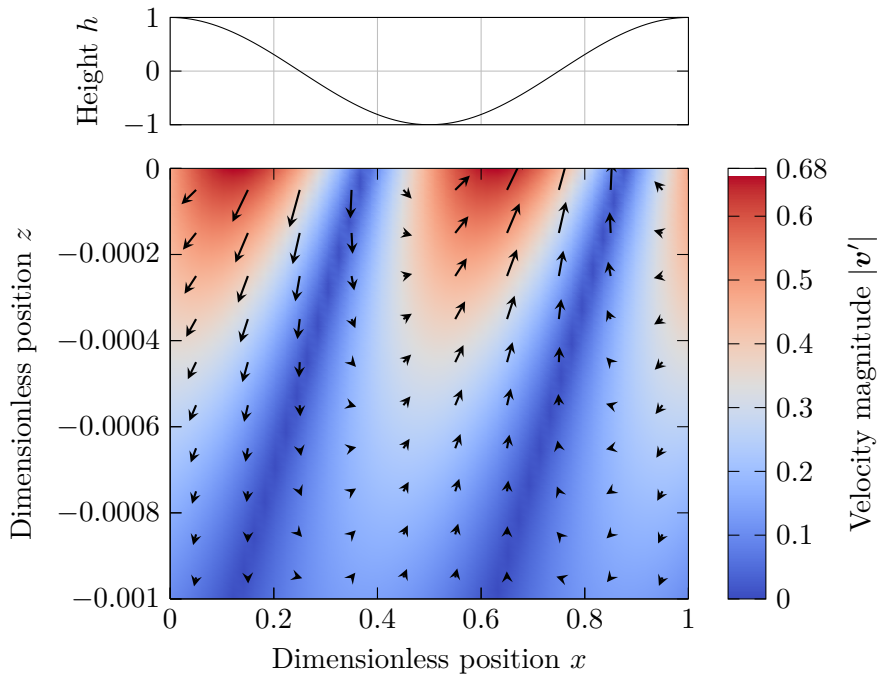


**Figure 3.22:** Perturbation of the velocity field  $\mathbf{v}'$  in the inertial magnetic case. Color indicates the magnitude of the dimensionless velocity. The black arrows indicate the direction. The top panel shows the shape of the topography. Note the different scales of the abscissæ and the ordinates in both panels.

on the leading side and positive on the trailing side of the boundary topography. This behavior is expected, because the trailing side of the topography induces a backward flow of fluid.

The shift of the solution relative to the topography can also be seen in the pressure perturbation in Fig. 3.23. In this figure, the  $z$ -coordinate ranges from  $z = -0.004$  to  $z = 0$ , which corresponds to a vertical extension which is four times larger than that of Fig. 3.22. While the velocity perturbation in Fig. 3.22 almost vanishes at  $z = -0.001$ , this is not the case for the pressure perturbation. This is due to the presence of a long-range component of the solution, whose pressure amplitude is not as small as the corresponding velocity amplitude. Nevertheless, the short-range component still dominates the pressure perturbation. The shift of the long-range component relative to the topography is small, such that this component cannot generate an effective average traction on the boundary topography. However, the short-range component shifts the minimum and the maximum of the pressure perturbation, such that an effective averaged stress on the topography is present.

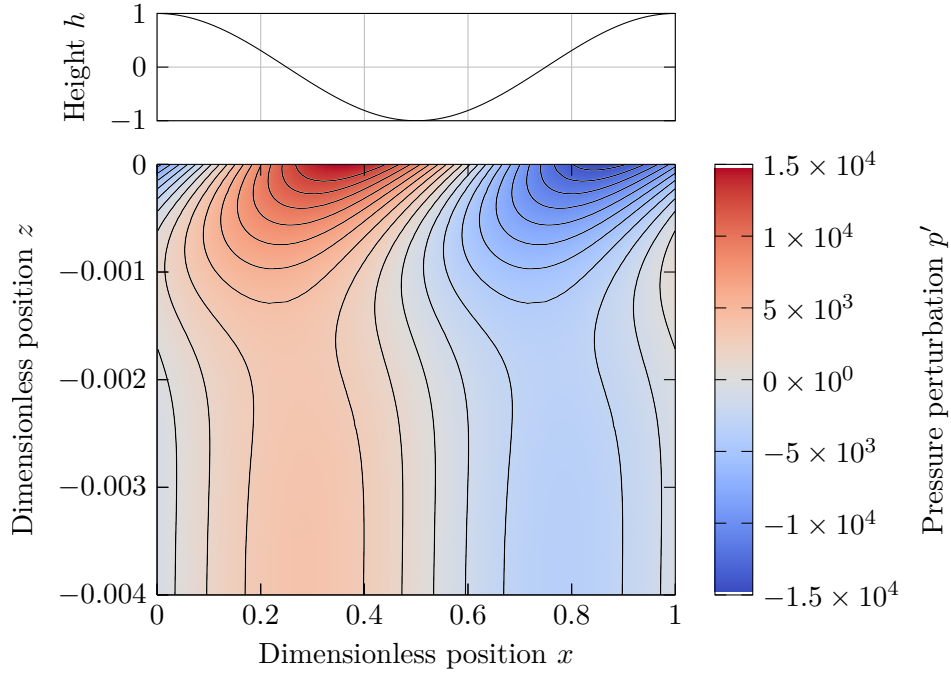


**Figure 3.23:** Perturbation of the pressure field  $p'$  in the inertial magnetic case. Color indicates the magnitude of the pressure perturbation. The black curves are isobars. The top panel shows the shape of the topography. Note the different scales of the abscissæ and the ordinates in both panels.

### 3.4 Extension for a 2D topography

This section discusses the extension of the results obtained for a one-dimensional topography to the case of a two-dimensional counterpart. An example of a two-dimensional topography with a sinusoidal functional dependence with respect to the two in-plane coordinates  $x$  and  $y$  is shown in Fig. 3.24. The height of a two-dimensional topography can, for example, be described by the function  $h = \hat{h} \cos(k_x x) \cos(k_y y)$ . In a complex notation, this product of two trigonometric functions can be expressed as the real part of the following complex function  $h$

$$h(x, y) = \frac{\hat{h}}{2} (\exp(i\mathbf{k}_{T,1} \cdot \mathbf{x}) + \exp(i\mathbf{k}_{T,2} \cdot \mathbf{x})), \quad (3.82)$$

where  $\hat{h}$  is the real-valued amplitude of the topography and  $\mathbf{k}_{T,1} = k_x \mathbf{e}_x + k_y \mathbf{e}_y$  and  $\mathbf{k}_{T,2} = k_x \mathbf{e}_x - k_y \mathbf{e}_y$  are two wave numbers. Several alternative representations of complex functions exist, whose real parts have the functional dependence  $\cos(k_x x) \cos(k_y y)$ . These representations only differ in the functional dependencies of the respective imaginary parts. Here, a compact representation is used for convenience.

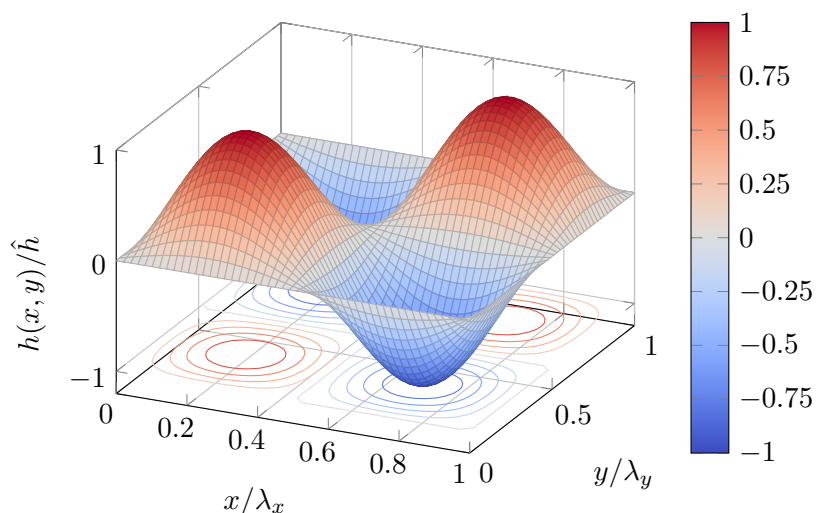


**Figure 3.24:** Graphical representation of a two-dimensional topography. Color indicates the dimensionless height of the boundary topography.

The linearized system of Eqs. (3.27) is now treated with an *ansatz* that involves two plane waves. This means that the perturbations are expanded as follows:

$$\rho = \hat{\rho}_1 \exp(i\mathbf{k}_1 \cdot \mathbf{x}) + \hat{\rho}_2 \exp(i\mathbf{k}_2 \cdot \mathbf{x}), \quad \mathbf{v} = \hat{\mathbf{v}}_1 \exp(i\mathbf{k}_1 \cdot \mathbf{x}) + \hat{\mathbf{v}}_2 \exp(i\mathbf{k}_2 \cdot \mathbf{x}) \quad (3.83)$$

and likewise for the perturbations of the pressure and the magnetic field,  $p'$  and  $\mathbf{b}'$ , respectively. In Eqs. (3.83), the two wave numbers  $\mathbf{k}_1$  and  $\mathbf{k}_2$  are given by

$$\mathbf{k}_1 = k_x \mathbf{e}_x + k_y \mathbf{e}_y + k_{z,1} \mathbf{e}_z, \quad \mathbf{k}_2 = k_x \mathbf{e}_x - k_y \mathbf{e}_y + k_{z,2} \mathbf{e}_z. \quad (3.84)$$

Hence, the horizontal components of the wave numbers  $\mathbf{k}_1$  and  $\mathbf{k}_2$ , *i.e.*, the  $x$ - and  $y$ -components, are the same as those of the wave number of the boundary topography  $\mathbf{k}_{T,1}$  and  $\mathbf{k}_{T,2}$ , respectively. If these expressions for the perturbations are substituted into Eqs. (3.27), the spatial dependencies of the two components of the *ansatz* cannot be eliminated by a simple division, because the two components do not share a common spatial dependence. However, the following orthogonality relations hold for the two complex exponential functions:

$$\begin{aligned} \int_0^{\frac{\lambda_y}{\lambda_x}} \int_0^1 e^{i\mathbf{k}_1 \cdot \mathbf{x}} e^{-i\mathbf{k}_1 \cdot \mathbf{x}} dx dy &= 1, & \int_0^{\frac{\lambda_y}{\lambda_x}} \int_0^1 e^{i\mathbf{k}_1 \cdot \mathbf{x}} e^{-i\mathbf{k}_2 \cdot \mathbf{x}} dx dy &= 0, \\ \int_0^{\frac{\lambda_y}{\lambda_x}} \int_0^1 e^{i\mathbf{k}_2 \cdot \mathbf{x}} e^{-i\mathbf{k}_1 \cdot \mathbf{x}} dx dy &= 0, & \int_0^{\frac{\lambda_y}{\lambda_x}} \int_0^1 e^{i\mathbf{k}_2 \cdot \mathbf{x}} e^{-i\mathbf{k}_2 \cdot \mathbf{x}} dx dy &= 1. \end{aligned} \quad (3.85)$$

These integrals represent spatial integrations over one period of the two-dimensional topography. These orthogonality relations allow to eliminate the spatial dependencies from the system of equations, which is obtained by a substitution of Eqs. (3.83) in Eqs. (3.27). A multiplication of the resulting equations with either  $\exp(-i\mathbf{k}_1 \cdot \mathbf{x})$  or  $\exp(-i\mathbf{k}_2 \cdot \mathbf{x})$  and a subsequent integration over one period of the two-dimensional topography allows to eliminate the spatial dependence completely. The results are two independent systems of algebraic equations of the following form:

$$i\mathbf{k}_i \cdot \hat{\mathbf{v}}_i = 0, \quad i\mathbf{k}_i \cdot \hat{\mathbf{b}}_i = 0, \quad (3.86a)$$

$$-\frac{St^2 Fr^2}{Ro^2} \hat{\mathbf{v}}_i \cdot \mathbf{e}_z + (\bar{\mathbf{V}} \cdot i\mathbf{k}_i) \hat{\rho}_i = 0, \quad (3.86b)$$

$$\chi(\bar{\mathbf{V}} \cdot i\mathbf{k}_i) \hat{\mathbf{v}}_i + \frac{2}{Ro} \boldsymbol{\Omega} \times \hat{\mathbf{v}}_i = -i\mathbf{k}_i \hat{\rho}_i + \frac{1}{Fr^2} \hat{\rho}_i \mathbf{g} + Al^2 (\bar{\mathbf{B}} \cdot i\mathbf{k}_i) \hat{\mathbf{b}}_i, \quad (3.86c)$$

$$Rm((\bar{\mathbf{B}} \cdot i\mathbf{k}_i) \hat{\mathbf{v}}_i - (\bar{\mathbf{V}} \cdot i\mathbf{k}_i) \hat{\mathbf{b}}_i) = \mathbf{k}_i^2 \hat{\mathbf{b}}_i, \quad (3.86d)$$

where  $i = 1, 2$  and the EINSTEIN summation convention does not apply. The Eqs. (3.86) are very similar to Eqs. (3.28) which are obtained in Sect. 3.2 for the one-dimensional problem. For the case of  $i = 1$ , the only difference is that  $k_y \neq 0$  in the two-dimensional case. Furthermore, comparing Eq. (3.86) for the cases corresponding to the wave numbers  $\mathbf{k}_1$  and  $\mathbf{k}_2$ , *i.e.*, for  $i = 1$  and  $i = 2$ , shows that several terms, which involve the  $y$ -component of the respective wave numbers, change their signs if  $i = 2$ . For example, the  $y$ -component of the product  $-i\mathbf{k}_i \hat{\rho}_i$  changes its sign if  $i = 2$ , *viz.*,  $-\mathbf{e}_y \cdot i\mathbf{k}_1 \hat{\rho}_1 = -ik_y \hat{\rho}_1$  and  $-\mathbf{e}_y \cdot i\mathbf{k}_2 \hat{\rho}_2 = ik_y \hat{\rho}_2$ . This is due to the fact that the second wave number  $\mathbf{k}_2$  has a negative  $y$ -component, whereas the first wave number  $\mathbf{k}_1$  has a positive one.

Similarly to Sect. 3.2.3, an algebraic elimination of the unknowns in Eq. (3.86) can be performed and two separate solutions as well as two separate eigenvalue problems are obtained. The eigenvalue problems determine the unknown vertical wave numbers  $k_{z,1}$  and  $k_{z,2}$ . The procedure is very similar to that described in Sect. 3.2.3 and, therefore, is not detailed here any further. In summary, the two pressure perturbations are given by

$$\hat{\rho}_1 = \left( -\chi \frac{k_x}{k_{z,1}} + \frac{1}{k_x k_{z,1}} \frac{St^2}{Ro^2} + ik_{z,1} \frac{RmAl^2}{\mathbf{k}_1^2 + ik_x Rm} \right) \hat{v}_{z,1}, \quad (3.87a)$$

$$\hat{\rho}_2 = \left( -\chi \frac{k_x}{k_{z,2}} + \frac{1}{k_x k_{z,2}} \frac{St^2}{Ro^2} + ik_{z,2} \frac{RmAl^2}{\mathbf{k}_2^2 + ik_x Rm} \right) \hat{v}_{z,2}, \quad (3.87b)$$

where  $\mathbf{k}_1^2 = k_x^2 + k_y^2 + k_{z,1}^2$  and  $\mathbf{k}_2^2 = k_x^2 + k_y^2 + k_{z,2}^2$ . The expressions for the two pressure perturbation  $\hat{\rho}_1$  and  $\hat{\rho}_2$  are equivalent to those specified in Eq. (3.32). The only differences in the expressions are due to the sign change of the  $y$ -component of the second wave number.

Furthermore, the two eigenvalue problems, which are obtained as a result of the

algebraic elimination of the unknowns, are

$$\underbrace{\left( ik_x \mathbf{A}_1 + \frac{2}{Ro} \cos(\theta) \mathbf{B} + k_{z,1}^2 \frac{RmAl^2}{k_1^2 + ik_x Rm} \mathbf{C}_1 \right)}_{=: \mathbf{M}_1} \cdot \begin{bmatrix} \hat{v}_{x,1} \\ \hat{v}_{y,1} \end{bmatrix} = \mathbf{0}, \quad (3.88a)$$

$$\underbrace{\left( ik_x \mathbf{A}_2 + \frac{2}{Ro} \cos(\theta) \mathbf{B} + k_{z,1}^2 \frac{RmAl^2}{k_2^2 + ik_x Rm} \mathbf{C}_2 \right)}_{=: \mathbf{M}_2} \cdot \begin{bmatrix} \hat{v}_{x,2} \\ \hat{v}_{y,2} \end{bmatrix} = \mathbf{0}, \quad (3.88b)$$

where the matrix  $\mathbf{B}$  is specified in the context of Eq. (3.36) and the matrices  $\mathbf{A}_1$ ,  $\mathbf{A}_2$ ,  $\mathbf{C}_1$  and  $\mathbf{C}_2$  are given by

$$\mathbf{A}_1 = \begin{bmatrix} \chi \left( 1 + \frac{k_x^2}{k_z^2} \right) - \frac{1}{k_{z,1}^2} \frac{St^2}{Ro^2} & \chi \frac{k_x k_y}{k_{z,1}^2} - \frac{k_y}{k_x k_{z,1}^2} \frac{St^2}{Ro^2} \\ \chi \frac{k_x k_y}{k_{z,1}^2} - \frac{k_y}{k_x k_{z,1}^2} \frac{St^2}{Ro^2} & \chi \left( 1 + \frac{k_y^2}{k_{z,1}^2} \right) - \frac{k_x^2}{k_{z,1}^2} \frac{St^2}{Ro^2} \end{bmatrix}, \quad (3.88c)$$

$$\mathbf{A}_2 = \begin{bmatrix} \chi \left( 1 + \frac{k_x^2}{k_z^2} \right) - \frac{1}{k_{z,2}^2} \frac{St^2}{Ro^2} & -\chi \frac{k_x k_y}{k_{z,2}^2} + \frac{k_y}{k_x k_{z,2}^2} \frac{St^2}{Ro^2} \\ -\chi \frac{k_x k_y}{k_{z,2}^2} + \frac{k_y}{k_x k_{z,2}^2} \frac{St^2}{Ro^2} & \chi \left( 1 + \frac{k_y^2}{k_{z,2}^2} \right) - \frac{k_x^2}{k_{z,2}^2} \frac{St^2}{Ro^2} \end{bmatrix}, \quad (3.88d)$$

$$\mathbf{C}_1 = \begin{bmatrix} 1 + \frac{k_x^2}{k_{z,1}^2} & \frac{k_x k_y}{k_{z,1}^2} \\ \frac{k_x k_y}{k_{z,1}^2} & 1 + \frac{k_y^2}{k_{z,1}^2} \end{bmatrix}, \quad \mathbf{C}_2 = \begin{bmatrix} 1 + \frac{k_x^2}{k_{z,2}^2} & -\frac{k_x k_y}{k_{z,2}^2} \\ -\frac{k_x k_y}{k_{z,2}^2} & 1 + \frac{k_y^2}{k_{z,2}^2} \end{bmatrix}. \quad (3.88e)$$

For  $k_y = 0$ , both eigenvalue problems reduce to that of the one-dimensional case. Moreover, the matrices  $\mathbf{M}_1$  and  $\mathbf{M}_2$  only differ in the off-diagonal elements, which have opposing signs. As a consequence, the determinants of  $\mathbf{M}_1$  and  $\mathbf{M}_2$  are equal, *i.e.*,  $\det(\mathbf{M}_1) = \det(\mathbf{M}_2)$ . Therefore the characteristic equations governing the wave numbers  $k_{z,1}$  and  $k_{z,2}$  are the same and the wave numbers are equal, *i.e.*,  $k_{z,1} = k_{z,2}$ . However, the corresponding eigenvectors of  $\mathbf{M}_1$  and  $\mathbf{M}_2$  are still different because of the different off-diagonal entries.

For brevity, only the results of the inertial magnetic case are subsequently discussed and the case of  $k_y = k_x$  is considered. Only three distinct wave numbers are found from the eigenvalue problem, because the wave numbers  $k_{z,1}$  and  $k_{z,2}$  are equal. Therefore, the wave numbers are denoted simply by  $k_z^{(1)}$ ,  $k_z^{(2)}$  and  $k_z^{(3)}$  from here on. The dependencies of these wave numbers on the previously considered dimensionless parameters  $St$ ,  $\bar{V}$  and  $Al$  are similar to those of the one-dimensional case. Therefore, only numerical values of the wave numbers are subsequently discussed. If the values of the dimensionless parameters are those of the “standard case” specified in Table 3.4, the wave numbers are given by

$$k_z^{(1)} = -2207.03 - 2208.44i, \quad k_z^{(2)} = 12.68 - 15.48i, \quad k_z^{(3)} = 0.54 - 0.05i. \quad (3.89)$$

The numerical values of the second and the third wave number, *i.e.*,  $k_z^{(2)}$  and  $k_z^{(3)}$ , are comparable to those obtained in the one-dimensional case. In contrast, the real

and imaginary parts of the wave number  $k_z^{(1)}$  are substantially larger than those obtained in the one-dimensional case. Nevertheless, the phases are the same.

The two-dimensional problem is solved by applying the same procedure as for the one-dimensional case. In doing so, the fact that the wave number vectors  $\mathbf{k}_1$  and  $\mathbf{k}_2$  differ with respect to their  $y$ -components needs to be taken into account. Furthermore, the two corresponding eigenvectors are different. In the derivation of the boundary conditions in the one-dimensional case in Eqs. (3.44) and (3.46), the spatial dependence was removed by applying a zeroth-order TAYLOR expansion with respect to the parameter  $H$ , which characterizes the height of the boundary topography. Although this expansion is applied in the two-dimensional case as well, a projection of the resulting equations using the orthogonality relations in Eqs. (3.85) is required. This is necessary to obtain a sufficient number of independent linear equations to determine the coefficients of the solutions uniquely.

The average traction consists of two components in the two-dimensional case, which are associated to the wave numbers  $\mathbf{k}_1$  and  $\mathbf{k}_2$ . The direction of the traction vector of these two components is equal to the corresponding wave number vector. By the same argument as for the one-dimensional case, the average traction in the vertical direction, *i.e.*, the  $z$ -direction, vanishes, *viz.*,  $\langle t_z \rangle = 0$ . Since the  $y$ -components of the two vectors  $\mathbf{k}_1$  and  $\mathbf{k}_2$  are opposite and equal, it is likely that the contributions of the two parts of the solution to the  $y$ -component of the average traction cancel each other out. If the numerical values of the dimensionless parameter are those of the “standard case” specified in Table 3.4, the average traction is given by

$$\langle \mathbf{t} \rangle = 7.06 \mathbf{e}_x - 6.69 \times 10^{-4} \mathbf{e}_y. \quad (3.90)$$

The  $y$ -component of the average traction is four orders of magnitude smaller than the  $x$ -component. Moreover, the value of the  $x$ -component is similar to that found in the one-dimensional case. Therefore, the results of the two dimensional case are at least comparable to that of the one-dimensional case, although the  $y$ -component of the average traction does not vanish in the two-dimensional case.

In the discussion of the average traction in the one-dimensional inertial magnetic case in Sect. 3.3.4, it was pointed out that the average traction can be dominated by fluctuations which occur because of numerical instabilities. These instabilities occur at values of the dimensionless parameters which were close to those of the reference state. If the variation of the stratification parameter  $St$  is considered for the one-dimensional case, the fluctuations become dominant if  $St > 20$ ; no fluctuations are present if  $St < 20$ . In the weakly stratified case with a value of  $St = 10^{-2}$ , the numerical value of the average traction is given by

$$\langle \mathbf{t} \rangle = 9.04 \times 10^{-5} \mathbf{e}_x - 1.74 \times 10^{-14} \mathbf{e}_y. \quad (3.91)$$

However, the fact that the numerical values of the  $y$ -component is very small indicates that this component vanishes in the weakly stratified regime. Moreover, the value of this component for the “standard case” may already be influenced by

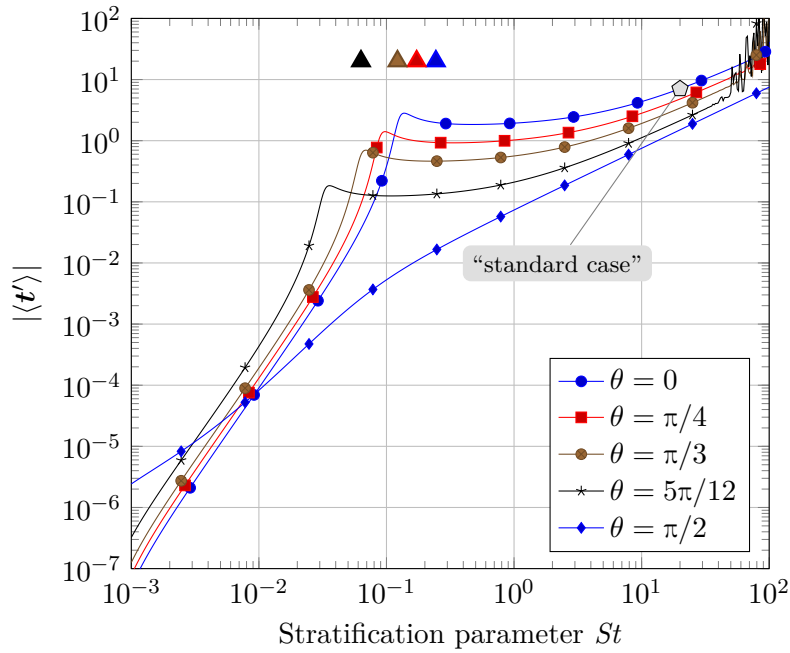


**Figure 3.25:** Dependence of the magnitude of the average traction in the two-dimensional inertial magnetic case on the stratification parameter  $St$  for different values of the colatitude  $\theta$ . The four colored triangles are located at the positions where the coefficient  $b$  vanishes, see Eq. (3.71) on page 95.

fluctuations due to the numerical problems with the evaluation of the symbolic expressions. The  $x$ -component of the average traction in the weakly stratified case in Eq. (3.91) is comparable with that obtained for the one-dimensional problem. Moreover, the  $x$ -component of the average traction has decreased by five orders of magnitude compared to the strongly stratified case in Eq. (3.90). In contrast, the  $y$ -component has decreased by ten orders of magnitude. This fact supports the hypothesis that the  $y$ -component vanishes if numerical problems would not occur.

In the one-dimensional problem, the average traction experiences fluctuations, which are related to the numerical instabilities in the evaluation of the symbolic expressions. In order to assess whether these fluctuations also occur in the two-dimensional problem, the dependence of the average traction is analyzed similarly to Sect. 3.3. In this context, only the magnitude of the average traction is analyzed, instead of considering its  $x$ - and  $y$ -components separately.

First, the dependence on the stratification parameter  $St$  is considered. This dependence is shown in Fig. 3.25 for different values of the colatitude. In Fig. 3.25, the curves experience fluctuations if the stratification parameter becomes larger than 50. The case of a vanishing rotation is an exception in this regard, because no fluctuations are visible in the curve for a colatitude of  $\theta = \pi/2$ . Furthermore, the fluctuations of the curve in Fig. 3.25, which corresponds to a colatitude of

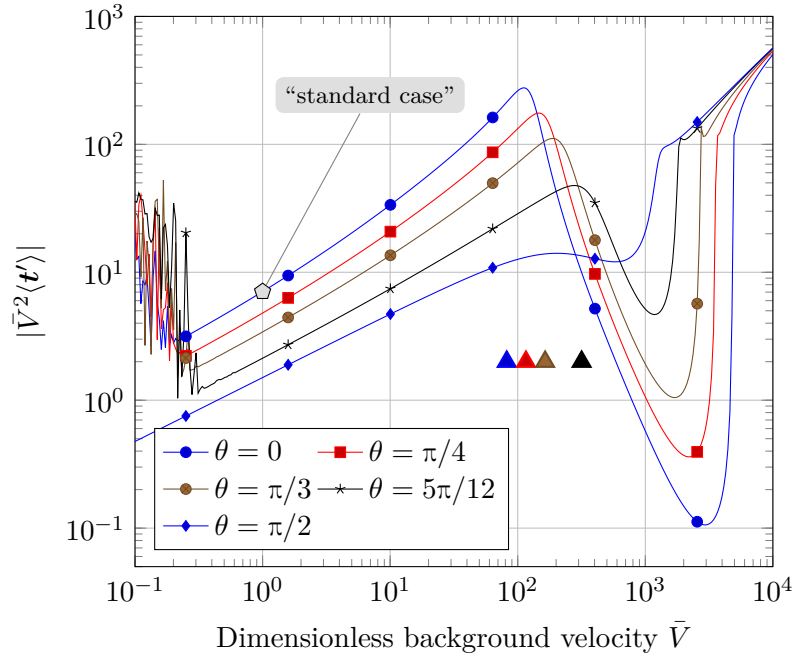


**Figure 3.26:** Dependence of the magnitude of the average traction in the two-dimensional inertial magnetic case on the dimensionless background velocity  $\bar{V}$  for different values of the colatitude  $\theta$ . The four colored triangles are located at the positions where the coefficient  $b$  vanishes, see Eq. (3.71) on page 95.

$\theta = 5\pi/12$ , dominate possible fluctuations of the other curves. Comparing the curves in Fig. 3.25 with those in Fig. 3.16 shows that the fluctuations are much weaker in the two-dimensional than in the one-dimensional case in Fig. 3.16. Thus, the incorporation of a variation of the boundary topography with respect to the  $y$ -coordinate seems to have a stabilizing effect regarding the numerical evaluation of the underlying symbolic expressions. At this stage, the stabilizing effect can only be confirmed with respect to a variation of the stratification parameter  $St$ .

The dependence of the magnitude of the average traction on the dimensionless background velocity  $\bar{V}$  is shown in Fig. 3.26 for the two-dimensional problem and for different values of the colatitude. The curves in Fig. 3.26 begin to fluctuate due to numerical instabilities, if the dimensionless background velocity is less than 0.4. Comparing the curves in Fig. 3.26 with those of the one-dimensional problem in Fig. 3.18 shows that the fluctuations are much more moderate in the two-dimensional than in the one-dimensional case. In the one-dimensional case, the fluctuations result in a dimensionless average traction, whose magnitude is larger than 1000. This is not observed in the two-dimensional case, where the fluctuations are smaller such that the dimensionless average traction only reaches a maximum value of 50. Moreover, the onset of the fluctuations occurs at a smaller value of the background velocity in the two-dimensional case. It can be seen in Fig. 3.26 that

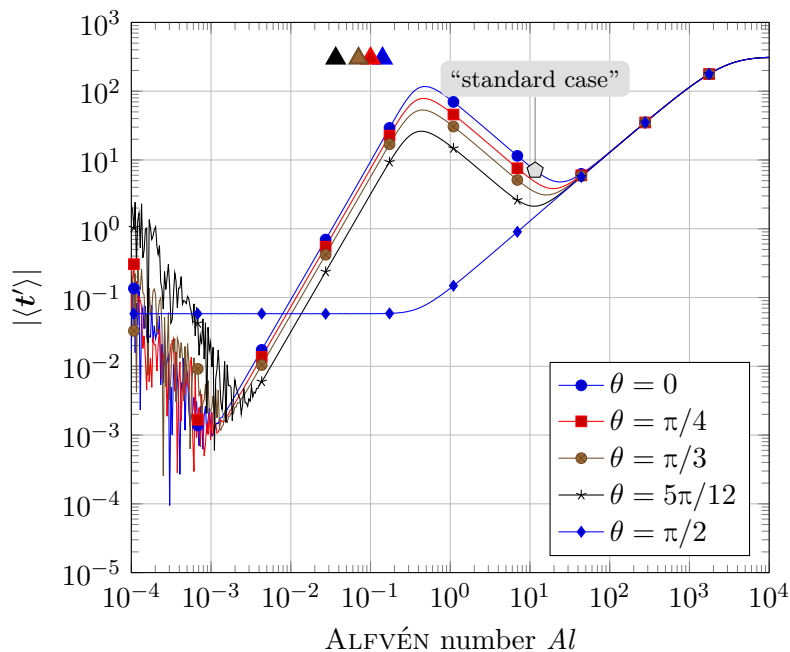


**Figure 3.27:** Dependence of the magnitude of the average traction in the two-dimensional inertial magnetic case on the ALFVÉN number  $Al$  for different values of the colatitude  $\theta$ . The four colored triangles are located at the positions where the coefficient  $b$  vanishes, see Eq. (3.71) on page 95.

the onset occurs at a dimensionless background velocity of approximately  $\bar{V} \approx 0.4$ . This value is at least half the size of the value of the dimensionless background velocity at which the fluctuations begin in the one-dimensional case, see Fig. 3.18. Besides these differences regarding the fluctuations, major differences between the curves of the one- and the two-dimensional case are not observed. The overall dependence of the average traction on the dimensionless background is not changed if the two-dimensional problem is considered. However, the numerical evaluation of the symbolic expressions is more stable for the two-dimensional problem because of the differences regarding the size and the onset of the fluctuations of the curves. Thus, the stabilizing effect, which was suggested from the results for the dependence of the average traction on the stratification parameter, can be confirmed.

Finally, the dependence of the magnitude of the average traction on the ALFVÉN number  $Al$  is shown in Fig. 3.27 for different values of the colatitude. The curves in Fig. 3.27 represent an exception in comparison to those in Figs. 3.25 and 3.26, because in Fig. 3.27 the fluctuations are stronger in comparison to the one-dimensional case for certain values of the ALFVÉN number. Comparing the curves of the two-dimensional problem in Fig. 3.27 with those of the one-dimensional problem in Fig. 3.20 shows that the fluctuations in the interval  $10 < Al < 100$  are not present in the two-dimensional case. In this region, the smooth curves do not indicate any fluctuations and hence numerical instabilities do not occur. In contrast to this, the

curves in Fig. 3.27 experience strong fluctuations if the ALFVÉN number is below  $2 \times 10^{-2}$ . If these fluctuations are compared to those of the one-dimensional case shown in Fig. 3.20, it is found that their onset occurs at a larger ALFVÉN number and that they are much larger in magnitude. This suggests that a numerical evaluation of the underlying symbolic expressions for small ALFVÉN numbers is critical. While the extension of the problem to a two-dimensional topography is beneficial with respect to the numerical instabilities, which occur for large values of the stratification parameter and low values of the dimensionless background velocity, this benefit is compromised by the stronger fluctuations in the small ALFVÉN number regime. Nevertheless, the fluctuations of the average traction, which occur in the one-dimensional problem in the interval  $10 < Al < 100$ , are not present in the two-dimensional case. This fact meliorates the undesired behavior in the low ALFVÉN number region.

In summary, the analysis of the two-dimensional problem revealed that the qualitative behavior of the solution is not altered much by adding a variation of the boundary topography with respect to the  $y$ -coordinate. Although the eigenvalue problem in Eq. (3.88) is more cumbersome than for the one-dimensional case and two waves are present in the two-dimensional case, these two waves have identical vertical wave numbers  $k_z$ , because identical characteristic equations arise from the two eigenvalue problems. Moreover, the numerical values of the vertical wave numbers, which were analyzed, are comparable to the one-dimensional case. The qualitative behavior of the average traction is also the same as that of the one-dimensional problem. Although the nominal value of the average traction is approximately 30% less than that of the one-dimensional case, the analysis of Figs. 3.26, 3.26 and 3.27 reveals that the dependencies of the average traction on the considered parameters are corresponding to those of the one-dimensional case. With the exception of the low ALFVÉN number regime, the two-dimensional problem is more stable with respect to the fluctuations and numerical instabilities addressed in Sect. 3.3.4. In conclusion, the results of the two-dimensional case are in agreement with those of the previously discussed one-dimensional cases. Evidence for a fundamental change of the character of the solution or for a substantial decrease of the average traction was not found.

## 3.5 Summary

In this chapter, a stratified layer of an electrically conducting inviscid fluid was analyzed in a rotating system. A linear analysis was performed using a perturbation expansion of the solution. Fundamental assumptions, the solution procedure and related approximations were discussed and described extensively for a dimensionless formulation of the problem in Sect. 3.2. Following this theoretical part, results were presented and analyzed in detail in Sect. 3.3 for certain special cases. Finally, the solution approach of the one-dimensional problem was extended for a two-dimensional boundary topography in Sect. 3.4.

Below, the main results of the analysis in Sects. 3.3 and 3.4 are summarized. The strategy of considering simplified problems, in which either certain terms are neglected or certain approximations are made, has proved to be successful. Several effects were analyzed and explained, which would not be possible if a non-simplified version of the problem were considered. The approximated non-inertial case is of fundamental importance in this regard, because an analytical solution can be obtained in a closed form. In the analysis of this closed-form solution numerical problems do not occur. Furthermore, the dependences on the dimensionless parameters and characteristics of this closed-form solution also transfer to the other cases. In the approximate non-inertial problem, the average traction possesses a singularity if the magnetic background field becomes very large. Therefore, certain approximations and the neglect of the inertial term are not possible if a regularized solution is required. However, the unsimplified non-approximate cases are characterized by the complex algebraic structure of the underlying symbolic expressions, which make a numerical evaluation of the solution challenging. This fact leads to numerical instabilities in certain parameter regions. A summary of the properties of the solutions obtained in the different cases is given in Table 3.5. According to Table 3.5, the non-inertial cases have regular solutions in the sense that a finite average traction is found if the considered dimensionless parameters become very small. Although numerical instabilities are present in the inertial cases, the regularity is justified because the solutions obey certain proportionalities before the numerical instabilities occur. Furthermore, it was found that the instabilities mainly occur in the components of the average traction which are associated with the second and the third wave number. In the region where the instabilities are present, these components do not contribute substantially to the average traction. Thus, a reliable computation of the average traction in regions, where numerical instabilities are present, can be achieved by considering only the component associated to the first wave number.

The presence of the instabilities compromises an accurate computation of the average traction. However, the limitations regarding accuracy are not problematic for an application of the considered model to the CMB, because the information

**Table 3.5:** Properties and nominal dimensionless average tractions of the different cases considered in Sect. 3.3. A checkmark (✓) indicates that the case is either stable or regular w.r.t. the considered parameter. An X mark (✗) indicates the opposite.

Case	$ \langle t \rangle $	Stability			Regularity		
		<i>St</i>	$\bar{V}$	<i>Al</i>	<i>St</i>	$\bar{V}$	<i>Al</i>
approx. non-inertial magnetic case	7.66	✓	✓	✓	✓	✓	✗
non-inertial magnetic case	7.66	✓	✗	✗	✓	✓	✓
inertial magnetic case	11.08	✗	✗	✗	✓	✓	✓
inertial magnetic case in 2D	7.06	✗	✗	✗	✓	✓	✓

about the CMB region is also limited and inaccurate. For example, the amplitude of the boundary topography and its wavelength are not very well known. If the modest approximation of 30 m used in this chapter is changed to 60 m, the average traction would at least double. Moreover, the strength of the stratification and the thickness of the stratified layer are uncertain for the CMB region. Altering the strength of the stratification corresponds to a modification of the buoyancy frequency or of the dimensionless stratification parameter. The results in Sect. 3.3 show that a modification of this parameter can easily change the order of magnitude of the average traction. Therefore, uncertainties regarding the parameters which are realistic for the CMB of the Earth, are at least on the same level as the numerical inaccuracies.

The nominal value of the average traction obtained for the model presented in this chapter is given by  $0.2 \text{ N m}^{-1}$ , which is one half of the estimated value required to account for fluctuations in the length of day at periods of several decades [Hide (1969b)]. This supports the idea that the considered combined model of this chapter including topography, stratification and electromagnetic effects is a possible candidate for a viable core-mantle coupling mechanism. The application of this model to the CMB and its combination with numerical results for the background velocity and magnetic field is presented and discussed in Chap. 5.

## 4 Aspects of the numerical modeling of a dynamo process

This chapter discusses aspects of the numerical simulation of magnetohydrodynamic processes in the outer core of the Earth. The presented content is based on the theory of rotating BOUSSINESQ convection, which is discussed in Chap. 2. In the first section, the boundary value problem of rotating convection as it is found in the literature is presented in a dimensionless form. Subsequently, the numerical solution of the problem using a discretization customized for spherical shells is outlined in the second section. In this context, the toroidal-poloidal decomposition is discussed whose details are also covered in the paper by Glane, Reich, and Müller [2018]. Following these two theoretical sections, numerical results which were computed using the pseudo-spectral numerical library called *Rayleigh* are presented in the third section. The numerical results shall serve as an input for the local core-mantle coupling presented in Chap. 3. Therefore, the discussion and assessment in Sect. 4.4 is confined to the question whether the numerical results are representative for the outer core of the Earth. In Chap. 5, the numerical results presented in this chapter will be used and combined with the core-mantle coupling model in order to analyze the implications of the coupling mechanism on the length of day.

The strategy of combining the three-dimensional numerical model for rotating magnetohydrodynamic convection and the analytical core-mantle coupling model is pursued because of three reasons. *First*, the numerical libraries available for simulating rotating magnetohydrodynamic convection are mostly based on spectral methods. Therefore, they can only be applied to problems with a perfectly spherical geometry and an inclusion of a topographic Core-Mantle Boundary (CMB) is not possible. *Second*, most of the available codes for solving rotating magnetohydrodynamic problems can solve the anelastic equations and thus a variable adiabatic density profile can be included. However, the inclusion of stratification by means of a localized density gradient is not possible without severe modifications of the existing highly complex codes. *Third*, even if a stratified layer can be included in some way, a transport equation for the density perturbation also needs to be implemented in the existing software. Thus a setup of the core-mantle coupling model similar to that described in Chap. 3 in a three-dimensional code is not feasible.

---

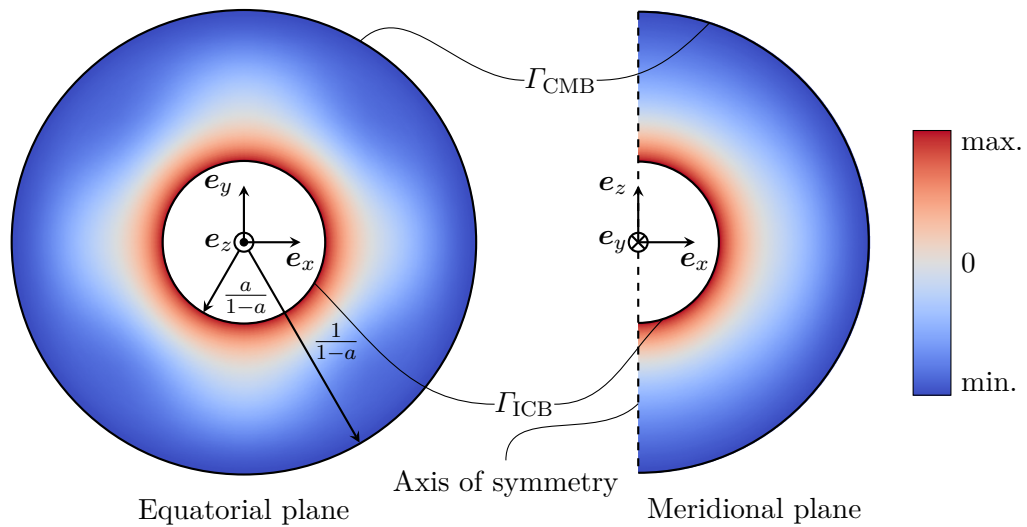


**Figure 4.1:** Boundary value problem of a numerical dynamo. The equatorial plane ( $x$ - $y$ -plane) is shown on left-hand side and the meridional plane ( $x$ - $z$ -plane) is shown on the right-hand side. In both planes the color indicates the initial condition for the dimensionless temperature field. The aspect ratio of the spherical shell radii is denoted by  $a$ .

## 4.1 Problem statement

In the following, the boundary value problem of a convection-driven magnetohydrodynamic dynamo in a rotating spherical shell is formulated. The boundary and initial conditions are those of the benchmark problem outlined in Christensen et al. [2001]. The pseudo-spectral numerical library *Rayleigh* [Featherstone and Hindman (2016); Matsui et al. (2016)] will be used to solve the problem numerically. In contrast to the paper by Christensen et al., a different dimensionless formulation is applied in the following, which corresponds to that used in the *Rayleigh* software. The *Rayleigh* software can solve the equations of the anelastic and the BOUSSINESQ approximation numerically in a spherical shell. Although benchmark problems were formulated for the anelastic approximation, see Jones et al. [2011], and the *Rayleigh* software can solve such problems, the BOUSSINESQ approximation is applied in the following. The anelastic approximation would be appropriate for stars or gas giants but not for the Earth, where the effect of the compressibility of the material is negligible.

The boundary value problem for a numerical dynamo is shown in Fig. 4.1. Here, the symbol  $a$  is related to the aspect ratio of the spherical shell radii and is computed by  $a = R_{\text{ICB}}/R_{\text{CMB}}$  where  $R_{\text{ICB}}$  and  $R_{\text{CMB}}$  denote the radii of the inner core boundary and the core-mantle boundary, respectively. For the Earth, this value is given by  $a = 0.35$ . The problem is normalized with respect to the shell thickness  $D = R_{\text{CMB}} - R_{\text{ICB}}$  such that the radii of the inner core and the CMB

**Table 4.1:** Parameters of the dynamo problem and resulting reference values for the outer core of the Earth. The value of the magnetic diffusivity  $\eta$  is computed from  $\eta = 1/(\mu_0\sigma)$  for an electrical conductivity of  $\sigma = 7 \times 10^5 \text{ S m}^{-1}$ , see Table 2.2.

Quantity	Value	Reference
<i>parameters related to the Earth</i>		
$\Omega_0$	$7.27 \times 10^{-5} \text{ s}^{-1}$	Dehant and Mathews [2015]
$D$	2280 km	Olson [2015]
$g$	$10.68 \text{ m s}^{-2}$	see Table 2.2
$T_{\text{ICB}}$	5200 K	see Table 2.1
$T_{\text{CMB}}$	4000 K	see Table 2.1
<i>material parameters</i>		
$\rho$	$1.09 \times 10^4 \text{ kg m}^{-3}$	see Table 2.2
$\alpha$	$1.5 \times 10^{-5} \text{ K}^{-1}$	see Table 2.2
$\kappa$	$5 \times 10^{-5} \text{ m}^2 \text{ K}^{-1}$	see Table 2.2
$\eta$	$1.13 \text{ m}^2 \text{ s}^{-2}$	see caption
$\nu$	$1 \times 10^{-5} \text{ m}^2 \text{ s}^{-1}$	see Table 2.2
<i>parameters calculated from previous values</i>		
$t_{\text{ref}}$	$16.47 \times 10^9 \text{ a}$	
$B_{\text{ref}}$	1.06 mT	
$T_{\text{ref}}$	1200 K	

as specified in Fig. 4.1 result. From a geometric point of view, the problem is spherically symmetric but the presence of rotation introduces an axis of symmetry. As indicated in Fig. 4.1, the axis of rotation is chosen as the  $z$ -axis of the CARTESIAN coordinate system.

In the following, the differential equations of the boundary value problem shown in Fig. 4.1 are presented briefly. In this context, the dimensionless formulation, which is solved by the *Rayleigh* software, is discussed. It should be remarked that this formulation differs considerably from those presented in, *e.g.*, Christensen et al. [2001] or Jones et al. [2011] because of a different choice of the reference timescale. The reference timescale that is employed in the *Rayleigh* software is the viscous timescale [Featherstone (2018)]

$$t_{\text{ref}} = \frac{D^2}{\nu}, \quad (4.1)$$

in which  $\nu$  ( $\text{m}^2 \text{ s}^{-1}$ ) is a kinematic viscosity and  $D$  is the shell thickness of the outer core of the Earth. The reference temperature is chosen as the temperature difference in the outer core of the Earth, *i.e.*,  $T_{\text{ref}} = T_{\text{ICB}} - T_{\text{CMB}}$ . Moreover, the reference magnetic field is chosen as  $B_{\text{ref}} = \sqrt{\rho\mu_0\eta\Omega_0}$ . Table 4.1 specifies the material and geometric parameters which govern the dynamo problem. In this table, the resulting values of the reference scales  $t_{\text{ref}}$ ,  $B_{\text{ref}}$  and  $T_{\text{ref}}$  are also specified.

**Table 4.2:** Values of the dimensionless numbers of the dynamo problem in comparison to those specified in Olson [2015].

Dimensionless number	Value computed from Table 4.1	Value/range specified in Olson [2015]
$Ek$	$2.65 \times 10^{-14}$	$\approx 3 \times 10^{-14}$
$Ra$	$4.56 \times 10^{28}$	$\approx 10^{20}$
$Pr$	2	0.1 to 0.5
$Pm$	$8.85 \times 10^{-6}$	not specified

Applying these reference scales, the following dimensionless magnetohydrodynamic system is obtained from Eq. (2.111)

$$\begin{aligned}
\nabla \cdot \mathbf{v} &= 0, & \nabla \cdot \mathbf{B} &= 0, \\
\frac{\partial \mathbf{v}}{\partial t} + \mathbf{v} \cdot \nabla \mathbf{v} + \frac{2}{Ek} \mathbf{e}_z \times \mathbf{v} &= \nabla^2 \mathbf{v} - \frac{1}{Ek} \nabla p - \frac{Ra}{Pr} \mathbf{g} + \frac{1}{Ek Pr} (\nabla \times \mathbf{B}) \times \mathbf{B}, \\
\frac{\partial T}{\partial t} + \mathbf{v} \cdot \nabla T &= \frac{1}{Pr} \nabla^2 T, \\
\frac{\partial \mathbf{B}}{\partial t} &= \nabla \times (\mathbf{v} \times \mathbf{B}) + \frac{1}{Pm} \nabla \times \nabla \times \mathbf{B}.
\end{aligned} \tag{4.2}$$

In this system, a linear gravity profile is assumed, *i.e.*,  $\mathbf{g} = -(1-a)r\mathbf{e}_r$ , and the reference value of the gravity field is given by the value at the CMB. Furthermore,  $Ek$  denotes the EKMAN number,  $Ra$  the RAYLEIGH number,  $Pr$  the PRANDTL number, and  $Pm$  the magnetic PRANDTL number. These dimensionless numbers characterize the system and are given by

$$Ek = \frac{\nu}{\Omega_0 D^2}, \quad Ra = \frac{\alpha T_{\text{ref}} g D^3}{\nu \kappa}, \quad Pr = \frac{\nu}{\kappa}, \quad Pm = \frac{\nu}{\eta}, \tag{4.3}$$

where  $D = R_{\text{CMB}} - R_{\text{ICB}}$  denotes the thickness of the shell. Table 4.2 specifies the values of the dimensionless numbers which govern the dynamo problem. Comparing the values in Table 4.2 with those specified in Olson [2015] shows that significant differences arise for the RAYLEIGH number and the PRANDTL number. These differences are due to the fact that different values were used for the kinematic viscosity, the thermal diffusivity and the reference temperature. This reflects the uncertainties regarding the values of the material parameters and the temperature profile in the outer core of the Earth. The dimensionless numbers also have a strong influence on the character of the solution and also on the numerical work, which is required to obtain such a solution.

In order to solve the system in Eq. (4.2), appropriate boundary conditions are required. While there is a common agreement on the boundary conditions for the velocity and the magnetic field, different temperature boundary conditions are addressed often in the literature. However, in this study the standard approach

of choosing DIRICHLET boundary conditions at the inner core and the CMB is pursued for two reasons, because an analysis of the influence of different boundary conditions for the temperature or the heat flux at the ICB or the CMB is out of scope of this work. The boundary conditions of the dynamo problem for the dimensionless temperature and the dimensionless velocity are given by

$$T(\mathbf{x}, t) = 1, \quad \mathbf{v}(\mathbf{x}, t) = \mathbf{0}, \quad \mathbf{x} \in \Gamma_{\text{ICB}}, \quad (4.4)$$

$$T(\mathbf{x}, t) = 0, \quad \mathbf{v}(\mathbf{x}, t) = \mathbf{0}, \quad \mathbf{x} \in \Gamma_{\text{CMB}}. \quad (4.5)$$

The boundary condition for the velocity field is the no-slip condition. The temperature boundary condition arise from the way the temperature is non-dimensionalized. In fact, the temperature is shifted by the (unknown) temperature at the CMB and scaled by the temperature difference in the outer core of the Earth. Hence, the shifted dimensionless temperature is equal to unity at the inner core boundary and equal to zero at the outer core boundary. The boundary conditions for the magnetic field are obtained by assuming a non-conducting inner core and mantle. In this case, the magnetic field is a potential field both in the inner core and the mantle. Therefore, the transition conditions read

$$\mathbf{B}(\mathbf{x}, t) = \nabla V_{\text{IC}}(\mathbf{x}, t), \quad \mathbf{x} \in \Gamma_{\text{ICB}}, \quad \mathbf{B}(\mathbf{x}, t) = \nabla V_{\text{M}}(\mathbf{x}, t), \quad \mathbf{x} \in \Gamma_{\text{CMB}}, \quad (4.6)$$

where  $V_{\text{IC}}$  and  $V_{\text{M}}$  denote the scalar potentials of the magnetic field in the inner core and the mantle, respectively. Note that the boundary conditions specified above correspond to those of the benchmark cases presented in Christensen et al. [2001] and Jones et al. [2011].

The initial conditions of the numerical dynamo problem are also chosen as those specified in the benchmark case in Christensen et al. [2001]. The initial condition for the temperature field is shown in the equatorial and the meridional plane in Fig. 4.1. Applying the normalization, which is used in the *Rayleigh* software, the initial condition for the dimensionless temperature of the benchmark case defined in Christensen et al. [2001] is given by

$$T(r, \theta, \varphi, t = 0) = \frac{a}{(1-a)^2} \left( \frac{1}{r} - (1-a) \right) + \frac{21}{\sqrt{17920\pi}} (1 - 3\xi^2 + 3\xi^4 - \xi^6) \sin^4(\theta) \cos(4\varphi), \quad (4.7)$$

where  $\xi = 2r - (1+a)/(1-a)$ . Here,  $r$  denotes the radius,  $\theta$  the polar angle and  $\varphi$  the azimuthal angle. The terms in the first line of Eq. (4.7) represent the solution of a stationary spherically symmetric heat conduction problem. This solution is perturbed by the terms in the second line of Eq. (4.7). This perturbation is shown in Fig. 4.2. The minima and maxima of the temperature perturbation are located at a dimensionless radius of  $r = (3+a)/(1-a)/4$  in the equatorial plane. In the equatorial plane in Fig. 4.2, four oscillations between a low and high value of the

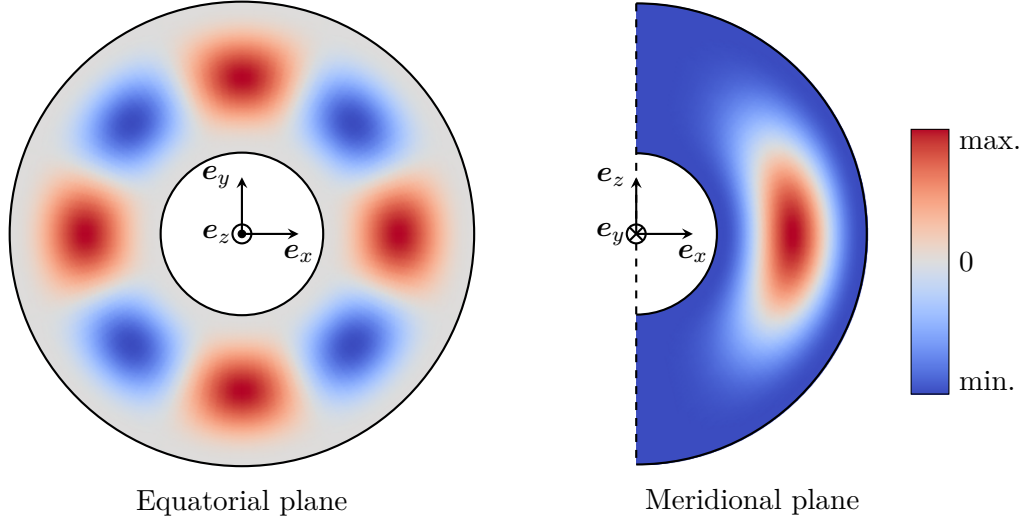


**Figure 4.2:** Initial temperature perturbation in the equatorial and meridional plane.

temperature perturbation are visible in the azimuthal direction. These oscillations are due to the term  $\cos(4\varphi)$ , which occurs in the temperature perturbation in Eq. (4.7). Therefore, the perturbation is referred to as a perturbation with an azimuthal wave number of  $m = 4$ .

Regarding the boundary conditions for the other fields, the fluid is initially at rest and therefore  $\mathbf{v} = \mathbf{0}$  is the initial condition for the velocity field. The initial conditions for the components of the magnetic field are given by

$$B_r(r, \theta, \varphi, t = 0) = \frac{5}{8} \left( \frac{1}{1-a} - 6r - \frac{a^4}{(1-a)^4} \frac{2}{r^3} \right) \cos(\theta), \quad (4.8)$$

$$B_\theta(r, \theta, \varphi, t = 0) = \frac{5}{8} \left( 9r - \frac{8}{1-a} - \frac{a^4}{(1-a)^4} \frac{1}{r^3} \right) \sin(\theta), \quad (4.9)$$

$$B_\varphi(r, \theta, \varphi, t = 0) = 5 \sin \left( \pi \left( r - \frac{a}{1-a} \right) \right) \sin(2\theta). \quad (4.10)$$

The  $r$ - and the  $\theta$ -components of this magnetic field constitute a dipole field and the  $\varphi$ -component represents a perturbation of the dipolar character.

The initial and boundary conditions of the problem presented here are the same as those of the benchmark case presented in Christensen et al. [2001]. For the choice of the dimensionless parameters of  $Ek = 10^3$ ,  $Ra = 10^5$ ,  $Pr = 1$  and  $Pm = 3$ , a quasi-stationary solution with a self-sustaining magnetic field is found [Christensen et al. (2001)]. This solution is referred to as quasi-stationary, because the fixed spatial pattern of the solution is slightly rotating with respect to this axis of rotation. All fields in this solution have a similar spatial pattern, which is clearly defined by a temperature perturbation with an azimuthal wave number of  $m = 4$ . However, the parameter region, for which the benchmark case is specified,

corresponds to a highly viscous fluid, which does not mimic the situation in the outer core of the Earth. Therefore, the values of the dimensionless parameters are changed such that they are more similar to values suggested for the outer core of the Earth. This aspect will be detailed further in Sect. 4.3.

## 4.2 Discretization based on the toroidal-poloidal decomposition

In this section, the discretization and numerical solution of the dynamo problem in the *Rayleigh* software is outlined briefly. The discussion focuses on the pseudo-spectral approach applied in the *Rayleigh* software and the related toroidal-poloidal decomposition. First, the concept of the toroidal-poloidal decomposition of a vector field is reviewed in Sect. 4.2.1. The presented material is largely based on the paper by Glane, Reich, and Müller. Following the discussion of this topic, Sect. 4.2.2 presents the radial and temporal discretization, which is the basis for the discussion of the pseudo-spectral approach used in the *Rayleigh* software. It should be remarked that the *Rayleigh* software is the successor of the *ASH code*, whose construction is similar to that of the *Rayleigh* software. Details on the *ASH code* can be found in Clune et al. [1999] and Brun, Miesch, and Toomre [2004].

### 4.2.1 Toroidal-poloidal decomposition

The usage of toroidal and poloidal vector fields for the dynamo problem was part of the pioneering work of ELSASSER in the 1940s [Elsasser (1946a); Elsasser (1946b); Elsasser (1947)]. According to Simpson and Weiner, the introduction of the terms *toroidal* and *poloidal* in context with magnetic fields is also due to ELSASSER [Simpson and Weiner (1989)]. In the case of spherical coordinates, it is customary to define the toroidal and the poloidal vector fields as

$$\mathbf{T}(r, \theta, \varphi, t) := \nabla \times T(r, \theta, \varphi, t) \mathbf{e}_r, \quad \mathbf{P}(r, \theta, \varphi, t) := \nabla \times \nabla \times P(r, \theta, \varphi, t) \mathbf{e}_r, \quad (4.11)$$

where  $T$  and  $P$  are referred to as toroidal and poloidal scalars, respectively. In the literature, several definitions of toroidal and poloidal vector fields with different explicit dependencies on the radius  $r$  are used. Here, the definition of BULLARD and GELLMAN is applied, because it is also used in *Rayleigh* [Bullard and Gellman (1954)].

By construction, the toroidal and the poloidal vector fields are solenoidal, *i.e.*,  $\nabla \cdot \mathbf{T} = 0$  as well as  $\nabla \cdot \mathbf{P} = 0$ . The solenoidality holds regardless of  $T$  and  $P$ , because the divergence of the curl of any vector field vanishes. However, if the dependence of the two functions  $T$  and  $P$  on the polar and azimuthal angles is, respectively, expressed in a series using spherical harmonics, beneficial orthogonality properties can be exploited. Thus, the two functions  $T$  and  $P$  are expressed in

terms of the followings series:

$$T(r, \theta, \varphi, t) = \sum_{l=1}^{\infty} \sum_{m=-l}^l t_l^m(r, t) Y_l^m(\theta, \varphi), \quad (4.12a)$$

$$P(r, \theta, \varphi, t) = \sum_{l=1}^{\infty} \sum_{m=-l}^l p_l^m(r, t) Y_l^m(\theta, \varphi), \quad (4.12b)$$

where  $Y_l^m$  denotes a spherical harmonic of degree  $l$  and order  $m$ . Note that all fields of the dynamo problem are generally time-dependent. Therefore, the scalar functions  $t_l^m$  and  $p_l^m$  in Eq. (4.12) depend on the radius  $r$  and time  $t$ . Furthermore, the complex-valued spherical harmonics are given by

$$Y_l^m(\theta, \varphi) = N_l^m P_l^m(\cos(\theta)) \exp(im\varphi), \quad N_l^m = \sqrt{\frac{2l+1}{4\pi} \frac{(l-m)!}{(l+m)!}}. \quad (4.13)$$

The factor  $N_l^m$  is a normalization factor and chosen such that the two spherical harmonics are orthonormal with respect to the inner product on a spherical surface. For two complex-valued functions  $f$  and  $g$ , this inner product is defined as

$$\langle f, g \rangle := \oint_{\partial\mathcal{B}_r} f(\mathbf{x}) g^*(\mathbf{x}) d\Omega, \quad (4.14)$$

where  $g^*$  denotes the complex conjugate of the function  $g$  and  $d\Omega = \sin(\theta) d\theta d\varphi$ . Here,  $\partial\mathcal{B}_r$  denotes the surface of a sphere of radius  $r$ . Using this inner product, the orthogonality of the spherical harmonics reads

$$\langle Y_k^m, Y_l^n \rangle = \delta^{mn} \delta_{kl}, \quad (4.15)$$

where  $\delta^{ij} = \delta_{ij}$  denotes the KRONECKER symbol.

A collection of spherical harmonics is shown in Fig. 4.3. From this illustration, it can be observed that the indices  $l$  and  $m$  determine the number of sign changes of a spherical harmonic on the surface of a sphere. On a circle of a constant polar angle  $\theta$ , the value of  $m$  specifies the number of sign changes. Furthermore, on a line of a constant azimuthal angle  $\varphi$ ,  $n - m$  sign changes occur.

The series expansion of the toroidal and poloidal scalars  $T$  and  $P$  in terms of spherical harmonics implies an expansion of the toroidal and poloidal vector fields in terms of corresponding harmonic components. This expansion reads

$$\mathbf{T}(r, \theta, \varphi, t) = \sum_{l=1}^{\infty} \sum_{m=-l}^l \mathbf{t}_l^m(r, \theta, \varphi, t), \quad (4.16a)$$

$$\mathbf{P}(r, \theta, \varphi, t) = \sum_{l=1}^{\infty} \sum_{m=-l}^l \mathbf{p}_l^m(r, \theta, \varphi, t), \quad (4.16b)$$

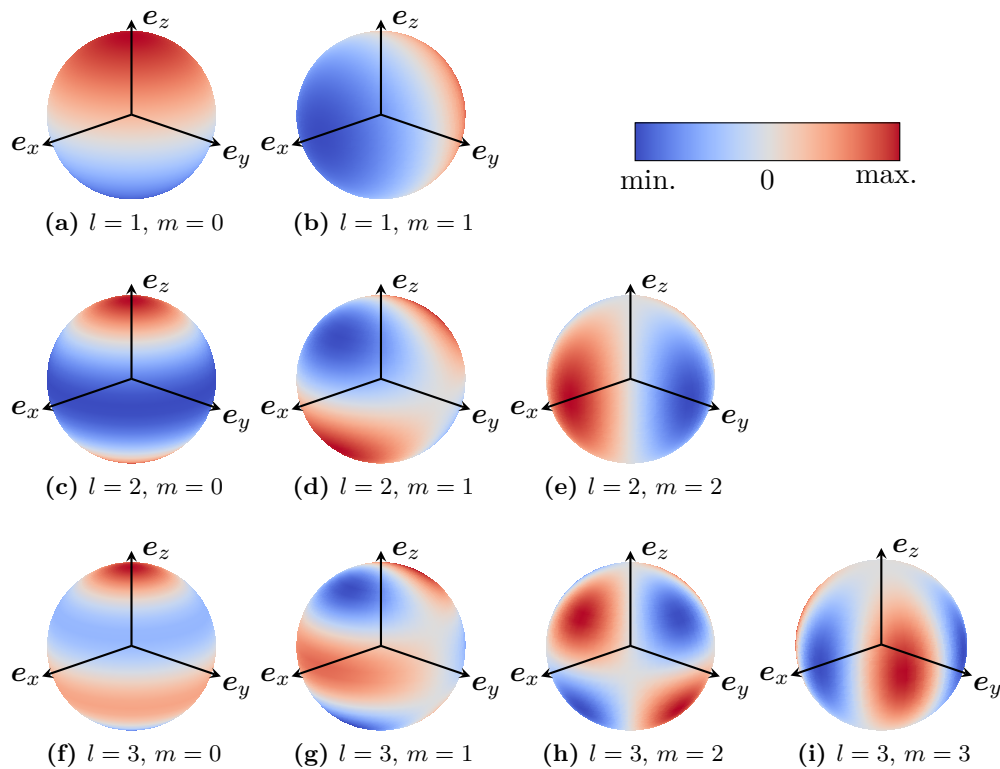


**Figure 4.3:** Illustration of the spherical harmonics up to the third degree on the surface of a sphere. The real parts of the normalized spherical harmonics (or more precisely:  $2\Re(Y_n^m)$ ) are visualized, which correspond to the cosine parts. The spherical harmonic of degree zero is omitted because it is constant.

where the toroidal and poloidal components  $\mathbf{t}_l^m$  and  $\mathbf{p}_l^m$  are given by

$$\mathbf{t}_l^m(r, \theta, \varphi, t) = \nabla \times t_l^m(r, t) Y_l^m(\theta, \varphi) \mathbf{e}_r, \quad (4.17a)$$

$$\mathbf{p}_l^m(r, \theta, \varphi, t) = \nabla \times \nabla \times p_l^m(r, t) Y_l^m(\theta, \varphi) \mathbf{e}_r. \quad (4.17b)$$

Figure 4.4 shows some toroidal components  $\mathbf{p}_l^m$  on the surface of a sphere. The visualization on a surface of a sphere is sufficient for toroidal fields, since their components are tangential to the surface. By examining the fields in Fig. 4.4, it is apparent that for  $m = 0$  the vector field is purely circumferential, *i.e.*, there is no component in the  $\theta$ -direction. If  $m$  is non-zero, then vortex-like structures appear and the number of vortices increases with increasing  $l$  and  $m$ . Complementary, Fig. 4.5 depicts some poloidal components  $\mathbf{p}_l^m$ . These fields are visualized partly on the surface of the sphere and on additional planes resulting from a cut with one-eighth of the sphere. These cutting planes are used to gain insight into the interior structure of poloidal fields, which is strongly dominated by the choice of

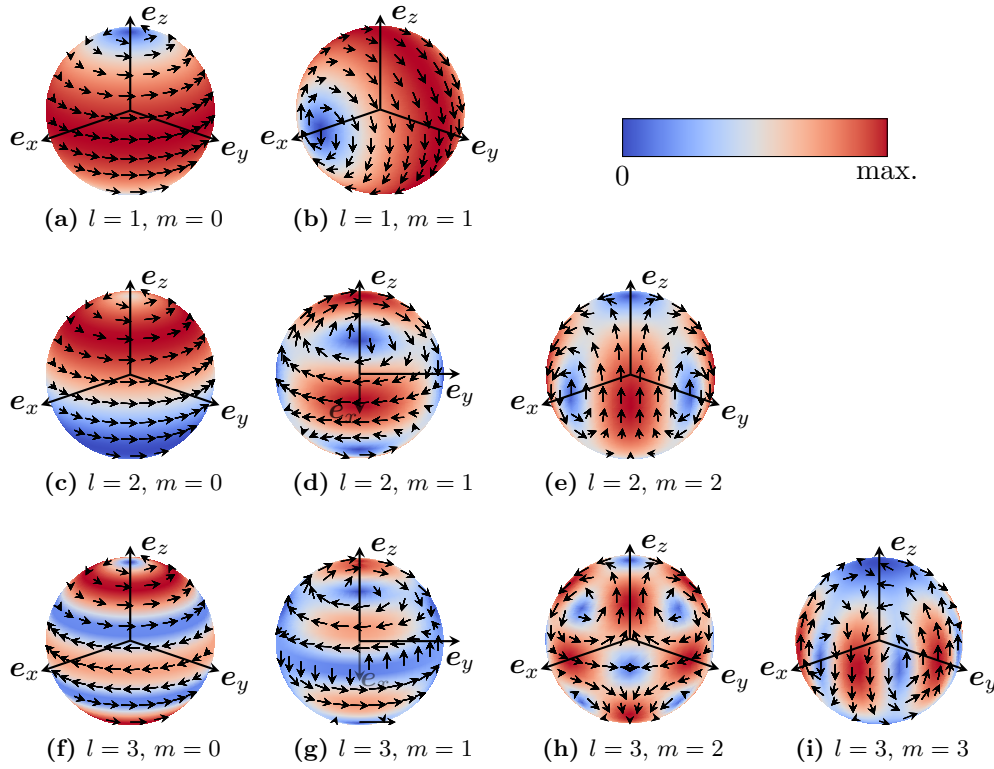


**Figure 4.4:** Illustration of toroidal vector fields  $\mathbf{t}_l^m$  up to the third degree on the surface of a sphere. The real parts of complex-valued toroidal vector fields are visualized. The fields are plotted on a spherical surface and therefore the radial functions are irrelevant. Color indicates the magnitude, and the arrows represent the directions of the vector fields.

the radial functions  $p_l^m$ . It should also be noted that for  $l = 1$  the poloidal fields  $\mathbf{p}_1^m$  are constant and proportional to the CARTESIAN basis vectors.

In the following, the orthogonality of the toroidal and poloidal vector fields is demonstrated by means of an operator-based formalism. More precisely, the orthogonality of the toroidal and poloidal components  $\mathbf{t}_l^m$  and  $\mathbf{p}_l^m$  is considered. If the inner product in Eq. (4.14) is applied for vector fields, *e.g.*,  $\mathbf{f}$  and  $\mathbf{g}$ , then the scalar product  $\mathbf{f} \cdot \mathbf{g}^*$  needs to be used in the integral. Both the toroidal and poloidal vector fields represent an invariant subspace of the curl-operator, because the curl of a toroidal field is a poloidal field and *vice versa*. The first property is obvious from the definitions of the fields and the second property will be shown in the following. In order to do so, it is convenient to introduce the following two operators  $\nabla_{\theta,\varphi}$  and  $\mathcal{D}_{\theta,\varphi}$

$$\nabla_{\theta,\varphi} := \mathbf{e}_\theta \frac{\partial}{\partial \theta} + \mathbf{e}_\varphi \frac{1}{\sin(\theta)} \frac{\partial}{\partial \varphi}, \quad \mathcal{D}_{\theta,\varphi} := \mathbf{e}_\theta \frac{1}{\sin(\theta)} \frac{\partial}{\partial \varphi} - \mathbf{e}_\varphi \frac{\partial}{\partial \theta}. \quad (4.18)$$

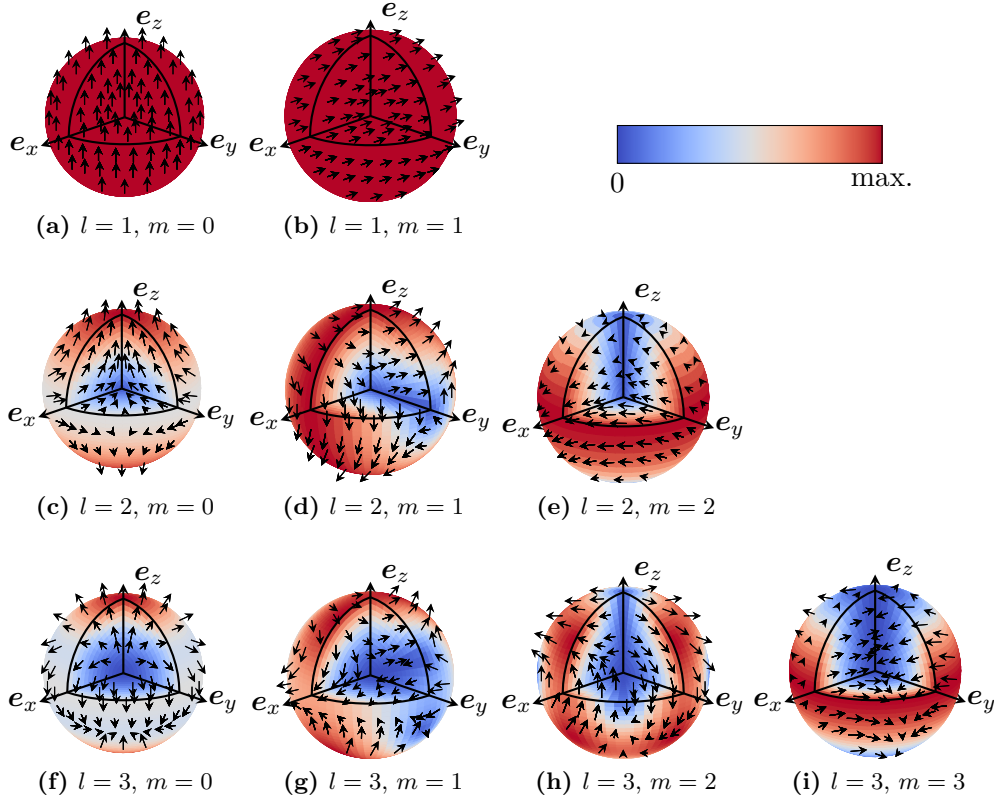


**Figure 4.5:** Illustration of poloidal vector fields  $\mathbf{p}_l^m$  up to the third degree. The real parts of complex-valued poloidal vector fields are visualized with the radial functions  $p_l^m(r) = r^{l+1}$ . Color indicates the magnitude and the arrows represent the directions of the vector fields.

This leads to the following compact representations of toroidal and poloidal vector fields:

$$\mathbf{t}_l^m(r, \theta, \varphi, t) = \frac{1}{r} t_l^m(r, t) \mathcal{D}_{\theta, \varphi} [Y_l^m], \quad (4.19a)$$

$$\mathbf{p}_l^m(r, \theta, \varphi, t) = l(l+1) \frac{p_l^m(r, t)}{r^2} Y_l^m(\theta, \varphi) \mathbf{e}_r + \frac{1}{r} \frac{dp_l^m}{dr} \nabla_{\theta, \varphi} Y_l^m. \quad (4.19b)$$

In order to obtain the representations above, the representation of the curl in spherical coordinates is applied. For toroidal fields, the curl of a purely radial vector field is required and the evaluation is rather simple. By using this preliminary result for the toroidal field, a second application of the curl leads to the expression for the poloidal field stated above. In order to determine the curl of a poloidal field, its additive nature and linearity is exploited. The curl of the first term directly yields an expression containing the operator  $\mathcal{D}_{\theta, \varphi}$  and the second term needs to be computed using the curl in spherical coordinates. Finally, the curl of a poloidal

field reads

$$\nabla \times \mathbf{p}_l^m = \frac{1}{r} \left( l(l+1) \frac{p_l^m(r, t)}{r^2} - \frac{d^2 p_l^m}{dr^2} \right) \mathcal{D}_{\theta, \varphi} [Y_l^m]. \quad (4.20)$$

This confirms the statement above regarding the representation of the invariant subspace of toroidal and poloidal functions.

In order to show the orthogonality, the following properties of the introduced operators are stated:

$$\mathcal{D}_{\theta, \varphi} \cdot \nabla_{\theta, \varphi} f = \nabla_{\theta, \varphi} \cdot \mathcal{D}_{\theta, \varphi} [f] = 0, \quad (4.21a)$$

$$\mathcal{D}_{\theta, \varphi} [f] \cdot \mathcal{D}_{\theta, \varphi} [g] = \frac{\partial f}{\partial \theta} \frac{\partial g}{\partial \theta} + \frac{1}{\sin^2(\theta)} \frac{\partial f}{\partial \varphi} \frac{\partial g}{\partial \varphi} = \nabla_{\theta, \varphi} f \cdot \nabla_{\theta, \varphi} g, \quad (4.21b)$$

$$\mathcal{D}_{\theta, \varphi} \cdot \mathcal{D}_{\theta, \varphi} [f] = \nabla_{\theta, \varphi}^2 f. \quad (4.21c)$$

All of these relations may be derived from the definitions of the operators and the partial derivatives of the spherical basis vectors w.r.t. to the coordinates  $r$ ,  $\theta$  and  $\varphi$ . Note that the two latter relations for the operator  $\mathcal{D}_{\theta, \varphi}$  are similar to the respective properties of the del-operator  $\nabla_{\theta, \varphi}$ .

In order to discuss the orthogonality properties of the considered vector fields, the divergence theorem on a closed surface is required [Elsasser (1946a)]: On a closed surface  $S \subset \mathbb{R}^3$ , *i.e.*,  $\partial S = \emptyset$ , the surface integral of the surface divergence  $\nabla_S \cdot \mathbf{f}$  vanishes if the vector field  $\mathbf{f}$  is tangential, *i.e.*,  $\mathbf{f} \cdot \mathbf{n} = 0$  holds everywhere on  $S$ . Hence,

$$\oint_S \nabla_S \cdot \mathbf{f} \, dA = 0. \quad (4.22)$$

For a proof of this theorem see Glane, Reich, and Müller [2018]. By construction, the fields generated by the operators  $\mathcal{D}_{\theta, \varphi}$  and  $\nabla_{\theta, \varphi}$  are tangential to any spherical surface  $\partial \mathcal{B}_r$  of radius  $r$ . Thus, the theorem above is applicable and GREEN'S identity for a spherical surface reads

$$\begin{aligned} \oint_{\partial \mathcal{B}_r} \nabla_{\theta, \varphi} f \cdot \nabla_{\theta, \varphi} g \, dA &= \oint_{\partial \mathcal{B}_r} \nabla_{\theta, \varphi} \cdot (f \nabla_{\theta, \varphi} g) \, dA - \oint_{\partial \mathcal{B}_r} f \nabla_{\theta, \varphi}^2 g \, dA \\ &= - \oint_{\partial \mathcal{B}_r} f \nabla_{\theta, \varphi}^2 g \, dA. \end{aligned} \quad (4.23a)$$

By using Eq. (4.21) in combination with the statement above, the inner products are given by

$$\langle \mathcal{D}_{\theta, \varphi} [f], \mathcal{D}_{\theta, \varphi} [g] \rangle = \langle \nabla_{\theta, \varphi} f, \nabla_{\theta, \varphi} g \rangle = - \oint_{\partial \mathcal{B}_r} f \nabla_{\theta, \varphi}^2 g^* \, d\Omega. \quad (4.23b)$$

By substituting the general functions  $f$  and  $g$  with two spherical harmonics and using Eq. (4.15) as well as  $\nabla_{\theta, \varphi}^2 Y_l^m = -l(l+1)Y_l^m$ , the following orthogonality

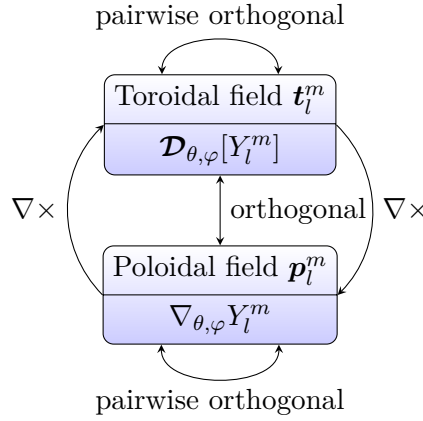


**Figure 4.6:** Properties of toroidal and poloidal vector fields in relation to orthogonality and the curl-operation. Pairwise orthogonality refers to the orthogonality of two vector fields with non-matching index pairs. Adopted from Glane, Reich, and Müller [2018].

properties of the operators  $\nabla_{\theta, \varphi}$  and  $\mathcal{D}_{\theta, \varphi}$  are established:

$$\langle \mathcal{D}_{\theta, \varphi}[Y_k^m], \mathcal{D}_{\theta, \varphi}[Y_l^n] \rangle = l(l+1) \langle Y_k^m, Y_l^n \rangle = l(l+1) \delta^{mn} \delta_{kl}, \quad (4.24a)$$

$$\langle \nabla_{\theta, \varphi} Y_k^m, \nabla_{\theta, \varphi} Y_l^n \rangle = l(l+1) \langle Y_k^m, Y_l^n \rangle = l(l+1) \delta^{mn} \delta_{kl}, \quad (4.24b)$$

$$\langle \mathcal{D}_{\theta, \varphi}[Y_k^m], \nabla_{\theta, \varphi} Y_l^n \rangle = 0. \quad (4.24c)$$

This result demonstrates that the pairwise orthogonality of  $\mathcal{D}_{\theta, \varphi}[Y_k^m]$  and  $\nabla_{\theta, \varphi} Y_l^n$  is an immediate consequence of the pairwise orthogonality of the related spherical harmonics. Hence, toroidal and poloidal vector fields are pairwise orthogonal as well. This directly follows because the vector  $\mathbf{e}_r$  is orthogonal to the operators  $\nabla_{\theta, \varphi}$  and  $\mathcal{D}_{\theta, \varphi}$  because of the geometry.

Figure 4.6 briefly summarizes the introduced operators and the properties of the corresponding vector fields. It presents an overview of the orthogonality properties of toroidal and poloidal vector fields w.r.t. the inner product introduced in Eq. (4.14). In this regard, pairwise orthogonality means that the corresponding vector fields are orthogonal if two toroidal or poloidal harmonic components with non-matching index pairs are considered. In Fig. 4.6, the operators introduced in relation to the respective fields are also indicated. Moreover, the mapping properties of the curl-operator w.r.t. toroidal and poloidal vector fields are visualized. Hence, the curl of a toroidal vector field is poloidal and *vice versa*.

Next, some of the advantages of the application of the toroidal-poloidal decomposition to the numerical dynamo problem are discussed. The most obvious advantage is that the considered fields are by definition solenoidal. Thus, the decomposition is suitable for the magnetic field and the velocity field. The toroidal-poloidal decomposition was used for the first time in a numerical code for a kinematic dynamo problem by [Bullard and Gellman (1954)]. In order to do so, the magnetic field as well as the velocity field are expressed in terms of a toroidal-poloidal series.

As a result, a system of ordinary differential equations of the kinematic dynamo problem is obtained in the toroidal-poloidal decomposition [Bullard and Gellman (1954)]. The resulting system is formulated in terms of an eigenvalue problem for the radial functions of the magnetic field for an arbitrary solenoidal velocity field and up to any degree of the toroidal-poloidal expansion. However, the methods and steps for obtaining this system are not elaborated in greater detail and cannot be deduced for an arbitrary degree of expansion by using basic mathematical procedures. A detailed overview of the steps required is presented in Glane, Reich, and Müller [2018].

As indicated above, the kinematic dynamo problem constitutes an eigenvalue problem, in which the magnetic field is the only solution variable. In contrast to this, the fully coupled numerical dynamo problem requires to evolve all fields as functions of time. Therefore, the treatment of the fully coupled problem is significantly different. In both cases, a projection of the governing partial differential equations to a toroidal-poloidal space (spectral space) is applied to obtain ordinary differential equations governing the radial functions. However, for the kinematic dynamo problem, the projections of the toroidal-poloidal decomposition of the non-linear term  $\nabla \times (\mathbf{v} \times \mathbf{B})$  are required. For the coupled problem, explicit expressions of the projections of the non-linear terms are not required which significantly simplifies the numerical implementation and the solution procedure. The solution technique for the coupled problem is referred to as a pseudo-spectral method. In this regard it should be remarked that this technique can only be applied if certain time stepping schemes are used. In other words, the pseudo-spectral method limits the time stepping schemes which can be applied.

The so-called projections of the governing partial differential equations to a toroidal-poloidal space (spectral space) is similar to a GALERKIN method. From this perspective, the toroidal and poloidal projectors  $\mathbf{t}_n^m$  and  $\mathbf{p}_n^m$  are the test functions and the *ansatz* or trial functions are given by the toroidal and poloidal components of the respective field. However, after a projection, the result still depends on the time and on the radius. Therefore, the presented method is not a GALERKIN method in its original sense. Only the angular dependencies are eliminated through integration.

Subsequently, the toroidal-poloidal decomposition is discussed with respect to the formulation of the magnetic induction equation in Eqs. (4.2). The magnetic field is expressed in terms of its toroidal and poloidal components in the following way:

$$\mathbf{B}(r, \theta, \varphi, t) = \sum_{l=1}^{\infty} \sum_{m=-l}^l (\mathbf{t}_l^m(r, \theta, \varphi, t) + \mathbf{p}_l^m(r, \theta, \varphi, t)). \quad (4.25)$$

Because of the fact that the non-linear terms are treated in a pseudo-spectral way, they are not considered any further.<sup>1</sup> As a consequence, only the linear terms

<sup>1</sup>Note that the full spectral treatment of the magnetic induction equation is presented in Glane, Reich, and Müller [2018].

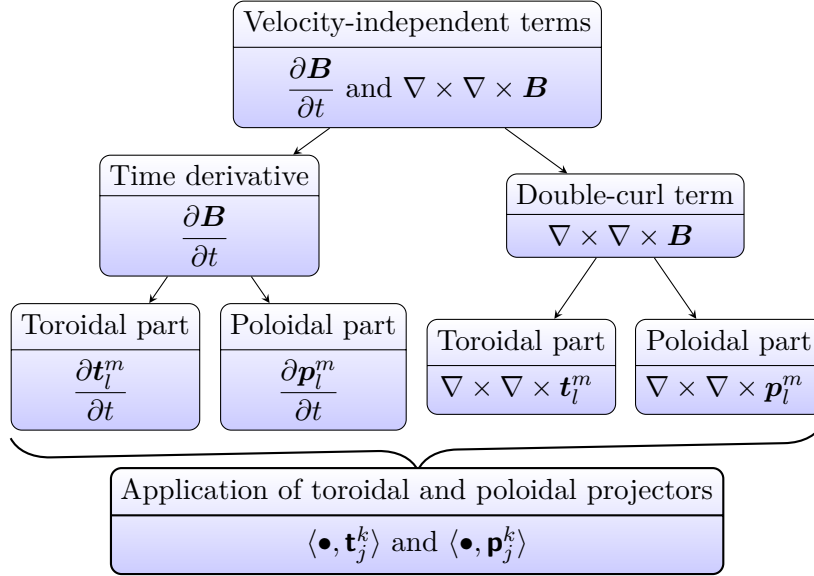


**Figure 4.7:** Toroidal-poloidal decomposition of the velocity-independent terms in the magnetic induction equation. Adopted from Glane, Reich, and Müller [2018].

in the magnetic induction equation and their projections need to be considered. The toroidal-poloidal decomposition of these terms is shown in Fig. 4.7. When the projections of the individual terms in Fig. 4.7 are considered, specifications of the toroidal and poloidal projectors  $\mathbf{t}_l^m$  and  $\mathbf{p}_l^m$  are required. While several variants of projectors are possible [Glane, Reich, and Müller (2018)], the projectors used by BULLARD and GELLMAN will be considered subsequently. These projectors are

$$\mathbf{t}_l^m(r, \theta, \varphi) := \frac{1}{r} \mathcal{D}_{\theta, \varphi}[Y_l^m](\theta, \varphi), \quad \mathbf{p}_l^m(r, \theta, \varphi) := l(l+1) \frac{1}{r^2} Y_l^m(\theta, \varphi) \mathbf{e}_r. \quad (4.26)$$

If the projections of two terms in Fig. 4.7, which involve the time derivative, are considered, the orthogonality of the toroidal and poloidal components can be exploited directly. This orthogonality also holds regarding the projectors, and the non-vanishing projections are given by

$$\left\langle \frac{\partial \mathbf{t}_k^m}{\partial t}, \mathbf{t}_l^n \right\rangle = \frac{1}{r^2} \frac{\partial t_k^m}{\partial t} \delta_{kl} \delta^{mn}, \quad (4.27a)$$

$$\left\langle \frac{\partial \mathbf{p}_k^m}{\partial t}, \mathbf{p}_l^n \right\rangle = k(k+1)l(l+1) \frac{1}{r^4} \frac{\partial p_k^m}{\partial t} \delta_{kl} \delta^{mn}. \quad (4.27b)$$

Note that the presence of the two KRONECKER symbols indicates the orthogonality and that the toroidal and poloidal components are uncoupled regarding the terms involving the time derivative. This orthogonality and the property of uncoupling also applies for the terms in Fig. 4.7, which involve the double-curl. This can be concluded because, for example, the curl of a poloidal vector field is toroidal

and the curl of the resulting toroidal vector field is a poloidal vector field again. Thus, the double-curl operator does not change the type of the field with respect to the toroidal-poloidal decomposition. Due to the orthogonality of toroidal and poloidal vector fields, the double-curl terms in Fig. 4.7 are orthogonal as well. In order to obtain the related expressions in an explicit form, the double-curl of the toroidal and the poloidal components are computed by a straight-forward calculation, namely,

$$\nabla \times \nabla \times \mathbf{t}_l^m = \frac{1}{r} \left( \frac{l(l+1)}{r^2} t_l^m(r, t) - \frac{\partial^2 t_l^m}{\partial r^2} \right) \mathcal{D}_{\theta, \varphi}[Y_l^m], \quad (4.28a)$$

$$\begin{aligned} \nabla \times \nabla \times \mathbf{p}_l^m &= \frac{l(l+1)}{r^2} \left( \frac{l(l+1)}{r^2} p_l^m(r, t) - \frac{\partial^2 p_l^m}{\partial r^2} \right) Y_l^m(\theta, \varphi) \mathbf{e}_r + \\ &+ \frac{1}{r^2} \frac{\partial}{\partial r} \left( \frac{l(l+1)}{r^2} p_l^m(r, t) - \frac{\partial^2 p_l^m}{\partial r^2} \right) \nabla_{\theta, \varphi} Y_l^m. \end{aligned} \quad (4.28b)$$

Applying the projectors defined in Eq. (4.26) yields the two non-vanishing double-curl terms

$$\langle \nabla \times \nabla \times \mathbf{t}_k^m, \mathbf{t}_l^n \rangle = \frac{1}{r^2} \left( \frac{l(l+1)}{r^2} t_k^m(r, t) - \frac{\partial^2 t_k^m}{\partial r^2} \right) \delta_{kl} \delta^{mn}, \quad (4.29a)$$

$$\langle \nabla \times \nabla \times \mathbf{p}_k^m, \mathbf{p}_l^n \rangle = k(k+1)l(l+1) \frac{1}{r^4} \left( \frac{l(l+1)}{r^2} p_k^m(r) - \frac{\partial^2 p_k^m}{\partial r^2} \right) \delta_{kl} \delta^{mn}. \quad (4.29b)$$

In summary, the brief analysis of the linear and velocity-independent terms in the magnetic induction equation shows that these terms are mutually orthogonal regarding their toroidal and poloidal components. As a consequence, after projection the double summation in Eq. (4.25) reduces to the evaluation of a single term with the same index pair as the toroidal or poloidal projector, respectively. The two resulting equations are, thus, given by

$$\frac{\partial t_l^m}{\partial t} + \frac{1}{Pm} \left( \frac{\partial^2 t_l^m}{\partial r^2} - \frac{l(l+1)}{r^2} t_l^m(r, t) \right) = r^2 \langle \nabla \times (\mathbf{v} \times \mathbf{B}), \mathbf{t}_l^m \rangle, \quad (4.30a)$$

$$\frac{\partial p_l^m}{\partial t} + \frac{1}{Pm} \left( \frac{\partial^2 p_l^m}{\partial r^2} - \frac{l(l+1)}{r^2} p_l^m(r, t) \right) = \frac{r^4}{l^2(l+1)^2} \langle \nabla \times (\mathbf{v} \times \mathbf{B}), \mathbf{p}_l^m \rangle, \quad (4.30b)$$

where the two right-hand sides are treated in a pseudo-spectral way, which is described in Sect. 4.2.3, below.

The orthogonality of the toroidal-poloidal decomposition is exploited in the *Rayleigh* software and allows a simplified and efficient discretization of the dynamo problem. Apart from the magnetic field, the toroidal-poloidal decomposition is also applied to the velocity field  $\mathbf{v}$ . This requires to compute projections of the momentum equation. Note that the scalar fields of pressure and temperature are also expressed in terms of spherical harmonics, which also allows to exploit the related orthogonality properties when the temperature equation and the

incompressibility constraint are considered. Details regarding the incompressibility constraint, which leads to a POISSON equation for the pressure, and the treatment of the momentum and the heat conduction equation are not detailed further in this context but can be found in the appendix of the paper by Brun, Miesch, and Toomre [2004], where the resulting equations of the full problem are stated.

## 4.2.2 Radial and temporal discretization

While the discretization of the dynamo problem with respect to the angular coordinates  $\theta$  and  $\varphi$  was described in Sect. 4.2.1, this section considers the radial and temporal discretization. The choice of using the toroidal-poloidal decomposition together with a pseudo-spectral approach restricts the types of time discretization schemes which can be applied in practice. This means that the different discretization methods applied for the time and the spatial coordinates cannot be regarded independently but rather depend upon each other. For the sake of brevity, the discretization of the radial coordinate and the time is discussed with respect to the magnetic induction equation, because the discretization of the other equations of the dynamo problem can be inferred from that of the magnetic induction equation.

In *Rayleigh*, the radial coordinate  $r$  is discretized using CHEBYSHEV polynomials  $T_k$ . CHEBYSHEV polynomials are orthogonal polynomials on the interval  $(-1, 1)$  and their application requires the transformation of the radial domain to this interval. Using CHEBYSHEV polynomials, the series expansions of the functions  $t_l^m$  and  $p_l^m$ , which are describing the dependence of toroidal and poloidal scalars in Eq. (4.12) on the radius and the time, are given by

$$t_l^m(r, t) = \sum_{k=1}^{\infty} t_{l,k}^m(t) T_k(\xi(r)), \quad p_l^m(r, t) = \sum_{k=1}^{\infty} p_{l,k}^m(t) T_k(\xi(r)), \quad (4.31)$$

where the function  $\xi(r) = (1+a)/(1-a) - 2r$  transforms the radial coordinate to the interval  $(-1, 1)$ .

The time is discretized in *Rayleigh* using an implicit-explicit (IMEX) scheme. These schemes treat linear terms implicitly and the non-linear terms explicitly. The designations “implicit” and “explicit” refer to ‘at which timestep the respective terms are evaluated.’ Implicit treatment means that the terms are evaluated at the sought-for time  $t_{n+1}$  and may also be evaluated at previous times  $t_n$ ,  $t_{n-1}$ , etc., in order to obtain a solution. Explicit treatment refers to an evaluation at previous times only, *i.e.*, at  $t_n$  and  $t_{n-1}$ . There are several variants of IMEX schemes [Ascher, Ruuth, and Wetton (1995)]. However, in *Rayleigh* only the second order CRANK–NICOLSON–ADAMS–BASHFORTH scheme is available, whose version for fixed timesteps of size  $\Delta t$  will be presented below. A version for variable timestepping is presented in Wang and Ruuth [2008] and is also available in *Rayleigh*. Using the notation  $\mathbf{B}^i = \mathbf{B}(\mathbf{x}, t_i)$ , the application of the considered

timestepping scheme to the magnetic induction equation (4.2)<sub>5</sub> yields

$$\begin{aligned} \frac{\mathbf{B}^{n+1} - \mathbf{B}^n}{\Delta t} - \frac{1}{Pm} \frac{1}{2} (\nabla \times \nabla \times \mathbf{B}^{n+1} + \nabla \times \nabla \times \mathbf{B}^n) \\ = \frac{3}{2} \nabla \times (\mathbf{v}^n \times \mathbf{B}^n) - \frac{1}{2} \nabla \times (\mathbf{v}^{n-1} \times \mathbf{B}^{n-1}). \end{aligned} \quad (4.32)$$

This equation is solved for the magnetic field  $\mathbf{B}^{n+1}$  at the sought-for time  $t_{n+1}$ . While this formulation of the timestepping scheme is formulated in a way that is independent of the spatial discretization, the scheme is actually applied to Eqs. (4.30) to compute the coefficients  $t_{l,k}^m$  and  $p_{l,k}^m$ . More precisely, the equations governing the coefficients are obtained from a version of Eqs. (4.30), which incorporates the time discretization indicated above after a substitution of Eq. (4.31). In conclusion, a linear system for the CHEBYSHEV coefficients of each toroidal and poloidal component results. The right-hand side of this linear system consists of the linear terms from the previous timesteps and the non-linear terms, which are treated using a pseudo-spectral approach.

### 4.2.3 Pseudo-spectral treatment

The pseudo-spectral treatment of the non-linear terms of the dynamo problem in *Rayleigh* is addressed in the following. While the linear terms are treated in the spectral space, which means that, *e.g.*, the magnetic field is described by the coefficients  $t_{l,k}^m$  and  $p_{l,k}^m$ , this is not the case for the non-linear terms. These terms are transformed from the spectral  $(k, l, m)$  to the physical space  $(r, \theta, \varphi)$  and then back to the spectral space, which requires the availability of highly performant transformations between the two spaces. The transforms between the two spaces consists of a sequential application of a discrete CHEBYSHEV, LEGENDRE and FOURIER transform. The discrete CHEBYSHEV and FOURIER transforms can be performed by applying a fast FOURIER transform, which is computationally highly efficient. Figure 4.8 illustrates the transformation of the scalar toroidal and poloidal components from the spectral to the physical space. Because of the fact that the toroidal-poloidal decomposition also involves derivatives of the respective scalars, these derivatives are also computed in the process of the transformation by applying recurrence relations of the respective functions. Furthermore, note that the resulting physical space is represented by a discrete grid  $(r_k, \theta_l, \varphi_m)$ . If the values of the toroidal and poloidal scalars and their derivatives are known on this grid, the magnetic field can be computed as well. If, additionally, the same transformation is applied to the toroidal and poloidal scalars, which are associated to the velocity field, both the magnetic and velocity field are known in the physical space and their cross product  $\mathbf{v} \times \mathbf{B}$  can be computed in a simple manner. In order to obtain the toroidal-poloidal decomposition of this cross product, *i.e.*, the projections with respect to the projectors  $\mathbf{t}_l^m$  and  $\mathbf{p}_l^m$ , the transformation

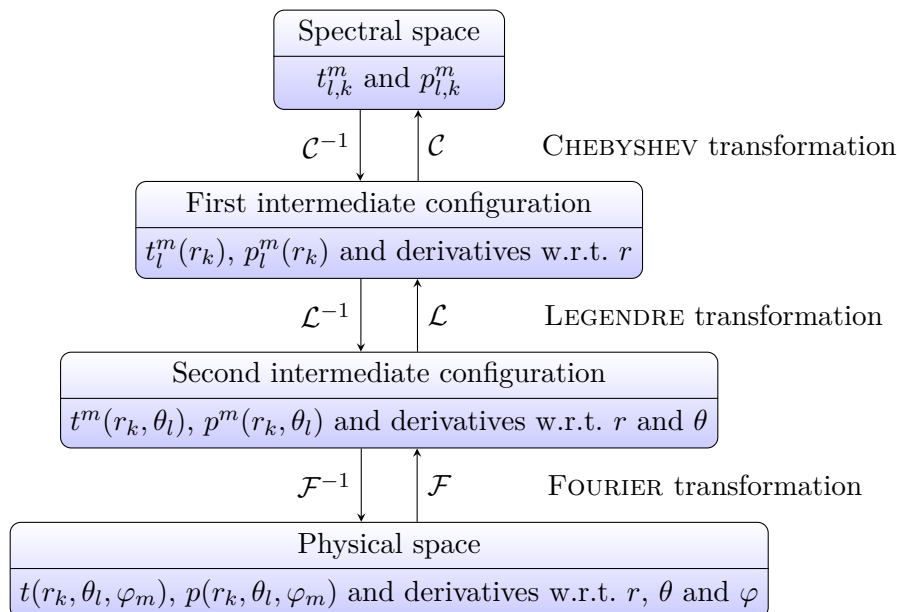


**Figure 4.8:** Transformation of the magnetic field from the spectral to the physical space. Note that  $\mathcal{C}$  denotes the (discrete) CHEBYSHEV transformation,  $\mathcal{L}$  the LEGENDRE transformation and  $\mathcal{F}$  the FOURIER transformation.

procedure is reverse. In the reverse transformation, the derivatives associated to the curl  $\nabla \times (\mathbf{v} \times \mathbf{B})$  are taken into account.

This section concludes the brief discussion of the numerical treatment of the dynamo problem. Due to the complexity of the problem, not all aspects of the numerical code could be addressed in detail. For further information regarding the pseudo-spectral treatment, the numerical implementation of the CHEBYSHEV–LEGENDRE–FOURIER transformation and aspects of parallelization, the reader is referred to Glatzmaier [1984], Clune et al. [1999] and Brun, Miesch, and Toomre [2004].

### 4.3 Results

The results, which were obtained using the pseudo-spectral code *Rayleigh*, are presented in the following. Beforehand, the dimensionless parameters of the numerical model are discussed. Moreover, the procedure to obtain a so-called equilibrated solution is also briefly addressed.

As already outlined in Sect. 4.1, the rotating magnetohydrodynamic problem is characterized by the RAYLEIGH number  $Ra$ , the EKMAN number  $Ek$ , the PRANDTL number  $Pr$ , and the magnetic PRANDTL number  $Pm$ . For the outer core of the Earth, Christensen and Wicht specify the following ranges for estimates of some of these parameters  $Ek = 10^{-15}$  to  $10^{-14}$ ,  $Pr = 0.1$  to  $1$  and  $Pm = 10^{-6}$  to  $10^{-5}$  [Christensen and Wicht (2015)]. Due to the low values of the EKMAN number

and the magnetic PRANDTL number, the simulation of a model with dimensionless parameters similar to those of the outer core of the Earth is not feasible, because highly turbulent flows are dominated by extremely small length scales, which require an extremely fine mesh. In fact, such a model cannot be realized on the largest high performance computing centers existing today.

The parameters, which are realistic for the core of the Earth, cannot be applied directly. Therefore, the results presented below make use of higher values of the critical parameters. If this is done, the RAYLEIGH number needs to be chosen appropriately. For the core of the Earth, it is suggested that the ratio of the RAYLEIGH number to the critical RAYLEIGH number  $Ra_c$  for the onset of convection is much larger than unity [Christensen and Wicht (2015)]. However, the exact ratio is not well known due to the uncertainties regarding the thermal evolution of the core of the Earth, see Chap. 2. Numerical dynamo models are generally distinguished with respect to the ratio  $Ra/Ra_c$ . For  $Ra/Ra_c > 10$ , the numerical model is referred to as a strongly driven dynamo, whereas  $Ra/Ra_c < 10$  characterizes a weakly driven dynamo [Christensen and Wicht (2015)]. In order to determine an appropriate critical RAYLEIGH number, the fact that the critical RAYLEIGH number depends on the EKMAN number needs to be taken into account. In fact, the scaling law  $Ra \propto Ek^{-4/3}$  can be inferred by studying the related stability problem [Jones (2007)]. The model parameters in this study were chosen as  $Ra = 2 \times 10^7$ ,  $Ek = 5 \times 10^{-5}$ ,  $Pr = 1$  and  $Pm = 3$ . According to Christensen and Aubert for an EKMAN number of  $Ek = 5 \times 10^{-5}$ , the critical RAYLEIGH number is approximately  $Ra_c \approx 2 \times 10^{-6}$  and thus the considered model with a RAYLEIGH number of  $Ra = 2 \times 10^{-7}$  corresponds to a strongly driven dynamo [Christensen and Aubert (2006)].

For the dynamo model, the initial and boundary conditions of the benchmark case specified in Christensen et al. [2001], which was presented in Sect. 4.1, are applied. While the dimensionless parameters of the benchmark case leads to a quasi-stationary solution without small structures, the solution for the parameters specified above is turbulent and possesses small-scale structures, which require a high spatial resolution. Starting the simulation with the dimensionless parameters specified above and using the initial conditions of the benchmark case is not feasible, because it takes at least 100 viscous diffusion times to equilibrate the solution and approximately 10 million timesteps are required to simulate one viscous diffusion time. Equilibration refers to a limitation of the turbulent fluctuations of the field to a certain range. This range is defined with respect to the volumetric root-mean square values of the temperature and the kinetic and magnetic energies. A start of the model with the benchmark initializations leads to a strong vigorous exchange of energy between the different fields. This process does not only take long because of the low diffusivities, but it also requires small timesteps, which additionally increases the amount of numerical computations required. In order to circumvent a direct cumbersome equilibration of the model, the equilibration is performed in three subsequent steps. Based on an equilibrated benchmark case, a simulation of a preliminary and an intermediate model is performed. The parameters and

**Table 4.3:** Overview of equilibration simulations performed and their parameters.  $\Delta t$  denotes a characteristic size of a timestep of the respective model.  $N_r$  and  $\ell_{\max}$  denote the resolutions with respect to the radial coordinate  $r$  and the angular coordinates  $\theta$ ,  $\varphi$ , respectively.

Designation	Discretization parameters			Model parameters			
	$\ell_{\max}$	$N_r$	$\Delta t$	$Ra$	$Pr$	$Pm$	$Ek$
benchmark case	63	64	$10^{-4}$	$10^5$	1	5	$10^{-3}$
preliminary model	63	64	$10^{-5}$	$3.68 \times 10^5$	1	3	$10^{-3}$
intermediate model	71	72	$10^{-6}$	$7.94 \times 10^6$	1	3	$10^{-4}$
final model	95	120	$10^{-7}$	$2 \times 10^7$	1	3	$5 \times 10^{-5}$

resolutions of all of these models are specified in Table 4.3. Each of the models is simulated for a period of one viscous diffusion time, which corresponds to a dimensionless time of unity. The viscous diffusion time is chosen as the simulation period, because it is the largest timescale in the model. After a simulation of this period, the major part of the vigorous exchange of energy due to inconsistent initial conditions has occurred and the solution is considered as equilibrated. For each of the simulations, the equilibrated solution of the previous model is applied as an initial condition. For example, the intermediate model uses the solution of the preliminary model as an initial condition. Then this model is equilibrated again by simulating a period of one viscous diffusion time.

The discretization parameters of each model are specified in Table 4.3. The resolution with respect to the angular coordinates  $\theta$  and  $\varphi$  is expressed by the degree  $\ell_{\max}$ , at which the spherical harmonic expansion is truncated. The radial resolution is specified by the number of points  $N_r$  in the radial direction, which also implies a truncation of the corresponding CHEBYSHEV series expansion. While the radial resolution can be chosen freely, the angular resolution needs to be adjusted to the number of processors used in the computation [Featherstone (2018)]. The radial and the angular resolutions are refined if the RAYLEIGH number is increased and the EKMAN number is decreased, see Table 4.3. This refinement is required because the solution has finer spatial scales due to the lower viscosity and stronger convection. If these scales are not resolved properly, numerical instabilities can occur. As a consequence of the spatial refinement, the characteristic size of a timestep also decreases by several orders of magnitude. This is due to the COURANT–FRIEDRICHS–LEWY criterion, which is employed in *Rayleigh* to control the size of the timestep. According to Table 4.3, the final model requires approximately ten million timesteps to simulate a dimensionless time period of unity, which is a hundred times more than the preliminary model. However, because of the higher spatial resolution, the numerical effort required

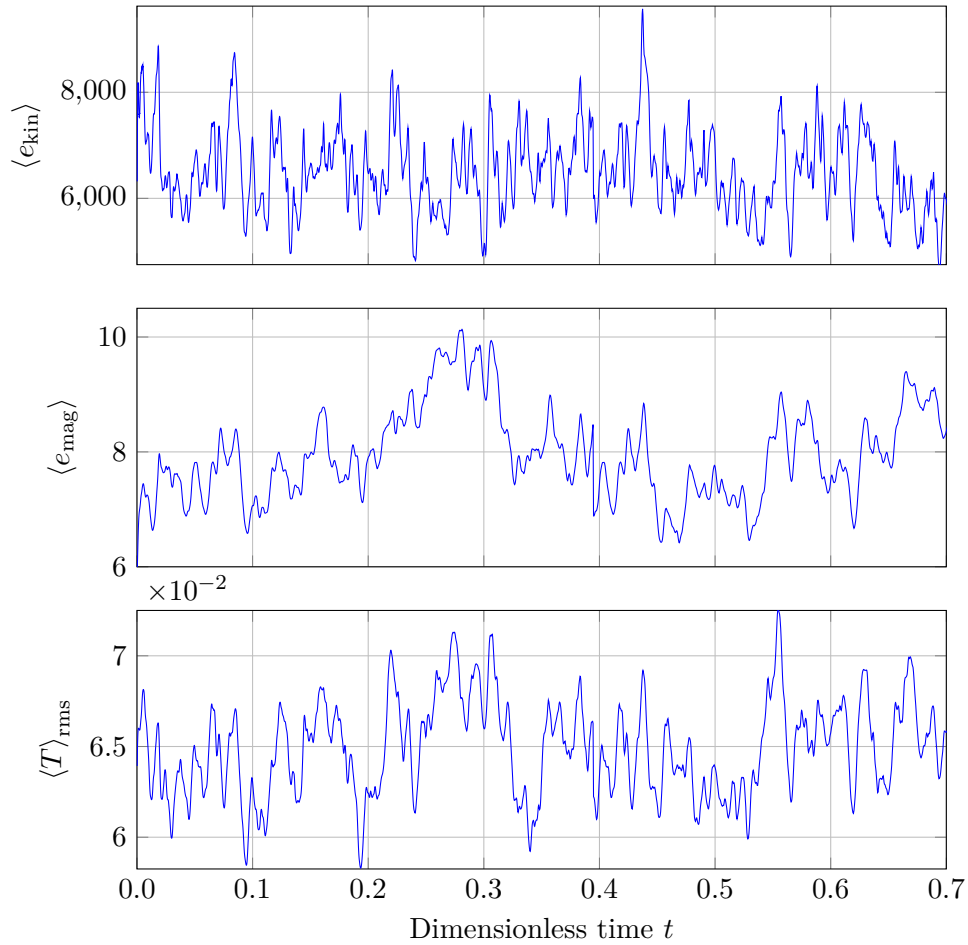


**Figure 4.9:** Turbulent fluctuations of the dimensionless volumetric mean kinetic and magnetic energies and the root mean square of the dimensionless temperature over time.

to simulate the final model exceeds that of the preliminary one by more than a thousand times.

The results of the equilibrated final model are presented subsequently. The evolution of the dimensionless volumetric mean kinetic and magnetic energies over time is shown in Figure 4.9. Furthermore, the volumetric root mean square of the dimensionless temperature is also shown in Fig. 4.9. It is characteristic for the internal energy and is computed according to

$$\langle T \rangle_{\text{rms}}(t) = \sqrt{\frac{1}{V} \int_V T(\mathbf{x}, t)^2 dV} . \quad (4.33)$$

Although the fluctuations in all three quantities are significant, they are limited to a certain range over a period of more than one-half of a viscous diffusion time. Moreover, a clear trend is not observable in any of the quantities and the running

temporal averages are almost constant. The existing fluctuations occur due to the turbulent nature of the solution and are random. Although this randomness is present in all three fields, the fluctuations of the velocity field have a much higher frequency than those of the temperature or the magnetic field. In conclusion, the procedure of a subsequent equilibration of the models can be regarded as successful. The curves in Fig. 4.9 suggest that the temporal fluctuations are solely due to the turbulent nature of the solution. The bulk of the outer core of the Earth is considered to be in a turbulent convective state, which is not affected by any other external interfering source. Thus, the temporal characteristics of the considered dynamo model can be regarded as similar to the core of the Earth. However, because of the large distance of the considered numerical model to the outer core of the Earth in the parameter space, the turbulent fluctuations are not directly comparable with respect to their spatial and temporal features.

In order to provide a visual impression of the spatial features of the equilibrated solution, snapshots of the solution are shown in Fig. 4.10 in the meridional plane. In these snapshots, the solution is shown at the end of the equilibration over one viscous diffusion time. Moreover, a slice of the  $x$ - $z$ -plane is shown and azimuthal averaging was not applied. In a discussion of the spatial structures and features of the solution, the snapshots in Fig. 4.10 cannot be considered individually, because they only give a two-dimensional impression of a three-dimensional field. Therefore, Fig. 4.11, in which the snapshots of the solution are shown in the equatorial plane ( $x$ - $y$ -plane), needs to be taken into account as well.

In general, all fields possess small-scale structures and the length scales of these structures are comparable among all fields. Apart from the radial magnetic field  $B_r$  in the meridional plane, which is shown in Fig. 4.10d, the fields do not seem to have a preferred organization and the size and shape of the structures are rather random. Furthermore, some tendency of organization could be inferred from the radial velocity  $v_r$  in the meridional plane in Fig. 4.10a. For example, in the lower part of Fig. 4.10a below the inner core two large-scale structures are visible in the field of the radial velocity. These structures correspond to an upwelling and downwelling of the fluid and are located inside an imaginary cylinder which has the radius of the inner core. However, if the polar and azimuthal components of the velocity field are considered, a correlation with the two large-scale structure in the radial velocity field cannot be found, which comprises the tendency of an organization of the velocity field.

In summary, from a visual inspection, the solution of the numerical dynamo model suggest that the model experiences a convective motion of the fluid through the entire shell. Moreover, the solution is dominated by random turbulent small-scale structures. While an influence of the inner core may be present, which may yield different features of the solution in- and outside of the imaginary tangent cylinder, this effect is dominated by the features of the turbulent flow. Regarding the inner core, a detailed analysis of its influence is not feasible by considering only two snapshots and is therefore out of the scope of this chapter.

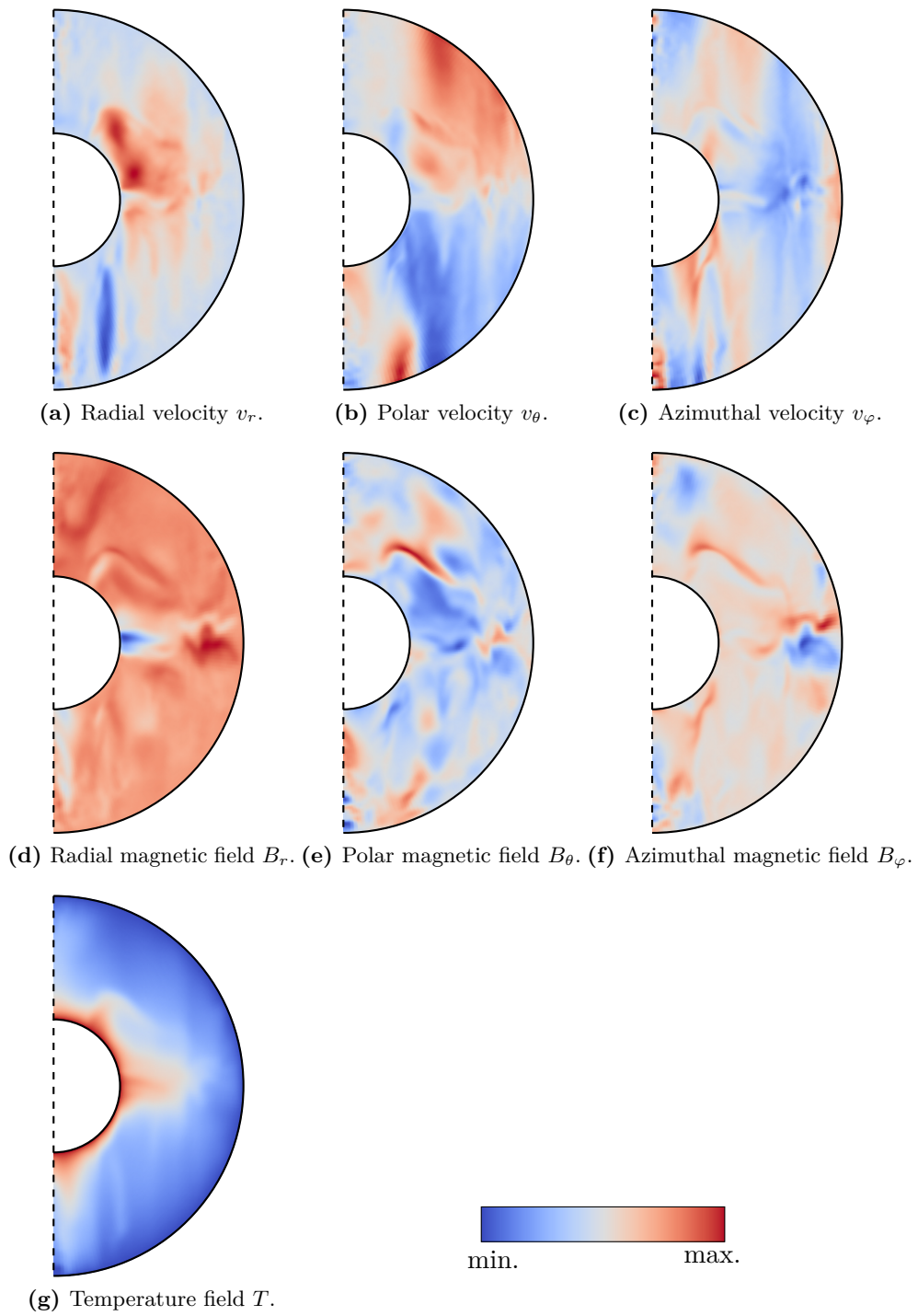


**Figure 4.10:** Snapshots of the equilibrated solution of the final model in the meridional cross section ( $x$ - $z$ -plane).

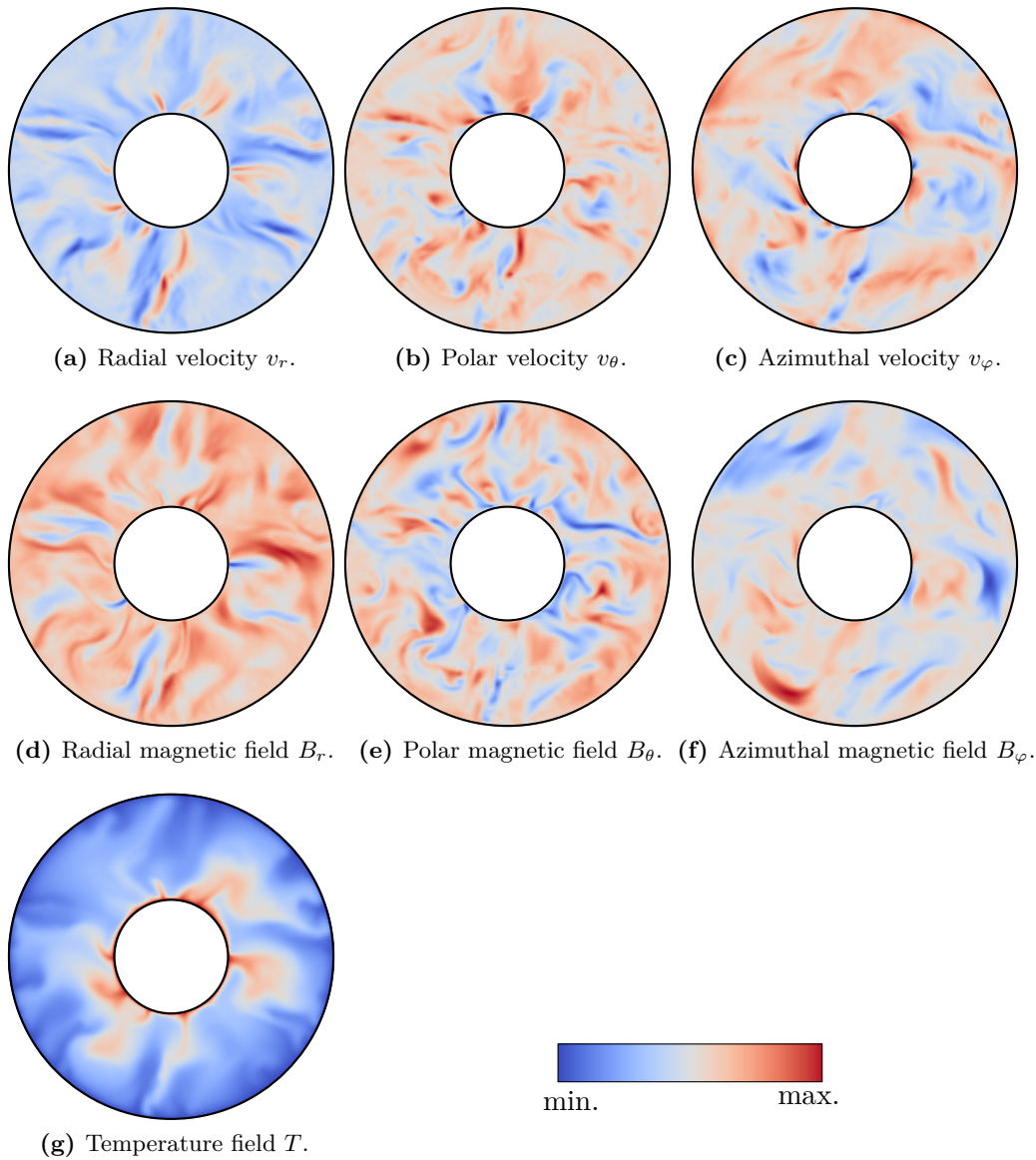


**Figure 4.11:** Snapshots of the equilibrated solution of the final model in the equatorial cross section ( $x$ - $y$ -plane).

## 4.4 Discussion

In this section, the two questions, whether the results presented above are representative for the Earth and whether they are suitable for an application to the core-mantle coupling model presented in Chap. 3, are investigated. While the two snapshots of the solution in Figs. 4.10 and 4.11 give a visual impression of the solution, they are not suitable to assess the model results with respect to the

criteria stated above. Therefore, the model results are assessed by considering dimensionless numbers, which characterize the solution. These numbers are then compared to those estimated for the outer core of the Earth.

As outlined in Sect. 4.1, the numerical dynamo model is described by several dimensionless numbers. These numbers characterize the relative importance of different physical effects but do not entirely characterize the solution, which is obtained from the numerical model. In some cases the dynamo process might fail, which results in a decay of the magnetic field with time. The decay of the magnetic field is not reflected in the model parameters but may be described, *e.g.*, by the ELSASSER number  $\Lambda$ . This dimensionless number represents the ratio of the LORENTZ force to the CORIOLIS acceleration and is defined as

$$\Lambda = \frac{\langle \mathbf{B} \rangle_{\text{rms}}^2}{\rho \mu_0 \eta \Omega^2}. \quad (4.34)$$

Due to the definition of the reference magnetic field in *Rayleigh*, see Sect. 4.1, the ELSASSER number can be obtained from the dimensionless numerical results by simply computing the root mean square of the magnetic field. If the temporal average of this value is computed, the ELSASSER number of the solution is given by  $\Lambda = 16.9$ . For the outer core of the Earth, Olson specifies an approximate ELSASSER number of  $\Lambda \approx 1$  [Olson (2015)]. This value is an order of magnitude smaller than that obtained from the numerical model. However, when comparing the two values it should be kept in mind that the approximation of  $\Lambda \approx 1$  originates from an extrapolation of the strength of the magnetic field at the core-mantle boundary to the entire core of the Earth. Thus the value of the numerical model is not completely unrealistic. Moreover, Christensen and Aubert report that the ELSASSER number varies from  $\Lambda = 0.1$  to  $\Lambda = 100$  in their numerical models [Christensen and Aubert (2006)]. Therefore, the difference of the ELSASSER number of the numerical results considered in this chapter is not surprising. In conclusion, the ELSASSER number does not exactly match the expected value for the outer core of the Earth but it is in the range expected for numerical dynamo models, which are representative for the Earth.

Apart from the ELSASSER number, the (kinetic) REYNOLDS number  $Re$  or the magnetic REYNOLDS number  $Rm$  can be used to characterize the ratio of the inertial acceleration to the viscous forces. Note that the ratio of the REYNOLDS number and the magnetic REYNOLDS number is constant, because the magnetic PRANDTL number is constant, *i.e.*,  $Rm/Re = Pm$ . Due to the choice of the reference velocity, the (kinetic) REYNOLDS number can be obtained from the dimensionless numerical results by computing the root mean square value of the velocity field. This yields a REYNOLDS number of  $Re = 112.6$ , which is several orders of magnitude lower than the value of  $Re = 10^6$  suggested for the outer core of the Earth [Olson (2015)]. However, this discrepancy is due to the high viscosity of the numerical model. Multiplying the (kinetic) REYNOLDS number with the magnetic PRANDTL number gives a magnetic REYNOLDS number of  $Rm = 337.6$ . Using observations of the

magnetic field of the Earth, the magnetic REYNOLDS number of the core can be confined to the range  $300 \leq Rm \leq 600$  [Olson (2015)]. Regarding the magnetic REYNOLDS number, the solution of the numerical model agrees with the range of values expected for the outer core of the Earth. Because of the agreement of the magnetic REYNOLDS number, the numerical dynamo model produces a solution, which is complying with the outer core of the Earth if the ratio of the terms in the magnetic induction equation is considered.

An analysis of the solution regarding thermal characteristics can also be performed by considering the NUSSELT number [Christensen and Aubert (2006)]. Due to the fact that the core-mantle coupling model presented in Chap. 3 does not involve the temperature as variable and that the results of the numerical dynamo model shall serve as an input for the coupling model, an analysis of the solution regarding thermal characteristics is not performed.

Besides an assessment of numerical models using representative dimensionless numbers, a study by Christensen, Aubert, and Hulot analyzes the magnetic fields of a series of numerical simulations by comparing their morphology to that of the Earth. The study has considered over 150 simulations and analyzed the compliance of the fields with that of the Earth regarding, for example, the axial dipole momentum and the equatorial symmetry [Christensen, Aubert, and Hulot (2010)]. Based on these results, the authors identified a parameter regime, for which the magnetic field of the numerical models can be considered as Earth-like. This parameter regime is characterized by the magnetic EKMAN number  $Em$  and the magnetic REYNOLDS number  $Rm$ . The former dimensionless number is given by  $Em = Ek/Pm$ . The parameter regime, for which a compliance of the magnetic field was found, is shown Fig. 4.12 by a gray quadrilateral. The blue circles in Fig. 4.12 indicate some of the numerical simulations performed by Christensen, Aubert, and Hulot. For the model of this study, the magnetic EKMAN number is given by  $Em = 1.6 \times 10^{-5}$ . Using this value of the magnetic EKMAN number and that for the magnetic REYNOLDS number specified above results in a point in the parameter space which corresponds to the brown pentagon in Fig. 4.12. This point lies well within the regime for which an Earth-like magnetic field was found. Therefore, the numerical model matches the range of parameters proposed by Christensen, Aubert, and Hulot. Although a direct comparison regarding the field morphology was not performed, this fact further supports the idea that the obtained numerical solution is representative for the Earth.

In conclusion, the dynamo model is not Earth-like with respect to current estimates of the Earth's EKMAN and magnetic PRANDTL number. Nevertheless, the good agreement of the magnetic REYNOLDS number and the fact that the ELSASSER number is comparable and matches typical values found in the literature suggests that the numerical results are at least representative. This idea is also supported by the fact that the considered model matches the parameter regime for which an Earth-like magnetic field is expected. Thus, the numerical solution is suitable for an application of the core-mantle coupling model. Nevertheless, the mismatch of the REYNOLDS and the EKMAN number with estimates for the

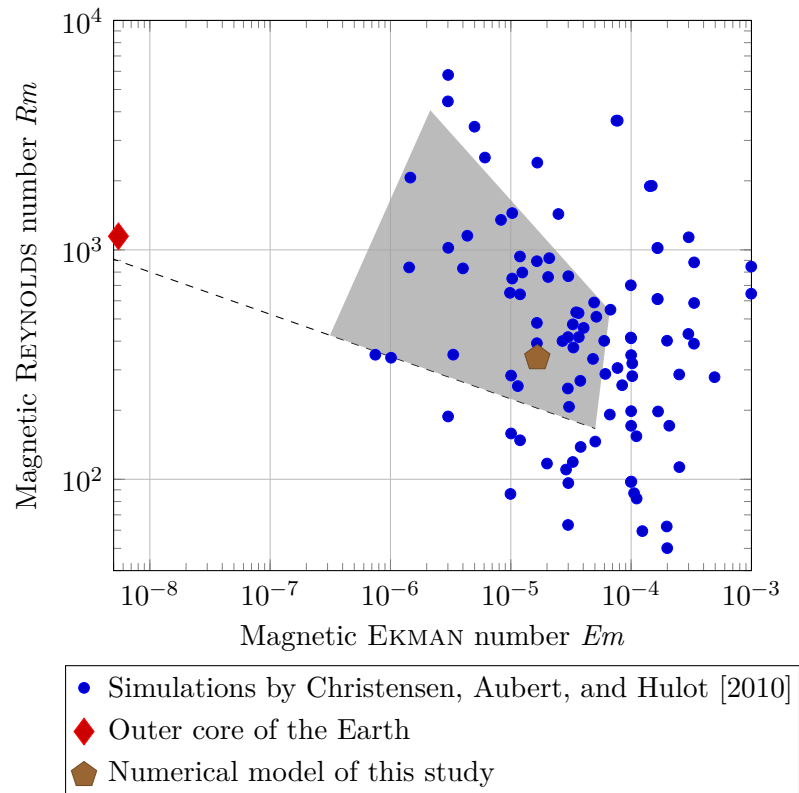


**Figure 4.12:** Parameter regime for an Earth-like magnetic field of a numerical dynamo model. Illustration adopted from Christensen, Aubert, and Hulot [2010].

outer core of the Earth results in a solution, for which the ratios of the different terms in the momentum equation are biased towards the highly viscous regime. However, this bias will not be resolved in the next decade due to limitations in the computing power which is available in foreseeable future.

## 5 Signatures of a core-mantle coupling model including topography and stratification

In this chapter, a core-mantle coupling model is presented that accounts for topography and stratification. The results of the model discussed in this chapter represent a synthesis of the analytical model discussed in Chap. 3 and the numerical dynamo simulations presented in Chap. 4. In order to assess whether the analytical core-mantle coupling model is a possible candidate for explaining variations in the Length of Day (LOD) on decadal and larger timescales, a forward model is constructed. This model uses the magnetic and velocity fields of the numerical dynamo simulations presented in Chap. 4 as an input to the analytical model; the fields of the numerical model serve as the background fields in the analytical model. This allows to construct a synthetic model from which a resulting torque acting on the mantle of the Earth can be computed. Using this torque, the model can finally predict hypothetical LOD fluctuations which can be compared with historical records.

The core-mantle coupling model is a forward model because there is no feedback from the analytical model to the model of the numerical dynamo. However, several feedback mechanisms are possible. *First*, the resulting torque acting on the mantle can increase or decrease the angular velocity of the mantle. This yields a variation of the EKMAN number in time. This means that one of the dimensionless parameters governing the differential equations of the dynamo in Eq. (4.2) is changing in time.

*Second*, the analytical model assumes that all fields in the stratified layer are stationary but the fields of the numerical dynamo model are changing in time. Hence, the time variation of the background fields is ignored and an instantaneous adjustment of the solution in the stratified layer is assumed. In reality, however, this may not be the case, because the time-varying background fields might excite waves in the stratified layer. Magnetic ARCHIMEDEAN-CORIOLIS waves (MAC waves), for instance, are a possible candidate for these waves [Buffett, Knezek, and Holme (2016)].

*Third*, in reality, the fields in the (bulk) outer core of the Earth are coupled to those in the stratified layer. In the analytical model, the bottom of the stratified layer was considered to be located infinitely far away from the Core-Mantle Boundary (CMB). At the bottom of the stratified layer, the traction vector vanishes because of the asymptotic boundary conditions which are applied. In reality, however, the stratified layer has a finite extension and thus the traction vector

---

does not necessarily vanish at the bottom of the stratified layer. Especially, if the perturbations of the analytical model are not confined to the top of the stratified layer, the presence of a non-vanishing traction at the bottom of the stratified layer may no longer be negligible. The non-vanishing traction is an example of a feedback from the analytical to the numerical dynamo model. Another possible feedback arises if the electric currents are considered. In conclusion, the background fields which are primarily due to the buoyancy-driven flow of the electrically conducting fluid in the outer core of the Earth are influenced by those in the stratified layer by multiple feedback mechanisms. This fact is neglected in the core-mantle coupling model that is subsequently discussed.

In this chapter, the discussion of the core-mantle coupling begins with a literature review in Sect. 5.1. Subsequently, the core-mantle coupling model considered in this work is presented in Sect. 5.2. Section 5.2 focuses on the combination of the results of the numerical simulations of a dynamo with those of the analytical model. Afterwards, the results of the coupling model are presented with a focus on the spatial structures of the traction field on the CMB and the temporal features of the resulting torque in Sect. 5.3. Following this, historical LOD records are presented in Sect. 5.4 and the LOD fluctuations predicted by the core-model coupling model are compared with these records. The results of the comparison are also discussed. Finally, the results of this chapter are summarized in Sect. 5.5 and a conclusion is drawn.

## 5.1 Core-mantle coupling models

This section contains a brief literature review on core-mantle coupling models. The review presented in the following is neither comprehensive nor covers the physical details of the proposed models. For more extensive reviews, the reader is referred to Gross [2015] and Buffett [2015]. Furthermore, mathematical details of most core-mantle coupling models are discussed in Roberts and Aurnou [2012].

The LOD variations after removing the tidal and atmospheric components are commonly associated to a redistribution of mass or a net torque acting inside the Earth [Hide and Dickes (1991)]. Those with periods of several decades are commonly explained by the exchange of angular momentum between the core and the mantle of the Earth [Gross (2015)]. On geological timescales with periods of hundreds of thousand year, the redistribution of mass, tectonic motion of plates, melting of ice or mantle convection changes the moment of inertia of the mantle which also yields LOD variations. Furthermore, Hide and Dickes mention that a deflection of the CMB by the underlying fluid flow in the outer core could also contribute to LOD variations [Hide and Dickes (1991)].

In the analysis of LOD variations due to some interaction of the outer core with the mantle of the Earth, two principle approaches are taken. The first approach makes use of the principle of conservation of angular momentum. If the angular momentum of the core changes, the angular momentum of the mantle changes by

an equal but opposite amount. Thus, if the angular momentum of the core can be obtained from a model, a relation to existing LOD records can be established and the contribution of the core can be assessed. The second approach is referred to as core-mantle coupling and tries to construct a model which predicts the torque acting on the mantle from the physical processes inside the outer core. From the variations of the torque, variations of the rotation rate of the mantle can be obtained and compared with available LOD records.

In *core angular momentum models*, core flow inversions are applied which reconstruct the velocity field below the CMB from the secular variation of the magnetic field. This reconstruction makes use of several assumptions such as the frozen-flux hypothesis, *i.e.*, the fluid in the core is a perfect electrical conductor and that the mantle is an insulator. Mathematically speaking, the velocity field is reconstructed by an inversion of the radial component of the magnetic induction equation. Then the assumption of a geostrophic flow is made, *i.e.*, the viscous and the inertial term are neglected in the momentum equation, to construct a velocity field inside the bulk of the outer core. In the geostrophic model, the fluid motion is described by an axisymmetric flow which is invariant with respect to the axis of rotation. This yields a flow structure consisting of nested annular cylinders, *i.e.*, geostrophic cylinders, which move relative to each other. The paper of Jault, Gire, and Le Mouél was the first to show that such a model can predict LOD variations on decadal timescales [Jault, Gire, and Le Mouél (1988)]. Following this study, methods of core flow inversion became more sophisticated and several other studies predicted LOD fluctuations with a magnitudes and phases which are comparable to available LOD records, see, for example, Jackson, Bloxham, and Gubbins [1993] and Pais and Hulot [2000].

*Torsional oscillations* represent an additional mechanism which can yield LOD variations in the framework of the geostrophic flow model. Torsional oscillations refer to an oscillation of the relative motion of the nested fluid cylinders, which are caused by electromagnetic forces. These forces are generated because of the distortion of the magnetic field due to the relative motion of the cylinders. In 1970, Braginski analyzed this problem and proposed a relation between the LOD variations and the oscillations of the geostrophic cylinders due to these forces [Braginski (1970)]. Moreover, evidence for LOD variations associated with these torsional waves was found recently [Gillet et al. (2010)].

Regarding core-mantle coupling models, the review paper of Roberts and Aurnou states four principal processes contributing to the net torque which is acting on the mantle: viscous, topographic, gravitational and magnetic couplings [Roberts and Aurnou (2012)]. Topographic core-mantle coupling considers a deviation of the CMB from a spherical surface and argues that a torque is generated by the pressure acting on the non-spherical surface. A possibly dominant contribution of a topographic torque was first suggested by Hide [1969a]. By using the geostrophic momentum balance together with a tangential magnetic field, an average stress comparable to that inferred from the LOD records was obtained [Moffatt (1977)]. If the magnetic field is neglected, topographic torques are ineffective in a geostrophic

model because the resulting pressure is equal on the leading and trailing sides of the topography [Jault and Finlay (2015)]. As a result, the average horizontal traction exerted on the topography vanishes. The inclusion of the influences of the magnetic field can restore the topographic torque [Anufriyev and Braginski (1977)]. However, plausible values for the magnetic field at the CMB suggest that the resulting torques are small [Mound and Buffett (2005)]. This work considers a novel topographic core-mantle coupling model which takes the effects of a stratified layer below the CMB into account.

Electromagnetic core-mantle coupling was first proposed by Bullard et al. and refers to a torque generated by LORENTZ forces acting on the CMB if the mantle is electrically conducting [Bullard et al. (1950)]. Based on the LORENTZ force model, it was shown that the strength of the magnetic field at the CMB and the electrical conductivity of the mantle material govern the predicted electromagnetic torque [Rochester (1962)]. These torques are a viable explanation for the LOD variations, as long as the conductance of the lower mantle exceeds  $10^8 \text{ S m}^{-1}$  [Holme (1998)]. The origin of this conductive material on the mantle side of the CMB is currently unknown. Suggestions include unusual mantle mineralogy [Wicks, Jackson, and Sturhahn (2010); Ohta et al. (2010)], infiltration of core material [Buffett, Garnero, and Jeanloz (2000); Kanda and Stevenson (2006); Otsuka and Karato (2012)] and partial melt [Lay, Williams, and Garnero (1998); Miller, Montési, and Zhu (2015)].

Viscous core-mantle coupling refers to a torque generated by stresses in the viscous boundary layer below the CMB. The strength of the coupling depends on the viscosity of the fluid in the outer core of the Earth. Because of the current estimates of a low viscosity of the fluid, this coupling mechanism is considered as ineffective [Roberts and Aurnou (2012)].

Gravitational core-mantle coupling refers to a gravitational attraction of density anomalies in the outer core of the Earth and the mantle [Gross (2015)]. Moreover, a gravitational coupling of the inner core with the mantle was proposed [Buffett et al. (1996)]. According to Stevenson, gravitational coupling between the mantle and the outer core is probably too weak to account for the LOD variations because density variations in the fluid core are expected to be very small [Stevenson (1987)]. However, gravitational coupling between the mantle and the inner core can be effective [Buffett et al. (1996)]. This mechanism proposes that a torque is acting on the mantle because of anomalies in the gravity field, which are caused by an aspherical inner core. This coupling mechanism is supported by a super-rotation of the inner core, which can be inferred from seismology and excites harmonic oscillations between the inner core and the mantle [Song and Richards (1996); Buffett et al. (1996)]. One restriction on this particular form of gravitational coupling is that fluid motions must first transfer (angular) momentum to the inner core by electromagnetic coupling which is then transferred to the mantle by gravitational coupling with the inner core. Because of the fact that the fluid motion in the outer core tends to be nearly invariant with respect to the direction of the rotation axis [Jault (2008)], there are large regions of the outer core that do not directly couple to the inner core which challenges the proposed mechanism.

Apart from core angular momentum and core-mantle coupling models, a correlation of the secular variation of the geomagnetic field and the LOD variations was found at occurrences of so-called geomagnetic jerks. Geomagnetic jerks refer to abrupt changes in the magnetic field of the Earth. At the event of a geomagnetic jerk, a correlated sudden change of the rotation rate of the Earth was observed which indicates a coupling to a yet unknown process in the outer core of the Earth [Holme and de Viron (2005); Holme and de Viron (2013)].

## 5.2 Model description

The core-mantle coupling model discussed in this chapter combines the results of the analytical model presented in Chap. 3 with those of the numerical model presented in Chap. 4. As indicated in Fig. 5.1, the CMB is imagined as a spherical surface with a topography. The stratified layer is located between the outer core of the Earth and the CMB. The dynamo process occurs in the outer core of the Earth where the magnetic and velocity fields are dominated by the turbulent flow of the electrically conducting fluid. The mantle is considered to be a solid rigid body. The stratified layer shall transfer momentum from the outer core to the mantle of the Earth which is manifested in a resulting torque  $\mathbf{M}$  that is acting on the mantle. This torque yields LOD fluctuations. As discussed in Sect. 2.2, in a first order approximation, LOD fluctuations are related to changes of the  $z$ -component of the torque vector  $\mathbf{M}$ , which is computed with respect to the center of the Earth. Thus, only this component is of interest in the subsequent analysis.

The resulting torque on the mantle is obtained by integrating the torque density over the CMB. This torque density is given by  $\mathbf{x}_{\text{CMB}} \times \mathbf{t}_{\text{CMB}}$  and, for a perfectly spherical CMB, the associated integral reads

$$\mathbf{M}(t) = \int_0^{2\pi} \int_0^\pi \mathbf{x}_{\text{CMB}}(\theta, \varphi) \times \mathbf{t}_{\text{CMB}}(\theta, \varphi, t) R_{\text{CMB}}^2 \sin(\theta) \, d\theta \, d\varphi, \quad (5.1)$$

where  $\mathbf{x}_{\text{CMB}}$  refers to the position vector of a point on the CMB,  $\mathbf{t}_{\text{CMB}}$  denotes the traction vector acting on the mantle and  $R_{\text{CMB}}$  is the radius of the CMB. The reference point with respect to which the resulting moment is computed is the center of the Earth. In spherical coordinates, the two vector fields in Eq. (5.1) are given  $\mathbf{x}_{\text{CMB}} = R_{\text{CMB}} \mathbf{e}_r$  and  $\mathbf{t}_{\text{CMB}} = t_r \mathbf{e}_r + t_\theta \mathbf{e}_\theta + t_\varphi \mathbf{e}_\varphi$ . Hence,

$$\mathbf{x}_{\text{CMB}} \times \mathbf{t}_{\text{CMB}} = R_{\text{CMB}}(t_\theta \mathbf{e}_\varphi - t_\varphi \mathbf{e}_\theta). \quad (5.2)$$

Only the  $z$ -component of the resulting torque on the mantle is relevant for LOD fluctuations and, therefore, only the  $z$ -component of the cross product  $\mathbf{x}_{\text{CMB}} \times \mathbf{t}_{\text{CMB}}$  is considered subsequently. Because of  $\mathbf{e}_z \cdot \mathbf{e}_\theta = -\sin(\theta)$  and  $\mathbf{e}_z \cdot \mathbf{e}_\varphi = 0$ , the  $z$ -

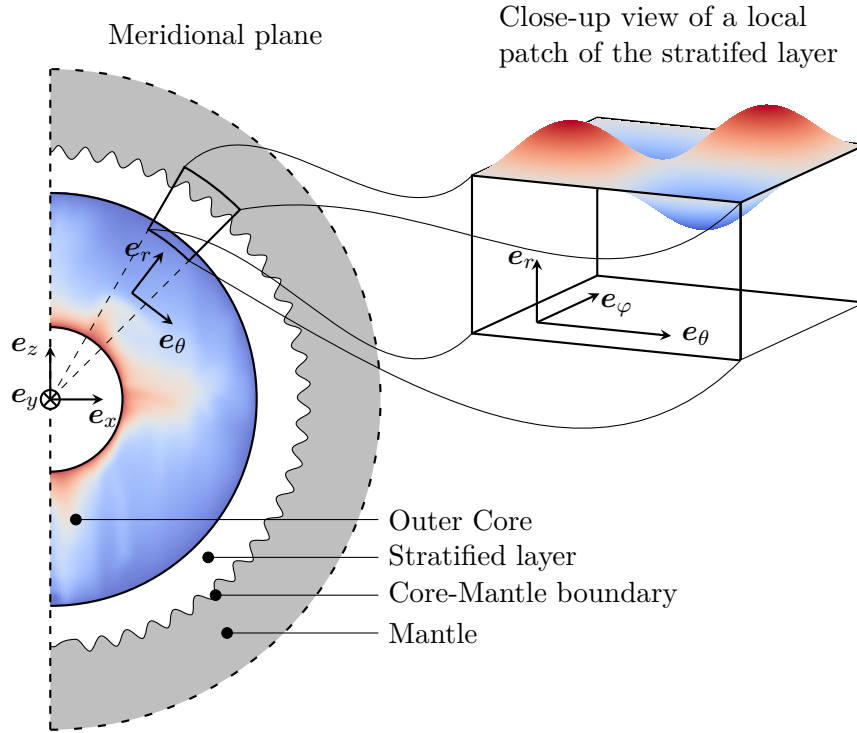


**Figure 5.1:** Illustration of the core-mantle coupling model and the local approximation of the boundary value problem of the stratified layer. Note that the sizes of the outer core of the Earth, the stratified layer at the CMB and the mantle of the Earth are not true to scale.

component of Eq. (5.1) is given by

$$M_z(t) = R_{\text{CMB}}^3 \int_0^{2\pi} \int_0^{\pi} \underbrace{t_\varphi(\theta, \varphi, t) \sin^2(\theta)}_{=: m_z(\theta, \varphi, t)} d\theta d\varphi. \quad (5.3)$$

Here, the integrand  $m_z$  is interpreted as a torque density which takes the position (lever arm) and the surface area of the considered patch on the spherical surface into account. In summary, the analysis shows that the resulting torque, which is relevant for an assessment of the considered core-mantle coupling model, depends only on the  $\varphi$ -component of the surface traction.

For the computation of the transfer of momentum from the outer core to the mantle of the Earth, the results of the analysis of the stratified layer with a boundary topography from Chap. 3 are used. These results were computed using a CARTESIAN coordinate system; effects due to the curvature of the spherical CMB were not taken into account. A solution of the problem for a spherical shell with a boundary topography is not available. Therefore, the results of the local CARTESIAN approximation are used and applied on patches of the CMB, see Fig. 5.1. On each

path, the magnetic and velocity fields of the numerical dynamo simulation serve as an input to the analytical model, *viz.*, the fields of the numerical simulation serve as the background fields in the analytical model. Then, the average traction which is obtained from the analytical model is assigned to each of the patches. Finally, the resulting torque on the mantle is computed according to Eq. (5.3). In doing so, the integral is replaced by a sum of the average traction over all of the patches.

The application of the local CARTESIAN approximation deserves special attention because, as indicated in Fig. 5.1, a different local spherical coordinate system applies on each patch. Only the radial component of the angular velocity vector of the Earth is used as the angular velocity vector in the analytical model. Furthermore, an analysis similar to that in Sect. 3.2, in which the angular velocity vector of the analytical model is not constrained, shows that non-radial components of the angular velocity vector of the Earth do not change the characteristic equation of the underlying eigenvalue problem. This suggests that the non-radial components of the angular velocity vector of the Earth do not significantly alter the results regarding the average traction.

Additionally, the spherical components of the magnetic and velocity fields of the numerical dynamo model need to be related to the background fields of the analytical model, which are specified in CARTESIAN coordinates. In the analytical model, the background magnetic field was always assumed to be purely vertical, which corresponds to a purely radial magnetic field, see Fig. 5.1. Therefore, the value of the magnetic background field  $\bar{B}$  is equal to the (local) radial component of the magnetic field  $B_r$ , *i.e.*,  $\bar{B} = B_r$ . From the geometry, it is clear that the background velocity is related to the local polar and azimuthal components of the velocity, *i.e.*,  $v_\theta$  and  $v_\varphi$ , respectively. Furthermore, it was shown in Chap. 3 that the average traction, which is acting on the boundary, assumes a maximum if the velocity field is aligned with the boundary topography. Moreover, the local contribution of the traction to the torque is a maximum if its azimuthal component is a maximum. Therefore, the value of the background velocity  $\bar{V}$  is chosen to be equal to the azimuthal component of the velocity field  $v_\varphi$ , *i.e.*,  $\bar{V} = v_\varphi$ . This, of course, assumes that the CMB has some (local) topographic variation in the azimuthal direction and yields the corresponding maximum value of the average traction which can possibly occur. In conclusion, the choices of the background magnetic and velocity background fields imply that the radial and azimuthal directions correspond to the  $x$ - and  $z$ -directions of the analytical model in Chap. 3.<sup>1</sup>

Due to the choices regarding the association of the magnetic and velocity fields obtained from the numerical simulations to the respective background fields of the analytical model, the average traction  $\langle t_x \rangle$  of the analytical model corresponds to the azimuthal component of the (local) traction vector, *i.e.*,  $t_\varphi = \langle t_x \rangle$ . Therefore, the azimuthal component of the traction vector can be computed from the analytical

---

<sup>1</sup>Here, the  $x$ - and  $z$ -directions of the analytical model shall not be confused with those of the (global) coordinate system indicated in Fig. 5.1.

model according to

$$t_\varphi(\theta, \varphi) = \langle t_x \rangle (\bar{B} = B_r, \bar{V} = v_\varphi, \theta), \quad (5.4)$$

where the fields  $B_r$  and  $v_\varphi$  also depend on the polar and azimuthal angles. Here, the polar angle  $\theta$ , *i.e.*, the angle of the colatitude, occurs explicitly as an argument on the right-hand side, because the local angular velocity, which is used in the analytical model, is proportional to  $\cos(\theta)$ .

Equation (5.4) allows to compute the relevant component of the traction for a patch of the CMB once the radial magnetic and the azimuthal velocity fields are specified. This assumes that the other parameters which are governing the analytical model, namely the strength of the stratification, the height and the wavelength of the topography and the material parameters, are constant. While longitudinal and latitudinal variations of the material parameters are possible but probably have a smaller effect, this is not the case if the topography of CMB is considered. For instance, a larger average traction is possible due to an increase of the amplitude of the topography. Furthermore, a variation of the wavelength also yields significant changes of the average traction [Glane and Buffett (2018)]. The same also holds with respect to the variation of the strength of the stratification.

The topography of the CMB is analyzed in the literature using seismic inversion techniques. These techniques try to recover the topography of the CMB by some possibly stochastic inversion of seismic observations [Garcia and Souriau (2000)]. Some studies also make use of sophisticated models which account for mantle heterogeneity [Soldati, Boschi, and Forte (2012)] and mineralogy [Soldati et al. (2013)]. According to Garcia and Souriau, large discrepancies with respect to the CMB topography arise in the literature because of the difficulty to separate signals due to a heterogeneous region in the lower mantle, *i.e.*, the  $D''$  region,<sup>2</sup> from those of the CMB topography [Garcia and Souriau (2000)]. Thus, there is no general agreement on the maximum amplitude of the CMB topography. For example, maximum amplitudes of 10 km [Greff-Lefftz and Legros (1996)], 4 km [Garcia and Souriau (2000)], 0.9 km to 2.1 km [Soldati, Boschi, and Forte (2012)] and less than 5 km [Soldati et al. (2013)] are obtained in four different studies. Apart from the maximum amplitude, discrepancies also occur if the wavelengths of the CMB topography and the associated amplitude are considered.

In the subsequent analysis, a boundary topography with an amplitude of 30 m and a wavelength of 100 km is considered. This corresponds to a modest topography in comparison to the estimate of an amplitude of 1 km which is specified in Garcia and Souriau [2000] for a wavelength of less than 300 km. A latitudinal and longitudinal variation of the CMB is not considered. Furthermore, the material parameters

---

<sup>2</sup>The  $D''$  region refers to the lowermost 200 km to 300 km of the mantle above the CMB [Lay (2015)]. In this region, the variations of the seismic velocities cannot be explained by a simple homogeneous model and thermal boundary layer effects play an important role. Additionally, phase transitions and chemical interactions with the outer core may also explain the changes of the seismic velocities in this region [Lay (2015)].

and the stratification parameter are chosen to have the same “standard values” as in Chap. 3. The thickness of the stratified layer is assumed to be constant such that the radial magnetic and azimuthal velocity fields  $B_r$  and  $v_\varphi$  are sampled on a spherical shell with a constant radius. This radius, then, allows to introduce a “virtual” thickness  $\delta$  of the stratified layer, namely,

$$\delta = R_{\text{CMB}} - r_s, \quad (5.5)$$

where  $r_s$  denotes the radius of the spherical shell which is sampled. In conclusion, the average traction is computed on each patch of a spherical shell by an evaluation of the analytical model and, subsequently, the resulting torque acting on the mantle is computed according to Eq. (5.3).

In Chap. 3, the analytical model was analyzed and solved using a dimensionless framework. Furthermore, the results of the numerical dynamo simulations presented in Chap. 4 are also dimensionless. Therefore, the numerical results need to be rescaled because they serve as an input to the analytical model. A rescaling is also required because the two models do not share the same set of dimensionless parameters. The parameters of the numerical dynamo model are far away from realistic values for the outer core of the Earth. Therefore, there is no unique way of rescaling the dimensionless solution to a dimensional one, because several timescales are present in the problem [Christensen, Aubert, and Hulot (2010); Wicht, Stellmach, and Harder (2015)]. These are the characteristic time scales associated with rotation, fluid convection and magnetic, viscous and thermal diffusion. Several ways of rescaling the dimensionless solutions are proposed in the literature. Solutions are rescaled such that the strength of the dimensional magnetic field matches that of the Earth. An alternative approach makes use of the secular variation of the magnetic field of the Earth. The dimensionless solution is rescaled such that the timescale of either magnetic diffusion or rotation matches that inferred from the secular variation of the magnetic field of the Earth [Christensen, Aubert, and Hulot (2010)].

In Chap. 4, it was emphasized that the magnetic REYNOLDS number of the numerical model is comparable to that of the Earth. This magnetic REYNOLDS number is the ratio of the timescale of magnetic diffusion to that of convection [Wicht, Stellmach, and Harder (2015)]. Thus, for a comparable magnetic REYNOLDS number, a rescaling of the dimensionless solution using the magnetic diffusion time yields results which are comparable to those obtained from a rescaling using the timescale of convection. Therefore, the dimensionless solutions of the numerical dynamo simulation are rescaled based on the timescale of magnetic diffusion. Hence, the timescale is given by  $t_{\text{ref}} = D^2/\eta$ , where  $D = 2280$  km denotes the shell thickness of the outer core and  $\eta = 0.8 \text{ m}^2 \text{ s}^{-1}$  the magnetic diffusivity. Consequently, the reference magnetic field is given by  $B_{\text{ref}} = \sqrt{\rho\mu_0\eta\Omega_0}$ , where the density is given by  $\rho = 10^4 \text{ kg m}^{-3}$  and  $\Omega_0$  is the standard value for the angular velocity of the mantle. Moreover, it can be shown that the reference velocity is given by  $v_{\text{ref}} = \eta Pm/D$ .

Based on this rescaling, the dimensional radial magnetic and azimuthal velocity

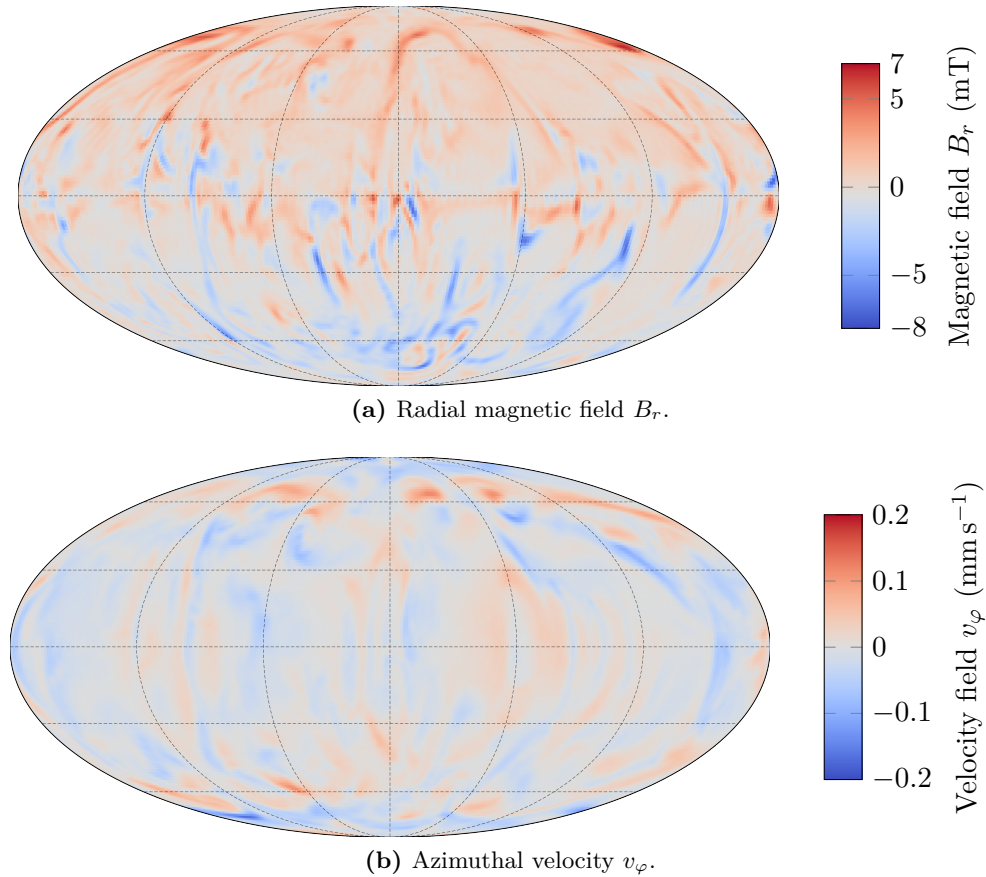


**Figure 5.2:** Snapshots of (a) the radial magnetic  $B_r$  field and (b) the azimuthal velocity field  $v_\varphi$  on a spherical shell with a radius of  $r_s = 3336$  km. This radius corresponds to a virtual thickness of the stratified layer of  $\delta = 144$  km. The time of the snapshot is  $t = 318$  a.

fields  $B_r$  and  $v_\varphi$  may be analyzed on spherical shells with different radii below the CMB. A snapshot of such a spherical shell is shown in Fig. 5.2. In this figure, the two dimensional fields  $B_r$  and  $v_\varphi$  are shown and the small-scale structure of the solution becomes apparent once more. Close to the equator, it can be seen that the sign of both fields is alternating in the azimuthal direction. While this pattern continues to extend to lower and higher latitudes for the azimuthal velocity, this is not the case for the radial magnetic field. At lower and higher latitudes, the dipole character of the magnetic field becomes dominant. Hence, the radial component is positive in the northern and negative in the southern hemisphere. The structure velocity field is governed by the alternation of regions of an upwelling and downwelling of the fluid due to convection.

For the sampled spherical shells and the entire simulation period, the azimuthal velocity field  $v_\varphi$  varies from  $-0.90$   $\text{mm s}^{-1}$  to  $0.99$   $\text{mm s}^{-1}$  and the radial magnetic field  $B_r$  from  $-16.1$  mT to  $19.7$  mT. Regarding the velocity field, the numerical

model predicts the same order of magnitude as suggested by core flow inversions [Holme (2015)]. The magnetic field is roughly an order of magnitude too large when compared to estimates inferred from geomagnetic observations [Finlay et al. (2016)]. However, this is not surprising. As outlined in Chap. 4, the ELSASSER number  $\Lambda$  is an order of magnitude larger than the expected value of unity for the outer core of the Earth.

The numerical dynamo simulation consists of two million timesteps. A storage of the radial magnetic and the azimuthal velocity fields on spherical shells of different radii for each timestep is not possible due to memory limitations. Therefore, the two fields are saved in every 40<sup>th</sup> timestep on spherical shells with five different radii. This creates data with a size of approximately 250 GB. After a rescaling of the dimensionless time, the chosen sampling rate regarding the spherical shells allows to post-process the results approximately every 1.5 a.<sup>3</sup> The corresponding simulated time period is approximately 70 000 years. Thus, the sampling rate and the simulated time interval is sufficient to analyze LOD fluctuations with intra-decadal or larger periods.

Spherical shells with five different radii are chosen for the sampling of the numerical model. The choice of a sampling radius corresponds to a certain thickness of the stratified layer  $\delta$  and for the five different shells, which are sampled, thicknesses of 5 km, 22 km, 51 km, 92 km and 144 km result.

The question which one of the spherical shells or which radius is the correct choice to obtain a realistic core-mantle coupling model is debatable. The analytical model assumes an infinitely thick stratified layer and the perturbations decay rapidly with increasing distance from the boundary topography. This confinement of the perturbations to the top of the stratified layer suggests that a relatively small thickness of the stratified layer of 5 km would be a suitable choice. This thickness is small compared to the values specified in the literature of, for example, 60 km [Buffett and Seagle (2010)], 100 km [Lister and Buffett (1998); Gubbins and Davies (2013)], 140 km [Buffett, Knezek, and Holme (2016)], and 400 km [Olson, Landeau, and Reynolds (2018)].

As discussed in Sect. 3.2.1, the thickness of the viscous boundary in the outer core of the Earth is on the order of the meters. Therefore, it is hypothesized for the outer core of the Earth that the thickness of the stratified layer is larger than that of any other boundary layer. Therefore, the free-stream part of the magnetohydrodynamic flow, *i.e.*, the part which is unaffected by the CMB, needs to be used for the background magnetic and velocity fields. The numerical model possesses a (viscous) boundary layer whose thickness is much larger than that of the boundary layer in the outer core of the Earth. This is due to the fact that the viscosity in the numerical model is much larger than that of the fluid in the outer core of the Earth. By virtue of the formula given in Footnote 1 in Sect. 3.2.1 with an EKMAN number of  $Ek = 5 \times 10^{-5}$ , the thickness of the EKMAN layer in the

---

<sup>3</sup>Here, 1.5 a refers to 1.5 years and the unit of time is the Julian year, which is abbreviated using the symbol a.

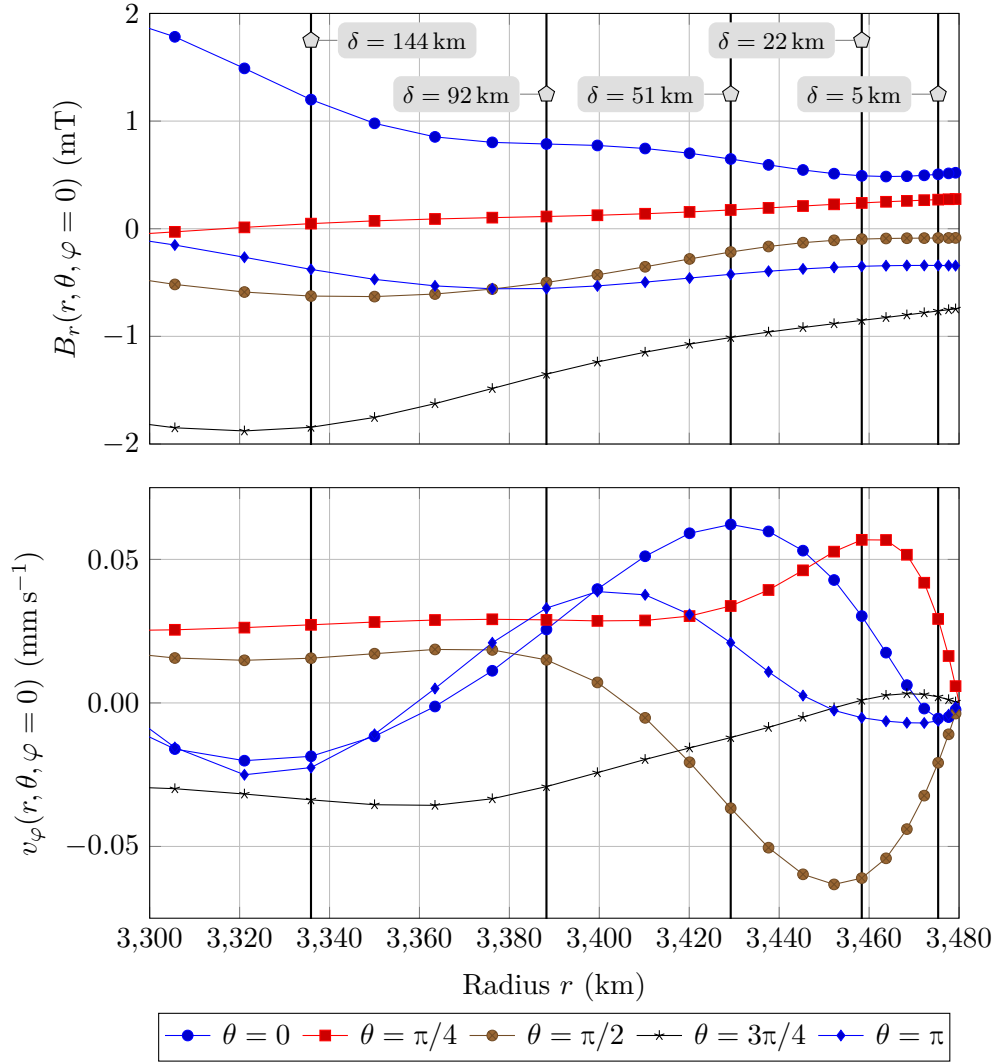


**Figure 5.3:** Radial profiles of the radial magnetic and azimuthal velocity fields  $B_r$  and  $v_\varphi$  for different values of the colatitude  $\theta$ . The azimuthal angle is equal to zero for all profiles, *i.e.*,  $\varphi = 0$ . The snapshots of the radial profiles are shown at the time  $t = 37819$  a.

numerical model can be approximated as  $\delta_E = 22$  km. Thus, a spherical shell with a radius corresponding to a thickness  $\delta$  of at least 22 km would be an appropriate choice.

Figure 5.3 shows radial profiles of the radial magnetic and azimuthal velocity fields for different values of the colatitude. The magnitude of the radial magnetic field, which is shown in the top panel of Fig. 5.3, increases gradually with distance from the CMB and the sign does not change. The CMB does not affect the magnetic field significantly compared to its effect on the velocity field, which is shown in the bottom panel. In the velocity field, a boundary layer is clearly present. The curves

in Fig. 5.3 show that its thickness varies with the colatitude. For example, for the curve of a colatitude of  $\theta = \pi/4$ , the thickness is given by  $\delta \approx 20$  km because the azimuthal velocity is maximum there. A thickness of  $\delta \approx 25$  km is obtained for the curve of colatitude of  $\theta = \pi/2$ . In some of the curves, the sign of the azimuthal velocity changes several times with increasing distance from the CMB. The changes of the sign are due to the CORIOLIS acceleration and the convective upwelling and downwelling of the fluid. The changes of the sign make it more difficult to decide on the thickness of the boundary layer. For example, for the curve of a colatitude of  $\theta = 0$ , a thickness of  $\delta \approx 50$  km is obtained if the negative values of the azimuthal velocity very close to the CMB are not taken into account. In conclusion, the thickness of the boundary layer is not constant but varies with the colatitude and, of course, also with the longitude. Moreover, the fields are not stationary and therefore the variation of the boundary layer thickness is also time-dependent. A definite choice of a “correct” thickness or corresponding radius of the spherical shell cannot be made, but the five different radii specified above are a representative and suitable selection for the sampling of the free-stream part of the fields of the numerical dynamo model.

The objective is to compute the resulting torque which the core-mantle coupling model would predict if, for example, the fields shown in Fig. 5.2 apply. Due to the local approximation, the average traction is required for each patch on the spherical shell. However, a separate computation of the average traction for each patch by using *Mathematica* is not feasible because of the complexity of the symbolic calculations associated with the analytical model presented in Chap.3. Therefore, the average traction is interpolated on each patch using a pre-computed set of values. Details on the generation of this pre-computed set and the interpolation are given Sect. 5.2.1. Following Sect. 5.2.1, the procedure of the computation of the resulting torque acting on the mantle is briefly summarized in Sect. 5.2.2.

### 5.2.1 Interpolation of the average traction

For each timestep, the average traction needs to be determined on each patch of the considered spherical shell. In order to do so, a set of values of the average traction is computed for different values of the background magnetic and velocity fields and of the colatitude using the analytical model described in Chap.3. Based on this pre-computed dataset, the average traction is then interpolated on each patch.

In the numerical dynamo model, the radial magnetic and the azimuthal velocity fields are both either positive or negative in certain regions of a spherical shell. This would require to generate a set of values of the average traction on all four quadrants of the space created from the values of the background magnetic and velocity fields. However, this is not necessary because the average traction obeys several symmetry properties with respect to the background magnetic field, the

background velocity field and the colatitude, *viz.*,

$$\begin{aligned}\langle t_x \rangle(-\bar{B}, \bar{V}, \theta) &= \langle t_x \rangle(\bar{B}, \bar{V}, \theta), \\ \langle t_x \rangle(\bar{B}, -\bar{V}, \theta) &= -\langle t_x \rangle(\bar{B}, \bar{V}, \theta), \\ \langle t_x \rangle(\bar{B}, \bar{V}, \pi - \theta) &= \langle t_x \rangle(\bar{B}, \bar{V}, \theta).\end{aligned}\tag{5.6}$$

The first property was found by solving the problem discussed in Chap. 3 for a reversed direction of the magnetic field. The same holds for the second and the third property, whereas the former is obvious since a change of the direction of the fluid flow will also change the direction of the average traction. The last property in Eq. (5.6) only requires to compute the average traction for patches which lie in the northern hemisphere, *i.e.*, for values of the colatitude which lie in the interval  $0 \leq \theta \leq \pi/2$ . For a patch in the southern hemisphere, the average traction is that of a corresponding patch in the northern hemisphere.

In order to create the pre-computed dataset of values of the average traction, discrete grids need to be chosen for the background magnetic and velocity fields and the colatitude. For the colatitude, seven grid points are chosen, whose distances to each other become smaller the closer the colatitude approaches the value  $\theta = \pi/2$ . This refinement is applied because of the dependence of the average traction on the colatitude discussed in Sects. 3.3 and 3.4. In Chap. 3, several simplified models were analyzed and it was found that the only model, which provides a regularity for small values of the background magnetic field and the background velocity, is the inertial magnetic model, see Sect. 3.5. However, this model experiences numerical instabilities, especially if the value of the background velocity becomes very small. Moreover, the magnitude of the average traction varies by several orders of magnitude if the background magnetic and velocity fields vary and the dependence is non-linear. Because of Eq. (5.6) and the ranges of values obtained after a diffusive rescaling of the results of the numerical dynamo model, the grid points of the background velocity field lie in the interval  $0 \leq \bar{V} \leq 1 \text{ mm s}^{-1}$  and for the background magnetic field the interval for the grid points are given by  $0 \leq \bar{B} \leq 20 \text{ mT}$ .

The fact that numerical instabilities occur is taken into account in the construction of the grid used for the background magnetic and velocity fields. Furthermore, the grid is constructed such that the non-linear dependence of the average traction on the background magnetic and velocity fields can be adequately resolved. A refinement of the two grids is performed when the respective value becomes less than a certain threshold. Above the threshold, the grid points are spaced linearly and 15 grid points are used for each background field. Below the threshold, a logarithmic spacing with ten grid point is applied. The resulting grid points of the background magnetic and velocity fields are shown in Fig. 5.4. In this figure, the transition from the linear to logarithmic spacing is clearly visible. The thresholds for the two background fields were heuristically determined. For the background magnetic field, the threshold is given by  $\bar{B}_{\text{thld.}} = 0.25 \text{ mT}$ . For the background

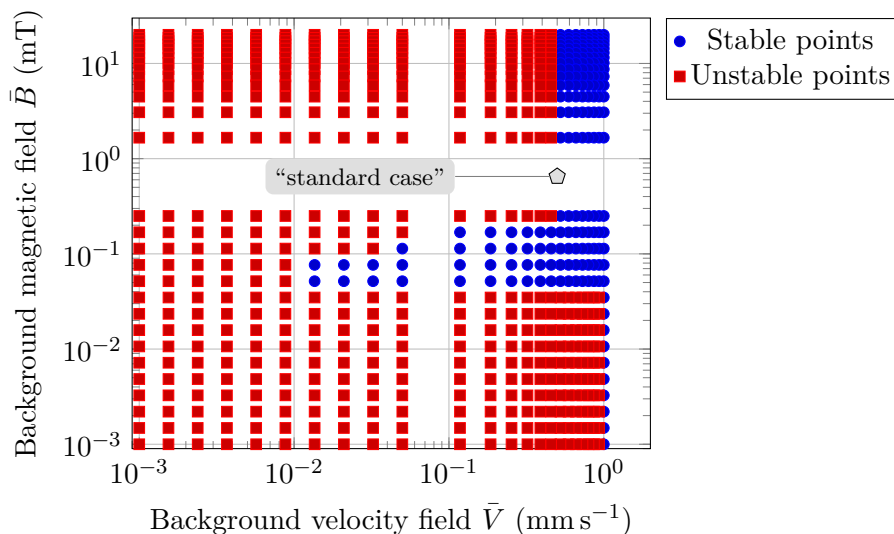


**Figure 5.4:** Grid points of the background magnetic and velocity fields  $\bar{B}$  and  $\bar{V}$  used for computing the average traction with the analytical model in a double-logarithmic chart. Stable points refer to values of  $\bar{B}$  and  $\bar{V}$  for which a reliable computation of the average traction is possible, and unstable points belong to those for which this not the case.

velocity field, it is given by  $\bar{V}_{\text{thld.}} = 0.05 \text{ mm s}^{-1}$ . It should be remarked that not all grid points are shown in Fig. 5.4. For completeness and in order to also account better for a zero crossing of one of the background field, the grid points for the values  $\bar{B} = 0$  and  $\bar{V} = 0$  are added to the final grid. However, these grid points cannot be shown in Fig. 5.4 because of the logarithmic scaling of both axes.

The ALFVÉN number is one of the critical dimensionless parameters of the analytical model which changes if one or both of the background fields change. For the intervals of the background fields specified above, it varies considerably. The ALFVÉN number is inversely proportional to the background velocity, *i.e.*,  $Al \propto \bar{B}/\bar{V}$ . Thus, the ALFVÉN number becomes infinitely large for  $\bar{V} \rightarrow 0$  if the magnetic field does not vanish. However, the case of  $\bar{V} = 0$  yields the trivial solution and a vanishing average traction and, therefore, is not of interest here. If the grid point with smallest non-vanishing value of the background velocity is used instead of  $\bar{V} = 0$ , the ALFVÉN number is in the interval  $0 \leq Al \leq 178\,412$ . For this range of the ALFVÉN number, it is expected from the results in Sect. 3.3 that the average traction will experience numerical instabilities and also vary by several orders of magnitude.

Regarding numerical instabilities, the second critical dimensionless parameter of the analytical model is the background velocity itself. Its variation was studied in Sect. 3.3 by considering a variation of the dimensionless background velocity. The reference value of the background velocity in Sect. 3 is  $0.5 \text{ mm s}^{-1}$  and numerical instabilities occur in the analytical model if the dimensionless background velocity becomes less than unity. Thus, numerical instabilities will occur in the interval

specified for the background velocity above, especially if the background velocity becomes small. Furthermore, the interval of the magnetic REYNOLDS number can be directly related to the background velocity. Using the values specified for the background velocity above, the interval of the magnetic REYNOLDS number is given by  $0 \leq Rm \leq 125$ .

In the process of generating the set of the values of the average traction on the grid points, it is necessary to identify combinations of the background magnetic and velocity fields (and the colatitude) for which a reliable computation of the average traction is not possible because of the presence of numerical instabilities. A heuristic strategy was developed to identify these combinations. In order to classify a combination of values of the background magnetic and velocity fields as an unstable point, several criteria are applied:

1. A point is classified as unstable if the associated total average traction is negative.
2. A point is classified as unstable if the associated total average traction exceeds the value that is suggested from an extrapolation using neighboring stable points by a certain (heuristic) threshold.
3. It is expected that the average traction is largest when the background velocity is largest. For large values of the background velocity, a reliable computation of the average traction without any numerical instabilities is possible. Therefore, a point is classified as unstable if the associated total average traction exceeds the value which is obtained for the largest possible velocity and an identical value of the background magnetic field.
4. In Sect. 3.3, it was discussed that the total average traction is composed of three components which are associated to three different wave numbers. The rapidity of the decay of the associated perturbations with an increasing distance to the boundary differs considerably. Moreover, it was shown that the component of traction, which is associated to the wave number which yields the largest decay (first component), exerts the largest traction. Moreover, a reliable computation of this component is possible for lower values of the background velocity than for the other two components, see Fig. 3.19. Therefore, a point is classified as unstable if the traction of either or both of the other two components exceeds that which is associated with the first stable component.

In Fig. 5.4, the points which are classified as unstable according to these criteria are indicated by red squares whereas the stable points are indicated by blue circles. The majority of the points in Fig. 5.4 are classified as unstable. In fact, approximately 60% of points are classified as such. Most of the stable points are located in the region where the background velocity is large; below a certain value of the background velocity all points are classified as unstable. Although the background

velocity is large, some points are also classified as unstable if the background magnetic field becomes very small.

For the unstable points, the analytical model is not yielding a physically meaningful value of the average traction, because one or more of the components of the average traction associated to the different wave numbers are polluted by the numerical instabilities. Therefore, an alternative strategy to obtain a physically valid value of the average traction is applied. The way the average traction is computed for an unstable point depends on which of the criteria specified above was violated. In general, two cases can be distinguished. *First*, the case that one or two of the components of the average traction are unstable. This corresponds to the case that the fourth criterion is not met. Then, the average traction associated with the first stable component is used. *Second*, the case that none of the components is stable. In this case, an average traction is obtained from interpolation by using only physically valid values. The interpolation is only performed with respect to the background velocity and the background magnetic field is kept constant. Moreover, for a vanishing background velocity, the fact that the average traction is also vanishing is taken into account when the interpolation is performed. Furthermore, the interpolation also makes use of the values of the average traction of the unstable points, which belong to the first case (fourth criterion not met) and whose associated average traction can therefore also be regarded as physically valid. The interpolation of the average traction for some of the points is not desirable but it is the only way to obtain physically valid values based on the linear analytical model discussed in Chap. 3. For low values of the background velocity, an interpolation is inevitable, but the majority of the unstable points shown in Fig. 5.4 belong to the first case. Therefore, the set of values of the average traction, which is used for an interpolation on the patches of the spherical shell, is suitable for an assessment of the topographic core-mantle coupling.

Figure 5.5 shows the resulting set of values of the average traction on the grid points of the background magnetic and velocity fields and for the colatitude  $\theta = 0$ . The value of average traction which was obtained for the so-called “standard case” in Sect. 3.3 is indicated by a gray filled pentagon. A remarkable feature of the average traction shown in Fig. 5.5 is that it is largest for small values of the background magnetic field. This behavior is complying with the dependencies discussed in Sect. 3.3. Especially Fig. 3.20 confirms the results shown in Fig. 5.5 because it shows an increase and subsequent decrease of the average traction with a decreasing ALFVÉN number. A decreasing ALFVÉN number corresponds to a decreasing background magnetic field. The subsequent decrease of the average traction in Fig. 3.20 also applies for the values of average traction shown in Fig. 5.5. However, it is not visible in Fig. 5.5 because of the perspective of the plot.

### 5.2.2 Procedure of the computation of the resulting torque

In order to finalize the discussion of the core-mantle coupling model, its implementation is briefly discussed and the steps required to obtain the torque on the

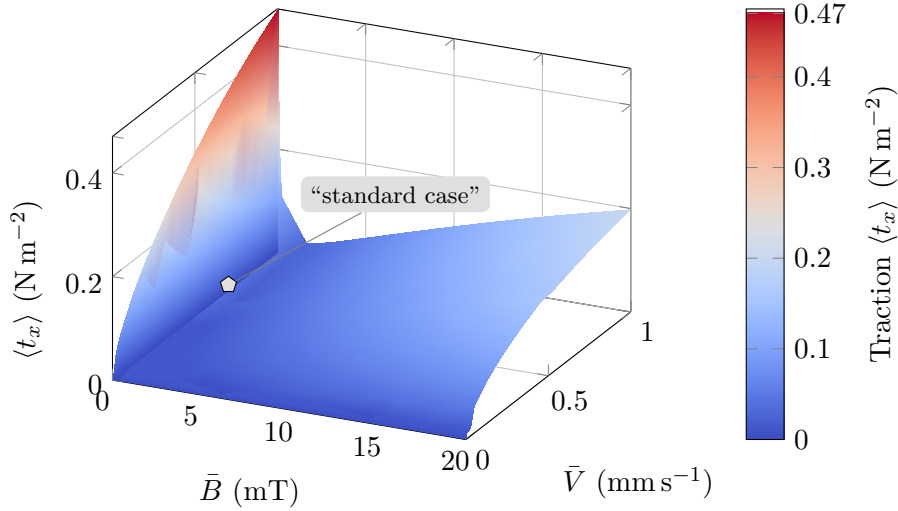


**Figure 5.5:** Average traction at the grid points of the background magnetic and velocity fields  $\bar{B}$  and  $\bar{V}$ , see Fig. 5.4. These values are computed using the analytical model for the colatitude  $\theta = 0$ .

mantle are described. The program which computes the torque is implemented in the *python* programming language [van Rossum and Drake (2009)] and makes use of the *python* software packages *NumPy* and *SciPy* [Virtanen et al. (2020)]. The *Rayleigh* software has a *python* interface and allows to load simulation results from a binary file into *python* by means of *NumPy* arrays. Together with the dataset, which is generated from the analytical model and used for an interpolation of the average traction on each of the patches, the resulting torque which is acting on the mantle is computed for a single timestep by going through the following steps:

1. For a timestep of the simulation, the radial magnetic and the azimuthal velocity fields on a spherical shell are read from the disk into memory. Additionally, the grid of the corresponding spherical grid is also read from disk into memory.
2. The dimensionless fields are rescaled by using diffusive scaling. At this point, two two-dimensional arrays which contain the dimensional radial magnetic and the azimuthal velocity fields on the spherical shell are available.
3. Each point of the grid of the spherical shell is associated with a patch for which the (local) average traction is determined according to Eqs. (5.4) and (5.6). On each patch, the average traction is determined from a first order interpolation on the pre-computed dataset obtained from the analytical model. The interpolation is performed with respect to the values of the background magnetic and velocity fields and the colatitude.
4. Finally, the torque which results on the mantle is computed from Eq. (5.3).

The trapezoidal rule is applied in order to compute the integral in Eq. (5.3) with respect to the angles  $\theta$  and  $\varphi$  from the local traction on the grid points on the spherical shell. The *SciPy* software package provides an implementation of the trapezoidal rule for the integration of a function of a single variable. In order to compute the integral of local traction with respect to the two variables  $\theta$  and  $\varphi$ , the trapezoidal rule is applied sequentially. First, the trapezoidal rule is applied with respect to the angle  $\theta$  for the different values of the angle  $\varphi$ . Then, a second application with respect to the angle  $\varphi$  yields the torque which is acting on the mantle; this result is finally stored in the memory.

The steps described above are repeated for all of the timesteps of the numerical dynamo simulation which were saved.

### 5.3 Resulting core-mantle boundary torque

In the following, the results of the core-mantle coupling model described in the previous section will be presented. At first, the spatial features of the traction and the associated torque density are discussed. Then, the temporal features of the torque are analyzed and the dependence of the resulting torque on the radius of the considered spherical shell is addressed. The implications of the core-mantle coupling model and its predicted resulting torque on changes in the length of day are discussed separately in Sect. 5.4.

#### 5.3.1 Spatial features of the traction and the torque density

The spatial features of the traction and the torque density are of interest because they provide information about which regions of a spherical shell contribute the most to the torque on the mantle. Apart from the traction, the torque density  $m_z$ , which was introduced in Eq. (5.3), is also considered because it takes the position and the size of the patch into account, where the corresponding traction is acting. Because of the amount of timesteps for which the average traction is computed, only a snapshot in time on a single spherical shell is considered in the following. The selected snapshot is shown in Fig. 5.6 and the time of the snapshot is the same as that in Fig. 5.2.

Figure 5.6 shows the traction and the torque density on a spherical shell with a radius of  $r_s = 3336$  km in two separate panels. Comparing the two panels in this figure shows that the traction as well as the torque density have the same spatial pattern close to the equator and in mid-latitude regions. Close to the poles, the spatial structure differs which is not surprising because the factor  $\sin^2(\theta)$  becomes vanishingly small in these regions. Because of the similarity of the spatial patterns of the traction and the torque, the discussion is confined to the traction in the following.

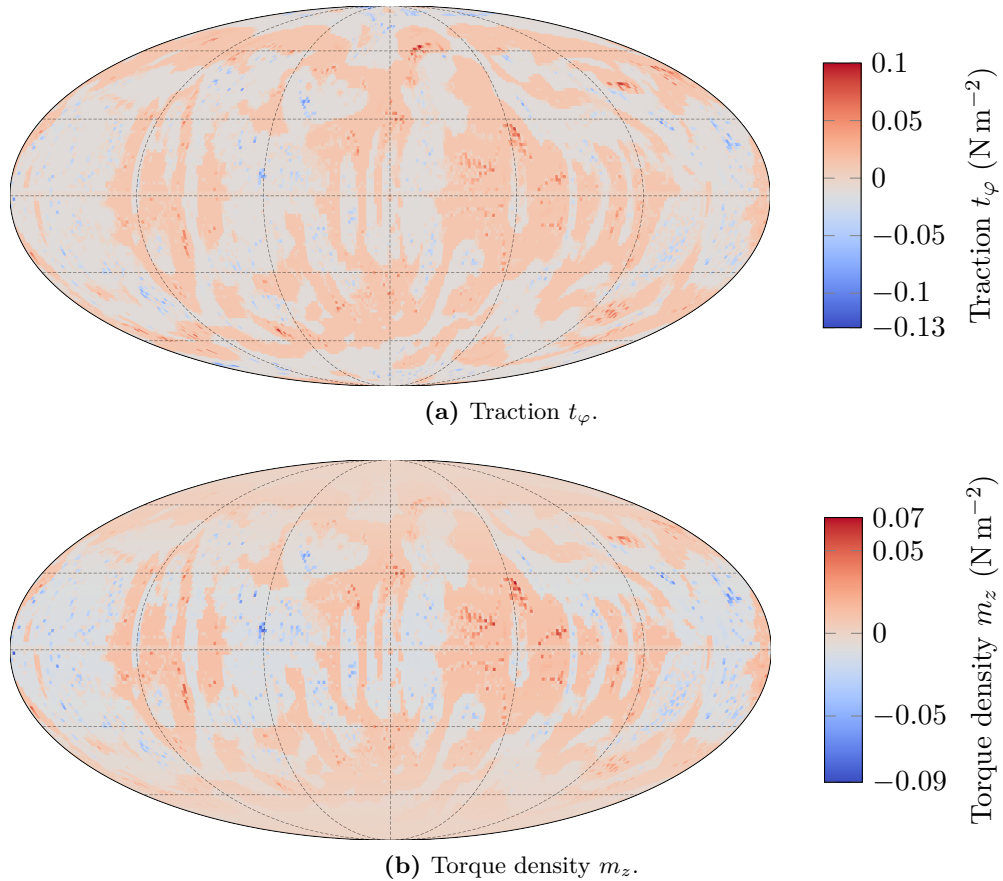


**Figure 5.6:** Snapshots of the traction  $t_\varphi$  (a) and the torque density  $m_z$  (b) on a spherical shell with a radius of  $r_s = 3336$  km. This radius corresponds to a virtual thickness of the stratified layer of  $\delta = 144$  km. The time of the snapshot is  $t = 318$  a.

For a comparison of Fig. 5.6 with Fig. 5.2, the color scales need to be taken into account because the color scales in both panels of Fig. 5.6 are not centered at zero whereas this is the case in Fig. 5.2. Nevertheless, it can be seen that there is an agreement of the coarser spatial patterns of the traction in Fig. 5.6a and the azimuthal velocity in Fig. 5.2b because the signs of the traction and the azimuthal velocity coincide. A good correlation of the spatial patterns of the traction with the radial magnetic field is not found when Figs. 5.6a and 5.2a are compared. In several spots, the value of the traction is increasing significantly compared to the neighboring regions which results in a concentration of either deep red or deep blue dots. If the radial magnetic field shown in Fig. 5.2a is analyzed in the vicinity of these spots, it is found that it is reversing its sign. Hence, the presence of these localized minima and maxima of the traction (and the torque density) is due to the fact that the radial magnetic field becomes small such that the analytical model yields a large traction.

The resulting torque acting on the mantle is obtained by an integration of the torque density shown in Fig. 5.6b. Analyzing Fig. 5.6b shows that the equatorial and the mid-latitude regions contribute the most, which is expected from geometry. There are regions with a negative or positive torque density which are either colored light red or light blue. The area of these regions seems to be fairly equal and, therefore, it is not possible from visual inspection to determine whether the resulting torque is positive or negative. Moreover, several localized minima and maxima of the torque density are located in the equatorial and the mid-latitude regions. These are due to the respective values of the traction. Thus, the dependence of the average traction of the analytical model on the magnetic field, which yields an increase and subsequent decrease for a decreasing magnetic field, has an influence on the resulting torque. However, the number of patches, in which the analytical model is sampled with a small magnitude of the magnetic field, is small compared to the overall number of patches which are contributing a significant amount to the resulting torque.

Figure 5.6 considers only a snapshot in time. In order to assess whether the patterns of the traction and the torque density are similar to the azimuthal velocity a temporal and azimuthal average of the radial magnetic and azimuthal velocity fields as well as of the traction and the torque density is considered in the following. This also allows to determine whether the equatorial and the mid-latitude regions are dominantly contributing to the resulting torque. This average can be designated as the temporal mean value of the azimuthally averaged field and is computed according to

$$\langle \bullet \rangle_{\varphi,t}(r_s, \theta) = \frac{1}{T} \frac{1}{2\pi} \int_0^T \int_0^{2\pi} (\bullet)(r_s, \theta, \varphi, t) d\varphi dt, \quad (5.7)$$

where  $(\bullet)$  denotes the field whose average is computed,  $r_s$  the radius of the spherical shell on which the field is considered and  $T$  the time period. Figure 5.7 shows the averages of the radial magnetic field, the azimuthal velocity field, the traction and the torque density. In addition to these, the interval of a standard deviation is also indicated in Fig. 5.7 by a dashed line. The standard deviation  $\sigma_t$  of each of the fields is only computed with respect to the time, *viz.*,

$$\sigma_t\{\bullet\}(r_s, \theta) = \sqrt{\frac{1}{T} \int_0^T (\langle \bullet \rangle_{\varphi}(r_s, \theta, t) - \langle \bullet \rangle_{\varphi,t}(r_s, \theta))^2 dt}. \quad (5.8)$$

Considering the mean values of the radial magnetic and the azimuthal velocity fields shown in Fig. 5.7, their minima and maxima are approximately an order of magnitude less than those which are obtained if the averaging is not applied. The temporal mean value of the radial magnetic field is anti-symmetric with respect to the equator. In the majority of the northern hemisphere, *i.e.*,  $0 \leq \theta \leq \pi/2$ , the radial magnetic field is positive whereas it is negative in the majority of the

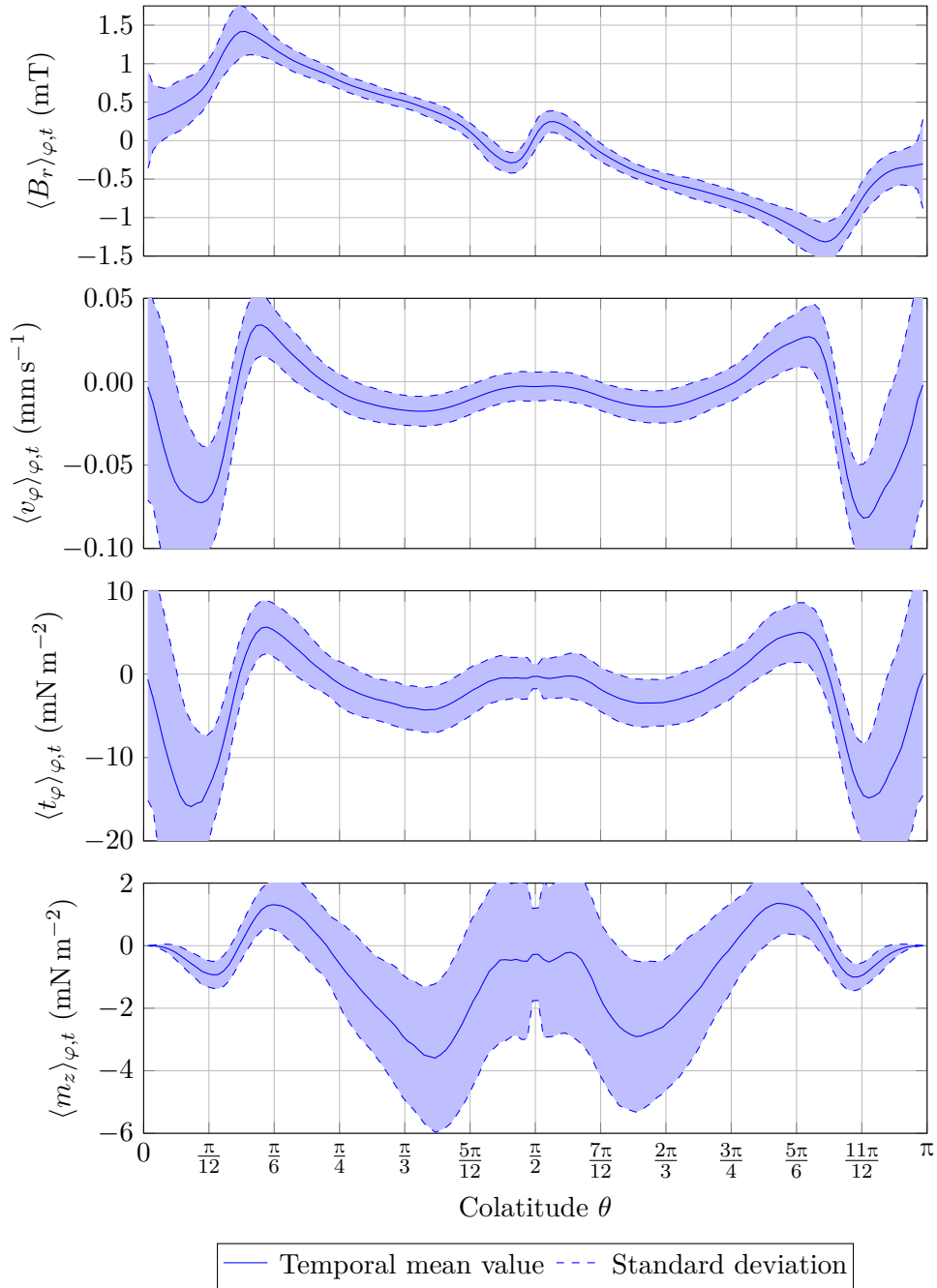


**Figure 5.7:** Azimuthal and temporal averages of the radial magnetic field, the azimuthal velocity field, the traction and the torque density for a virtual thickness of the stratified layer of  $\delta = 144$  km as a function of the colatitude  $\theta$ .

southern hemisphere, *i.e.*,  $\pi/2 < \theta \leq \pi$ . As opposed to the radial magnetic field, the average of the azimuthal velocity field is symmetric with respect to the equator.

For both fields, the minima and maxima are located close to the north or south pole and only modest values are found close to the equator. Furthermore, for both fields, the standard deviation is small in equatorial and mid-latitude regions and is large close to the poles. This holds especially for the azimuthal velocity whose standard deviation is much larger close to the north and south pole than that of the radial magnetic field.

If the mean temporal values of the traction are considered, it is found that they closely resemble those of the azimuthal velocity. Hence, the correlation of the traction with the azimuthal velocity, which is inferred from Figs. 5.2 and 5.6, is confirmed by Fig. 5.7. For the standard deviation of the average traction, the same holds true as for the azimuthal velocity—it is increasing towards the north and the south poles. At the equator, *i.e.*, for  $\theta = \pi/2$ , the mean value of the traction and especially its standard deviation significantly departs from the smooth course of the curve which is expected from that of the azimuthal velocity. This deviation is due to the fact that the local rate of rotation, which is applied in the analytical model, vanishes at the equator. In the analytical model, the case of a vanishing rotation was found to be an exceptional case, if the ALFVÉN number and thus the background magnetic field becomes small, see Fig. 3.20. The radial component of a dipole-dominated magnetic field is small close to the equator. Therefore, the local ALFVÉN number is expected to be small for the patches, which are located in the vicinity of the equator; this explains the different standard deviation of the traction and the torque density close to the equator.

The temporal mean values of the torque density are shown in the fourth panel of Fig. 5.7. Comparing them with those obtained for the traction shows that the extreme values of the traction close to the north and the south pole are not resembled in the torque. Although the tractions are large in these regions, the torque density, which is obtained from the traction after a multiplication with  $\sin^2(\theta)$ , is not exceeding that obtained in the mid-latitude and equatorial regions. Thus, the two pole regions do not yield a significant contribution to the resulting torque. This means that the large deviations of fields from their temporal mean values close to both poles are not important for the resulting torque acting on the mantle. Hence, instead of the maximum values of the traction in the vicinity of the poles, the modest values in the mid-latitude and equatorial regions are contributing the main part of the resulting torque. In these regions, the standard deviations of the torque from its temporal mean value are also largest. Moreover, the exceptional case of a vanishing local rate of rotation for  $\theta = \pi/2$  is visible in the torque density. For  $\theta = \pi/2$ , the standard deviation of the torque density is significantly different from those found for neighboring values of the colatitude. Nevertheless, it is expected that the case of a vanishing rotation is not influencing the resulting torque a lot because the standard deviation of the torque density obtained in this case is less than those obtained in the neighboring regions. Additionally, the temporal mean value of the torque does almost vanishing for  $\theta = \pi/2$ .

In conclusion, a similarity of the field of the traction to that of the azimuthal velocity can be confirmed from the snapshots shown in Fig. 5.2 and 5.6 and from

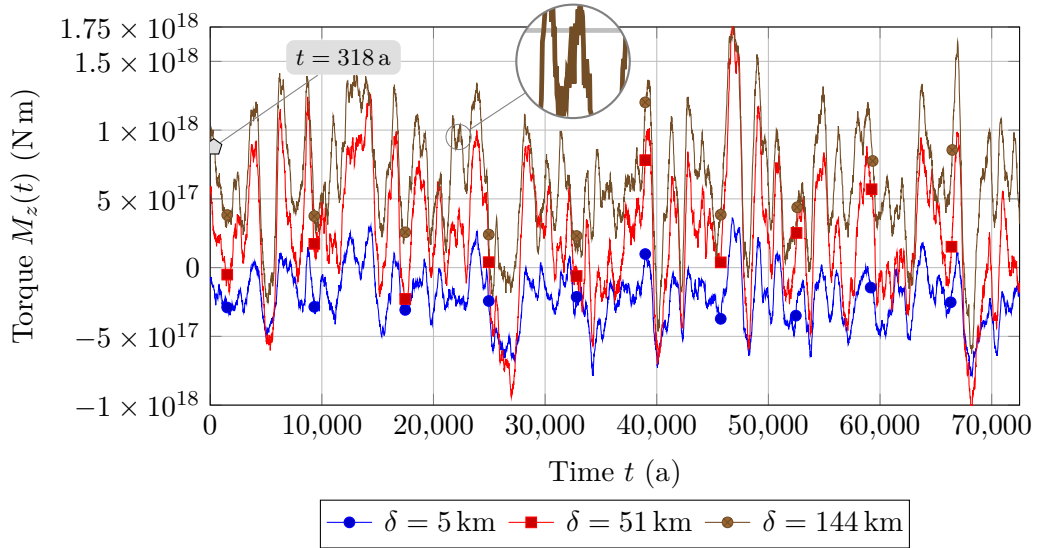


**Figure 5.8:** Time series of the core-mantle boundary torque for three spherical shells of different radii. Here,  $\delta$  denotes a virtual thickness of the corresponding stratified layer and can be related to the sampling radius by means of Eq. (5.5). Only every tenth point in time, for which the torque was obtained, is shown in the plot.

the azimuthal and temporal averages shown in Fig. 5.7. Furthermore, particular features of the traction could be explained based on the analytical model. It was found that the major part of the resulting torque is generated in the equatorial and mid-latitude regions. Despite the fact that the largest absolute values of the radial magnetic and the azimuthal velocity fields and of the traction are located in the vicinity of the poles, these regions do not contribute significantly to the resulting torque. In the equatorial and mid-latitude regions, the temporal averages of the torque density and the standard deviations from the temporal mean are largest. This suggests that the temporal fluctuations of the resulting torque are also governed by those of the radial magnetic and azimuthal velocity fields in these regions.

### 5.3.2 Temporal features of the resulting core-mantle boundary torque

The temporal features of the resulting core-mantle boundary torque are of interest to analyze fluctuations in the Length of Day (LOD), because on long timescales these fluctuations are due to the core-mantle boundary torque. In this section, only the temporal features of the resulting core-mantle torque and their dependence on the radius of the spherical shell, which is used for the computation of the resulting torque, are discussed. The associated LOD fluctuations are compared to observations separately in Sect. 5.4.

Figure 5.8 shows the time series of the core-mantle boundary torque for three

spherical shells of different radii. In all three curves, strong fluctuations of the torque are visible. There are fluctuations with a period of several thousand years. Moreover, the inset in Fig. 5.8, which shows a magnification of the torque, suggests that there are also fluctuations with shorter timescales with periods of less than approximately one hundred years. In fact, these short timescales cannot be identified well in Fig. 5.8 because of the scaling of the temporal axis. Moreover, the curves shown in Fig. 5.8 do not contain every point in time for which the resulting torque was computed. Due to limitations of the memory capacities of the program, which is used for the generation of the plot, only every tenth point in time is shown. Thus, it can be expected that the temporal spectrum is even richer regarding the shorter timescales. In summary, the core-mantle boundary torque experiences fluctuations on multiple timescales which are due to the turbulent nature of the magnetohydrodynamic flow in the outer core of the Earth.

Apart from the timescales involved, Fig. 5.8 shows that the core-mantle boundary torque strongly depends on the radius of the spherical shell or on the virtual thickness of the stratified layer  $\delta$ , for which the resulting torque is computed. In general, the magnitude of the torque increases with the virtual thickness  $\delta$ . While the resulting torque is negative most of the time for a virtual thickness of  $\delta = 5$  km, it is mostly positive for a virtual thickness of  $\delta = 144$  km. The case of a virtual thickness of  $\delta = 51$  km yields maximum values of the resulting torque, which are comparable to those obtained for a virtual thickness of  $\delta = 144$  km. However, the corresponding minimum values do not comply with those obtained for a virtual thickness of  $\delta = 144$  km but rather coincide to those obtained with those obtained for a virtual thickness of  $\delta = 5$  km.

In order to assess the dependence on the virtual thickness more systematically, the sample correlation coefficients of the resulting torques, which are obtained for the different virtual thicknesses, are considered. These correlation coefficients represent a measure of the similarity of the two corresponding torques. For the computation of the sample correlation coefficients, the torque obtained for the different thicknesses is interpolated to an equidistantly sampled time interval. Then, the sample correlation coefficient  $c$  is computed according to

$$c(\bullet, \star) = \frac{\sum_{k=1}^N \left( ((\bullet)(t_k) - \langle \bullet \rangle) ((\star)(t_k) - \langle \star \rangle) \right)}{\sqrt{\sum_{k=1}^N ((\bullet)(t_k) - \langle \bullet \rangle)^2 \sum_{k=1}^N ((\star)(t_k) - \langle \star \rangle)^2}}, \quad (5.9)$$

where  $(\bullet)$  and  $(\star)$  denote the time series which are considered, and  $\langle (\bullet) \rangle$  and  $\langle (\star) \rangle$  are the respective temporal mean value and  $N$  the number of sampling points. The resulting (symmetric) correlation matrix is visualized in Fig. 5.9. In general, the torques obtained for all thicknesses are correlated well because a negative correlation coefficient indicating an anti-correlation is not found. The minimum of the correlation coefficients is approximately 0.8. Moreover, two “neighboring” spherical shells yield time series of the resulting torque which are always well

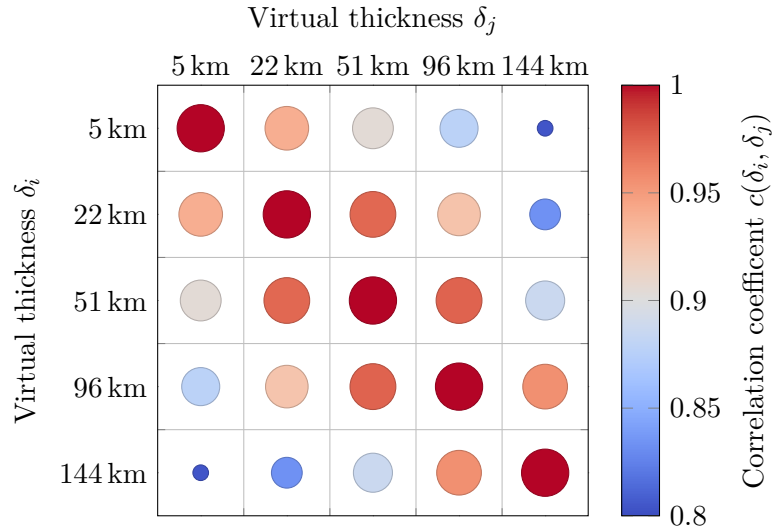


**Figure 5.9:** Correlation coefficients  $c$  of the core-mantle boundary torques obtained for spherical shells of different radii. The correlation coefficients are computed according to Eq. (5.9). Here,  $\delta_i$  denotes a virtual thickness of the corresponding stratified layer and can be related to the sampling radius by means of Eq. (5.5). The sizes of the circles and their colors indicate the values of the correlation coefficients.

correlated because all of the correlation coefficients on the first upper diagonal of the correlation matrix are larger than 0.9. Moreover, the time series corresponding to virtual thicknesses of 22 km, 51 km and 96 km are well correlated among each other because the associated correlation coefficients are larger than 0.925. This fact indicates that similar results regarding the temporal features of the core-mantle boundary torque are obtained, if the numerical model is sampled on spherical shells with radii which are corresponding to virtual thicknesses ranging from 22 km to 96 km.

However, for an assessment of a suitable sampling radius, the magnitude of the associated core-mantle torque also needs to be taken into account. In the computation of the correlation coefficient, the mean value is subtracted from the time series and, therefore, differences regarding the minimum and maximum values of the torque are not reflected very well in the correlation coefficient. For example, although the correlation of the torques corresponding to the virtual thicknesses of  $\delta = 22$  km and  $\delta = 96$  km is 0.925, the two maximum absolute values of the associated torques are  $1.14 \times 10^{18}$  N m and  $1.88 \times 10^{18}$  N m, respectively. Hence, the peak value of the torque obtained for a virtual thickness of  $\delta = 96$  km is 60 % larger than that obtained for a virtual thickness of  $\delta = 22$  km. For a virtual thickness of  $\delta = 51$  km, the maximum absolute value of the torque is  $1.78 \times 10^{18}$  N m. Comparing this value to that obtained for  $\delta = 96$  km indicates that the differences between the spherical shells reduce the larger the virtual thicknesses become. The trend that the resulting torque becomes independent of

the virtual thickness cannot be confirmed if the case of  $\delta = 144$  km is considered. On the one hand, the maximum absolute value of the torque is  $1.88 \times 10^{18}$  N m, which is the same as that obtained for a virtual thickness of  $\delta = 96$  km. On the other hand, the torque obtained for a virtual thickness of  $\delta = 144$  km is not correlated to those obtained for virtual thicknesses of 22 km, 51 km and 96 km as well as the torques associated with these three different virtual thicknesses are correlated among each other. For example, the correlation coefficient of the torques obtained for  $\delta = 51$  km and  $\delta = 144$  km is 0.88; this indicates that the temporal features of two torques are not in such a good agreement as those obtained for  $\delta = 51$  km and  $\delta = 96$  km.

In summary, the turbulent nature of the magnetohydrodynamic flow in the outer core of the Earth is reflected in the presence of multiple timescales and strong fluctuations in the resulting torque, which is predicted by the core-mantle coupling model. Moreover, the order of magnitude of the resulting torque of  $10^{17}$  N m to  $10^{18}$  N m is sufficiently large to cause significant changes in the LOD. The resulting torque depends on the virtual thickness associated with the radius of the spherical shell, at which the numerical model is sampled. This dependence is related to the presence of boundary layers in the numerical model. From analyzing the correlation coefficients of the torques obtained for the different virtual thicknesses, a tendency that the resulting torque becomes independent of the virtual thickness was found for intermediate values of the virtual thickness ranging from 22 km to 96 km. For a larger virtual thickness of  $\delta = 144$  km, a similar maximum absolute value of the resulting torque is obtained, but the trend of a very good correlation with the torques obtained for lower values of the virtual thickness cannot be confirmed. The torque obtained for a very small virtual thickness of  $\delta = 5$  km is not comparable to those obtained for other virtual thicknesses and the corresponding spherical shell is most likely located inside the viscous boundary layer of the numerical model.

## 5.4 Implications for the Length of Day

In the following, the variations in the Length of Day (LOD) which are obtained from the results of the core-mantle coupling model are compared to historical records. Before a comparison is performed, available records of historical LOD fluctuations which are from astronomical observations are presented and discussed in Sect. 5.4.1. Moreover, the principle components of a selected historical record are identified by using Singular Spectrum Analysis (SSA). Following this initial discussion of LOD records, the LOD fluctuations which are predicted by the core-mantle coupling are presented and discussed in Sect. 5.4.2. Finally, a comparison of the predicted LOD fluctuations with the historical record is presented in Sect. 5.4.3.

### 5.4.1 Observational data for changes in the Length of Day

In Sect. 2.2, daily-sampled LOD fluctuations from 1973 to 2020 AD<sup>4</sup> are shown in Fig. 2.6. This LOD record is provided by the *International Earth Rotation and Reference Systems Service* and determined by using multiple sources of geodetic observations *e.g.*, very long baseline interferometry, the global positioning system and satellite radio positioning [IERS (2019)]. However, this highly accurate record is not suitable for an assessment of the influence of the core of the Earth on LOD fluctuations, because the available time period of 50 years is too small. Thus, alternative records of LOD fluctuations are considered. These rely on astronomy and the LOD is determined from information on the occurrences of past lunar and solar eclipses and also lunar occultations [Stephenson (2003)]. Several of these records, which differ in the sampling frequencies, the precision and the considered time periods, are found in the literature [McCarthy and Babcock (1986); Jordi et al. (1994); Stephenson, Morrison, and Smith (1995); Stephenson, Morrison, and Hohenkerk (2016)]. More precisely, the references contain LOD records from 1657 to 1984 AD [McCarthy and Babcock (1986)], from 1830 to 1992 AD [Jordi et al. (1994)], from 500 BC<sup>5</sup> to 1600 AD [Stephenson, Morrison, and Smith (1995)] and from 2000 BC to 2016 AD [Stephenson, Morrison, and Hohenkerk (2016)]. The sampling rate of the LOD records also differs in all of the aforementioned references. Additionally, the error regarding the LOD increases the further the record goes back in time. Especially, LOD values which go back to the pre-telescopic period, *i.e.*, those prior to 1620 AD, have an insufficient precision to reveal short-term variations [Stephenson (2003)]. Nevertheless, errors regarding the LOD also become considerable in the telescopic period. For example, for 1750 AD, the LOD error is specified as 17.2 ms by McCarthy and Babcock and as 0.8 ms by Stephenson, Morrison, and Hohenkerk, although both references specify a comparable value for the LOD variation of 0.4 ms and 0.6 ms. Additionally, the LOD error is not specified in all of the aforementioned references.

Two curves of LOD changes from 1800 to 2016 AD are shown in Fig. 5.10. In this figure, historical LOD records from two selected references are shown for a period in which the LOD error is at least on the same scale as the LOD changes themselves. Comparing the two curves shows that there is a good agreement from 1900 AD onward. However, for the period from 1800 to 1900 AD, considerable differences of the two curves are visible. These differences are due to the fact that the data of McCarthy and Babcock are, *first*, sampled semiannually whereas those of Stephenson, Morrison, and Hohenkerk are sampled annually. *Second*, the LOD error of the record of the former authors is much larger than that of the latter. Thus, although the LOD data of the former authors are sampled with a lower frequency, their higher reliability makes them more suitable for a comparison with the considered core-mantle coupling model. Moreover, the more recent study of Stephenson, Morrison, and Hohenkerk provides a time series which

<sup>4</sup>AD refers to *Anno Domini*.

<sup>5</sup>BC refers to before Christ.

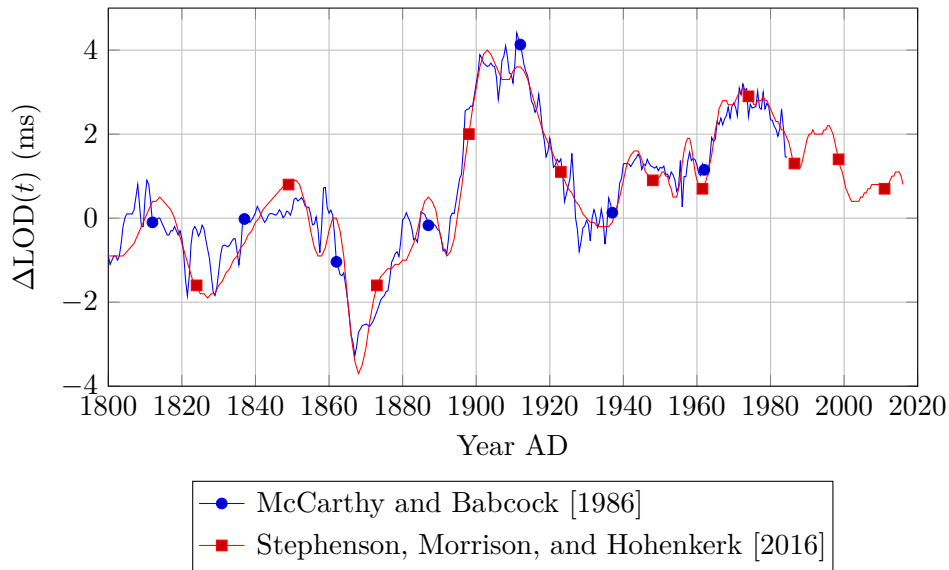


**Figure 5.10:** Long-term fluctuations of the Length of Day according to McCarthy and Babcock [1986] and Stephenson, Morrison, and Hohenkerk [2016]. The LOD record of McCarthy and Babcock [1986] is sampled semiannually from 1657 to 1984 AD. The LOD record of Stephenson, Morrison, and Hohenkerk [2016] is sampled irregularly from 2000 BC to 2016 AD, but annually sampled data is available from 1800 AD and from 1950 AD the data is semiannually sampled.

is 30 years longer than that of McCarthy and Babcock, which allows to extract more information about the temporal dynamics of the LOD variation.

In both curves shown in Fig. 5.10, LOD changes on intra-decadal, decadal and centennial timescales are present which shall be analyzed subsequently. For an analysis of the frequencies, which are present in a time series, the FOURIER analysis is a standard method. However, due to the fact that the number of 216 equidistantly sampled annual values in the record of Stephenson, Morrison, and Hohenkerk is small, “the” FOURIER analysis is not suitable, because the FOURIER analysis theoretically requires that the signal is periodic in time. Moreover, the NYQUIST limits the frequencies which can be resolved and, in practice, for a good identification of a frequency or associated timescale, a multiple of the associated period needs to be contained in the signal. For these reasons, an alternative to the FOURIER analysis is applied. In the analysis of intra-decadal timescales in the LOD time series, several studies manipulate the time series by either smoothing and de-trending them or by taking into account a model for the atmospheric angular momentum [Holme and de Viron (2005); Holme and de Viron (2013)]. While these analyses make use of a second model or directly manipulate the data in order to extract certain information, the *Singular Spectrum Analysis* (SSA) represents a method which does not require any additional model or a specification of, for example, an averaging period. The SSA diagonalizes a covariance matrix

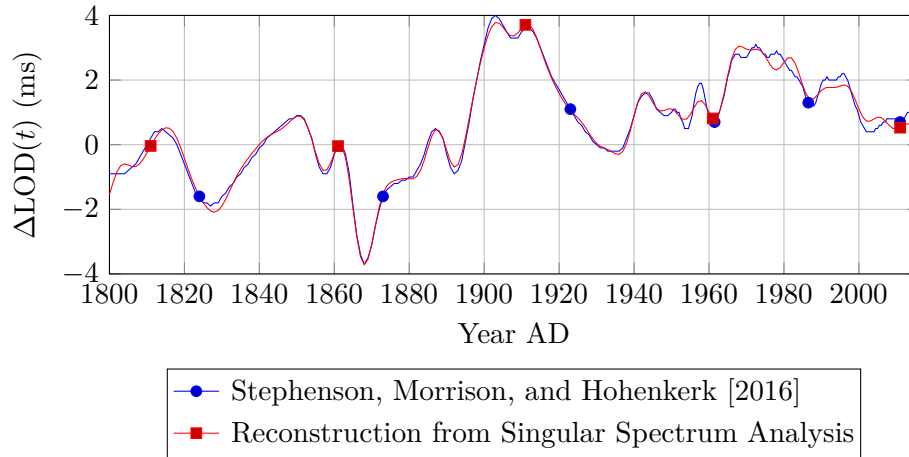


**Figure 5.11:** Reconstruction of the historical LOD record using the first eight modes of a Singular Spectrum Analysis.

which is computed from the time-lagged parts of the considered time series and yields a decomposition of the time series into mutually orthogonal components. These components are also referred to as principal components. Details on the SSA are given, for example, in Golyandina, Nekrutkin, and Zhigljavsky [2001] and Vautard, Yiou, and Ghil [1992] or Korobeynikov [2010]. Furthermore, in climate sciences, SSA is referred to as the method of empirical orthogonal functions and it is also widely used, see, *e.g.*, Vautard, Yiou, and Ghil [1992] for an application and Ghil et al. [2002] for an extensive review. Because of the fact that the SSA is a non-parametric method to compute a spectral decomposition of a time series, it is in the following applied to the LOD record of Stephenson, Morrison, and Hohenkerk. The idea behind the method is that the different principle components can be associated to different physical processes.

In Fig. 5.11, the results of the SSA of the LOD record of Stephenson, Morrison, and Hohenkerk are shown. The time series, which is reconstructed from the first eight principal components identified in the SSA, agrees well with the original one and reproduces its major long-term components very well. Only from 1950 AD onward, differences between the original and the reconstructed time series become visible. These are due to the fact that the original LOD record of Stephenson, Morrison, and Hohenkerk is not equidistantly sampled from 1800 to 2016 AD but rather semiannually sampled data are available from 1950 to 2016 AD. However, in the SSA, only annually sampled data is used and, thus, the original record is under-sampled from 1950 to 2016 AD.

The first four principal components which are obtained in the SSA are shown in Fig. 5.12. Additionally, the fifth to eighth principal components are shown Fig. E.2 in Appendix E. The principal components are sorted according to their root mean square values, which can be interpreted as the power of the corresponding principal component. The reconstructed LOD time series shown in Fig. 5.11 is obtained as

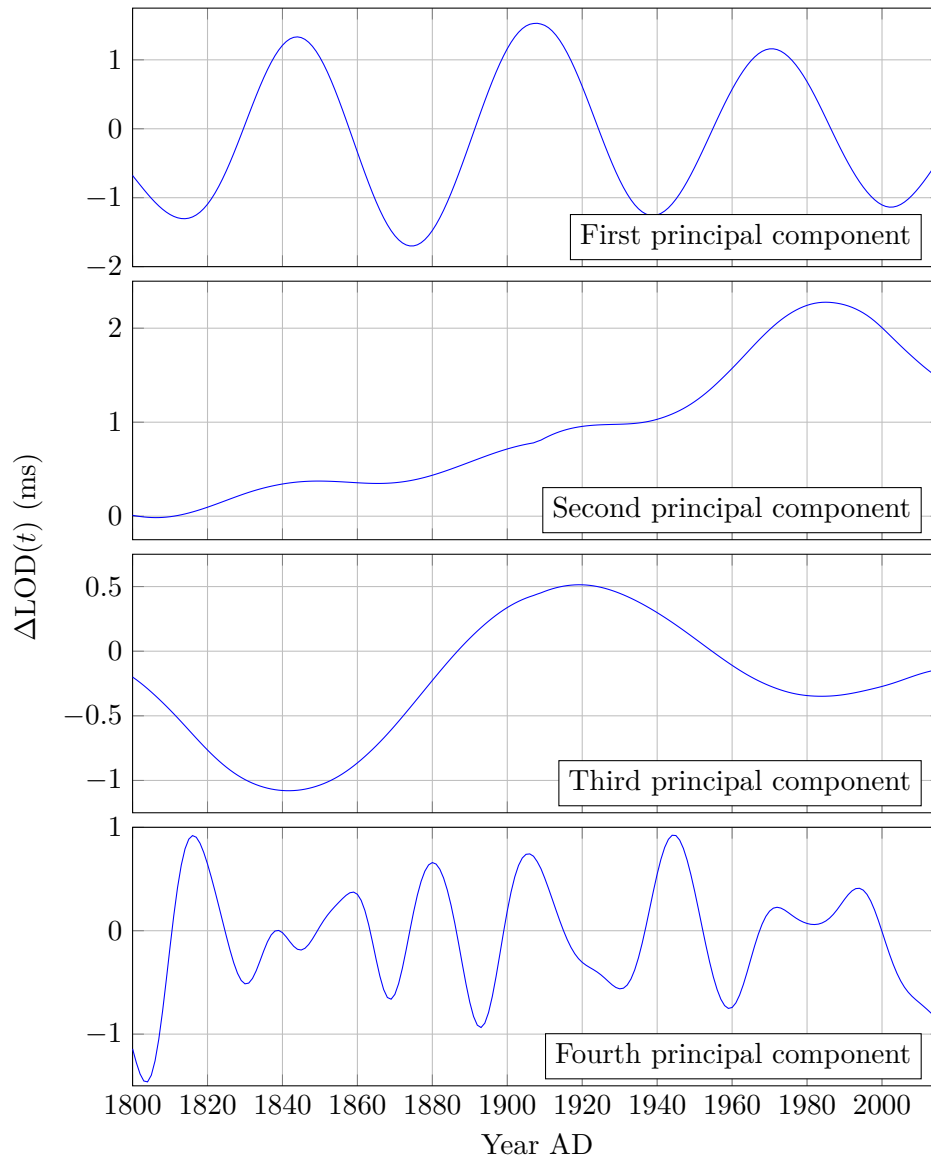


**Figure 5.12:** First four principal components obtained in the Singular Spectrum Analysis of the LOD data of Stephenson, Morrison, and Hohenkerk [2016].

a (linear) superposition of the principal components shown in Figs. 5.12 and E.2. The sixth to eighth principal components shown in Fig. E.2 in Appendix E are similar to modulated sinusoidal curves with periods of approximately ten years. The modulation of these principal components indicates that a full separation of the signal is not feasible due to the limited amount of sampling points, which are available. Thus, principal components of a higher degree are not considered in the reconstruction of the LOD record shown in Fig. 5.11.

In the following, the temporal features of the different principal components are

discussed briefly. Subsequently, the discussion is limited to the first four principal components, because the timescales associated with these first four components are largest. A discussion of the principal components with a degree larger than four is given in Appendix E. The first principal component which is shown in the top panel of Fig. 5.12 is an oscillation with a period of approximately 60 years and an amplitude of approximately 1.25 ms. From the second principal component, a linear increase of the LOD value, which is modulated by oscillation, can be inferred. The same also holds for the third principal component. For this component, the modulation is more prominent and has a period of approximately 140 years. Moreover, the linear increase is weaker in the third than in the second component. The facts, that both components show a modulation and that the modulation becomes larger in the second component from 1950 AD onward, suggest that a perfect separation of the two components could not be achieved due to the limited number of sampling points which are available. In the SSA, the original time series is under-sampled from 1950 AD onward which might also cause the strong modulation of the second principal component in this time period. The fourth principal component, which is shown in the bottom panel of Fig. 5.12, cannot be interpreted clearly. It is an oscillatory component but, in contrast to the first component, multiple frequencies with periods of a decade or more are present in the time series. Similar to the second and the third component, the fourth and the fifth component might not have been separated well by the SSA because the fifth component also contains multiple fluctuations of the similar periods.

In conclusion, the SSA of the LOD variations has identified principal components of which two have periods of 60 and 140 years. Periods of approximately a decade have also been identified, but the associated components cannot be interpreted clearly and might not be separated well from one another due to a limited number of available sampling points. Altogether, the available historical records of LOD variations are sparse and reliable values are not available on geological timescales. Comparing the time interval of 200 years, for which annually sampled data are available, with the simulated time interval of the core-mantle model of approximately 70 000 years shows the large disparity. This compromises the objective of identifying similar temporal patterns in the LOD fluctuations as predicted by the core-mantle coupling model and the available historical records. Nevertheless, an identification of, for example, signals with periods in the range between 60 and 140 years in the predicted LOD fluctuations could confirm the validity of the proposed core-mantle coupling model.

#### **5.4.2 Predicted variations in the Length of Day by the core-mantle coupling model**

In this section, the LOD fluctuations, which are predicted by the core-mantle coupling, are presented and discussed. The LOD fluctuations are obtained by an integration of the equation, which describes the rotation of the mantle of the Earth using the torque predicted by the core-mantle coupling model. In Sect. 2.2,

it was discussed that the mantle can be considered as a rigid body if its rotational dynamics is considered. Moreover, for the LOD fluctuations, the nutation and precession of the mantle can be neglected and the motion is regarded as the rotation of a rigid body about an axis which is fixed in space. Thus, as already outlined in Sect. 2.2, the relevant component of the EULER equations of rigid body dynamics is given by

$$J_{zz}\dot{\omega}_z(t) = M_z(t), \quad (5.10)$$

where  $J_{zz}$  denotes the first principal moment of inertia of the mantle of the Earth,  $\omega_z$  the angular velocity with respect to this first principal axis and  $M_z$  the predicted torque which is computed according to Eq. (5.3).<sup>6</sup> As discussed in Sect. 2.2,  $\omega_z = 2\pi/(T_0 + \Delta\text{LOD})$  relates the angular velocity  $\omega_z$  to the LOD variations. Thus, the angular acceleration  $\dot{\omega}_z$  is related to the LOD fluctuation in a non-linear way by

$$\dot{\omega}_z(t) = -\frac{2\pi}{(T_0 + \Delta\text{LOD}(t))^2} \frac{d\Delta\text{LOD}}{dt}. \quad (5.11)$$

A substitution of this expression for the angular acceleration in Eq. (5.10) yields the differential equation describing the LOD fluctuations, *i.e.*,

$$\frac{d\Delta\text{LOD}}{dt} = -\frac{(T_0 + \Delta\text{LOD}(t))^2}{2\pi} \frac{M_z(t)}{J_{zz}}. \quad (5.12)$$

This equation is the non-linear variant of Eq. (2.7) in the derivation of which the approximation  $T_0 + \Delta\text{LOD} \approx T_0$  was made. However, it is expected (and also confirmed by an integration of both variants) that the non-linearity of the first term on the right-hand side of Eq. (5.12) can be neglected.

In order to obtain the predicted LOD fluctuations, Eq. (5.12) is integrated in time over the interval for which the resulting torque acting on the mantle was computed. For the mantle including the crust of the Earth, the principal moment of inertia is given by  $J_{zz} = 7.1 \times 10^{37} \text{ kg m}^2$ , which is obtained from the Preliminary Reference Earth Model (PREM) [Mathews et al. (1991); Gross (2015)]. For the reference value of the length of day, the standard value of  $T_0 = 86\,400 \text{ s}$  is applied. The initial condition of the difference in the length of day from its reference value is chosen as  $\Delta\text{LOD}(t = 0) = 0$ . Finally, based on the time series of the predicted torque  $M_z(t)$  and using the specified values for  $J_{zz}$  and  $T_0$ , Eq. (5.12) is integrated in time.

The results which are obtained from integrating Eq. (5.12) are shown in Fig. 5.13. The LOD fluctuations clearly depend on the virtual thickness  $\delta$ , for which the torque is computed. For a small value of the virtual thickness, the LOD is increasing, whereas it is decreasing for a virtual thicknesses larger than 22 km. For the case of  $\delta = 22 \text{ km}$ , the LOD is almost constant over the considered time period. A

<sup>6</sup>Here, the direction of the principal axis is given by the vector  $e_z$  whereas this vector was denoted by  $e_3$  in Sect. 2.2.

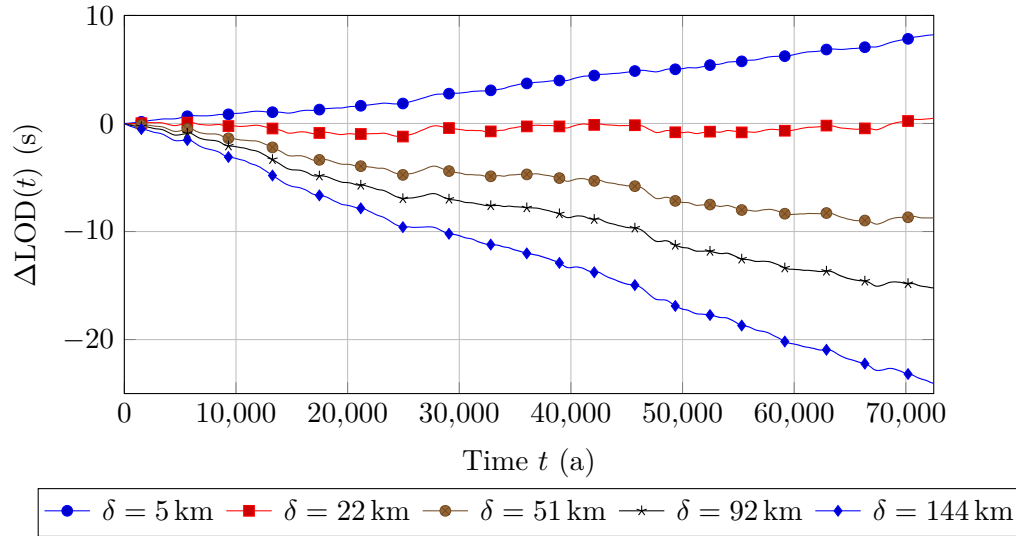


**Figure 5.13:** Changes in the Length of Day predicted by the core-mantle coupling model for spherical shells of different radii. Here,  $\delta$  denotes a virtual thickness of the corresponding stratified layer and can be related to the sampling radius by means of Eq. (5.5) on page 171.

decreasing LOD value corresponds to an acceleration of the mantle and *vice versa*. The deceleration of the rotation of the mantle for a virtual thickness of the stratified layer of  $\delta = 5$  km and its acceleration for virtual thicknesses larger than 22 km agrees with the results for the torque shown in Fig. 5.8. The acceleration is larger the larger the virtual thickness is which also complies with the expectations that larger torques are obtained the larger the azimuthal velocity is and that this velocity increases with an increasing distance from the viscous boundary layer at the CMB. The results obtained for a virtual thickness of  $\delta = 22$  km are remarkable because neither a net acceleration nor deceleration is predicted. For this thickness, the temporal mean of the torque is almost vanishing, which indicates that the azimuthal velocity field, which determines the sign of the local traction and thus of the resulting torque, does not have a dominant direction.

In general, the curves in Fig. 5.13 follow a linear trend. This is not expected from the time series of the resulting torque shown in Fig. 5.8 because strong fluctuations on a multitude of timescales are present in the torque. Moreover, the amplitudes of the fluctuations with larger periods are considerable in comparison to the mean value of the torque. The curves in Fig. 5.13 only slightly deviate from their corresponding linear trends which indicates that the inertia of the mantle is simply too large to yield significant LOD variations from the predicted fluctuations of the resulting torque. Moreover, the periods in which the torque reaches its peak value are too short to cause a significant change of the LOD. Thus, the curves in Fig. 5.13 are dominated by the temporal mean of the resulting torque and fluctuations play a secondary role.

The question, whether the acceleration or deceleration of the rotation of the

mantle which is implied from the linear trend of the curves in Fig. 5.13 is realistic, is discussed in the following. The acceleration or deceleration of the rotation of the mantle would cause an increase or decrease of the kinetic energy of the mantle. The work which is causing this change of the kinetic energy is performed by the fluid in the outer core of the Earth. Considering only the linear trend, the change of the kinetic energy of the mantle can be estimated to range from  $1.7 \times 10^{21}$  J to  $1.6 \times 10^{22}$  J, which corresponds to a power ranging from 0.7 GW to 6.4 GW. For the outer core of the Earth, estimates of its kinetic energy are not found in the literature. However, comparing the power required for the predicted LOD fluctuations with estimates for the heat fluxes across the inner core and the core-mantle boundary of 3 TW to 6 TW and 7 TW to 17 TW shows the predicted LOD fluctuations are not completely implausible because the power required is only a fraction of the two heat fluxes. Nevertheless, it can be doubted whether the continuous trends would also occur in reality because the core-mantle coupling model does not include a feedback between the analytical and the numerical model. In the framework of this chapter, the traction which is predicted by the analytical model only acts on the CMB and, in reality, it would, of course, also act on the fluid in the opposite direction. Thus, the fluid would decelerate locally if the traction would predict an acceleration of the mantle. As a consequence, the traction and, hence, also the resulting torque would be weaker because the azimuthal velocity would be lower. No account is taken for this type of feedback in the current framework and thus the prediction of the core-mantle coupling model of continuous linear trends in the LOD remains questionable. Furthermore, the lack of a feedback mechanism is inconsistent with respect to the energy balance. The fluid contained in the outer core is not losing the energy which corresponds to the work which the predicted traction (or resulting torque) is doing on the CMB (or the mantle of the Earth).

In summary, the core-mantle coupling model predicts LOD changes of several seconds over a period of 70 000 years. Such large LOD variations are not reported in the literature which only forecasts LOD values for a period of approximately 4000 years. The large changes are primarily caused by a linear trend in the predicted values and depend on the virtual thickness of the stratified layer, *i.e.*, the radius of the spherical shell, which is used for the computation of the torque. Since there is no feedback between the numerical and the analytical model, inconsistencies arise which question whether the predicted linear increases or decreases of the LOD value due to core-mantle coupling occur in reality.

### 5.4.3 Comparison of the predicted changes in the Length of Day with observations

In the following, the predicted LOD fluctuations are compared to those obtained from historical records. First, the long-term trends present in both of the time series of LOD variations are discussed and, subsequently, the correlations of both are analyzed. Finally, the validity of the predicted LOD fluctuations is assessed.

**Table 5.1:** Long-term increase of the difference of the Length of Day from the standard value. The data is reproduced from Stephenson, Morrison, and Hohenkerk [2016].

Year	2000 BC	1000 BC	0 AD	1000 AD	2000 AD
$\Delta\text{LOD}$ (ms)	-69	-53	-29	-12	0.9

From astronomical observations by Babylonian and Chinese astronomers dating back to 720 BC, the length of day can be extrapolated backward in time until 2000 BC [Stephenson (2003); Stephenson, Morrison, and Hohenkerk (2016)]. The obtained observational data show an increase of the LOD value over a period of 4000 years [Stephenson, Morrison, and Hohenkerk (2016)]. This increase of the LOD value follows a linear trend. From the millennial sampled LOD values specified in Table 5.1, a rate of change of the LOD of  $1.78 \text{ ms ha}^{-1}$  is obtained in Stephenson, Morrison, and Hohenkerk [2016], which corresponds to a deceleration of the mantle of the Earth.<sup>7</sup>

The torque predicted by the core-mantle coupling model either yields an acceleration or a deceleration of the mantle which is large in comparison to the historical records. Depending on the virtual thickness of the stratified layer, the core-mantle coupling model predicts either an increase or a decrease of the LOD value. For virtual thicknesses of  $\delta = 5 \text{ km}$  and  $\delta = 144 \text{ km}$ , the rates of change of the LOD value are approximately given by  $0.1 \text{ ms a}^{-1}$  and  $-0.3 \text{ ms a}^{-1}$ , respectively. Both of these values are more than two orders of magnitude larger than that obtained from historical records. This raises further doubts regarding the reality of the predicted LOD fluctuations. Moreover, the linear trend found in the observations is attributed to tidal friction, *i.e.*, gravitational interaction with the moon, and post-glacial rebound, *i.e.*, the uplift of the continents after the last ice age, and to core-mantle interaction [Stephenson, Morrison, and Hohenkerk (2016)]. Both of these processes can be analyzed in detail with the available geodetic data. For example, the rate of increase of the LOD value which is associated to tidal friction is given by  $2.3 \text{ ms ha}^{-1}$ ; this value is comparable to that found in the observational LOD data. In conclusion, the long-term linear trend predicted by the core-mantle coupling cannot be associated to a similar pattern found in the observational LOD data.

Linear trends dominate the predicted LOD fluctuations. These are due to an (energetic) inconsistency regarding the coupling of the numerical dynamo model and the analytical model which is used to determine the local value of the traction at the CMB. As discussed, a feedback between the two models is missing and, therefore, it is questionable whether a fully coupled model would predict these linear trends as well. Although all of the predicted LOD fluctuations show linear trends, correlations between the predicted and the observed LOD fluctuations are

<sup>7</sup>Here, the unit  $\text{ms ha}^{-1}$  denotes milliseconds per 100 years. The symbol h refers to the SI prefix *hecto*, *i.e.*,  $10^2$ . In the original paper of Stephenson, Morrison, and Hohenkerk, the same unit is also used but denoted by  $\text{ms cy}^{-1}$ , *i.e.*, milliseconds per century.

computed in order to assess whether similarities between both data sets can be identified. The predicted and observed LOD values are available on different sets of points in time. Therefore, a direct computation of the correlation is not feasible because the number of samples differs considerably. From the LOD observation, annually sampled data are available at 217 sampling points whereas the core-mantle coupling predicts LOD values at approximately 50 000 points in time. Besides, the difference regarding the considered time periods of approximately 200 years of annual observations and 72 500 years of predicted LOD values represents an additional challenge.

In order to compute a correlation, the predicted LOD values are considered on time windows whose lengths correspond to that of the historical record. Then, the predicted LOD fluctuations are interpolated on each of these windows such that two equidistant annually sampled sets of the predicted and observed LOD fluctuations are available. For these two data sets, a correlation coefficient is computed. Furthermore, two adjacent windows shall overlap and, therefore, the time difference between two adjacent time windows is chosen as 50 years. This yields a division of the time period of 72 500 years for which predicted LOD fluctuations are available into 1450 separate time windows which are partially overlapping. This represents a different time period and the correlation coefficient obtained for each of these time windows indicates whether there is a similarity between the predicted and observed LOD variations during the considered (simulated) period of time.

As discussed, considering separate overlapping time windows yields a set of computed correlation coefficients which are shown in the form of a histogram in Fig. 5.14 for three selected different virtual thicknesses of the stratified layer. The results in Fig. 5.14 show that the correlation of the predicted and observed LOD fluctuations also depends on the virtual thickness of the stratified layer. In all of the shown histograms, the correlation coefficients are either close to  $-0.6$  or  $0.5$  for most of the time windows. For the smallest virtual thickness of  $\delta = 5$  km, the correlation is positive, *i.e.*,  $c \approx 0.5$  in most cases, whereas it is in most cases opposite in sign for a virtual thickness of  $\delta = 144$  km. Regarding two previously discussed cases, the histogram obtained for a virtual thickness of  $\delta = 22$  km represents an intermediate case, because the correlation coefficients are either close to  $-0.6$  or  $0.5$ . Histograms for virtual thicknesses of  $\delta = 51$  km and  $\delta = 92$  km were also computed, but they are similar to that obtained for the case of  $\delta = 144$  km. Therefore, these histograms are not shown here.

The results shown in Fig. 5.14 may suggest that a good correlation is obtained for a virtual thickness of  $\delta = 5$  km and that the predicted and observed LOD values become anti-correlated if the virtual thickness is above some critical value. However, if the histograms are interpreted together with the time series of the observed and predicted LOD fluctuations shown in Fig. 5.10 and 5.13, respectively, a different conclusion arises. The observed LOD fluctuations show a modest increase of the LOD value which was also identified in the Singular Spectrum Analysis. In addition, the predicted LOD fluctuations are dominated by linear trends which yield either

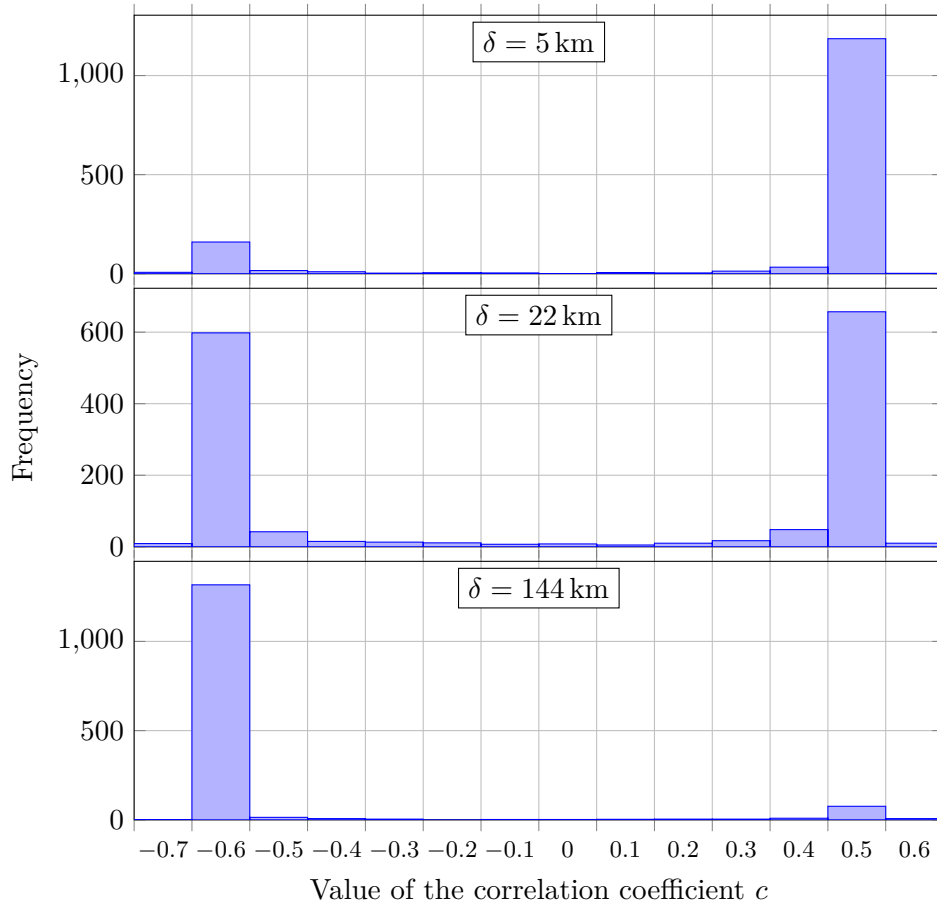


**Figure 5.14:** Histograms of the correlation coefficients of the predicted and the observed LOD fluctuations for three spherical shells of different radii. Here,  $\delta$  denotes a virtual thickness of the corresponding stratified layer, which can be related to the sampling radius by Eq. (5.5).

an increase or a decrease of the LOD value depending on the virtual thickness. The only case which does not show one of these trends is that of a virtual shell thickness of  $\delta = 22$  km. The fact that the histograms shown in Fig. 5.14 predict a positive correlation for the case in which the predicted LOD value is increasing and a negative correlation for the cases, in which the predicted LOD value is decreasing, supports the idea that the histograms are biased regarding the linear trend. In most of the time windows, the predicted LOD values are either increasing or decreasing and the deviations from these dominant linear trends play a minor role. Thus, the correlation is always either positive or negative depending on the virtual thickness which is considered. In other words, the timescales of the deviations from the dominant linear trends are larger than 200 years and thus not reflected in the correlation coefficients. For a virtual thickness of  $\delta = 22$  km, there are two dominant bins in the histogram shown in Fig. 5.14, which supports the idea that

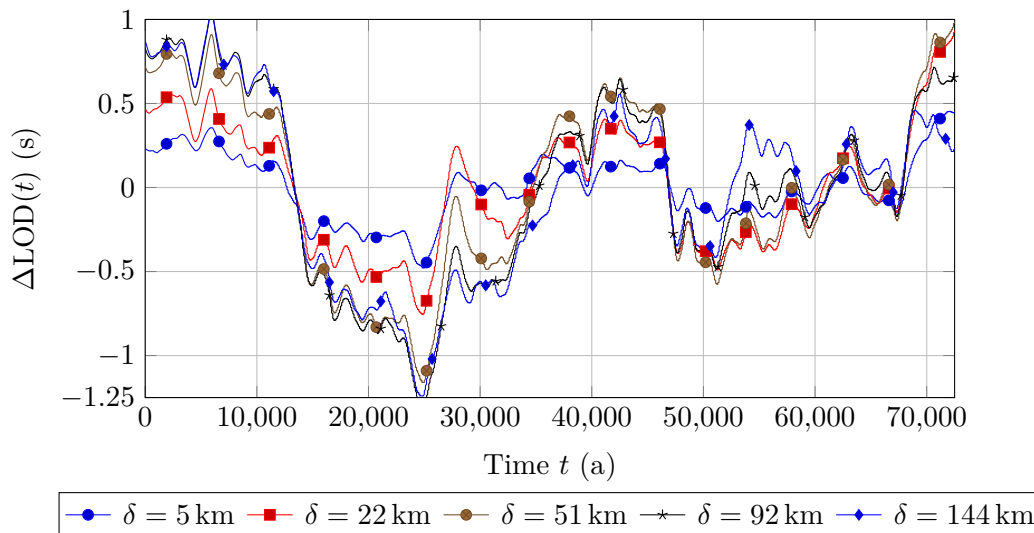


**Figure 5.15:** De-trended changes in the Length of Day predicted by the core-mantle coupling model for spherical shells of different radii. Here,  $\delta$  denotes a virtual thickness of the corresponding stratified layer, which can be related to the sampling radius by Eq. (5.5).

on almost each of the considered time windows the correlation coefficient either reflects a linear increase or decrease of the predicted LOD value. In conclusion, the histograms shown in Fig. 5.14 are biased because of the presence of a linear trend in almost all of the predicted LOD variations. Moreover, it is likely that the fluctuations of the predicted LOD variations occur on timescales which are larger than the period for which a regular sampled historical LOD record is available.

Because of the fact that the presence of linear trends do not allow to compute meaningful correlations between the prediction and the observation of the LOD value, the predicted time series of the LOD value are de-trended. Another justification for de-trending the predicted LOD values is given by the deficiencies of the core-mantle coupling with a lacking feedback, which were addressed previously. De-trending refers to the subtraction of a linear function from the original time series which is fitted to the time series by means of the method of least squares. The resulting de-trended LOD fluctuations are shown in Fig. 5.15. The deviations from the linear trend shown in Fig. 5.15 are barely visible in the original time series shown in Fig. 5.13 but are also on the level of seconds. Furthermore, the curves in Fig. 5.15 confirm that the correlation coefficients are only reflecting the linear trends in the time series but not the temporal fluctuations. The curves in Fig. 5.15 obtained for the different shell thicknesses are comparable and correlated at least on a timescale of approximately 25 000 years. Furthermore, they reveal a rich temporal dynamic on the millennial or larger timescales. In fact, in a FOURIER analysis, dominant periods ranging from 1000 to 100 000 years were identified. These periods exceed those which can be inferred from the LOD records

by several orders of magnitude. In summary, the fact that the timescales identified by de-trending the predicted LOD variations exceed those of the historical LOD record does not allow a direct comparison by means of a direct correlation.

Nevertheless, histograms of correlation coefficients similar to those shown in Fig. 5.14 were also analyzed for the de-trended LOD time series. For all shell thicknesses, the histograms are similar to that shown in the middle panel of Fig. 5.14 with either a positive correlation coefficient close to 0.6 or a negative correlation coefficient close to  $-0.6$  in the majority of the time windows. Thus, these histograms would indicate that the two time series are either correlated or anti-correlated, depending on the considered time period. However, due to the mismatch of the timescales of the predicted and the historical LOD record, even these histograms do not allow for a meaningful interpretation. Even though only the de-trended LOD variations are analyzed on the time windows with a period of 200 years, they can be approximated well by simple linear functions. This is because the periods of the time windows are smaller in comparison to those of the timescales, which are dominating the de-trended time series. In summary, a direct correlation of the two time series is not feasible due to the mismatch of the timescales.

For a direct comparison, long-term data of the LOD value over a period of at least 25 000 years is required. Some information about the secular changes of the rotation and the orientation of the Earth are available. For example, the VSOP model (Variations Séculaires des Orbites Planétaires), which is based on celestial mechanics, predicts the obliquity of the Earth over geological timescales [Bretagnon and Francou (1988)]. Furthermore, changes of the momentum of inertia of the Earth can be related to changes of the sea level, which are inferred from sediment records [Peltier (2015)]. However, the length of day can neither be predicted from celestial mechanics nor from sediment records.

Anyway, a comparison of the predicted LOD variations with the available records could be performed, if the timescale of the predicted time series is modified. Of course, there is no physical reasoning for this, because the timescale of the considered model is determined when the dimensionless results of the numerical dynamo simulations are rescaled. In doing so, the timescale is chosen as the magnetic diffusion time inferred from observations of the geomagnetic field. As discussed in Chap. 4, the parameters of the numerical dynamo model do not agree with those of the Earth but the magnetic REYNOLDS number of the numerical model is in agreement with that of the Earth. Moreover, the temporal characteristics of the numerical model directly imply those of the resulting torque, because the analytical model used for the computation of the traction on the CMB does not depend on time. It was shown that there is a (spatial) correlation between the azimuthal velocity field and the traction, which is acting on the CMB. Hence, it is likely that the temporal features of the traction and, thus, also those of the resulting torque are dominated by the azimuthal velocity field rather than the magnetic field. The REYNOLDS number obtained from the results of the numerical dynamo model is four orders of magnitude lower than that predicted for the flow in the outer

core of the Earth. Furthermore, the timescale of the turbulent fluctuations of the (azimuthal) velocity is larger than in reality, because the timescale of turbulence of a flow is inversely proportional to the square root of the REYNOLDS number [Pope (2000)]. Thus, a rescaling of the time series to a shorter timescale can be justified if it can be supposed that the timescale of the predicted LOD variations is comparable with that of the azimuthal velocity.

A rescaling of the time series was performed by adjusting the period of the time windows for which the correlation coefficients are determined. This period was successively doubled and the associated correlation coefficients were computed. The histograms show a distribution of the correlation coefficients, if the periods of the time windows increase. However, a clear tendency towards a positive correlation was not observed.

If the periods of the time windows are increased to approximately 25 000 years, the correlation coefficients are mostly positive but, nevertheless, some negative correlation coefficients are obtained for certain shell thicknesses. However, due to the limited number of windows, which are available to compute a correlation if the period of the time windows is 25 000 years, the results cannot be regarded as statistically significant. In conclusion, a simple rescaling of the de-trended LOD variations does not allow to confirm an agreement of the temporal features of the predicted variations with the historical LOD record.

## 5.5 Summary

In this chapter, a synthetic core-mantle boundary coupling model was analyzed which assumes that the CMB has a topography below which a stratified layer is present. The traction and resulting torque which is acting on the mantle was computed from the analytical model presented in Chap. 3. Combining this linear analytical model with the numerical dynamo model discussed in Chap. 4 a forward model leads to the predictions of a resulting torque whose order of magnitude is sufficiently large to account for LOD variations inferred from historical records.

The predicted viable torque possesses multiple timescales with periods ranging from one hundred to ten thousand years, which are primarily due to the turbulent nature of the flow of fluid in the outer core of the Earth. Furthermore, it was shown that the majority of the torque results from traction acting in the equatorial and midlatitude regions. It was also found that the field of the azimuthal velocity is very similar to that of the traction on the CMB and, thus, the azimuthal velocity is important for the resulting torque. Additionally, it was found that the virtual thickness of the stratified layer, which needs to be specified in order to compute the resulting torque, strongly influences the torque which is predicted by the model.

When the LOD variations predicted by the core-mantle coupling model are compared to the available historical records, the deficiencies of the simplified model become apparent. Depending on the virtual thickness of the stratified layer, the core-mantle coupling model predicts an increase or decrease of the LOD whose

rate exceeds that determined from long-term historical records by several orders of magnitude. Due to the lack of feedback between the analytical and the numerical dynamo model, the predicted LOD variations are dominated by vigorous linear trends. The considered forward model does not take into account that the traction, which is predicted by the analytical model, must also be present in the numerical model. Otherwise, there is not only a mechanical but also an energetic inconsistency between both models. The inconsistency of the two models explains the presence of the linear increase or decrease of the LOD.

The predicted LOD variations are dominated by a linear trend; this further complicates the comparison with historical records. By an analysis of histograms of correlation coefficients, it was found that only a de-trended time series of the LOD variations can serve for a comparison. However, as the fluctuations of the predicted LOD variations occur on timescales of periods of 1000 to 25 000 years, a positive correlation between the two time series can only be obtained if the timescale of the predicted LOD variation is rescaled. In general, the timescale of the predicted LOD variations does not match that of the historical records. Moreover, the unavailability of longer historical records of LOD variations disallows to identify timescales with periods larger than 100 years. Therefore, the core-mantle coupling model cannot be finally assessed by considering available historical records. In the considered model, the timescale associated with the magnetic field is comparable with that of the Earth, but the timescale of the (turbulent) convective transport is too large. However, for the computation of the traction, both timescales are of importance.

Despite the problem regarding the different timescales and the lack of a feedback between the analytical and numerical dynamo model, the core-mantle model has several other deficiencies which are shortly summarized. First, by combining the stationary analytical model with the dynamic numerical dynamo model, it is assumed that the solution in the stratified layer is stationary, even though the background fields are changing in time. Furthermore, the considered model does not take the local thickness of the boundary layer in the numerical dynamo model into account. It was shown that the virtual thickness influences the result significantly. Thus, a variable thickness of the boundary layer will, most likely, change the results substantially. For completeness, it should be mentioned that the variations of the boundary topography, the thickness of the stratified layer and the stratification are not taken into account. In a model of a real outer core of the Earth, these parameters must be variable.

Finally, the results of this chapter neither confirm nor disapprove the idea that parts of the LOD variations can be explained by a topographic core-mantle coupling in a stratified layer. The predicted torque is on the right order of magnitude, but the predicted LOD variations are too large compared to the historical records. In conclusion, the primitive setup of the coupling model has several deficiencies and does not allow a direct comparison with the available historical LOD records, which could confirm the proposed coupling mechanism.

## 6 Conclusion

In this thesis, a core-mantle coupling was proposed and analyzed that is based on the assumption that the Core-Mantle Boundary (CMB) has a topography below which a stratified layer is located. These two assumptions are a prerequisite for the core-mantle coupling model to be viable. Evidence for both prerequisites is found in the literature. In the outer core of the Earth, a stably stratified layer can form due to thermal or chemical interactions with the mantle. Moreover, deviations of the CMB from a perfectly spherical shape resulting in a topography are caused by the process of mantle convection. In the literature, other core-mantle coupling models which do not rely on the simultaneous presence of stratification and boundary topography have been proposed. These models include topographic, gravitational, viscous and magnetic coupling of which the latter two can be ruled out because of the low viscosity of the fluid in the outer core and the low electrical conductivity of the mantle.

Core-mantle coupling models are invoked to explain minute variations of the Length of Day (LOD) on decadal or larger timescales. The considered hybrid coupling model which accounts for the presence of both, a boundary topography and a stratified layer, predicts an average traction which is comparable with estimates from historical LOD records. Moreover, combining this model with the results of a numerical dynamo simulation also predicts a torque which is acting on the mantle that yields large LOD variations.

The starting point of this thesis is a discussion and derivation of the principle equations governing the flow of the electrically conducting fluid in the outer core of the Earth, which are obtained from the magnetohydrodynamic and the BOUSSINESQ approximations. These equations are the basis for the further analysis of the proposed core-mantle coupling model. This model is analyzed in a simplified manner using a CARTESIAN geometry. The assumptions made in the first order perturbation analysis of the equivalent dimensionless problem are discussed and justified. In particular, it is emphasized that the balance of mass needs to be split into two equations in order to obtain an equation governing the density perturbation. Following a description of the solution procedure, several simplified cases are analyzed and their dependence on the relevant dimensionless parameters of the problem is studied. Although some of the simplified cases predict an equivalent nominal value of the average traction, only the solution of the non-inertial magnetic case, which does not comprise any simplifications, is regular if either the velocity or the magnetic field becomes vanishingly small. In summary, the analysis of the simplified CARTESIAN model problem predicts a sufficiently large average traction

---

whose value varies by several orders of magnitude, depending on the strength of the stratification and the magnitude of the magnetic and velocity fields.

In order to obtain an estimate of the LOD variations which would result from the considered core-mantle coupling model, a numerical dynamo model is set up which solves the problem of the buoyancy-driven magnetohydrodynamic flow in the outer core of the Earth. In doing so, the numerical tools used to solve the dimensionless problem are outlined. Due to computational limitations, the orders of magnitude of the dimensionless parameters of the numerical model are far from those estimated for the outer core of the Earth. Nevertheless, an analysis of the ELSASSER and the magnetic REYNOLDS numbers obtained from the results shows that the model is, at least, Earth-like regarding the structure and the timescale of the magnetic field. This is further supported by a comparison of the magnetic EKMAN and the magnetic REYNOLDS numbers with those obtained in an extensive study which analyzes the magnetic fields of a series of numerical simulations and compares their morphology to that of the Earth.

The resulting torque and related LOD variations predicted by a synthetic model, which combines the results of the simplified analytical with those of the numerical dynamo model, are analyzed and compared with historical LOD records. The analysis shows that the spatial structure of the predicted traction on the CMB is governed by the azimuthal velocity field. Moreover, the majority of the torque is generated in the equatorial and mid-latitude regions. The predicted torque of the synthetic model highly depends on a parameter which mimics the thickness of the stratified layer, *i.e.*, the virtual thickness. The time series of the computed torque and associated LOD variations covers a period of approximately 70 000 years. Depending on the virtual thickness, the synthetic model either predicts a linear increase or decrease of the Length of Day on the order of seconds. In one case, an almost constant Length of Day is predicted. The rate of the increase or decrease and the order of magnitude of the LOD variations are large in comparison to those inferred from a historical LOD record. This is due to an inconsistency of the synthetic model, which lacks a feedback between the numerical and the analytical model, *i.e.*, the transfer of energy due to the work on the mantle is not taken into account. The predicted LOD variations are not comparable with the historical record of approximately 200 years because of the differences regarding the time periods of the two time series; also the timescales of the predicted LOD variations exceed those of the record. This prohibits the identification of similar temporal features in both time series which could confirm that the hybrid mechanism yields LOD variations on decadal or centennial timescales.

In conclusion, the proposed core-mantle coupling mechanism can neither be confirmed nor ruled out as a possible candidate for explaining LOD variations due to the outer core. The results of this thesis suggest that topographic core-mantle coupling in a stratified layer is viable and that more sophisticated approaches based on coupled models or observations of the secular variation of the geomagnetic field might confirm the proposed mechanism.

## 6.1 Contributions of the thesis

In this work, novel contributions and additions to the existing literature were made. Moreover, certain well established approaches and approximations were re-visited in a rational manner. These comprise:

- A rational discussion and derivation of the magnetohydrodynamic approximation for a rotating frame of reference with the application of the concept of successive LORENTZ boost transformations.
- A concise and rigorous derivation of the anelastic and the BOUSSINESQ approximation, which follows that given in Braginsky and Roberts [1995] but clarifies the thermodynamic argumentation and simplifications given in Anufriev, Jones, and Soward [2005].
- An in-depth analysis of the dimensionless problem of topographic core-mantle coupling inside a stratified layer in a simplified CARTESIAN geometry. The dependence of the solution on the relevant dimensionless parameters is studied over a large range of values and it is found that certain simplified models yield a solution possessing singularities. At this point, it should be mentioned that the considered core-mantle coupling mechanism was re-investigated recently in Jault [2020]. This paper confirms the results of the analysis presented in this thesis.
- The combination of the analytical model with the results of numerical dynamo simulations, which predicts a resulting torque on the mantle. The torque is of an order of magnitude comparable to estimates inferred from historical LOD records, but the predicted LOD variations exceed the historical ones. The models would yield a rapid increase (or decrease) of the rotation rate of the Earth.

## 6.2 Outlook

The results of this thesis provide the motivation for further studies using more sophisticated models. There are many opportunities for future work and further improvements.

Non-linear effects were not considered in this thesis. Therefore, it would be of interest whether a non-linear analysis of the dimensionless problem confirms the results of the linear model. Such an analysis could make use of a second order perturbation expansion or solve the non-linear problem numerically. A symbolic closed-form solution can only be found with the aid of a computer algebra system, in which numerical instabilities can arise. Therefore, it is likely that a reliable evaluation of the solution of the second order perturbation expansion is not feasible.

Thus, approaches towards a numerical solution of the problem are more promising. Rather than spectral methods commonly used in geosciences, only local methods

such as the finite element or the finite volume method can capture the presence of the boundary topography. However, two additional obstacles complicate the numerical treatment of the problem. These are the lack of a stabilizing “viscous term” in the transport equation of the density perturbation and the coupling of the magnetic field to the scalar potential at the CMB. For example, a combination of the entropy viscosity method [Guermond, Pasquetti, and Popov (2011)] with adaptive mesh refinement could resolve the former problem. Regarding the latter obstacle, possible approaches are the extension of the mesh to the mantle and an inclusion of the scalar potential inside this region, or, alternatively, the use of the so-called pseudo-vacuum boundary condition [Jackson et al. (2013)].

It is not likely that numerical dynamo models will yield both Earth-like velocity and magnetic fields in the foreseeable near future. Therefore, an alternative to the prediction of a resulting torque on the mantle from the results of a dynamo model would be very valuable. Core flow inversion models can (under certain assumptions) predict the large-scale velocity field below the CMB from the variations of the magnetic field of the Earth. Using time series of this velocity field and also of the magnetic field at the CMB, a refined synthetic model could be used to predict more realistic values of the torque. The timescales and time periods of this torque would then coincide with those inferred from the secular variation of the geomagnetic field. Thus, this approach could possibly confirm the considered model, because the time period, for which records of the secular variation of the geomagnetic field are available, correspond to those of the historical LOD record. However, the presence of the stratified layer and the boundary topography require compromises with respect to the accuracy of the core flow inversion model.

Apart from this approach of using observations in the synthetic model, the structure of the solution is not clear in a three-dimensional setup. In this thesis and also in the literature, compare, *e.g.*, Jault [2020], only local CARTESIAN problems have been considered. However, once the numerical solution of the problem has been achieved in a CARTESIAN geometry with a local method, the solution for other geometries can be obtained by low amount of additional work. A solution of the problem inside a full spherical annulus with a small-scale boundary topography is probably not feasible due to the large number of degrees of freedom which such a geometry entails. However, a reasonable approach to tackle this issue could, for example, consider a sector of a sphere. This could help to assess the properties of the solution for the case of an intermediate boundary topography and a large-scale flow.

As remarked by Jault, an analysis of the problem in the non-stationary case could answer the question whether the solutions are stable or decay over time [Jault (2020)]. Moreover, in a non-period CARTESIAN or in a three-dimensional setup, waves could arise yielding a propagation of local features of the solution in space. Furthermore, the dynamical interaction of the core-mantle coupling model or, more generally, the stratified layer with the underlying bulk of fluid in the outer core of the Earth is not clear. Considering of a fully coupled model could answer the questions whether the boundary topography affects the underlying buoyancy

driven flow by means of the proposed coupling mechanism. Such a model would not be Earth-like, but it could predict hypothetical LOD variations and also assess whether the coupled model predicts variations which are significantly different from those of a synthetic one. Furthermore, studies involving an interaction of the stratified layer with the outer core could also contribute to the refinement of core flow inversion models, which neither take the topography of the CMB nor the stratification into account.



## List of Figures

2.1	Density, pressure and shear wave velocities in the interior of the Earth. . . . .	9
2.2	Reference planes and obliquity of the Earth. . . . .	15
2.3	Precession and nutation of the Earth and related frames of reference. . . . .	16
2.4	Rotation of the Earth and related frames of reference. . . . .	16
2.5	Orientation of the Earth. . . . .	19
2.6	Variations in the Length of Day. . . . .	20
2.7	Two observers denoted by the symbols $\mathcal{O}$ and $\tilde{\mathcal{O}}$ are describing the motion of a point P. . . . .	40
2.8	LORENTZ transformations between the observers $\mathcal{O}$ , $\mathcal{O}'$ and $\tilde{\mathcal{O}}$ . . . . .	42
2.9	Qualitative temperature profile in the outer core of the Earth. . . . .	51
3.1	Sketch of a two-dimensional Core-Mantle Boundary with a sinusoidal topography. . . . .	62
3.2	Imaginary part of the wave number $k_z^{(1)}$ as function of the ROSSBY number $R\sigma$ and different colatitudes $\theta$ . . . . .	84
3.3	Dependence of the magnitude of the wave number $k_z^{(1)}$ on the background velocity. . . . .	87
3.4	Dependence of the magnitude of the wave number $k_z^{(1)}$ in Eq. (3.64) on the ALFVÉN number $Al$ . . . . .	88
3.5	Dependence of the average traction in Eq. (3.68) on the background velocity $\bar{V}$ . . . . .	92
3.6	Dependence of the magnitude of the average traction in Eq. (3.68) on the ALFVÉN number $Al$ . . . . .	93
3.7	Dependence of the magnitude of the two wave numbers $k_z^{(1)}$ and $k_z^{(2)}$ in Eq. (3.69) on the stratification parameter $St$ . . . . .	97
3.8	Dependence of the magnitude of the two wave numbers $k_z^{(1)}$ and $k_z^{(2)}$ in Eq. (3.69) on the dimensionless background velocity $\bar{V}$ . . . . .	99
3.9	Dependence of the magnitude of the two wave numbers $k_z^{(1)}$ and $k_z^{(2)}$ in Eq. (3.69) on the ALFVÉN number $Al$ . . . . .	100
3.10	Dependence of the magnitude of the average traction in the non-inertial case on the stratification parameter $St$ . . . . .	103
3.11	Dependence of the magnitude of the average traction in the non-inertial case on the dimensionless background velocity $\bar{V}$ . . . . .	104
3.12	Dependence of the magnitude of the average traction in the non-inertial case on the ALFVÉN number $Al$ . . . . .	105

3.13	Dependence of the magnitude of the three wave numbers in the inertial magnetic case on the stratification parameter $St$ . . . . .	108
3.14	Dependence of the magnitude of the three wave numbers in the inertial magnetic case on the dimensionless background velocity $\bar{V}$ . . . . .	110
3.15	Dependence of the magnitude of the three wave numbers in the inertial magnetic case on the ALFVÉN number $Al$ . . . . .	113
3.16	Dependence of the magnitude of the average traction in the inertial magnetic case on the stratification parameter $St$ . . . . .	116
3.17	Dependence of the magnitude of the components of the average traction on the stratification parameter $St$ . . . . .	117
3.18	Dependence of the magnitude of the average traction in the inertial magnetic case on the dimensionless background velocity $\bar{V}$ . . . . .	118
3.19	Dependence of the magnitude of the components of the average traction on the dimensionless background velocity $\bar{V}$ . . . . .	119
3.20	Dependence of the magnitude of the average traction in the inertial magnetic case on the ALFVÉN number $Al$ . . . . .	120
3.21	Dependence of the magnitude of the components of the average traction on the ALFVÉN number $Al$ . . . . .	121
3.22	Perturbation of the velocity field $\mathbf{v}'$ in the inertial magnetic case. . . . .	123
3.23	Perturbation of the pressure field $p'$ in the inertial magnetic case. . . . .	124
3.24	Graphical representation of a two-dimensional topography. . . . .	125
3.25	Dependence of the magnitude of the average traction in the two-dimensional inertial magnetic case on the stratification parameter $St$ . . . . .	129
3.26	Dependence of the magnitude of the average traction in the two-dimensional inertial magnetic case on the dimensionless background velocity $\bar{V}$ . . . . .	130
3.27	Dependence of the magnitude of the average traction in the two-dimensional inertial magnetic case on the ALFVÉN number $Al$ . . . . .	131
4.1	Boundary value problem of a numerical dynamo. . . . .	136
4.2	Initial temperature perturbation in the equatorial and meridional plane. . . . .	140
4.3	Illustration of the spherical harmonics $Y_l^m$ . . . . .	143
4.4	Illustration of toroidal components $t_l^m$ . . . . .	144
4.5	Illustration of poloidal components $p_l^m$ . . . . .	145
4.6	Properties of toroidal and poloidal vector fields. . . . .	147
4.7	Toroidal-poloidal decomposition of the velocity-independent terms in the magnetic induction equation. . . . .	149
4.8	Transformation of the magnetic field from the spectral to the physical space. . . . .	153
4.9	Turbulent fluctuations of the kinetic and magnetic energies and the temperature over time. . . . .	156
4.10	Snapshots of the equilibrated solution of the final model in the meridional cross section. . . . .	158

4.11	Snapshots of the equilibrated solution of the final model in the equatorial cross section. . . . .	159
4.12	Parameter regime for an Earth-like magnetic field of a numerical dynamo model. . . . .	162
5.1	Illustration of the core-mantle coupling model and the local approximation of the boundary value problem of the stratified layer. . .	168
5.2	Snapshots of the radial magnetic and the azimuthal velocity fields on a spherical shell with a radius of $r = 3336$ km. . . . .	172
5.3	Radial profiles of the radial magnetic and azimuthal velocity fields $B_r$ and $v_\varphi$ for different values of the colatitude $\theta$ . . . . .	174
5.4	Grid points of the background magnetic and velocity fields $\bar{B}$ and $\bar{V}$ used for computing the average traction with the analytical model. . . . .	177
5.5	Average traction at the grid points of the background magnetic and velocity fields $\bar{B}$ and $\bar{V}$ . . . . .	180
5.6	Snapshots of the traction $t_\varphi$ and the torque density $m_z$ on a spherical shell. . . . .	182
5.7	Azimuthal and temporal averages of the radial magnetic field, the azimuthal velocity field, the traction and the torque density. . . . .	184
5.8	Time series of the core-mantle boundary torque for three spherical shells of different radii. . . . .	186
5.9	Correlation coefficients $c$ of the core-mantle boundary torques obtained for spherical shells of different radii. . . . .	188
5.10	Long-term fluctuations of the Length of Day. . . . .	191
5.11	Reconstruction of the historical LOD record using the first eight modes of a Singular Spectrum Analysis. . . . .	192
5.12	First four principal components obtained in the Singular Spectrum Analysis of the LOD data. . . . .	193
5.13	Changes in the Length of Day predicted by the core-mantle coupling model for spherical shells of different radii. Here, $\delta$ denotes a virtual thickness of the corresponding stratified layer and can be related to the sampling radius by means of Eq. (5.5) on page 171. . . . .	196
5.14	Histograms of the correlation coefficients of the predicted and the observed LOD fluctuations for three spherical shells of different radii. . . . .	200
5.15	De-trended changes in the Length of Day predicted by the core-mantle coupling model for spherical shells of different radii. . . . .	201
A.1	Displacement of a fluid parcel in a stratified reference state. . . . .	i
E.1	Correlation matrix of the Singular Spectrum Analysis of the LOD data. . . . .	xxiii
E.2	Fifth to eighth principal component obtained in the Singular Spectrum Analysis of the LOD data. . . . .	xxv



## List of Tables

2.1	Comparison of temperatures at the inner core and the core-mantle boundary assumed in five different studies. . . . .	10
2.2	Geometric and physical properties of the outer core of the Earth. . . . .	14
2.3	Order of magnitude of the free charge density. . . . .	28
3.1	Dimensions of the parameters of the boundary topography problem. . . . .	64
3.2	Values of the EKMAN, the REYNOLDS and the ROSSBY number for different wavelengths of the boundary topography. . . . .	69
3.3	Values of the parameter $St^2 Fr^2 / Ro^2$ , which characterizes the density gradient. . . . .	71
3.4	Values of the dimensionless parameters of the boundary problem in the “standard case.” . . . .	76
3.5	Properties and nominal dimensionless average tractions of the different cases considered in Sect. 3.3. . . . .	133
4.1	Parameters of the dynamo problem and resulting reference values for the outer core of the Earth. . . . .	137
4.2	Values of the dimensionless numbers of the dynamo problem. . . . .	138
4.3	Overview of equilibration simulations performed and their parameters. . . . .	155
5.1	Long-term increase of the difference of the Length of Day from the standard value. . . . .	198



## Bibliography

- Adam, J. M.-C. and Romanowicz, B. (2015). “Global scale observations of scattered energy near the inner-core boundary: Seismic constraints on the base of the outer-core”. In: *Physics of the Earth and Planetary Interiors* 245, pp. 103–116. ISSN: 0031-9201. DOI: 10.1016/j.pepi.2015.06.005.
- Alfè, D., Gillan, M. J., and Price, G. D. (1999). “The melting curve of iron at the pressures of the Earth’s core from ab initio calculations”. In: *Nature* 401, pp. 462–464. DOI: 10.1038/46758.
- Alfè, D., Price, G. D., and Gillan, M. J. (2002). “Iron under Earth’s core conditions: Liquid-state thermodynamics and high-pressure melting curve from ab initio calculations”. In: *Physical Review B* 65 (16), p. 165118. DOI: 10.1103/PhysRevB.65.165118.
- Anufriev, A. P., Jones, C. A., and Soward, A. M. (2005). “The Boussinesq and anelastic liquid approximations for convection in the Earth’s core”. In: *Physics of the Earth and Planetary Interiors* 152.3, pp. 163–190. DOI: 10.1016/j.pepi.2005.06.004.
- Anufriyev, A. P. and Braginski, S. I. (1977). “Effect of irregularities of the boundary of the Earth’s core on the speed of the fluid flow and on the magnetic field, III”. In: *Geomagnetism and Aeronomy* 17, pp. 492–496.
- Ascher, U., Ruuth, S., and Wetton, B. (1995). “Implicit-Explicit Methods for Time-Dependent Partial Differential Equations”. In: *SIAM Journal on Numerical Analysis* 32.3, pp. 797–823. DOI: 10.1137/0732037.
- Batchelor, G. K. (1953). “The conditions for dynamical similarity of motions of a frictionless perfect-gas atmosphere”. In: *Quarterly Journal of the Royal Meteorological Society* 79.340, pp. 224–235. DOI: 10.1002/qj.49707934004.
- Bertram, A. and Glüge, R. (2015). *Solid Mechanics*. Heidelberg, New York, Dordrecht: Springer.
- Bouffard, M., Choblet, G., Labrosse, S., and Wicht, J. (2019). “Chemical Convection and Stratification in the Earth’s Outer Core”. In: *Frontiers in Earth Science* 7, p. 99. DOI: 10.3389/feart.2019.00099.
- Braginski, S. I. (1970). “Torsional Magnetohydrodynamic Vibrations in the Earth’s Core and Variations in Day Length”. In: *Geomagnetism and Aeronomy* 10, pp. 3–12.
-

- Braginsky, S. I. (1993). “MAC-Oscillations of the Hidden Ocean of the Core”. In: *Journal of Geomagnetism and Geoelectricity* 45.11–12, pp. 1517–1538. DOI: 10.5636/jgg.45.1517.
- Braginsky, S. I. (2006). “Formation of the stratified ocean of the core”. In: *Earth and Planetary Science Letters* 243.3, pp. 650–656. DOI: 10.1016/j.epsl.2006.01.029.
- Braginsky, S. I. and Roberts, P. H. (1995). “Equations governing convection in earth’s core and the geodynamo”. In: *Geophysical & Astrophysical Fluid Dynamics* 79.1-4, pp. 1–97. DOI: 10.1080/03091929508228992.
- Bretagnon, P. and Francou, G. (1988). “Planetary Theories in rectangular and spherical variables: VSOP87 solution.” In: *Astronomy and Astrophysics* 202, pp. 309–315.
- Brun, A. S., Miesch, M. S., and Toomre, J. (2004). “Global-Scale Turbulent Convection and Magnetic Dynamo Action in the Solar Envelope”. In: *The Astrophysical Journal* 614.2, pp. 1073–1098. DOI: 10.1086/423835.
- Buffett, B. (2014). “Geomagnetic fluctuations reveal stable stratification at the top of the Earth’s core”. In: *Nature* 507, pp. 484–487. DOI: 10.1038/nature13122.
- Buffett, B., Knezek, N., and Holme, R. (2016). “Evidence for MAC waves at the top of Earth’s core and implications for variations in length of day”. In: *Geophysical Journal International* 204.3, pp. 1789–1800. DOI: 10.1093/gji/ggv552.
- Buffett, B. A. (2015). “Core-Mantle Interactions”. In: *Treatise on Geophysics*. Ed. by Schubert, G. 2nd ed. Vol. 8. Oxford: Elsevier. Chap. 8, pp. 213–224. DOI: 10.1016/B978-0-444-53802-4.00148-2.
- Buffett, B. A., Garnero, E. J., and Jeanloz, R. (2000). “Sediments at the Top of Earth’s Core”. In: *Science* 290.5495, pp. 1338–1342. DOI: 10.1126/science.290.5495.1338.
- Buffett, B. A., Huppert, H. E., Lister, J. R., and Woods, A. W. (1996). “On the thermal evolution of the Earth’s core”. In: *Journal of Geophysical Research: Solid Earth* 101.B4, pp. 7989–8006. DOI: 10.1029/95JB03539.
- Buffett, B. A. and Seagle, C. T. (2010). “Stratification of the top of the core due to chemical interactions with the mantle”. In: *Journal of Geophysical Research: Solid Earth* 115.B04407. DOI: 10.1029/2009JB006751.
- Bullard, E. C., Freeman, C., Gellman, H., and J., Nixon. (1950). “The westward drift of the Earth’s magnetic field”. In: *Philosophical Transactions of the Royal Society of London A* 243.859, pp. 67–92. DOI: 10.1098/rsta.1950.0014.

- Bullard, E. C. and Gellman, H. (1954). “Homogeneous dynamos and terrestrial magnetism”. In: *Philosophical Transactions of the Royal Society of London A* 247.928, pp. 213–278. DOI: 10.1098/rsta.1954.0018.
- Bullard, E. C. and Gubbins, D. (1977). “Generation of magnetic fields by fluid motions of global scale”. In: *Geophysical & Astrophysical Fluid Dynamics* 8.1, pp. 43–56. DOI: 10.1080/03091927708240370.
- Childress, S. and Gilbert, A. D. (1995). *Stretch, Twist, Fold: The Fast Dynamo*. Lecture Notes in Physics Monographs. Berlin, Heidelberg, New York: Springer.
- Christensen, U. R. and Aubert, J. (2006). “Scaling properties of convection-driven dynamos in rotating spherical shells and application to planetary magnetic fields”. In: *Geophysical Journal International* 166.1, pp. 97–114. DOI: 10.1111/j.1365-246X.2006.03009.x.
- Christensen, U. R., Aubert, J., Cardin, P., Dormy, E., Gibbons, S., Glatzmaier, G. A., Grote, E., Honkura, Y., Jones, C., Kono, M., Matsushima, M., Sakuraba, A., Takahashi, F., Tilgner, A., Wicht, J., and Zhang, K. (2001). “A numerical dynamo benchmark”. In: *Physics of the Earth and Planetary Interiors* 128.1, pp. 25–34. DOI: 10.1016/S0031-9201(01)00275-8.
- Christensen, U. R., Aubert, J., and Hulot, G. (2010). “Conditions for Earth-like geodynamo models”. In: *Earth and Planetary Science Letters* 296.3, pp. 487–496. DOI: 10.1016/j.epsl.2010.06.009.
- Christensen, U. R. and Wicht, J. (2015). “Numerical Dynamo Simulations”. In: *Treatise on Geophysics*. Ed. by Schubert, G. 2nd ed. Vol. 8. Oxford: Elsevier. Chap. 10, pp. 245–277. DOI: 10.1016/B978-0-444-53802-4.00145-7.
- Clune, T. C., Elliott, J. R., Miesch, M. S., Toomre, J., and Glatzmaier, G. A. (1999). “Computational aspects of a code to study rotating turbulent convection in spherical shells”. In: *Parallel Computing* 25.4, pp. 361–380. DOI: 10.1016/S0167-8191(99)00009-5.
- Coleman, B. D. and Noll, W. (1963). “The thermodynamics of elastic materials with heat conduction and viscosity”. In: *Archive for Rational Mechanics and Analysis* 13.1, pp. 167–178. DOI: 10.1007/BF01262690.
- de Wijs, G. A., Kresse, G., Vočadlo, L., Dobson, D., Alfè, D., Gillan, M. J., and Price, G. D. (1998). “The viscosity of liquid iron at the physical conditions of the Earth’s core”. In: *Nature* 392, pp. 805–807. DOI: 10.1038/33905.
- Dehant, V. and Mathews, P. M. (2015). “Earth Rotation Variations”. In: *Treatise on Geophysics*. Ed. by Schubert, G. 2nd ed. Vol. 3. Oxford: Elsevier. Chap. 10, pp. 263–305. DOI: 10.1016/B978-0-444-53802-4.00066-X.
- Dreyer, W. (2015). *Lectures notes on continuum physics*.

- Duncombe, R. L., Sinclair, A. T., and Tucker, R. H. (1977). “Report of Joint Meeting of Commissions 4, 8, 31 on the new System of Astronomical Constants”. In: *Reports of Meetings of Commissions: Comptes Rendus Des Séances Des Commissions*. Ed. by Müller, E. A. Vol. 16. 4. Cambridge University Press, pp. 52–67. DOI: 10.1017/S0251107X00002406.
- Durran, D. R. (1989). “Improving the Anelastic Approximation”. In: *Journal of the Atmospheric Sciences* 46.11, pp. 1453–1461. DOI: 10.1175/1520-0469(1989)046<1453:ITAA>2.0.CO;2.
- Dziewonski, A. M. and Anderson, D. L. (1981). “Preliminary reference Earth model”. In: *Physics of the Earth and Planetary Interiors* 25.4, pp. 297–356.
- Dziewonski, A. M. and Romanowicz, B. A. (2015). “Deep Earth Seismology: An Introduction and Overview”. In: *Treatise on Geophysics*. Ed. by Schubert, G. 2nd ed. Vol. 1. Oxford: Elsevier. Chap. 1, pp. 1–28. DOI: 10.1016/B978-0-444-53802-4.00001-4.
- Ekman, V. W. (1905). “On the influence of the earth’s rotation on ocean-currents.” In: *Arkiv för Matematik, Astronomi och Fysik* 2.11, pp. 1–52.
- Elsasser, W. M. (1946a). “Induction Effects in Terrestrial Magnetism Part I. Theory”. In: *Physical Review* 69 (3–4), pp. 106–116. DOI: 10.1103/PhysRev.69.106.
- Elsasser, W. M. (1946b). “Induction Effects in Terrestrial Magnetism Part II. The Secular Variation”. In: *Physical Review* 70 (3-4), pp. 202–212. DOI: 10.1103/PhysRev.70.202.
- Elsasser, W. M. (1947). “Induction effects in terrestrial magnetism. Part III. Electric modes”. In: *Physical Review* 72 (9), pp. 821–833. DOI: 10.1103/PhysRev.72.821.
- Featherstone, N. (2018). *geodynamics/Rayleigh: Bug-Fix-Release: 0.9.1*. Version v0.9.1. Zenodo. DOI: 10.5281/zenodo.1236565.
- Featherstone, N. A. and Hindman, B. W. (2016). “The Spectral Amplitude of Stellar Convection and its Scaling in the High-Rayleigh-Number Regime”. In: *The Astrophysical Journal* 818.1, pp. 18–32. DOI: 10.3847/0004-637x/818/1/32.
- Finlay, C. C., Olsen, N., Kotsiaros, S., Gillet, N., and Tøffner-Clausen, L. (2016). “Recent geomagnetic secular variation from Swarm and ground observatories as estimated in the CHAOS-6 geomagnetic field model”. In: *Earth Planets and Space* 68 (1), pp. 122–140. DOI: 10.1186/s40623-016-0486-1.
- Flügge, W. (1972). *Tensor Analysis and Continuum Mechanics*. Springer.
- Fumagalli, P. and Klemme, S. (2015). “Mineralogy of the Earth: Phase Transitions and Mineralogy of the Upper Mantle”. In: *Treatise on Geophysics*. Ed. by

- Schubert, G. 2nd ed. Vol. 2. Oxford: Elsevier. Chap. 2, pp. 7–31. DOI: 10.1016/B978-0-444-53802-4.00052-x.
- Garcia, R. and Souriau, A. (2000). “Amplitude of the core-mantle boundary topography estimated by stochastic analysis of core phases”. In: *Physics of the Earth and Planetary Interiors* 117.1, pp. 345–359. DOI: 10.1016/S0031-9201(99)00106-5.
- Ghil, M., Allen, M. R., Dettinger, M. D., Ide, K., Kondrashov, D., Mann, M. E., Robertson, A. W., Saunders, A., Tian, Y., Varadi, F., and Yiou, P. (2002). “Advanced spectral methods for climatic time series”. In: *Reviews of Geophysics* 40.1, pp. 1–41. DOI: 10.1029/2000RG000092.
- Gill, A. E. (1982). *Atmosphere-Ocean Dynamics*. 1st ed. Vol. 30. International Geophysics Series. San Diego: Academic Press.
- Gillet, N., Jault, D., Canet, E., and Fournier, A. (2010). “Fast torsional waves and strong magnetic field within the Earth’s core”. In: *Nature* 465, pp. 74–77.
- Glane, S. and Buffett, B. (2018). “Enhanced Core-Mantle Coupling Due to Stratification at the Top of the Core”. In: *Frontiers in Earth Science* 6, p. 171. DOI: 10.3389/feart.2018.00171.
- Glane, S., Reich, F. A., and Müller, W. H. (2018). “The kinematic dynamo problem, part I: analytical treatment with the Bullard–Gellman formalism”. In: *Continuum Mechanics and Thermodynamics* 30.4, pp. 731–774. DOI: 10.1007/s00161-018-0638-6.
- Glatzmaier, G. A. (1984). “Numerical simulations of stellar convective dynamos. I. the model and method”. In: *Journal of Computational Physics* 55.3, pp. 461–484. DOI: 10.1016/0021-9991(84)90033-0.
- Glüge, R. (2018). “Principles of Material Modeling”. In: *Encyclopedia of Continuum Mechanics*. Ed. by Altenbach, H. and Öchsner, A. Berlin, Heidelberg: Springer, pp. 1–8. DOI: 10.1007/978-3-662-53605-6\_262-1.
- Golyandina, N., Nekrutkin, V., and Zhigljavsky, A. (2001). *Analysis of Time Series Structure: SSA and Related Techniques*. Vol. 90. Monographs on Statistics and Applied Probability. Boca Raton, London, New York: Chapman and Hall.
- Gough, D. O. (1969). “The Anelastic Approximation for Thermal Convection”. In: *Journal of the Atmospheric Sciences* 26.3, pp. 448–456. DOI: 10.1175/1520-0469(1969)026<0448:TAAFTC>2.0.CO;2.
- Greff-Lefftz, M. and Legros, H. (1996). “Viscoelastic Mantle Density Heterogeneity and Core-Mantle Topograph”. In: *Geophysical Journal International* 125.2, pp. 567–576. DOI: 10.1111/j.1365-246X.1996.tb00019.x.

- Gross, R. S. (2015). “Earth Rotation Variations—Long Period”. In: *Treatise on Geophysics*. Ed. by Schubert, G. 2nd ed. Vol. 3. Oxford: Elsevier. Chap. 9, pp. 215–261. DOI: 10.1016/B978-0-444-53802-4.00059-2.
- Gubbins, D., Alfè, D., Masters, G., Price, D. G., and Gillan, M. J. (2003). “Can the Earth’s dynamo run on heat alone?” In: *Geophysical Journal International* 155.2, pp. 609–622. DOI: 10.1046/j.1365-246X.2003.02064.x.
- Gubbins, D. and Davies, C. J. (2013). “The stratified layer at the core–mantle boundary caused by barodiffusion of oxygen, sulphur and silicon”. In: *Physics of the Earth and Planetary Interiors* 215, pp. 21–28. DOI: 10.1016/j.pepi.2012.11.001.
- Gubbins, D., Masters, G., and Nimmo, F. (2008). “A thermochemical boundary layer at the base of Earth’s outer core and independent estimate of core heat flux”. In: *Geophysical Journal International* 174.3, pp. 1007–1018. DOI: 10.1111/j.1365-246X.2008.03879.x.
- Gubbins, D., Masters, T. G., and Jacobs, J. A. (1979). “Thermal evolution of the Earth’s core”. In: *Geophysical Journal International* 59.1, pp. 57–99. DOI: 10.1111/j.1365-246X.1979.tb02553.x.
- Guermond, J.-L., Pasquetti, R., and Popov, B. (2011). “Entropy viscosity method for nonlinear conservation laws”. In: *Journal of Computational Physics* 230.11, pp. 4248–4267. DOI: 10.1016/j.jcp.2010.11.043.
- Gutenberg, B. (1913). “Über die Konstitution des Erdinnern, erschlossen aus Erdbebenbeobachtungen”. In: *Physikalische Zeitschrift* 14, pp. 1217–1218.
- Hartmann, J. (1937). “Hg-Dynamics I. Theory of the laminar flow of an electrically conductive liquid in a homogeneous medium”. In: *Mathematisk-fysiske Meddelelser* 15.6, pp. 1–26.
- Hide, R. (1969a). “Dynamics of the Atmospheres of the Major Planets with an Appendix on the Viscous Boundary Layer at the Rigid Bounding Surface of an Electrically-Conducting Rotating Fluid in the Presence of a Magnetic Field”. In: *Journal of the Atmospheric Sciences* 26.5, pp. 841–853. DOI: 10.1175/1520-0469(1969)026<0841:DOTAOT>2.0.CO;2.
- Hide, R. (1969b). “Interaction between the Earth’s Liquid Core and Solid Mantle”. In: *Nature* 222, pp. 1055–1056. DOI: 10.1038/2221055a0.
- Hide, R. and Dikes, J. O. (1991). “Earth’s Variable Rotation”. In: *Science* 253.5020, pp. 629–637. DOI: 10.1126/science.253.5020.629.
- Holme, R. (1998). “Electromagnetic core–mantle coupling—I. Explaining decadal changes in the length of day”. In: *Geophysical Journal International* 132.1, pp. 167–180. DOI: 10.1046/j.1365-246x.1998.00424.x.

- Holme, R. (2015). “Large-Scale Flow in the Core”. In: *Treatise on Geophysics*. Ed. by Schubert, G. 2nd ed. Vol. 8. Oxford: Elsevier. Chap. 4, pp. 91–113. DOI: 10.1016/B978-0-444-53802-4.00138-X.
- Holme, R. and de Viron, O. (2005). “Geomagnetic jerks and a high-resolution length-of-day profile for core studies”. In: *Geophysical Journal International* 160.2, pp. 435–439. DOI: 10.1111/j.1365-246X.2004.02510.x.
- Holme, R. and de Viron, O. (2013). “Characterization and implications of intradecadal variations in length of day”. In: *Nature* 499, pp. 202–204. DOI: 10.1038/nature12282.
- Hütter, G. (2017). “Coleman–Noll Procedure for Classical and Generalized Continuum Theories”. In: *Encyclopedia of Continuum Mechanics*. Ed. by Altenbach, H. and Öchsner, A. Berlin, Heidelberg: Springer, pp. 1–8. DOI: 10.1007/978-3-662-53605-6\_57-1.
- Hutter, K. and Jöhnk, K. D. (2004). *Continuum Methods of Physical Modeling*. Berlin, Heidelberg: Springer.
- Hutter, K., van de Ven, A. A. F., and Ursescu, A. (2006). *Electromagnetic Field Matter Interactions in Thermoelastic Solids and Viscous Fluids*. Springer.
- IERS Rapid Service Prediction Centre (2019). *Standard Rapid EOP Data since 02 January 1973 (IAU1980)*. Online; accessed September 26, 2019. International Earth Rotation and Reference Systems Service (IERS). URL: <https://www.iers.org/IERS/EN/DataProducts/EarthOrientationData/eop.html>.
- Jackson, A., Bloxham, J., and Gubbins, D. (1993). “Time-Dependent Flow at the Core Surface and Conservation of Angular Momentum in The Coupled Core-Mantle System”. In: *Dynamics of Earth’s Deep Interior and Earth Rotation*. Ed. by Le Mouél, J.-L., Smylie, D., and Herring, T. Vol. 72. Geophysical Monograph Series. Chap. 11, pp. 97–107. DOI: 10.1029/GM072p0097.
- Jackson, A., Sheyko, A., Marti, P., Tilgner, A., Cébron, D., Vantieghem, S., Simitev, R., Busse, F., Zhan, X., Schubert, G., Takehiro, S., Sasaki, Y., Hayashi, Y.-Y., Ribeiro, A., Nore, C., and Guermond, J.-L. (Nov. 2013). “A spherical shell numerical dynamo benchmark with pseudo-vacuum magnetic boundary conditions”. In: *Geophysical Journal International* 196.2, pp. 712–723. DOI: 10.1093/gji/ggt425.
- Jackson, J. D. (1975). *Classical electrodynamics*. 2nd ed. New York, London, Sydney: Wiley.
- Jault, D. (2008). “Axial invariance of rapidly varying diffusionless motions in the Earth’s core interior”. In: *Physics of the Earth and Planetary Interiors* 166.1, pp. 67–76. DOI: 10.1016/j.pepi.2007.11.001.
- Jault, D. (2020). “Tangential stress at the core–mantle interface”. In: *Geophysical Journal International* 221.2, pp. 951–967. DOI: 10.1093/gji/ggaa048.

- Jault, D. and Finlay, C. C. (2015). “Waves in the Core and Mechanical Core–Mantle Interactions”. In: *Treatise on Geophysics*. Ed. by Schubert, G. 2nd ed. Vol. 8. Oxford: Elsevier. Chap. 9, pp. 225–244. DOI: 10.1016/B978-0-444-53802-4.00150-0.
- Jault, D., Gire, C., and Le Mouél, J. L. (1988). “Westward drift, core motions and exchanges of angular momentum between core and mantle”. In: *Nature* 333, pp. 353–356. DOI: 10.1038/333353a0.
- Jault, D. and Le Mouél, J. L. (1989). “The topographic torque associated with a tangentially geostrophic motion at the core surface and inferences on the flow inside the core”. In: *Geophysical & Astrophysical Fluid Dynamics* 48.4, pp. 273–295. DOI: 10.1080/03091928908218533.
- Jones, C. A. (2007). “Thermal and Compositional Convection in the Outer Core”. In: *Treatise on Geophysics*. Ed. by Schubert, G. 1st ed. Vol. 8. Oxford: Elsevier. Chap. 5, pp. 131–185. DOI: 10.1016/B978-044452748-6.00137-1.
- Jones, C. A., Boronski, P., Brun, A. S., Glatzmaier, G. A., Gastine, T., Miesch, M. S., and Wicht, J. (2011). “Anelastic convection-driven dynamo benchmarks”. In: *Icarus* 216.1, pp. 120–135. DOI: 10.1016/j.icarus.2011.08.014.
- Jordi, C., Morrison, L. V., Rosen, R. D., Salstein, D. A., and Rosselló, G. (1994). “Fluctuations in the Earth’s rotation since 1830 from high-resolution astronomical data”. In: *Geophysical Journal International* 117.3, pp. 811–818. DOI: 10.1111/j.1365-246X.1994.tb02471.x.
- Kanda, R. V. S. and Stevenson, D. J. (2006). “Suction mechanism for iron entrainment into the lower mantle”. In: *Geophysical Research Letters* 33.2, p. L02310. DOI: 10.1029/2005GL025009.
- Klauber, R. D. (1998). “New Perspectives on the Relativistically Rotating Disk and Non-Time-Orthogonal Reference Frames”. In: *Foundations of Physics Letters* 11.5, pp. 405–443. DOI: 10.1023/A:1022548914291.
- Klauber, R. D. (1999). “Comments regarding recent articles on relativistically rotating frames”. In: *American Journal of Physics* 67.2, pp. 158–159. DOI: 10.1119/1.19213.
- Kölbl-Ebert, M. (2001). “Inge Lehmann’s paper: ‘P’”. In: *Episodes* 24 (4), pp. 262–267. DOI: 10.18814/epiiugs/2001/v24i4/007.
- Korobeynikov, A. (2010). “Computation- and space-efficient implementation of SSA”. In: *Statistics and Its Interface* 3.3, pp. 357–368. DOI: 10.4310/SII.2010.v3.n3.a9.
- Kovetz, A. (2000). *Electromagnetic theory*. Oxford University Press.
- Labrosse, S. (2003). “Thermal and magnetic evolution of the Earth’s core”. In: *Physics of the Earth and Planetary Interiors* 140.1. Geophysical and Geo-

- chemical Evolution of the Deep Earth, pp. 127–143. DOI: 10.1016/j.pepi.2003.07.006.
- Lay, T. (2015). “Deep Earth Structure: Lower Mantle and  $D''$ ”. In: *Treatise on Geophysics*. Ed. by Schubert, G. 2nd ed. Vol. 1. Oxford: Elsevier. Chap. 22, pp. 683–723. DOI: 10.1016/B978-0-444-53802-4.00019-1.
- Lay, T., Williams, Q., and Garnero, E. J. (1998). “The core-mantle boundary layer and deep Earth dynamics”. In: *Nature* 392, pp. 461–468. DOI: 10.1038/33083.
- Lister, J. R. and Buffett, B. A. (1998). “Stratification of the outer core at the core–mantle boundary”. In: *Physics of the Earth and Planetary Interiors* 105.1, pp. 5–19. DOI: 10.1016/S0031-9201(97)00082-4.
- Liu, I.-S. (2002). *Continuum Mechanics*. Advanced Texts in Physics. Springer.
- Mao, H., Shen, G., Hemley, R. J., and Duffy, T. S. (1998). “X Ray Diffraction with a Double Hot-Plate Laser-Heated Diamond Cell”. In: *Properties of Earth and Planetary Materials at High Pressure and Temperature*. Ed. by Manghnani, M. H. and Yagi, T. Vol. 101. Geophysical Monograph Series. American Geophysical Union (AGU). Chap. 4, pp. 27–34. DOI: 10.1029/GM101p0027.
- Mao, H.-K. and Mao, W. L. (2015). “Theory and Practice: Diamond-Anvil Cells and Probes for High- $P$ - $T$  Mineral Physics Studies”. In: *Treatise on Geophysics*. Ed. by Schubert, G. 2nd ed. Vol. 2. Oxford: Elsevier. Chap. 11, pp. 263–291. DOI: 10.1016/B978-0-444-53802-4.00036-1.
- Mathews, P. M., Buffett, B. A., Herring, T. A., and Shapiro, I. I. (1991). “Forced nutations of the Earth: Influence of inner core dynamics: 2. Numerical results and comparisons”. In: *Journal of Geophysical Research: Solid Earth* 96.B5, pp. 8243–8257. DOI: 10.1029/90JB01956.
- Matsui, H., Heien, E., Aubert, J., Aurnou, J. M., Avery, M., Brown, B., Buffett, B. A., Busse, F., Christensen, U. R., Davies, C. J., Featherstone, N., Gastine, T., Glatzmaier, G. A., Gubbins, D., Guermond, J.-L., Hayashi, Y.-Y., Hollerbach, R., Hwang, L. J., Jackson, A., Jones, C. A., Jiang, W., Kellogg, L. H., Kuang, W., Landeau, M., Marti, P., Olson, P., Ribeiro, A., Sasaki, Y., Schaeffer, N., Simatev, R. D., Sheyko, A., Silva, L., Stanley, S., Takahashi, F., Takehiro, S., Wicht, J., and Willis, A. P. (2016). “Performance benchmarks for a next generation numerical dynamo model”. In: *Geochemistry, Geophysics, Geosystems* 17.5, pp. 1586–1607. DOI: 10.1002/2015GC006159.
- McCarthy, D. D. and Babcock, A. K. (1986). “The length of day since 1656”. In: *Physics of the Earth and Planetary Interiors* 44.3, pp. 281–292. DOI: 10.1016/0031-9201(86)90077-4.
- Miller, K. J., Montési, L. G. J., and Zhu, W. (2015). “Estimates of olivine-basaltic melt electrical conductivity using a digital rock physics approach”. In: *Earth*

- and Planetary Science Letters* 432, pp. 332–341. DOI: 10.1016/j.epsl.2015.10.004.
- Moffatt, H. K. (1977). “Topographic coupling at the core-mantle interface”. In: *Geophysical & Astrophysical Fluid Dynamics* 9.1, pp. 279–288. DOI: 10.1080/03091927708242332.
- Mound, J., Davies, C., Rost, S., and Aurnou, J. (2019). “Regional stratification at the top of Earth’s core due to core–mantle boundary heat flux variations”. In: *Nature Geoscience* 12 (7), pp. 575–580. DOI: 10.1038/s41561-019-0381-z.
- Mound, J. E. and Buffett, B. A. (2005). “Mechanisms of core-mantle angular momentum exchange and the observed spectral properties of torsional oscillations”. In: *Journal of Geophysical Research* 110.B8, B08103. DOI: 10.1029/2004JB003555.
- Müller, I. (1985). *Thermodynamics. Interaction of Mechanics and Mathematics* Series. Pitman.
- Müller, W. H. (2014). *An expedition to continuum theory. Solid mechanics and its applications* series. Berlin: Springer.
- Müller, W. H. and Weiss, W. (2016). *The State of Deformation in Earthlike Self-Gravitating Objects*. Ed. by Altenbach, H. and Öchsner, A. SpringerBriefs in Continuum Mechanics. Springer.
- Munk, W. H. and MacDonald, G. J. F. (1975). *The Rotation of the Earth*. Ed. by Batchelor, G. K. and Miles, J. W. Cambridge Monographs on Mechanics and Applied Mathematics. Cambridge, London, New York: Cambridge University Press.
- Nakagawa, T. (2015). “An implication for the origin of stratification below the core–mantle boundary region in numerical dynamo simulations in a rotating spherical shell”. In: *Physics of the Earth and Planetary Interiors* 247, pp. 94–104. DOI: 10.1016/j.pepi.2015.02.007.
- National Geospatial-Intelligence Agency (2014). *World Geodetic System 1984*. Fort Belvoir, Virginia.
- Nelson, R. A. (1987). “Generalized Lorentz transformation for an accelerated, rotating frame of reference”. In: *Journal of Mathematical Physics* 28.10, pp. 2379–2383. DOI: 10.1063/1.527774.
- Nimmo, F. (2015). “Energetics of the Core”. In: *Treatise on Geophysics*. Ed. by Schubert, G. 2nd ed. Vol. 8. Oxford: Elsevier. Chap. 2, pp. 27–55. DOI: 10.1016/B978-0-444-53802-4.00139-1.
- Ogura, Y. and Phillips, N. A. (1962). “Scale Analysis of Deep and Shallow Convection in the Atmosphere”. In: *Journal of the Atmospheric Sciences* 19.2,

- pp. 173–179. DOI: 10.1175/1520-0469(1962)019<0173:SAODAS>2.0.CO;2.
- Ohta, K., Hirose, K., Ichiki, M., Shimizu, K., Sata, N., and Ohishi, Y. (2010). “Electrical conductivities of pyrolitic mantle and MORB materials up to the lowermost mantle conditions”. In: *Earth and Planetary Science Letters* 289.3, pp. 497–502. DOI: 10.1016/j.epsl.2009.11.042.
- Olson, P. (2015). “Core Dynamics: An Introduction and Overview”. In: *Treatise on Geophysics*. Ed. by Schubert, G. 2nd ed. Vol. 8. Oxford: Elsevier. Chap. 1, pp. 1–25. DOI: 10.1016/B978-0-444-53802-4.00137-8.
- Olson, P., Landeau, M., and Reynolds, E. (2017). “Dynamo tests for stratification below the core-mantle boundary”. In: *Physics of the Earth and Planetary Interiors* 271, pp. 1–18. ISSN: 0031-9201. DOI: 10.1016/j.pepi.2017.07.003.
- Olson, P., Landeau, M., and Reynolds, E. (2018). “Outer Core Stratification From the High Latitude Structure of the Geomagnetic Field”. In: *Frontiers in Earth Science* 6, p. 140. DOI: 10.3389/feart.2018.00140.
- O’Rourke, J. G. and Stevenson, D. J. (2016). “Powering Earth’s dynamo with magnesium precipitation from the core”. In: *Nature* 529, pp. 387–389. DOI: 10.1038/nature16495.
- Otsuka, K. and Karato, S. (2012). “Deep penetration of molten iron into the mantle caused by a morphological instability”. In: *Nature* 492, pp. 243–246. DOI: 10.1038/nature11663.
- Pais, A. and Hulot, G. (2000). “Length of day decade variations, torsional oscillations and inner core superrotation: evidence from recovered core surface zonal flows”. In: *Physics of the Earth and Planetary Interiors* 118.3, pp. 291–316. DOI: 10.1016/S0031-9201(99)00161-2.
- Pedlosky, J. (1987). *Geophysical Fluid Dynamics*. 2nd ed. New York: Springer.
- Pedregosa, F., Varoquaux, G., Gramfort, A., Michel, V., Thirion, B., Grisel, O., Blondel, M., Prettenhofer, P., Weiss, R., Dubourg, V., Vanderplas, J., Passos, A., Cournapeau, D., Brucher, M., Perrot, M., and Duchesnay, E. (2011). “Scikit-learn: Machine Learning in Python”. In: *Journal of Machine Learning Research* 12, pp. 2825–2830.
- Pellegrini, G. N. and Swift, A. R. (1995). “Maxwell’s equations in a rotating medium: Is there a problem?” In: *American Journal of Physics* 63.8, pp. 694–705. DOI: 10.1119/1.17839.
- Peltier, W. H. (2015). “The History of the Earth’s Rotation: Impacts of Deep Earth Physics and Surface Climate Variability”. In: *Treatise on Geophysics*. Ed. by Schubert, G. 2nd ed. Vol. 9. Oxford: Elsevier. Chap. 9, pp. 221–279. DOI: 10.1016/B978-0-444-53802-4.00161-5.

- Petit, G. and Luzum, B. (2010). *IERS Conventions*. IERS Technical Note No. 36. Frankfurt.
- Pope, S. B. (2000). *Turbulent Flows*. Cambridge, London, New York: Cambridge University Press.
- Pozzo, M., Davies, C. A., Gubbins, D., and Alfè, D. (2012). “Thermal and electrical conductivity of iron at Earth’s core conditions”. In: *Nature* 485, pp. 355–359. DOI: 10.1038/nature11031.
- Price, G. D. and Stixrude, L. (2015). “Mineral Physics: An Introduction and Overview”. In: *Treatise on Geophysics*. Ed. by Schubert, G. 2nd ed. Vol. 2. Oxford: Elsevier. Chap. 1, pp. 1–5. DOI: 10.1016/B978-0-444-53802-4.00029-4.
- Rebeur-Paschwitz, E. von (1889). “The Earthquake of Tokio, April 18, 1889”. In: *Nature* 40, pp. 294–295. DOI: 10.1038/041032a0.
- Reich, F. A. (2017). “Coupling of continuum mechanics and electrodynamics”. PhD thesis. Technische Universität Berlin. DOI: 10.14279/depositonce-6518.
- Reich, F. A. and Müller, W. H. (2018). “Examination of electromagnetic powers with the example of a Faraday disc dynamo”. In: *Continuum Mechanics and Thermodynamics* 30.4, pp. 861–877. ISSN: 1432-0959. DOI: 10.1007/s00161-018-0646-6.
- Reich, F. A., Rickert, W., and Müller, W. H. (2017). “An investigation into electromagnetic force models: differences in global and local effects demonstrated by selected problems”. In: *Continuum Mechanics and Thermodynamics* 30.2, pp. 233–266. DOI: 10.1007/s00161-017-0596-4.
- Rickert, W., Glane, S., and Müller, W. H. (2020). “A Short Review of Rotations in Rigid Body Mechanics”. In: *Nonlinear Wave Dynamics of Materials and Structures*. Ed. by Altenbach, H., Eremeyev, V. A., Pavlov, I. S., and Porubov, A. V. Vol. 122. Advanced Structured Materials. Berlin, Heidelberg: Springer. Chap. 20, pp. 353–367. DOI: 10.1007/978-3-030-38708-2\_20.
- Roberts, P. H. (2015). “Theory of the Geodynamo”. In: *Treatise on Geophysics*. Ed. by Schubert, G. 2nd ed. Vol. 8. Oxford: Elsevier. Chap. 3, pp. 57–90. DOI: 10.1016/B978-0-444-53802-4.00144-5.
- Roberts, P. H. and Aurnou, J. M. (2012). “On the theory of core-mantle coupling”. In: *Geophysical & Astrophysical Fluid Dynamics* 106.2, pp. 157–230. DOI: 10.1080/03091929.2011.589028.
- Roberts, P. H., Jones, C. A., and Calderwood, A. (2003). “Energy fluxes and ohmic dissipation in the Earth’s core”. In: *Earth’s core and lower mantle*. Ed. by Jones, C. A., Soward, A. M., and Zhang, K. London: Taylor & Francis, pp. 100–129.

- Rochester, M. G. (1962). “Geomagnetic core-mantle coupling”. In: *Journal of Geophysical Research* 67.12, pp. 4833–4836. DOI: 10.1029/JZ067i012p04833.
- Romanowicz, B. (2003). “Global Mantle Tomography: Progress Status in the Past 10 Years”. In: *Annual Review of Earth and Planetary Sciences* 31.1, pp. 303–328. DOI: 10.1146/annurev.earth.31.091602.113555.
- Scheck, F. (2010). *Theoretische Physik 3*. 3rd ed. Berlin, Heidelberg, London: Springer.
- Seidelmann, P. K. (1982). “1980 IAU Theory of Nutation: The final report of the IAU Working Group on Nutation”. In: *Celestial mechanics* 27.1, pp. 79–106. DOI: 10.1007/BF01228952.
- Shankland, T. J., Peyronneau, J., and Poirier, J.-P. (1993). “Electrical conductivity of the Earth’s lower mantle”. In: *Nature* 366, pp. 453–455. DOI: 10.1038/366453a0.
- Silvestrelli, P. L., Alavi, A., and Parrinello, M. (1997). “Electrical-conductivity calculation in ab initio simulations of metals: Application to liquid sodium”. In: *Physical Review B* 55 (23), pp. 15515–15522. DOI: 10.1103/PhysRevB.55.15515.
- Simpson, J. and Weiner, E., eds. (1989). *The Oxford English dictionary*. 2nd ed. Oxford: Oxford University Press.
- Soldati, G., Boschi, L., and Forte, A. M. (2012). “Tomography of core–mantle boundary and lowermost mantle coupled by geodynamics”. In: *Geophysical Journal International* 189.2, pp. 730–746. DOI: 10.1111/j.1365-246X.2012.05413.x.
- Soldati, G., Koelemeijer, P., Boschi, L., and Deuss, A. (2013). “Constraints on core–mantle boundary topography from normal mode splitting”. In: *Geochemistry, Geophysics, Geosystems* 14.5, pp. 1333–1342. DOI: 10.1002/ggge.20115.
- Song, X. and Richards, P. G. (1996). “Seismological evidence for differential rotation of the Earth’s inner core”. In: *Nature* 382, pp. 221–224. DOI: 10.1038/382221a0.
- Souriau, A. and Poupinet, G. (1991). “The velocity profile at the base of the liquid core from PKP(BC+Cdiff) data: An argument in favour of radial inhomogeneity”. In: *Geophysical Research Letters* 18.11, pp. 2023–2026. DOI: 10.1029/91GL02417.
- Spiegel, E. A. and Veronis, G. (1960). “On the Boussinesq Approximation for a Compressible Fluid”. In: *Astrophysical Journal* 131, pp. 442–447.
- Spiegel, E. A. and Weiss, N. O. (1982). “Magnetic buoyancy and the Boussinesq approximation”. In: *Geophysical & Astrophysical Fluid Dynamics* 22.3–4, pp. 219–234. DOI: 10.1080/03091928208209028.

- Stephenson, F. R. (2003). “Historical eclipses and Earth’s rotation”. In: *Astronomy & Geophysics* 44.2, pp. 2.22–2.27. DOI: 10.1046/j.1468-4004.2003.44222.x.
- Stephenson, F. R., Morrison, L. V., and Hohenkerk, C. Y. (2016). “Measurement of the Earth’s rotation: 720 BC to AD 2015”. In: *Proceedings of the Royal Society A* 472.2196, p. 20160404. DOI: 10.1098/rspa.2016.0404.
- Stephenson, F. R., Morrison, L. V., and Smith, F. T. (1995). “Long-term fluctuations in the Earth’s rotation: 700 BC to AD 1990”. In: *Philosophical Transactions of the Royal Society of London. Series A: Physical and Engineering Sciences* 351.1695, pp. 165–202. DOI: 10.1098/rsta.1995.0028.
- Stevenson, D. J. (1987). “Limits on lateral density and velocity variations in the Earth’s outer core”. In: *Geophysical Journal International* 88.1, pp. 311–319. DOI: 10.1111/j.1365-246X.1987.tb01383.x.
- Trabant, C., Hutko, A. R., Bahavar, M., Karstens, R., Ahern, T., and Aster, R. (2012). “Data Products at the IRIS DMC: Stepping Stones for Research and Other Applications”. In: *Seismological Research Letters* 83.5, pp. 846–854. DOI: 10.1785/0220120032.
- Truesdell, C. A. and Toupin, R. (1960). “The classical field theories”. In: *Handbuch der Physik, Vol. III/1*. With an appendix on tensor fields by J.L. Ericksen. Springer, 226–793; appendix, pp. 794–858.
- van Rossum, G. and Drake, F. L. (2009). *Python 3 Reference Manual*. Scotts Valley, CA: CreateSpace.
- Vautard, R., Yiou, P., and Ghil, M. (1992). “Singular-spectrum analysis: A toolkit for short, noisy chaotic signals”. In: *Physica D: Nonlinear Phenomena* 58.1, pp. 95–126. DOI: 10.1016/0167-2789(92)90103-T.
- Virtanen, P., Gommers, R., Oliphant, T. E., Haberland, M., Reddy, T., Cournapeau, D., Burovski, E., Peterson, P., Weckesser, W., Bright, J., van der Walt, S. J., Brett, M., Wilson, J., Jarrod Millman, K., Mayorov, N., Nelson, A. R. J., Jones, E., Kern, R., Larson, E., Carey, C. J., Polat, İ., Feng, Y., Moore, E. W., VanderPlas, J., Laxalde, D., Perktold, J., Cimrman, R., Henriksen, I., Quintero, E. A., Harris, C. R., Archibald, A. M., Ribeiro, A. H., Pedregosa, F., van Mulbregt, P., and Contributors, SciPy 1.0 (2020). “SciPy 1.0: Fundamental Algorithms for Scientific Computing in Python”. In: *Nature Methods* 17, pp. 261–272. DOI: 10.1038/s41592-019-0686-2.
- Volland, H. (1996). “Atmosphere and Earth’s rotation”. In: *Surveys in Geophysics* 17.1, pp. 101–144. DOI: 10.1007/BF01904476.
- Vočadlo, L. (2015). “Earth’s Core: Iron and Iron Alloys”. In: *Treatise on Geophysics*. Ed. by Schubert, G. 2nd ed. Vol. 2. Oxford: Elsevier. Chap. 6, pp. 117–147. DOI: 10.1016/B978-0-444-53802-4.00137-8.

- Vočadlo, L., Alfè, D., Gillan, M. J., and Price, D. G. (2003). “The properties of iron under core conditions from first principles calculations”. In: *Physics of the Earth and Planetary Interiors* 140.1, pp. 101–125. DOI: 10.1016/j.pepi.2003.08.001.
- Wang, Dong and Ruuth, Steven J. (2008). “Variable step-size implicit-explicit linear multistep methods for time-dependent partial differential equations”. In: *Journal of Computational Mathematics* 26.6, pp. 838–855.
- Weber, T. A. (1997). “Measurements on a rotating frame in relativity, and the Wilson and Wilson experiment”. In: *American Journal of Physics* 65.10, pp. 946–953. DOI: 10.1119/1.18696.
- Weber, T. A. (1999). “Response to ‘Comments regarding recent articles on relativistically rotating frames’”. In: *American Journal of Physics* 67.2, pp. 159–161. DOI: 10.1119/1.19214.
- Wicht, J., Stellmach, S., and Harder, H. (2015). “Numerical Dynamo Simulations: From Basic Concepts to Realistic Models”. In: *Handbook of Geomathematics*. Ed. by Freeden, W., Nashed, M. Z., and Sonar, T. 2nd ed. Vol. 1. Berlin, Heidelberg: Springer, pp. 779–834. DOI: 10.1007/978-3-642-54551-1\_16.
- Wicks, J. K., Jackson, J. M., and Sturhahn, W. (2010). “Very low sound velocities in iron-rich (Mg,Fe)O: Implications for the core-mantle boundary region”. In: *Geophysical Research Letters* 37.15, p. L15304. DOI: 10.1029/2010GL043689.
- Williamson, E. D. and Adams, L. H. (1923). “Density distribution in the Earth”. In: *Journal of the Washington Academy of Sciences* 13.19, pp. 413–428.
- Wolfram Research, Inc. (2015). *Mathematica*. Version 10.1.
- Wong, J., Davies, C. J., and Jones, C. A. (2018). “A Boussinesq slurry model of the F-layer at the base of Earth’s outer core”. In: *Geophysical Journal International* 214.3, pp. 2236–2249. DOI: 10.1093/gji/ggy245.
- Xu, Y., Poe, B. T., Shankland, T. J., and Rubie, D. C. (1998). “Electrical Conductivity of Olivine, Wadsleyite, and Ringwoodite Under Upper-Mantle Conditions”. In: *Science* 280.5368, pp. 1415–1418. DOI: 10.1126/science.280.5368.1415.
- Xu, Y., Shankland, T. J., and Poe, B. T. (2000). “Laboratory-based electrical conductivity in the Earth’s mantle”. In: *Journal of Geophysical Research: Solid Earth* 105.B12, pp. 27865–27875. DOI: 10.1029/2000JB900299.
- Yoder, C. F., Williams, J. G., and Parke, M. E. (1981). “Tidal variations of Earth rotation”. In: *Journal of Geophysical Research: Solid Earth* 86.B2, pp. 881–891. DOI: 10.1029/JB086iB02p00881.



## A Static stability and the buoyancy frequency

In the following, the concept of static stability is considered and the buoyancy frequency, which is a parameter for characterizing the static stability of a reference state, is derived. In particular, the concept of static stability is important in atmospheric and ocean dynamics. Regarding the outer core of the Earth and especially the stratified layers at the top and the bottom of this domain, the buoyancy frequency is used to characterize and quantify the (radial) gradient of the density field. Considering static stability, the so-called well-mixed adiabatic reference state of the outer core of the Earth is stable, but, for example, in the troposphere this is not always the case.

In the following, it will be demonstrated that the buoyancy frequency

$$N := \sqrt{-\frac{g}{\rho} \frac{\partial \rho}{\partial z}} \quad (\text{A.1})$$

characterizes the angular frequency of the motion of a displaced fluid parcel in a stratified fluid. The situation under consideration is depicted in Fig. A.1. Inside a layer of a stratified fluid, a fluid parcel, *i.e.*, a small volume of fluid, is displaced to a different position without changing its density. The density of the fluid is increasing with depth. The coordinate of the center of the fluid parcel in the reference configuration is denoted by  $z_0$  and by  $z_0 + h$  in the displaced configuration. The reference configuration can be thought of as a hydrostatic state and is denoted by the subscript “a” to indicate the connection with the well-mixed adiabatic state of the core of the Earth, see Sect. 2.7.1. In this configuration, the fluid parcel is neutrally buoyant at the position  $z = z_0$ . Furthermore, it is assumed that the fluid parcel does not change its density when it is displaced to the position  $z = z_0 + h$ .

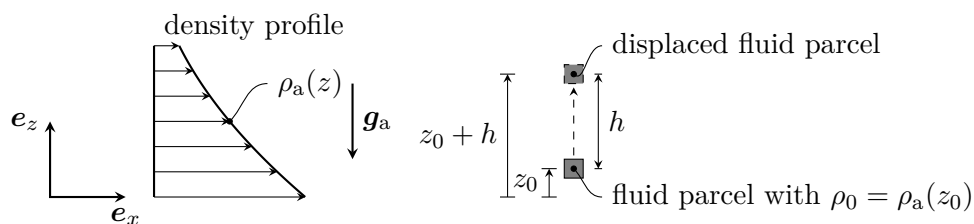


**Figure A.1:** Displacement of a fluid parcel in a stratified reference state. Illustration adopted from Pedlosky [1987], p. 351.

Moreover, it is assumed that the reference state, *i.e.*, the gravity and the associated pressure field, remain unchanged by the displacement of the fluid parcel.

The balance of momentum for the fluid parcel with mass  $M_p$  and (material) volume  $V_p$  is given by

$$\frac{d}{dt} \int_{M_p} \mathbf{v} dm = \oint_{\partial V_p} \mathbf{t}_a dA + \int_{M_p} \mathbf{g}_a dm. \quad (\text{A.2})$$

In this analysis, forces acting on the fluid parcel are constituted of the surface traction due to the reference state and the gravitational force. This means that possible viscous effects are neglected. Using Cauchy's argument and the stress tensor of the hydrostatic reference state, the surface traction vector can be expressed as  $\mathbf{t}_a = \boldsymbol{\sigma}_a \cdot \mathbf{n} = -p_a \mathbf{n}$ . The stress tensor is governed by the hydrostatic balance of momentum. Hence,  $-\nabla p_a + \rho_a \mathbf{g}_a = \mathbf{0}$ . The divergence theorem and the hydrostatic balance allow to express the global balance of momentum for the fluid parcel as

$$\frac{d}{dt} \int_{M_p} \mathbf{v} dm = - \int_{V_p} \rho_a \mathbf{g}_a dV + \int_{M_p} \mathbf{g}_a dm. \quad (\text{A.3})$$

It is assumed that the density of the fluid parcel does not change when it is displaced from  $z_0$  to  $z_0 + h$  and, therefore,  $dm = \rho_a(z_0) dV = \rho_0 dV$ . If it is additionally assumed that the volume of the parcel is (infinitesimally) small, Eq. (A.3) can be localized. In doing so, the velocity of the center of mass on the left-hand side and the reference density  $\rho_a$  on the right-hand side are evaluated at the current position of the parcel. If the current position of the parcel is denoted by  $z_p$ , *i.e.*,  $\mathbf{x}_p = z_p \mathbf{e}_z$ , the localization of Eq. (A.3) reads

$$\rho_0 \frac{d\mathbf{v}_p}{dt} = (-\rho_a(z_p) + \rho_0) \mathbf{g}_a \quad \Rightarrow \quad \rho_0 \ddot{z}_p(t) = -(\rho_a(z_p) - \rho_0)g, \quad (\text{A.4})$$

where  $g = \mathbf{g}_a \cdot \mathbf{e}_z$ .

This equation describes the motion of the fluid parcel. In case of a small displacement of the fluid parcel from the reference position, a first order TAYLOR series approximation of the reference density at the current position of the fluid parcel suffices. It is given by

$$\rho_a(z_p) \approx \rho_a(z_0) + \left. \frac{d\rho_a}{dz} \right|_{z_0} (z_p - z_0) = \rho_0 + \left. \frac{d\rho_a}{dz} \right|_{z_0} (z_p - z_0). \quad (\text{A.5})$$

This yields the following differential equation for the motion of the fluid parcel:

$$\ddot{z}_p + \frac{g}{\rho_0} \left. \frac{d\rho_a}{dz} \right|_{z_0} (z_p - z_0) = 0. \quad (\text{A.6})$$

The differential equation above has solutions of the form  $z_p(t) \propto \exp(\lambda t)$  with the

eigenvalues

$$\lambda_{1,2} = \pm \sqrt{-\frac{g}{\rho_0} \frac{d\rho_a}{dz}} \Big|_{z_0}. \quad (\text{A.7})$$

Apart from the evaluation of the density and the density gradient at the position  $z_0$ , the radical on the right-hand side is the buoyancy frequency  $N$  defined in Eq. (A.1), *i.e.*,  $N = \pm\lambda_{1,2}$ . Furthermore, the sign of the radicand determines the type of the solution. If it is positive, the eigenvalues are purely complex and the solution is stable. It is given by a harmonic oscillation about the neutrally buoyant position  $z_0$ . If it is negative, the eigenvalues are real and the solution is not stable, because one part of the solution is growing exponentially. In case of a stable situation, the solution for a parcel with initial position  $z_p = z_0 + h$ , that is released from rest, is given by

$$z_p(t) = z_0 + h \cos(Nt), \quad (\text{A.8})$$

which shows that the buoyancy frequency  $N$  is the angular frequency of the oscillation of a fluid parcel in a stably stratified fluid. Hence, the larger the density gradient, the smaller is the period of the oscillation.

---



## B The EULIDian transformation

The EULIDian transformation is an important transformation because it allows to derive relations between the position, velocity and acceleration vectors of two observers which move relative to each other and also change their relative orientation. Furthermore, the EULIDian transformation is also important when the transformation properties of the balance equations of continuum mechanics are considered. Moreover, the rule or principle of *material objectivity* states that the material laws or material functions must be invariant against the EUCLIDian transformation, see, *e.g.*, Hutter and Jöhnk [2004].

In Sect. 2.6, the EULIDian transformation was introduced in Eq. (2.75), which establishes a relation between the position vectors  $\mathbf{x}$  and  $\tilde{\mathbf{x}}$  of a point P observed by the two observers  $\mathcal{O}$  and  $\tilde{\mathcal{O}}$ , respectively. This relation is given by

$$\tilde{\mathbf{x}}(t) = \mathbf{x}(t) + \mathbf{c}(t), \quad (\text{B.1})$$

where the vector  $\mathbf{c}$  denotes the relative position of the two observers  $\mathcal{O}$  and  $\tilde{\mathcal{O}}$ . Apart from this relative position, the relative orientation of the two observers also needs to be taken into account in the EULIDian transformation. In order to describe this relative orientation, a tensor  $\tilde{\mathbf{Q}}$  may be introduced with the following property

$$\mathbf{e}_i = \tilde{\mathbf{Q}} \cdot \tilde{\mathbf{e}}_i, \quad \mathbf{e}_i \cdot \mathbf{e}_j = \delta_{ij}, \quad \tilde{\mathbf{e}}_i \cdot \tilde{\mathbf{e}}_j = \delta_{ij}, \quad (\text{B.2})$$

where  $\delta_{ij}$  denotes the KRONECKER symbol. This equation for the tensor  $\tilde{\mathbf{Q}}$  implies a pairwise linear mapping between the orthonormal basis vectors of the two observers. Here, the vectors  $\mathbf{e}_i$  and  $\tilde{\mathbf{e}}_i$ ,  $i = 1, 2, 3$ , denote the basis vectors of the observers  $\mathcal{O}$  and  $\tilde{\mathcal{O}}$ , respectively. These two sets of basis vectors are important for the following analysis because they are not only used to express the relative orientation of the two observers, but also allow to represent the components of the position, velocity and acceleration vectors of the two observers.

In the following, the properties of the tensor  $\tilde{\mathbf{Q}}$  are considered and analyzed. In doing so, its time derivative is also considered and the angular velocity vector is introduced. This vector is important for the analysis of the relations between the velocity and acceleration vectors of the two observers in Sect. B.1. Finally, the transformation of spatial gradients is briefly discussed in Sect. B.2.

Regarding the properties of the tensor  $\tilde{\mathbf{Q}}$ , Eq. (B.2) implies a representation of this tensor in the following mixed form

$$\tilde{\mathbf{Q}} = \mathbf{e}_k \otimes \tilde{\mathbf{e}}_k = \mathbf{e}_1 \otimes \tilde{\mathbf{e}}_1 + \mathbf{e}_2 \otimes \tilde{\mathbf{e}}_2 + \mathbf{e}_3 \otimes \tilde{\mathbf{e}}_3. \quad (\text{B.3})$$

Hence,

$$\tilde{\mathbf{Q}}^T = \tilde{e}_k \otimes e_k \quad \text{and} \quad \tilde{\mathbf{Q}}^T \cdot \tilde{\mathbf{Q}} = (\tilde{e}_i \otimes e_i) \cdot (e_j \otimes \tilde{e}_j) = \tilde{e}_i \otimes \tilde{e}_i = \mathbf{1}. \quad (\text{B.4})$$

Equation (B.2) implies that the tensor  $\tilde{\mathbf{Q}}$  is orthogonal, *i.e.*,  $\tilde{\mathbf{Q}}^T = \tilde{\mathbf{Q}}^{-1}$ . This means that the tensor  $\tilde{\mathbf{Q}}$  describes a transformation which does not change the length of a vector and the relative angle between two vectors.

The components of the tensor  $\tilde{\mathbf{Q}}$  with respect to the  $e$ -basis and the  $\tilde{e}$ -basis are obtained by computing the double contraction of  $\tilde{\mathbf{Q}}$  with  $e_i \otimes e_j$  and  $\tilde{e}_i \otimes \tilde{e}_j$ , respectively. In doing so, it turns out that the components with respect to both bases are equal to those specified in Eq. (2.74), which means that both observers measure the same relative orientation at every instance of time. In summary, the tensor  $\tilde{\mathbf{Q}}$  can be represented as follows

$$\tilde{\mathbf{Q}} = \tilde{Q}_{ij} \tilde{e}_i \otimes \tilde{e}_j = \tilde{Q}_{ij} e_i \otimes e_j. \quad (\text{B.5})$$

Note that Eq. (2.74) implies a time-dependence of the tensor  $\tilde{\mathbf{Q}}$ , which was not explicitly specified in the equations above.

However, this time-dependence is analyzed in the following. The fact that  $\tilde{\mathbf{Q}}^{-1} = \tilde{\mathbf{Q}}^T$  allows to derive two skew-symmetric angular velocity tensors—the so-called left and right angular velocity tensors. The angular velocity tensor, that is commonly used in the literature, is the left angular velocity tensor. It is defined as

$$\tilde{\mathbf{\Omega}} := \frac{d\tilde{\mathbf{Q}}}{dt} \cdot \tilde{\mathbf{Q}}^T = -\tilde{\mathbf{Q}} \cdot \frac{d\tilde{\mathbf{Q}}^T}{dt}, \quad \text{with} \quad \tilde{\mathbf{\Omega}}^T = -\tilde{\mathbf{\Omega}}. \quad (\text{B.6})$$

The fact that the tensor  $\tilde{\mathbf{\Omega}}$  is skew-symmetric further allows to introduce an angular velocity vector  $\tilde{\boldsymbol{\omega}}$  such that  $\tilde{\mathbf{\Omega}} \cdot \mathbf{a} = \tilde{\boldsymbol{\omega}} \times \mathbf{a}$  holds for all vectors  $\mathbf{a}$ . Using the antisymmetric tensor of third rank, the angular velocity vector  $\tilde{\boldsymbol{\omega}}$  may be expressed as [Bertram and Glüge (2015)]

$$\tilde{\boldsymbol{\omega}} = -\frac{1}{2} \overset{(3)}{\boldsymbol{\epsilon}} \cdot \tilde{\mathbf{\Omega}}, \quad (\text{B.7})$$

where the double contraction in one common orthonormal basis is given by  $\mathbf{A} \cdot \mathbf{B} = A_{ij} B_{ij}$ ; the EINSTEIN summation convention applies. Furthermore,  $\overset{(3)}{\boldsymbol{\epsilon}}$  denotes the LEVI-CIVITA tensor whose CARTESIAN components are given by the permutation symbol. The properties of this tensor are further detailed in Appendix C. The factor of one half is introduced for consistency with the formula  $\tilde{\mathbf{\Omega}} = -\tilde{\boldsymbol{\omega}} \cdot \overset{(3)}{\boldsymbol{\epsilon}}$ .

## B.1 Representations of the velocity and the acceleration

In the following, relations between the velocity and the acceleration measured by the two observers  $\mathcal{O}$  and  $\tilde{\mathcal{O}}$  are analyzed. First, the time derivative of Eq. (B.1) is considered in order to establish a relation between the two velocities. Then, this result is used to analyze the accelerations. The objective is to represent the

velocity and the acceleration observed by the observer  $\tilde{\mathcal{O}}$  in terms of those observed by the observer  $\mathcal{O}$ .

The components of the velocity vector measured by the observer  $\mathcal{O}$  are denoted by  $v_i = \dot{x}_i$  and those measured by the observer  $\tilde{\mathcal{O}}$  by  $\tilde{v}_i = \dot{\tilde{x}}_i$ . Hence,

$$\mathbf{v}(t) = (v_i \mathbf{e}_i)(t) = (\dot{x}_i \mathbf{e}_i)(t), \quad \tilde{\mathbf{v}} = (\tilde{v}_i \tilde{\mathbf{e}}_i)(t) = (\dot{\tilde{x}}_i \tilde{\mathbf{e}}_i)(t). \quad (\text{B.8})$$

The representation of the the velocity observed by the observer  $\tilde{\mathcal{O}}$  in terms of that observed by the observer  $\mathcal{O}$  is derived by considering the relation between the components of the associated position vectors given in Eq. (2.76). Taking the time derivative of Eq. (2.76) yields

$$\tilde{v}_i(t) = \tilde{Q}_{ij}(t)(v_j(t) + \dot{c}_j(t)) + \frac{d\tilde{Q}_{ij}}{dt}(x_j(t) + c_j(t)). \quad (\text{B.9})$$

Using Eq. (B.6), the time derivative of the components  $\tilde{Q}_{ij}$  can be expressed in terms of the components of the angular velocity tensor and the equation above can be written as

$$\tilde{v}_i(t) = \tilde{Q}_{ij}(t)(v_j(t) + \dot{c}_j(t)) + \tilde{\Omega}_{ik}(t)\tilde{Q}_{kj}(t)(x_j(t) + c_j(t)). \quad (\text{B.10})$$

A tensor equation is obtained from Eq. (B.10) by a multiplication with  $\tilde{\mathbf{e}}_i$  and a substitution of  $\tilde{Q}_{ij}$  according to Eq. (2.74), namely  $\tilde{Q}_{ij} = \tilde{\mathbf{e}}_i \cdot \mathbf{e}_j$ . For example, for the first term in the first parenthesis on the right-hand side, this yields

$$\tilde{\mathbf{e}}_i \tilde{Q}_{ij} v_j = \tilde{\mathbf{e}}_i (\tilde{\mathbf{e}}_i \cdot \mathbf{e}_j) v_j = \underbrace{(\tilde{\mathbf{e}}_i \otimes \tilde{\mathbf{e}}_i)}_{=\mathbf{1}} \cdot v_j \mathbf{e}_j = \mathbf{1} \cdot \mathbf{v} = \mathbf{v} \quad (\text{B.11})$$

In summary, the result, which is finally obtained, is given by

$$\tilde{\mathbf{v}}(t) = \tilde{v}_i(t) \tilde{\mathbf{e}}_i = \mathbf{v}(t) + \tilde{\boldsymbol{\omega}}(t) \times \mathbf{x}(t) + \dot{\tilde{\mathbf{c}}}(t), \quad (\text{B.12})$$

where  $\dot{\tilde{\mathbf{c}}}(t) = \dot{\mathbf{c}}(t) + \tilde{\boldsymbol{\omega}}(t) \times \mathbf{c}(t)$ . Equation (B.12) describes the transformation of the two velocities or, in other words, the representation of the velocity  $\tilde{\mathbf{v}}$  in terms of the velocity  $\mathbf{v}$ , the angular velocity  $\tilde{\boldsymbol{\omega}}$  and the relative velocity  $\dot{\tilde{\mathbf{c}}}$ .

In order to obtain a transformation of the acceleration, Eq. (B.10) is differentiated once more with respect to the time. Using  $\tilde{a}_i = \dot{\tilde{v}}_i$  and  $\tilde{a}_i = \dot{\tilde{v}}_i$  for the accelerations measured by the two observers  $\mathcal{O}$  and  $\tilde{\mathcal{O}}$ , respectively, the final result reads

$$\begin{aligned} \tilde{a}_i(t) = \frac{d\tilde{v}_i}{dt} = & \tilde{Q}_{ij}(t)(a_j(t) + \ddot{c}_j(t)) + 2\tilde{\Omega}_{ik}(t)\tilde{Q}_{kj}(t)(v_j(t) + \dot{c}_j(t)) + \\ & + \dot{\tilde{\Omega}}_{ik}(t)\tilde{Q}_{kj}(t)(x_j(t) + c_j(t)) + \tilde{\Omega}_{ik}(t)\dot{\tilde{\Omega}}_{kl}(t)\tilde{Q}_{lj}(t)(x_j(t) + c_j(t)). \end{aligned} \quad (\text{B.13})$$

Similar to Eq. (B.10), the corresponding tensor equation is obtained by a multipli-

cation with  $\tilde{\mathbf{e}}_i$  and a substitution of  $\tilde{Q}_{ij}$  according to Eq. (2.74). Thus,

$$\tilde{\mathbf{a}}(t) = \mathbf{a}(t) + 2\tilde{\boldsymbol{\omega}}(t) \times \mathbf{v}(t) + \dot{\tilde{\boldsymbol{\omega}}}(t) \times \mathbf{x}(t) + \tilde{\boldsymbol{\omega}}(t) \times (\tilde{\boldsymbol{\omega}}(t) \times \mathbf{x}(t)) + \ddot{\tilde{\mathbf{c}}}(t), \quad (\text{B.14})$$

where  $\ddot{\tilde{\mathbf{c}}}(t) = \ddot{\mathbf{c}}(t) + 2\tilde{\boldsymbol{\omega}}(t) \times \dot{\mathbf{c}}(t) + \dot{\tilde{\boldsymbol{\omega}}}(t) \times \mathbf{c}(t) + \tilde{\boldsymbol{\omega}}(t) \times (\tilde{\boldsymbol{\omega}}(t) \times \mathbf{c}(t))$ . This equation represents the acceleration  $\tilde{\mathbf{a}}$  measured by the observer  $\tilde{\mathcal{O}}$  in terms of the velocity  $\mathbf{v}$  and acceleration  $\mathbf{a}$  measured by the observer  $\mathcal{O}$ , the angular velocity  $\tilde{\boldsymbol{\omega}}$ , the angular acceleration  $\dot{\tilde{\boldsymbol{\omega}}}$ , and the relative velocity  $\dot{\tilde{\mathbf{c}}}$  and acceleration  $\ddot{\tilde{\mathbf{c}}}$ .

## B.2 Representations of spatial gradients

In the following, the representations of spatial gradients is discussed very briefly. First, the transformation of the del-operator is derived and, subsequently, consequences for the gradients of scalar and vector fields are considered with an emphasis on the gradient of the velocity.

The derivation of the transformation of the del-operator makes use of the fact that the tensor  $\tilde{\mathbf{Q}}$  not only relates the two sets of basis vectors  $\mathbf{e}_i$  and  $\tilde{\mathbf{e}}_i$ ,  $i = 1, 2, 3$ , to each other, but by virtue of Eq. (2.76) also allows to derive a relation between the derivatives with respect to the coordinates  $x_i$  and  $\tilde{x}_i$ . More precisely, differentiating Eq. (2.76) with respect to the coordinate  $x_j$  yields

$$\frac{\partial \tilde{x}_i}{\partial x_j} = \tilde{Q}_{ij}. \quad (\text{B.15})$$

Using this intermediate result, the transformation of the del-operator is obtained by going through the following steps

$$\tilde{\nabla} = \tilde{\mathbf{e}}_i \frac{\partial}{\partial \tilde{x}_i} = \tilde{\mathbf{Q}}^T \cdot \mathbf{e}_i \frac{\partial}{\partial \tilde{x}_i} = \tilde{Q}_{ij} \mathbf{e}_j \frac{\partial}{\partial \tilde{x}_i} = \mathbf{e}_j \frac{\partial \tilde{x}_i}{\partial x_j} \frac{\partial}{\partial \tilde{x}_i} = \mathbf{e}_j \frac{\partial}{\partial x_j} = \nabla, \quad (\text{B.16})$$

where the chain rule of differentiation was applied in the last step. This transformation of the del-operator has immediate consequences for those of scalar fields. If it is supposed that scalar fields such as the density  $\rho$ , the temperature  $T$  and the pressure  $p$  are invariant against EUCLIDIAN transformations, *i.e.*,  $\tilde{\rho} = \rho$ ,  $\tilde{T} = T$  and  $\tilde{p} = p$ , then gradients of these fields are invariant as well, *i.e.*,  $\tilde{\nabla}\tilde{\rho} = \nabla\rho$ ,  $\tilde{\nabla}\tilde{T} = \nabla T$  and  $\tilde{\nabla}\tilde{p} = \nabla p$ . Hence, for example, the FOURIER law for the heat flux vector is also invariant under the EUCLIDIAN transformation.

Finally, the transformation of the del-operator and the transformation of the velocity in Eq. (B.12) are used to analyze that of the velocity gradient. Taking the gradient of Eq. (B.12) yields

$$\tilde{\nabla} \otimes \tilde{\mathbf{v}} = \nabla \otimes \tilde{\mathbf{v}} = \nabla \otimes \mathbf{v} + \nabla \otimes (\boldsymbol{\omega} \times \mathbf{x}). \quad (\text{B.17})$$

The latter term on right-hand side can be simplified as follows:

$$\begin{aligned}\nabla \otimes (\boldsymbol{\omega} \times \boldsymbol{x}) &= \boldsymbol{e}_i \frac{\partial}{\partial x_i} \otimes (\boldsymbol{\omega} \times x_j \boldsymbol{e}_j) = \boldsymbol{e}_i \otimes (\boldsymbol{\omega} \times \boldsymbol{e}_i) = \boldsymbol{e}_i \epsilon_{jki} \omega_k \boldsymbol{e}_j \\ &= -\epsilon_{kji} \omega_k \boldsymbol{e}_i \otimes \boldsymbol{e}_j = \epsilon_{kij} \omega_k \boldsymbol{e}_i \otimes \boldsymbol{e}_j = \boldsymbol{\omega} \cdot \overset{(3)}{\boldsymbol{\epsilon}},\end{aligned}\quad (\text{B.18})$$

where the anti-symmetries of the permutation symbol  $\epsilon_{ijk}$  were exploited in the last two steps. Hence,

$$\tilde{\nabla} \otimes \tilde{\boldsymbol{v}} = \nabla \otimes \boldsymbol{v} + \boldsymbol{\omega} \cdot \overset{(3)}{\boldsymbol{\epsilon}}. \quad (\text{B.19})$$

This result shows that the velocity gradient is not invariant against the EUCLIDIAN transformation. However, the last term on the right-hand side is anti-symmetric. Therefore, the symmetric part of the velocity gradient,  $\boldsymbol{d}$ , is invariant, *i.e.*,  $\boldsymbol{d} = \tilde{\boldsymbol{d}}$ , which may be shown as follows

$$\begin{aligned}\tilde{\boldsymbol{d}} &= \frac{1}{2}(\tilde{\nabla} \otimes \tilde{\boldsymbol{v}} + \tilde{\boldsymbol{v}} \otimes \tilde{\nabla}) = \frac{1}{2}(\nabla \otimes \tilde{\boldsymbol{v}} + \tilde{\boldsymbol{v}} \otimes \nabla) \\ &= \frac{1}{2}(\nabla \otimes \boldsymbol{v} + \boldsymbol{v} \otimes \nabla + \boldsymbol{\omega} \cdot \overset{(3)}{\boldsymbol{\epsilon}} + (\boldsymbol{\omega} \cdot \overset{(3)}{\boldsymbol{\epsilon}})^T) \\ &= \frac{1}{2}(\nabla \otimes \boldsymbol{v} + \boldsymbol{v} \otimes \nabla + \boldsymbol{\omega} \cdot \overset{(3)}{\boldsymbol{\epsilon}} - \boldsymbol{\omega} \cdot \overset{(3)}{\boldsymbol{\epsilon}}) = \frac{1}{2}(\nabla \otimes \boldsymbol{v} + \boldsymbol{v} \otimes \nabla) = \boldsymbol{d}.\end{aligned}\quad (\text{B.20})$$

As a consequence, the NAVIER–STOKES law for the stress tensor of a fluid is also invariant against the EUCLIDIAN transformation, because both the pressure  $p$  and the symmetric velocity gradient  $\boldsymbol{d}$  are invariant.



## C Analysis of sequential rotations

In this appendix, the properties of sequential rotations are analyzed. The presentation in this appendix partly follows that in Rickert, Glane, and Müller [2020]. The provisional version of the analysis presented here served as the basis for the aforementioned publication.

Sequential rotations are represented by a proper orthogonal tensor  $\tilde{\mathbf{Q}}$ , which is composed of two or more elementary rotations. This means that the tensor  $\tilde{\mathbf{Q}}$  is given by, *e.g.*,  $\tilde{\mathbf{Q}} = \tilde{\mathbf{Q}}_1 \cdot \tilde{\mathbf{Q}}_2 \cdot \tilde{\mathbf{Q}}_3$  where the tensors  $\tilde{\mathbf{Q}}_i$  are orthogonal and  $\det(\tilde{\mathbf{Q}}_i) = 1$ ,  $i = 1, 2, 3$ . This multiplicative decomposition of the tensor  $\tilde{\mathbf{Q}}$  applies for the usage of the EULER angles, which were introduced and discussed in Sect. 2.2. In the following, rotations described by the EULER angles are analyzed in Sect. C.3 and the related angular velocity and angular acceleration vectors are derived. Prior to this, the formula for the angular velocity vector of a sequential rotation is derived in Sect. C.1 and, subsequently, the representation of a rotation by the RODRIGUES formula and its consequences are discussed in Sect. C.2.

### C.1 Angular velocity and angular acceleration vector

For the example, that the tensor  $\tilde{\mathbf{Q}}$  consists of three sequential rotations, it can be shown by computing the derivative of  $\tilde{\mathbf{Q}} = \tilde{\mathbf{Q}}_1 \cdot \tilde{\mathbf{Q}}_2 \cdot \tilde{\mathbf{Q}}_3$ , that the angular velocity tensor  $\tilde{\mathbf{\Omega}}$  is given by

$$\tilde{\mathbf{\Omega}} = \tilde{\mathbf{\Omega}}_1 + \tilde{\mathbf{Q}}_1 \star \tilde{\mathbf{\Omega}}_2 + (\tilde{\mathbf{Q}}_1 \cdot \tilde{\mathbf{Q}}_2) \star \tilde{\mathbf{\Omega}}_3, \quad (\text{C.1})$$

where  $\tilde{\mathbf{\Omega}}_i = \dot{\tilde{\mathbf{Q}}}_i \cdot \tilde{\mathbf{Q}}_i^{\text{T}}$ ,  $i = 1, 2, 3$ , are the angular velocity tensors related to the elementary rotations and the symbol  $\star$  denotes the RAYLEIGH product. For a second order tensor, the RAYLEIGH product is given by  $\tilde{\mathbf{Q}} \star \mathbf{A} = \tilde{\mathbf{Q}} \cdot \mathbf{A} \cdot \tilde{\mathbf{Q}}^{\text{T}}$ . The result in Eq. (C.1) can easily be generalized for an arbitrary number of elementary rotations.

According to Eq. (B.7), the angular velocity vector  $\tilde{\boldsymbol{\omega}}$  related to Eq. (C.1) is computed by a double contraction with the LEVI-CIVITA tensor  $\epsilon^{(3)}$ . Therefore, it is necessary to introduce this tensor properly. Furthermore, it is helpful to consider its transformation properties if the RAYLEIGH product is applied. The LEVI-CIVITA tensor  $\epsilon^{(3)}$  is given by

$$\epsilon^{(3)} = \epsilon_{ijk} \mathbf{e}_i \otimes \mathbf{e}_j \otimes \mathbf{e}_k = \tilde{\epsilon}_{ijk} \tilde{\mathbf{e}}_i \otimes \tilde{\mathbf{e}}_j \otimes \tilde{\mathbf{e}}_k. \quad (\text{C.2})$$

In this equation, the components with respect to the  $\mathbf{e}$ -basis are given by the

---

permutation symbol  $\epsilon_{ijk}$ , which has the properties as introduced, for example, in Flügge [1972]. The components with respect to the  $\tilde{e}$ -basis are denoted by  $\tilde{\epsilon}_{ijk}$ . In order to obtain a relation between these two different components, Eq. (C.2) is contracted with the triad  $\tilde{e}_i \otimes \tilde{e}_j \otimes \tilde{e}_k$  and scalar products of the different basis vectors are replaced by the respective components of the orthogonal tensor  $\tilde{\mathbf{Q}}$  as specified in Eq. (2.74), *i.e.*,  $\tilde{Q}_{ij} = \tilde{e}_i \cdot \tilde{e}_j$ . The resulting equation reads

$$\tilde{\epsilon}_{ijk} = \epsilon_{lmn} \tilde{Q}_{il} \tilde{Q}_{jm} \tilde{Q}_{kn} = \det(\tilde{\mathbf{Q}}) \epsilon_{ijk}, \quad (\text{C.3})$$

where the relation of the permutation symbol with determinant was used in the second step [Flügge (1972)]. This equation implies that the components of the LEVI-CIVITA tensor of the  $e$ -basis are the same as those of the  $\tilde{e}$ -basis if the tensor  $\tilde{\mathbf{Q}}$  is a proper orthogonal tensor, *i.e.*,  $\epsilon_{ijk} = \tilde{\epsilon}_{ijk}$  if  $\det(\tilde{\mathbf{Q}}) = 1$ .

This transformation rule for the two components has the consequence that the LEVI-CIVITA tensor is invariant against the RAYLEIGH product with a proper orthogonal tensor. This may be shown by the following calculation

$$\tilde{\mathbf{Q}} \star \overset{(3)}{\boldsymbol{\epsilon}} = \tilde{\epsilon}_{ijk} (\tilde{\mathbf{Q}} \cdot \tilde{e}_i) \otimes (\tilde{\mathbf{Q}} \cdot \tilde{e}_j) \otimes (\tilde{\mathbf{Q}} \cdot \tilde{e}_k) = \tilde{\epsilon}_{ijk} \mathbf{e}_i \otimes \mathbf{e}_j \otimes \mathbf{e}_k = \overset{(3)}{\boldsymbol{\epsilon}}, \quad (\text{C.4})$$

where  $\det(\tilde{\mathbf{Q}}) = 1$  must hold true in order to substitute  $\tilde{\epsilon}_{ijk}$  by  $\epsilon_{ijk}$  in the last step.

In the following, the previous relation is used to derive the angular velocity vector from Eq. (C.1). In the first step, the RAYLEIGH product of some anti-symmetric tensor of second rank  $\mathbf{A}$  is considered. This tensor may be represented by the associated axial vector  $\mathbf{a}$ , *viz.*,  $\mathbf{A} = -\overset{(3)}{\boldsymbol{\epsilon}} \cdot \mathbf{a}$ . Considering the RAYLEIGH product of the tensor  $\mathbf{A}$  yields

$$\begin{aligned} \tilde{\mathbf{Q}} \star \mathbf{A} &= \tilde{\mathbf{Q}} \star (-\overset{(3)}{\boldsymbol{\epsilon}} \cdot \mathbf{a}) = -\tilde{\mathbf{Q}} \star (\overset{(3)}{\boldsymbol{\epsilon}} \cdot \tilde{\mathbf{Q}}^T \cdot \tilde{\mathbf{Q}} \cdot \mathbf{a}) = -\tilde{\mathbf{Q}} \star (\overset{(3)}{\boldsymbol{\epsilon}} \cdot \tilde{\mathbf{Q}}^T) \cdot (\tilde{\mathbf{Q}} \cdot \mathbf{a}) \\ &= -[\tilde{\epsilon}_{ijk} (\tilde{\mathbf{Q}} \cdot \tilde{e}_i) \otimes (\tilde{\mathbf{Q}} \cdot \tilde{e}_j) \otimes (\tilde{\mathbf{Q}} \cdot \tilde{e}_k)] \cdot (\tilde{\mathbf{Q}} \cdot \mathbf{a}) = -\overset{(3)}{\boldsymbol{\epsilon}} \cdot (\tilde{\mathbf{Q}} \cdot \mathbf{a}). \end{aligned} \quad (\text{C.5})$$

In the second step, the axial vector of the RAYLEIGH product of the anti-symmetric tensor  $\mathbf{A}$  is considered. The result is obtained by going through the following steps

$$-\frac{1}{2} \overset{(3)}{\boldsymbol{\epsilon}} \cdot [\tilde{\mathbf{Q}} \star \mathbf{A}] = -\frac{1}{2} \overset{(3)}{\boldsymbol{\epsilon}} \cdot [\tilde{\mathbf{Q}} \star (-\overset{(3)}{\boldsymbol{\epsilon}} \cdot \mathbf{a})] = \frac{1}{2} \overset{(3)}{\boldsymbol{\epsilon}} \cdot \overset{(3)}{\boldsymbol{\epsilon}} \cdot (\tilde{\mathbf{Q}} \cdot \mathbf{a}) = \tilde{\mathbf{Q}} \cdot \mathbf{a}, \quad (\text{C.6})$$

where the identity  $\frac{1}{2} \overset{(3)}{\boldsymbol{\epsilon}} \cdot \overset{(3)}{\boldsymbol{\epsilon}} = \mathbf{1}$  was applied in the last step of the derivation above. In the final step, the previous result regarding the axial vector is used to compute the angular velocity vector associated with the angular velocity tensor  $\tilde{\boldsymbol{\Omega}}$  specified in Eq. (C.1):

$$\begin{aligned} \tilde{\boldsymbol{\omega}} &= -\frac{1}{2} \overset{(3)}{\boldsymbol{\epsilon}} \cdot \tilde{\boldsymbol{\Omega}}_1 - \frac{1}{2} \overset{(3)}{\boldsymbol{\epsilon}} \cdot [\tilde{\mathbf{Q}}_1 \star \tilde{\boldsymbol{\Omega}}_2] - \frac{1}{2} \overset{(3)}{\boldsymbol{\epsilon}} \cdot [(\tilde{\mathbf{Q}}_1 \cdot \tilde{\mathbf{Q}}_2) \cdot \tilde{\boldsymbol{\Omega}}_3] \\ &= \tilde{\boldsymbol{\omega}}_1 - \frac{1}{2} \overset{(3)}{\boldsymbol{\epsilon}} \cdot [\tilde{\mathbf{Q}}_1 \star (-\overset{(3)}{\boldsymbol{\epsilon}} \cdot \tilde{\boldsymbol{\omega}}_2)] - \frac{1}{2} \overset{(3)}{\boldsymbol{\epsilon}} \cdot [(\tilde{\mathbf{Q}}_1 \cdot \tilde{\mathbf{Q}}_2) \star (-\overset{(3)}{\boldsymbol{\epsilon}} \cdot \tilde{\boldsymbol{\omega}}_3)] \\ &= \tilde{\boldsymbol{\omega}}_1 + \tilde{\mathbf{Q}}_1 \cdot \tilde{\boldsymbol{\omega}}_2 + \tilde{\mathbf{Q}}_1 \cdot \tilde{\mathbf{Q}}_2 \cdot \tilde{\boldsymbol{\omega}}_3, \end{aligned} \quad (\text{C.7})$$

where  $\tilde{\boldsymbol{\omega}}_i$  are the axial vectors of the angular velocity tensors of the elementary

rotations  $\tilde{\mathbf{Q}}_i$ ,  $i = 1, 2, 3$ . The result in the previous equation concludes the computation of the angular velocity vector related to a rotation that is composed of three elementary ones. In summary, the angular velocity vector is given by a linear equation involving the three angular velocity vectors of the elementary rotations.

## C.2 The RODRIGUES formula

In the following, the RODRIGUES formula is considered. This formula allows to describe an arbitrary rotation in terms of an axis and an associated angle. Furthermore, it is very helpful for the analysis of the sequential rotation described by the EULER angles. Any tensor  $\mathbf{Q}$  which is describing a rotation may be expressed using the RODRIGUES formula, namely,

$$\mathbf{Q} = \cos(\alpha)\mathbf{1} + (1 - \cos(\alpha))\mathbf{q} \otimes \mathbf{q} - \sin(\alpha)\mathbf{q} \cdot \overset{(3)}{\boldsymbol{\epsilon}}, \quad (\text{C.8})$$

where  $\mathbf{q}$  denotes the axis of rotation and  $\alpha$  the angle of rotation w.r.t. this axis. The axis of rotation is a unit vector, *i.e.*,  $\mathbf{q} \cdot \mathbf{q} = 1$ . The axis and the angle of rotation may be computed for a given tensor  $\mathbf{Q}$  by computing its axial vector and its trace, respectively. Note that in this section and in the following the tildes are dropped in order not to overload the notation.

In the following, the angular velocity vector  $\boldsymbol{\omega}$  is derived for the case that the rotation tensor  $\mathbf{Q}$  is represented using the RODRIGUES formula. Through a straight-forward calculation, the time derivative of the tensor  $\mathbf{Q}$  specified in Eq. (C.8) is obtained as

$$\begin{aligned} \dot{\mathbf{Q}} = & -\sin(\alpha)\dot{\alpha}(\mathbf{1} - \mathbf{q} \otimes \mathbf{q}) + (1 - \cos(\alpha))(\mathbf{q} \otimes \dot{\mathbf{q}} + \dot{\mathbf{q}} \otimes \mathbf{q}) - \\ & - (\cos(\alpha)\dot{\alpha}\mathbf{q} + \sin(\alpha)\dot{\mathbf{q}}) \cdot \overset{(3)}{\boldsymbol{\epsilon}}. \end{aligned} \quad (\text{C.9})$$

In order to obtain a representation of the associated angular velocity tensor  $\boldsymbol{\Omega}$ , which is given by the product  $\dot{\mathbf{Q}} \cdot \mathbf{Q}^T$ , it is convenient to first compute the products of  $\dot{\mathbf{Q}}$  with the elementary tensors on the right-hand side of Eq. (C.8). This means that products of the tensor  $\dot{\mathbf{Q}}$  with  $\mathbf{q} \otimes \mathbf{q}$ ,  $\mathbf{q} \cdot \overset{(3)}{\boldsymbol{\epsilon}}$  and, for completeness, with  $\mathbf{1}$  are considered separately. In order to simplify the resulting expressions, the following identities related to the LEVI-CIVITA tensor are helpful

$$\frac{1}{2} \overset{(3)}{\boldsymbol{\epsilon}} \cdot \overset{(3)}{\boldsymbol{\epsilon}} = \mathbf{1}, \quad \overset{(3)}{\boldsymbol{\epsilon}} \cdot \overset{(3)}{\boldsymbol{\epsilon}} = \overset{(4)}{\mathbf{1}} - \overset{(4)}{\mathbf{T}}, \quad (\text{C.10a})$$

$$\overset{(3)}{\boldsymbol{\epsilon}} \cdot \mathbf{a} \cdot \overset{(3)}{\boldsymbol{\epsilon}} \cdot \mathbf{b} = \mathbf{a} \cdot \overset{(3)}{\boldsymbol{\epsilon}} \cdot \overset{(3)}{\boldsymbol{\epsilon}} \cdot \mathbf{b} = \mathbf{b} \otimes \mathbf{a} - (\mathbf{a} \cdot \mathbf{b})\mathbf{1}, \quad (\text{C.10b})$$

$$\mathbf{a} \otimes \mathbf{b} \cdot \overset{(3)}{\boldsymbol{\epsilon}} \cdot \mathbf{c} = -\mathbf{a} \otimes (\mathbf{b} \times \mathbf{c}), \quad (\text{C.10c})$$

$$\overset{(3)}{\boldsymbol{\epsilon}} \cdot \mathbf{a} \cdot \mathbf{b} \otimes \mathbf{c} = -(\mathbf{a} \times \mathbf{b}) \otimes \mathbf{c}, \quad (\text{C.10d})$$

where  $\overset{(4)}{\mathbf{1}}$  denotes the identity tensor of fourth rank,  $\overset{(4)}{\mathbf{T}}$  the “transposer”, *i.e.*, a tensor of fourth rank which yields for any tensor of second rank that  $\overset{(4)}{\mathbf{T}} \cdot \mathbf{A} = \mathbf{A}^T$ ,

and  $\mathbf{a}$  and  $\mathbf{b}$  are two arbitrary vectors. Furthermore, the GRASSMANN identities for the double cross product will be used in the following and may be expressed in terms of the LEVI-CIVITA tensor as follows:

$$\mathbf{a} \times (\mathbf{b} \times \mathbf{c}) = \overset{(3)}{\boldsymbol{\epsilon}} \cdot (\mathbf{a} \otimes (\mathbf{b} \times \mathbf{c})) = \mathbf{a} \cdot (\mathbf{c} \otimes \mathbf{b} - \mathbf{b} \otimes \mathbf{c}), \quad (\text{C.10e})$$

$$(\mathbf{a} \times \mathbf{b}) \times \mathbf{c} = \overset{(3)}{\boldsymbol{\epsilon}} \cdot ((\mathbf{a} \times \mathbf{b}) \otimes \mathbf{c}) = \mathbf{c} \cdot (\mathbf{a} \otimes \mathbf{b} - \mathbf{b} \otimes \mathbf{a}). \quad (\text{C.10f})$$

After some algebraic manipulations, the product of  $\dot{\mathbf{Q}}$  with the tensor  $\mathbf{q} \otimes \mathbf{q}$  is given by

$$\dot{\mathbf{Q}} \cdot \mathbf{q} \otimes \mathbf{q} = (1 - \cos(\alpha))\dot{\mathbf{q}} \otimes \mathbf{q} + \sin(\alpha)(\dot{\mathbf{q}} \times \mathbf{q}) \otimes \mathbf{q}. \quad (\text{C.11})$$

The final expression for the product of  $\dot{\mathbf{Q}}$  with the tensor  $\overset{(3)}{\boldsymbol{\epsilon}} \cdot \mathbf{q}$  reads

$$\begin{aligned} \dot{\mathbf{Q}} \cdot (\overset{(3)}{\boldsymbol{\epsilon}} \cdot \mathbf{q}) &= -\sin(\alpha)\dot{\alpha}\overset{(3)}{\boldsymbol{\epsilon}} \cdot \mathbf{q} - (1 - \cos(\alpha))\mathbf{q} \otimes (\dot{\mathbf{q}} \times \mathbf{q}) + \\ &\quad + \cos(\alpha)\dot{\alpha}(\mathbf{1} - \mathbf{q} \otimes \mathbf{q}) - \sin(\alpha)\mathbf{q} \otimes \dot{\mathbf{q}}. \end{aligned} \quad (\text{C.12})$$

Combining the two previous relations, the angular velocity tensor  $\boldsymbol{\Omega}$  can be expressed as

$$\begin{aligned} \boldsymbol{\Omega} &= \sin(\alpha)(1 - \cos(\alpha))[(\dot{\mathbf{q}} \times \mathbf{q}) \otimes \mathbf{q} - \mathbf{q} \otimes (\dot{\mathbf{q}} \times \mathbf{q})] - \\ &\quad - [\dot{\alpha}\mathbf{q} + \sin(\alpha)\cos(\alpha)\dot{\mathbf{q}}] \cdot \overset{(3)}{\boldsymbol{\epsilon}} + (1 - \cos(\alpha))[\dot{\mathbf{q}} \otimes \mathbf{q} - \mathbf{q} \otimes \dot{\mathbf{q}}]. \end{aligned} \quad (\text{C.13})$$

From this expression, the angular velocity vector  $\boldsymbol{\omega}$  may be obtained by computing the axial vector of  $\boldsymbol{\Omega}$ . The result is given by

$$\boldsymbol{\omega} = -\frac{1}{2}\overset{(3)}{\boldsymbol{\epsilon}} \cdot \boldsymbol{\Omega} = \dot{\alpha}\mathbf{q} + \sin(\alpha)\dot{\mathbf{q}} + (1 - \cos(\alpha))\mathbf{q} \times \dot{\mathbf{q}}. \quad (\text{C.14})$$

Note that the angular velocity is only co-linear with the current axis of rotation, *viz.*,  $\boldsymbol{\omega} = \dot{\alpha}\mathbf{q}$ , if this axis is fixed in space, *viz.*,  $\dot{\mathbf{q}} = \mathbf{0}$ .

### C.3 The EULER angles

The EULER angles describe a sequential rotation which is composed of three elementary rotations. The EULER angles were introduced when the rotational dynamics of the Earth was considered in Sect. 2.2. In the following, they are denoted by  $\psi$ ,  $\varepsilon$  and  $\varphi$ , which describe the rotations visualized in Figs. 2.3 and 2.4. The orthogonal tensor corresponding to the sequential rotation, which is composed of these three elementary rotations, is given by

$$\tilde{\mathbf{Q}} = \mathbf{Q}_\varphi \cdot \mathbf{Q}_\varepsilon \cdot \mathbf{Q}_\psi, \quad (\text{C.15})$$

where  $\mathbf{Q}_\varphi$ ,  $\mathbf{Q}_\varepsilon$  and  $\mathbf{Q}_\psi$  describe the elementary rotations from the  $\mathbf{k}$ -basis to the  $\mathbf{e}$ -basis, from the  $\mathbf{j}$ -basis to the  $\mathbf{k}$ -basis and from  $\mathbf{i}$ -basis to the  $\mathbf{j}$ -basis, respectively.

Hence,

$$\mathbf{e}_i = \mathbf{Q}_\varphi \cdot \mathbf{k}_i, \quad \mathbf{k}_i = \mathbf{Q}_\varepsilon \cdot \mathbf{j}_i, \quad \mathbf{j}_i = \mathbf{Q}_\psi \cdot \mathbf{i}_i, \quad i = 1, 2, 3. \quad (\text{C.16})$$

The definition of these bases is discussed in Sect. 2.2 and their relations are shown in Figs. 2.3 and 2.4. Using the RODRIGUES formula, the elementary rotations may be expressed as

$$\mathbf{Q}_\psi = \cos(\psi)\mathbf{1} + (1 - \cos(\psi))\mathbf{i}_3 \otimes \mathbf{i}_3 - \sin(\psi)\mathbf{i}_3 \cdot \overset{(3)}{\boldsymbol{\epsilon}}, \quad (\text{C.17})$$

$$\mathbf{Q}_\varepsilon = \cos(\varepsilon)\mathbf{1} + (1 - \cos(\varepsilon))\mathbf{j}_1 \otimes \mathbf{j}_1 - \sin(\varepsilon)\mathbf{j}_1 \cdot \overset{(3)}{\boldsymbol{\epsilon}}, \quad (\text{C.18})$$

$$\mathbf{Q}_\varphi = \cos(\varphi)\mathbf{1} + (1 - \cos(\varphi))\mathbf{k}_3 \otimes \mathbf{k}_3 - \sin(\varphi)\mathbf{k}_3 \cdot \overset{(3)}{\boldsymbol{\epsilon}}. \quad (\text{C.19})$$

In the following, the angular velocity vector of the sequential rotation described by the EULER angles is analyzed. According to Eq. (C.1), it is given by

$$\boldsymbol{\omega} = \boldsymbol{\omega}_\varphi + \mathbf{Q}_\varphi \cdot \boldsymbol{\omega}_\varepsilon + \mathbf{Q}_\varphi \cdot \mathbf{Q}_\varepsilon \cdot \boldsymbol{\omega}_\psi. \quad (\text{C.20})$$

Using Eq. (C.14), the angular velocity vectors of the elementary rotations may be expressed as follows:

$$\boldsymbol{\omega}_\psi = \dot{\psi}\mathbf{i}_3 + \sin(\psi)\dot{\mathbf{i}}_3 + (1 - \cos(\psi))\mathbf{i}_3 \times \dot{\mathbf{i}}_3, \quad (\text{C.21})$$

$$\boldsymbol{\omega}_\varepsilon = \dot{\varepsilon}\mathbf{j}_1 + \sin(\varepsilon)\dot{\mathbf{j}}_1 + (1 - \cos(\varepsilon))\mathbf{j}_1 \times \dot{\mathbf{j}}_1, \quad (\text{C.22})$$

$$\boldsymbol{\omega}_\varphi = \dot{\varphi}\mathbf{k}_3 + \sin(\varphi)\dot{\mathbf{k}}_3 + (1 - \cos(\varphi))\mathbf{k}_3 \times \dot{\mathbf{k}}_3. \quad (\text{C.23})$$

Note that the vector  $\mathbf{i}_3$  is fixed in space and, therefore, time derivatives of this vector vanish. Moreover, the fact that  $\mathbf{j}_3 = \mathbf{i}_3$  yields

$$\boldsymbol{\omega}_\psi = \dot{\psi}\mathbf{i}_3 \quad \Rightarrow \quad \mathbf{Q}_\varphi \cdot \mathbf{Q}_\varepsilon \cdot \boldsymbol{\omega}_\psi = \mathbf{Q}_\varphi \cdot \mathbf{Q}_\varepsilon \dot{\psi}\mathbf{j}_3 = \mathbf{Q}_\varphi \cdot \dot{\psi}\mathbf{k}_3 = \dot{\psi}\mathbf{e}_3. \quad (\text{C.24})$$

However, the time derivatives of the vectors  $\mathbf{j}_1$  and  $\mathbf{k}_3$  do not vanish, because these vectors change their direction with time. The relations between these time-dependent vectors to a fixed vector are given by  $\mathbf{j}_1 = \mathbf{Q}_\psi \cdot \mathbf{i}_1$  and  $\mathbf{k}_3 = \mathbf{Q}_\varepsilon \cdot \mathbf{Q}_\psi \cdot \mathbf{i}_3$ , respectively. Differentiating these relations with respect to time results in

$$\frac{d\mathbf{j}_1}{dt} = \boldsymbol{\omega}_\psi \times \mathbf{j}_1 \quad \text{and} \quad \frac{d\mathbf{k}_3}{dt} = (\boldsymbol{\omega}_\varepsilon + \mathbf{Q}_\varepsilon \cdot \boldsymbol{\omega}_\psi) \times \mathbf{k}_3. \quad (\text{C.25})$$

Hence,

$$\boldsymbol{\omega}_\varepsilon = \dot{\varepsilon}\mathbf{j}_1 + \sin(\varepsilon)\boldsymbol{\omega}_\psi \times \mathbf{j}_1 + (1 - \cos(\varepsilon))\mathbf{j}_1 \times (\boldsymbol{\omega}_\psi \times \mathbf{j}_1), \quad (\text{C.26})$$

$$\begin{aligned} \boldsymbol{\omega}_\varphi = & \dot{\varphi}\mathbf{k}_3 + \sin(\varphi)(\boldsymbol{\omega}_\varepsilon + \mathbf{Q}_\varepsilon \cdot \boldsymbol{\omega}_\psi) \times \mathbf{k}_3 + \\ & + (1 - \cos(\varphi))\mathbf{k}_3 \times ((\boldsymbol{\omega}_\varepsilon + \mathbf{Q}_\varepsilon \cdot \boldsymbol{\omega}_\psi) \times \mathbf{k}_3). \end{aligned} \quad (\text{C.27})$$

A re-arrangement of the last two terms on both right-hand sides yields

$$\boldsymbol{\omega}_\varepsilon = \dot{\varepsilon} \mathbf{j}_1 - \sin(\varepsilon) \mathbf{j}_1 \times \boldsymbol{\omega}_\psi - (1 - \cos(\varepsilon)) \mathbf{j}_1 \times (\mathbf{j}_1 \times \boldsymbol{\omega}_\psi), \quad (\text{C.28})$$

$$\begin{aligned} \boldsymbol{\omega}_\varphi &= \dot{\varphi} \mathbf{k}_3 - \sin(\varphi) \mathbf{k}_3 \times (\boldsymbol{\omega}_\varepsilon + \mathbf{Q}_\varepsilon \cdot \boldsymbol{\omega}_\psi) - \\ &\quad - (1 - \cos(\varphi)) \mathbf{k}_3 \times (\mathbf{k}_3 \times (\boldsymbol{\omega}_\varepsilon + \mathbf{Q}_\varepsilon \cdot \boldsymbol{\omega}_\psi)). \end{aligned} \quad (\text{C.29})$$

In the final step, the last two terms on both right-hand sides are expressed by virtue of the elementary rotations specified in Eqs. (C.18) and (C.19). For example, for the respective terms in Eq. (C.28), the following identity is found

$$-\sin(\varepsilon) \mathbf{j}_1 \times \boldsymbol{\omega}_\psi - (1 - \cos(\varepsilon)) \mathbf{j}_1 \times (\mathbf{j}_1 \times \boldsymbol{\omega}_\psi) = -\mathbf{Q}_\varepsilon \cdot \boldsymbol{\omega}_\psi + \boldsymbol{\omega}_\psi = (\mathbf{1} - \mathbf{Q}_\varepsilon) \cdot \boldsymbol{\omega}_\psi. \quad (\text{C.30})$$

Hence, Eqs. (C.28) and (C.29) can finally be expressed as follows

$$\boldsymbol{\omega}_\varepsilon = \dot{\varepsilon} \mathbf{j}_1 + (\mathbf{1} - \mathbf{Q}_\varepsilon) \cdot \boldsymbol{\omega}_\psi, \quad (\text{C.31})$$

$$\boldsymbol{\omega}_\varphi = \dot{\varphi} \mathbf{k}_3 + (\mathbf{1} - \mathbf{Q}_\varphi) \cdot (\boldsymbol{\omega}_\varepsilon + \mathbf{Q}_\varepsilon \cdot \boldsymbol{\omega}_\psi). \quad (\text{C.32})$$

In summary, the previous two equations show that the elementary angular velocity vectors do not only depend on the rate of the angle of the corresponding elementary rotation. The elementary angular velocity vectors rather have a nested structure. In fact, the following functional dependencies hold:  $\boldsymbol{\omega}_\psi = \hat{\boldsymbol{\omega}}_\psi(\psi, \dot{\psi})$ ,  $\boldsymbol{\omega}_\varepsilon = \hat{\boldsymbol{\omega}}_\varepsilon(\psi, \varepsilon, \dot{\psi}, \dot{\varepsilon})$  and  $\boldsymbol{\omega}_\varphi = \hat{\boldsymbol{\omega}}_\varphi(\psi, \varepsilon, \varphi, \dot{\psi}, \dot{\varepsilon}, \dot{\varphi})$ . The functional dependencies are linear regarding the time derivatives of the angles of the elementary rotations but are non-linear with respect to the angles themselves.

In the next step, the angular velocity vector  $\boldsymbol{\omega}$  is computed from the expressions obtained for the elementary angular velocities  $\boldsymbol{\omega}_\psi$ ,  $\boldsymbol{\omega}_\varepsilon$  and  $\boldsymbol{\omega}_\varphi$ . A substitution of Eqs. (C.24), (C.31) and (C.32) into Eq. (C.20) gives rise to

$$\begin{aligned} \boldsymbol{\omega} &= \dot{\varphi} \mathbf{k}_3 + (\mathbf{1} - \mathbf{Q}_\varphi) \cdot (\boldsymbol{\omega}_\varepsilon + \mathbf{Q}_\varepsilon \cdot \boldsymbol{\omega}_\psi) + \mathbf{Q}_\varphi \cdot \boldsymbol{\omega}_\varepsilon + \mathbf{Q}_\varphi \cdot \mathbf{Q}_\varepsilon \cdot \boldsymbol{\omega}_\psi \\ &= \dot{\varphi} \mathbf{k}_3 + \boldsymbol{\omega}_\varepsilon + (\mathbf{1} - \mathbf{Q}_\varphi) \cdot \mathbf{Q}_\varepsilon \cdot \boldsymbol{\omega}_\psi + \mathbf{Q}_\varphi \cdot \mathbf{Q}_\varepsilon \cdot \boldsymbol{\omega}_\psi \\ &= \dot{\varphi} \mathbf{k}_3 + \boldsymbol{\omega}_\varepsilon + \mathbf{Q}_\varepsilon \cdot \boldsymbol{\omega}_\psi \\ &= \dot{\varphi} \mathbf{k}_3 + \dot{\varepsilon} \mathbf{j}_1 + (\mathbf{1} - \mathbf{Q}_\varepsilon) \cdot \boldsymbol{\omega}_\psi + \mathbf{Q}_\varepsilon \cdot \boldsymbol{\omega}_\psi \\ &= \dot{\varphi} \mathbf{k}_3 + \dot{\varepsilon} \mathbf{j}_1 + \boldsymbol{\omega}_\psi = \dot{\varphi} \mathbf{k}_3 + \dot{\varepsilon} \mathbf{j}_1 + \dot{\psi} \mathbf{i}_3. \end{aligned} \quad (\text{C.33})$$

In conclusion, the nested structure was simplified significantly which is remarkable because this is not expected from the complex structure of the expressions of the elementary angular velocity vectors.

Subsequently, an expression for the angular acceleration  $\dot{\boldsymbol{\omega}}$  is derived from Eq. (C.33). A differentiation of Eq. (C.33) using the product rule yields

$$\begin{aligned} \dot{\boldsymbol{\omega}} &= \ddot{\varphi} \mathbf{k}_3 + \dot{\varphi} \frac{d\mathbf{k}_3}{dt} + \ddot{\varepsilon} \mathbf{j}_1 + \dot{\varepsilon} \frac{d\mathbf{j}_1}{dt} + \ddot{\psi} \mathbf{i}_3 \\ &= \ddot{\varphi} \mathbf{k}_3 + \ddot{\varepsilon} \mathbf{j}_1 + \ddot{\psi} \mathbf{i}_3 + \dot{\varphi} (\boldsymbol{\omega}_\varepsilon + \mathbf{Q}_\varepsilon \cdot \boldsymbol{\omega}_\psi) \times \mathbf{k}_3 + \dot{\varepsilon} \boldsymbol{\omega}_\psi \times \mathbf{j}_1, \end{aligned} \quad (\text{C.34})$$

where Eq. (C.25) was substituted for the time derivatives of the vectors  $\mathbf{j}_1$  and  $\mathbf{k}_3$  in the second step. By a substitution of Eqs. (C.24) and (C.31), the two latter terms on the right-hand side of this equation are simplified as follows

$$\begin{aligned}\dot{\varphi}(\boldsymbol{\omega}_\varepsilon + \mathbf{Q}_\varepsilon \cdot \boldsymbol{\omega}_\psi) \times \mathbf{k}_3 &= \dot{\varphi}(\dot{\varepsilon}\mathbf{j}_1 + (\mathbf{1} - \mathbf{Q}_\varepsilon) \cdot \boldsymbol{\omega}_\psi + \mathbf{Q}_\varepsilon \cdot \boldsymbol{\omega}_\psi) \times \mathbf{k}_3 \\ &= \dot{\varphi}\dot{\varepsilon}\mathbf{j}_1 \times \mathbf{k}_3 + \dot{\varphi}\boldsymbol{\omega}_\psi \times \mathbf{k}_3\end{aligned}\quad (\text{C.35})$$

$$\begin{aligned}&= -\dot{\varphi}\dot{\varepsilon}\mathbf{k}_2 + \dot{\varphi}\boldsymbol{\omega}_\psi \times \mathbf{k}_3, \\ \dot{\varepsilon}\boldsymbol{\omega}_\psi \times \mathbf{j}_1 &= \dot{\varepsilon}\dot{\psi}\mathbf{i}_3 \times \mathbf{j}_1 = -\dot{\varepsilon}\dot{\psi}\mathbf{j}_2.\end{aligned}\quad (\text{C.36})$$

where in the last step of the first and the second equation the relations  $\mathbf{j}_1 = \mathbf{k}_1$  and  $\mathbf{i}_3 = \mathbf{j}_3$  were exploited. In summary, the expression for the angular acceleration vector results as

$$\dot{\boldsymbol{\omega}} = \ddot{\varphi}\mathbf{k}_3 + \ddot{\varepsilon}\mathbf{j}_1 + \ddot{\psi}\mathbf{i}_3 - \dot{\varphi}\dot{\varepsilon}\mathbf{k}_2 + \dot{\varphi}\dot{\psi}\mathbf{i}_3 \times \mathbf{k}_3 - \dot{\varepsilon}\dot{\psi}\mathbf{j}_2. \quad (\text{C.37})$$

The discussion of the EULER angles is finalized by considering representations of the angular velocity and angular acceleration vectors in the  $\mathbf{e}$ -basis. This basis is of particular importance when the EULER equations of rigid body dynamics are solved because the (principle) components of the moment of inertia tensor of a rigid body are constant in the  $\mathbf{e}$ -basis. After some algebraic manipulations the angular velocity vector is obtained in the  $\mathbf{e}$ -basis from Eq. (C.33) and given by

$$\begin{aligned}\boldsymbol{\omega} &= \dot{\psi} \sin(\varepsilon)(\sin(\varphi)\mathbf{e}_1 + \cos(\varphi)\mathbf{e}_2) + \dot{\varepsilon}(\cos(\varphi)\mathbf{e}_1 - \sin(\varphi)\mathbf{e}_2) + \\ &\quad + (\dot{\varphi} + \dot{\psi} \cos(\varepsilon))\mathbf{e}_3.\end{aligned}\quad (\text{C.38})$$

Moreover, the resulting expression for the representation of the angular acceleration in the  $\mathbf{e}$ -basis is obtained from Eq. (C.37). After some (tedious) algebraic simplifications the following is obtained:

$$\begin{aligned}\dot{\boldsymbol{\omega}} &= [\ddot{\varphi} + \ddot{\psi} \cos(\varepsilon) - \dot{\varepsilon}\dot{\psi} \sin(\varepsilon)]\mathbf{e}_3 + [\ddot{\psi} + \dot{\varphi}\dot{\psi} \sin(\varepsilon)](c_\varphi\mathbf{e}_1 - s_\varphi\mathbf{e}_2) + \\ &\quad + [\ddot{\psi} \sin(\varepsilon) - \dot{\varphi}\dot{\varepsilon} + \dot{\varepsilon}\dot{\psi} \cos(\varepsilon)](s_\varphi\mathbf{e}_1 + c_\varphi\mathbf{e}_2),\end{aligned}\quad (\text{C.39})$$

where the abbreviations  $s_\varphi = \sin(\varphi)$  and  $c_\varphi = \cos(\varphi)$  have been used.

Equations (C.33) and (C.39) constitute the basis for solving the EULER equations for the co-moving observer. For this observer, the component matrix of the moment of inertia tensor  $\mathbf{J}$  is diagonal, because the basis vectors of the  $\mathbf{e}$ -basis are chosen collinearly with the principle axes. This simplifies the evaluation of the term  $\boldsymbol{\omega} \times \mathbf{J} \cdot \boldsymbol{\omega}$ . The product is given by

$$\begin{aligned}\boldsymbol{\omega} \times \mathbf{J} \cdot \boldsymbol{\omega} &= (J_1 - J_2)(\dot{\varphi} + \dot{\psi} \cos(\varepsilon))(s_\varphi\dot{\varepsilon} - c_\varphi\dot{\psi} \sin(\varepsilon))\mathbf{e}_2 - \\ &\quad - (J_1 - J_2)[s_\varphi c_\varphi(\dot{\varepsilon}^2 - \dot{\psi}^2 \sin^2(\varepsilon)) + \\ &\quad + (s_\varphi + c_\varphi)(s_\varphi - c_\varphi)\dot{\varepsilon}\dot{\psi} \sin(\varepsilon)]\mathbf{e}_3,\end{aligned}\quad (\text{C.40})$$

where the abbreviations  $s_\varphi$  and  $c_\varphi$  are the same as those used previously. With the help of the previous equation, the temporal evolution of the EULER angles could be fully analyzed by solving the EULER equations.

## D The LORENTZ transformation of the velocity

In the following, the LORENTZ transformation of the velocity is considered and a prove of Eq. (2.34) is given. In Footnote 2 of Chap. 2 on page 26, the LORENTZ transformation was specified as

$$t' = \gamma(t - \frac{1}{c^2} \mathbf{w} \cdot \mathbf{x}), \quad \mathbf{x}' = \mathbf{x} - \gamma \mathbf{w} t + (\gamma - 1) \mathcal{P}_{\parallel} \cdot \mathbf{x}, \quad (\text{D.1})$$

where  $\mathbf{w}$  denotes the relative velocity of the two observers  $\mathcal{O}$  and  $\mathcal{O}'$  as observed by  $\mathcal{O}$  and  $\gamma = (1 - w^2/c^2)^{-1/2}$  is the LORENTZ factor. Moreover, the parallel projector  $\mathcal{P}_{\parallel}$  and the perpendicular projector  $\mathcal{P}_{\perp}$  are given by

$$\mathcal{P}_{\parallel} = \frac{1}{w^2} \mathbf{w} \otimes \mathbf{w}, \quad \text{and} \quad \mathcal{P}_{\perp} = \mathbf{1} - \mathcal{P}_{\parallel}. \quad (\text{D.2})$$

In order to derive Eq. (2.34), it is necessary to invert Eq. (D.1), *i.e.*, to express the coordinates  $\mathbf{x}$  and  $t$  as functions of  $\mathbf{x}'$  and  $t'$ . There is a standard rule for the inversion, which states that  $\mathbf{x}'$  is interchanged with  $\mathbf{x}$  and  $t'$  with  $t$  and that the signs of the terms which explicitly contain the relative velocity  $\mathbf{w}$  are reversed. The inversion is derived rigorously in the following in order to show the correctness of the aforementioned rule.

Solving Eq. (2.80)<sub>1</sub> for the coordinate  $t$  yields

$$t = \frac{t'}{\gamma} + \frac{1}{c^2} \mathbf{w} \cdot \mathbf{x}. \quad (\text{D.3})$$

In the next step, Eq. (2.80)<sub>2</sub> is considered and multiplied by the perpendicular projector  $\mathcal{P}_{\perp}$ . Exploiting the facts that  $\mathcal{P}_{\perp} \cdot \mathbf{w} = \mathbf{0}$  and that  $\mathcal{P}_{\perp} \cdot \mathcal{P}_{\parallel} = \mathbf{0}$ , it is found that

$$\mathcal{P}_{\perp} \cdot \mathbf{x}' = \mathcal{P}_{\perp} \cdot \mathbf{x}. \quad (\text{D.4})$$

A multiplication of Eq. (2.80)<sub>2</sub> by the parallel projector  $\mathcal{P}_{\parallel}$  yields

$$\mathcal{P}_{\parallel} \cdot \mathbf{x}' = \mathcal{P}_{\parallel} \cdot \mathbf{x} - \gamma \mathbf{w} t + (\gamma - 1) \mathcal{P}_{\parallel} \cdot \mathbf{x} \quad \Leftrightarrow \quad \mathcal{P}_{\parallel} \cdot \mathbf{x} = \frac{1}{\gamma} \mathcal{P}_{\parallel} \cdot \mathbf{x}' + \mathbf{w} t. \quad (\text{D.5})$$

Thus, by an addition of Eqs. (D.4) and (D.5), the spatial coordinate  $\mathbf{x}$  may be expressed in terms of  $\mathbf{x}'$  and  $t$  as follows:

$$\mathbf{x} = \frac{1}{\gamma} \mathcal{P}_{\parallel} \cdot \mathbf{x}' + \mathcal{P}_{\perp} \cdot \mathbf{x}' + \mathbf{w} t. \quad (\text{D.6})$$

A substitution of this result in Eq. (D.3) allows to express the coordinate  $t$  in terms

---

of  $\mathbf{x}$  and  $t$ . The resulting expression is obtained by going through the following steps

$$\begin{aligned}
t &= \frac{t'}{\gamma} + \frac{1}{c^2} \left( \frac{1}{\gamma} \mathbf{w} \cdot \mathcal{P}_{\parallel} \cdot \mathbf{x}' + \mathbf{w} \cdot \mathcal{P}_{\perp} \cdot \mathbf{x}' + w^2 t' \right) \\
&= \frac{t'}{\gamma} + \frac{1}{c^2} \left( \frac{1}{\gamma} \mathbf{w} \cdot \mathbf{x}' + w^2 t' \right) \\
\Leftrightarrow \quad \left( 1 - \frac{w^2}{c^2} \right) t &= \frac{1}{\gamma} (t' + \frac{1}{c^2} \mathbf{w} \cdot \mathbf{x}') \\
\Leftrightarrow \quad t &= \gamma (t' + \frac{1}{c^2} \mathbf{w} \cdot \mathbf{x}').
\end{aligned} \tag{D.7}$$

A substitution of this expression for the time coordinate  $t$  in Eq. (D.6) yields

$$\begin{aligned}
\mathbf{x} &= \frac{1}{\gamma} \mathcal{P}_{\parallel} \cdot \mathbf{x}' + \mathcal{P}_{\perp} \cdot \mathbf{x}' + \gamma \mathbf{w} (t' + \frac{1}{c^2} \mathbf{w} \cdot \mathbf{x}') \\
&= \frac{1}{\gamma} \mathcal{P}_{\parallel} \cdot \mathbf{x}' + \mathcal{P}_{\perp} \cdot \mathbf{x}' + \gamma \mathbf{w} t' + \gamma \frac{1}{c^2} \mathbf{w} \otimes \mathbf{w} \cdot \mathbf{x}' \\
&= \frac{1}{\gamma} \mathcal{P}_{\parallel} \cdot \mathbf{x}' + \mathcal{P}_{\perp} \cdot \mathbf{x}' + \gamma \mathbf{w} t' + \gamma \frac{w^2}{c^2} \mathcal{P}_{\parallel} \cdot \mathbf{x}' \\
&= \frac{1}{\gamma} \mathcal{P}_{\parallel} \cdot \mathbf{x}' + (\mathbf{1} - \mathcal{P}_{\parallel}) \cdot \mathbf{x}' + \gamma \mathbf{w} t' + \gamma \frac{w^2}{c^2} \mathcal{P}_{\parallel} \cdot \mathbf{x}' \\
&= \mathbf{x}' + \left( \frac{1}{\gamma} - 1 + \frac{\gamma^2 - 1}{\gamma} \right) \mathcal{P}_{\parallel} \cdot \mathbf{x}' + \gamma \mathbf{w} t' \\
&= \mathbf{x}' + (\gamma - 1) \mathcal{P}_{\parallel} \cdot \mathbf{x}' + \gamma \mathbf{w} t',
\end{aligned} \tag{D.8}$$

where Eq. (D.2) was used in the third step and  $w^2/c^2 = (\gamma^2 - 1)/\gamma^2$  was applied in the fourth step. Altogether, the inverse of the LORENTZ transformation in Eq. (D.1) is given by

$$t = \gamma (t' + \frac{1}{c^2} \mathbf{w} \cdot \mathbf{x}'), \quad \mathbf{x} = \mathbf{x}' + \gamma \mathbf{w} t' + (\gamma - 1) \mathcal{P}_{\parallel} \cdot \mathbf{x}'. \tag{D.9}$$

This inverted transformation will be used together with the regular one in order to derive the LORENTZ transformation of the velocity.

In the following, the velocities observed by the two observers  $\mathcal{O}$  and  $\mathcal{O}'$  are denoted by  $\mathbf{v}$  and  $\mathbf{v}'$ , respectively. They are defined in terms of the respective coordinates of space and time as follows

$$\mathbf{v} := \frac{d\mathbf{x}}{dt}, \quad \mathbf{v}' := \frac{d\mathbf{x}'}{dt'}. \tag{D.10}$$

The objective is to obtain an expression that relates the two velocities  $\mathbf{v}$  and  $\mathbf{v}'$  to each other and, in the following, the velocity  $\mathbf{v}$  will be expressed as a function of  $\mathbf{v}'$  and the relative velocity  $\mathbf{w}$ . Therefore, Eq. (D.9)<sub>2</sub> is considered. This equation expresses the spatial coordinate  $\mathbf{x}$  as a function of the coordinates  $\mathbf{x}'$  and  $t'$ . The velocity  $\mathbf{v}$  is computed by an application of the chain rule of the differentiation

$$\mathbf{v} = \frac{d\mathbf{x}}{dt} = \frac{d\mathbf{x}}{dt'} \frac{dt'}{dt}. \tag{D.11}$$

The first term on the right-hand side of this equation can be computed from Eq. (D.9)<sub>2</sub>. If the symbol  $\hat{\mathbf{x}}$  denotes the function which expresses  $\mathbf{x}$  in terms of the

coordinates  $\mathbf{x}'(t')$  and  $t'$ , *i.e.*,  $\mathbf{x} = \hat{\mathbf{x}}(\mathbf{x}'(t'), t')$ , then

$$\frac{d\mathbf{x}}{dt} = \frac{\partial \hat{\mathbf{x}}}{\partial \mathbf{x}'} \cdot \frac{d\mathbf{x}'}{dt'} + \frac{\partial \hat{\mathbf{x}}}{\partial t'} = \mathbf{v}' + (\gamma - 1)\mathcal{P}_{\parallel} \cdot \mathbf{v}' + \gamma \mathbf{w}. \quad (\text{D.12})$$

In order to further treat the right-hand side of Eq. (D.11), a differentiation of Eq. (D.1)<sub>1</sub> is performed, *viz.*,

$$\frac{dt'}{dt} = \frac{\partial \hat{t}'}{\partial \mathbf{x}} \frac{d\mathbf{x}}{dt} + \frac{\partial \hat{t}'}{\partial t} = -\gamma \frac{1}{c^2} \mathbf{w} \cdot \mathbf{v} + \gamma = \gamma \left(1 - \frac{1}{c^2} \mathbf{w} \cdot \mathbf{v}\right). \quad (\text{D.13})$$

Finally, combining the latter two equations yields the following transformation of the velocity  $\mathbf{v}$

$$\mathbf{v} = \gamma(\mathbf{v}' + (\gamma - 1)\mathcal{P}_{\parallel} \cdot \mathbf{v}' + \gamma \mathbf{w}) \left(1 - \frac{1}{c^2} \mathbf{w} \cdot \mathbf{v}\right). \quad (\text{D.14})$$

However, in this relation, the velocity  $\mathbf{v}$  is still present on the right-hand side. Therefore, the equation is multiplied by  $\mathbf{w}$ . This yields

$$\begin{aligned} \mathbf{w} \cdot \mathbf{v} &= \gamma(\mathbf{w} \cdot \mathbf{v}' + (\gamma - 1)\mathbf{w} \cdot \mathcal{P}_{\parallel} \cdot \mathbf{v}' + \gamma w^2) \left(1 - \frac{1}{c^2} \mathbf{w} \cdot \mathbf{v}\right) \\ &= \gamma^2(\mathbf{w} \cdot \mathbf{v}' + w^2) \left(1 - \frac{1}{c^2} \mathbf{w} \cdot \mathbf{v}\right). \end{aligned} \quad (\text{D.15})$$

Rearranging this equation results in

$$\left(1 + \gamma^2 \frac{1}{c^2} (\mathbf{w} \cdot \mathbf{v}' + w^2)\right) \mathbf{w} \cdot \mathbf{v} = \gamma^2 (\mathbf{w} \cdot \mathbf{v}' + w^2). \quad (\text{D.16})$$

The factor in the parenthesis on the left-hand side can be simplified by recalling that  $w^2/c^2 = (\gamma^2 - 1)/\gamma^2$  as follows:

$$1 + \gamma^2 \frac{1}{c^2} (\mathbf{w} \cdot \mathbf{v}' + w^2) = 1 + \gamma^2 \frac{w^2}{c^2} + \gamma^2 \frac{\mathbf{w} \cdot \mathbf{v}'}{c^2} = 1 + \gamma^2 - 1 + \gamma^2 \frac{\mathbf{w} \cdot \mathbf{v}'}{c^2} = \gamma^2 \left(1 + \frac{\mathbf{w} \cdot \mathbf{v}'}{c^2}\right). \quad (\text{D.17})$$

Hence,

$$\mathbf{w} \cdot \mathbf{v} = \frac{\mathbf{w} \cdot \mathbf{v}' + w^2}{1 + \frac{\mathbf{w} \cdot \mathbf{v}'}{c^2}}. \quad (\text{D.18})$$

In order to finally obtain the LORENTZ transformation of the velocity, the expression in the last parenthesis on the right-hand side of Eq. (D.14) is simplified. Once more, the LORENTZ factor  $\gamma$  is invoked to replace the ratio  $w^2/c^2$ ; this yields

$$1 - \frac{1}{c^2} \mathbf{w} \cdot \mathbf{v} = 1 - \frac{\frac{1}{c^2} (\mathbf{w} \cdot \mathbf{v}' + w^2)}{1 + \frac{\mathbf{w} \cdot \mathbf{v}'}{c^2}} = \frac{1 - \frac{w^2}{c^2}}{1 + \frac{\mathbf{w} \cdot \mathbf{v}'}{c^2}} = \frac{1 - \frac{\gamma^2 - 1}{\gamma^2}}{1 + \frac{\mathbf{w} \cdot \mathbf{v}'}{c^2}} = \frac{1}{\gamma^2} \frac{1}{1 + \frac{\mathbf{w} \cdot \mathbf{v}'}{c^2}}. \quad (\text{D.19})$$

Substituting this expression in Eq. (D.14) gives the LORENTZ transformation of the velocity  $\mathbf{v}$ , which is now expressed in terms of the velocity  $\mathbf{v}'$  and the relative velocity  $\mathbf{w}$  by

$$\mathbf{v} = \frac{1}{\gamma} \frac{1}{1 + \frac{\mathbf{w} \cdot \mathbf{v}'}{c^2}} (\mathbf{v}' + (\gamma - 1)\mathcal{P}_{\parallel} \cdot \mathbf{v}' + \gamma \mathbf{w}). \quad (\text{D.20})$$

This concludes the derivation of the considered transformation and Eq. (2.34) is obtained from the latter by substituting  $\boldsymbol{w} = -\boldsymbol{w}'$ .

## E Results of the Singular Spectrum Analysis of LOD variations

In this appendix, additional results of the Singular Spectrum Analysis (SSA) of the LOD variations of Stephenson, Morrison, and Hohenkerk are presented. These results of the SSA were computed with a *python* program written by the author of this thesis which employs the *numpy* package.

The SSA yields a decomposition of a time series into mutual orthogonal modes. These modes are obtained from the singular value decomposition of the *trajectory matrix*. The columns of this matrix are vectors containing time lagged windows of the LOD variations such that the *trajectory matrix* is a HANKEL matrix. The

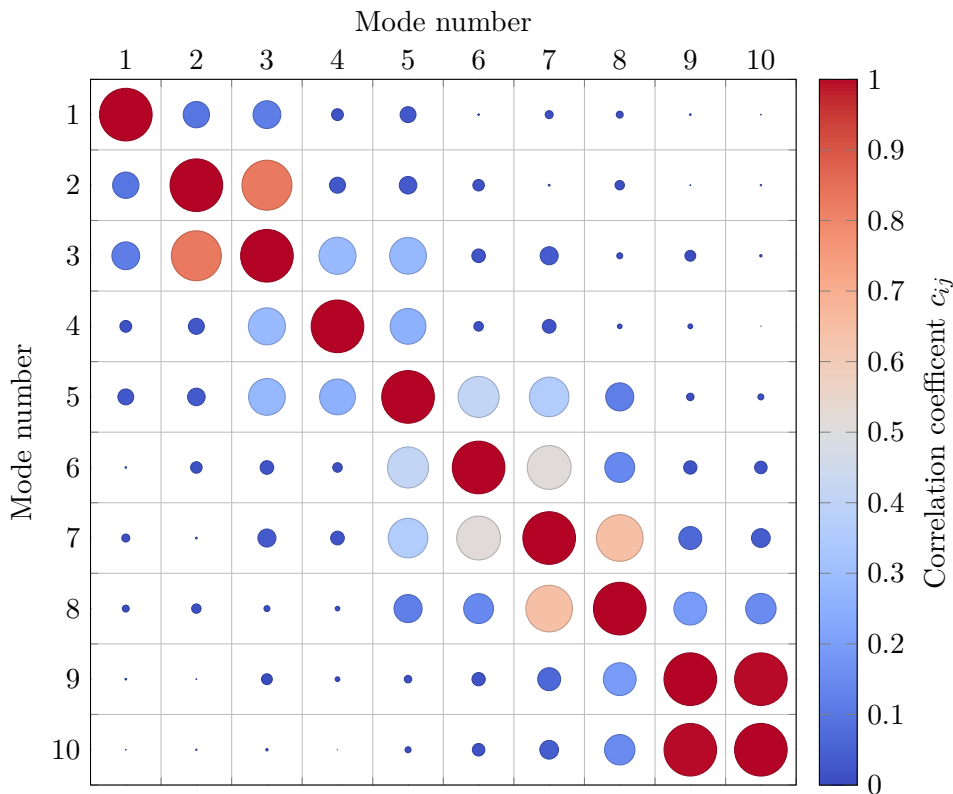


**Figure E.1:** Correlation matrix of the first ten principal components identified in the Singular Spectrum Analysis of the LOD data of Stephenson, Morrison, and Hohenkerk [2016].

singular value decomposition yields a representation of this matrix in terms of a set of left-singular and right-singular vectors with associated singular values. These vectors are mutually orthogonal and allow to re-construct an associated time series through the process of diagonal averaging. The time series reconstructed for a single singular value and the associated left-singular and right-singular vectors is referred to as a mode. The modes are sorted in decreasing order with respect to the associated singular values. The modes of a time series are not orthogonal with respect to some inner product in the temporal space but rather refer to the respective orthogonality of the underlying left-singular and right-singular vectors to those of other modes.

The separability of the signal by the SSA can be analyzed by considering the correlation coefficients of the different modes. The matrix formed from correlation coefficients of the first ten modes of the considered LOD time series is visualized in Fig. E.1. By the construction, the correlation coefficients are unity on the diagonal of this matrix. Close to the diagonal of the matrix, visualized in Fig. E.1, the correlations coefficients are large whereas they become vanishingly small with an increasing distance from the diagonal. This indicates that modes are correlated if the associated singular values are of similar size and uncorrelated otherwise. Despite the fact that some modes are uncorrelated with the other ones, some are also highly correlated to each other. In the matrix visualized in Fig. E.1, this is the case, for example, for the second and the third mode and for the ninth and the tenth mode. This correlation of the modes indicates that both describe very similar features of the time series and that the modes cannot be considered separately when the underlying physical processes are analyzed.

Therefore, the modes obtained from the singular value decomposition are usually grouped in the last step of the SSA. In this thesis, the groups are constructed using the DBSCAN clustering algorithm (Density-Based Spatial Clustering of Applications with Noise) from *Scikit-learn python* programming package [Pedregosa et al. (2011)]. This algorithm requires to provide a measure for the distance between the different data points which should be clustered. Regarding the LOD data, the correlation coefficients of the different modes are used for this purpose. The principal components resulting from the clustering are shown in Fig. 5.12 in Chap. 5 and in Fig. E.2 below. The original time series can be reconstructed from the linear superposition of these first eight principal components very accurately which is discussed in Chap. 5.

Each of the principal components represents a different feature type of the original time series which is hoped to be associated to an underlying physical process. Typically, the different feature types can be classified, for example, as trends or oscillations. The fifth principal component is regarded as an irregular oscillatory component with timescales of approximately 40 years, which may be superimposed by a weak linear trend. For the principal components of degree six to eight, it is clear from Fig. E.2 that they represent modulated oscillatory components. Since the associated timescale is approximately ten years for these components, they might not be perfectly separated through the SSA.

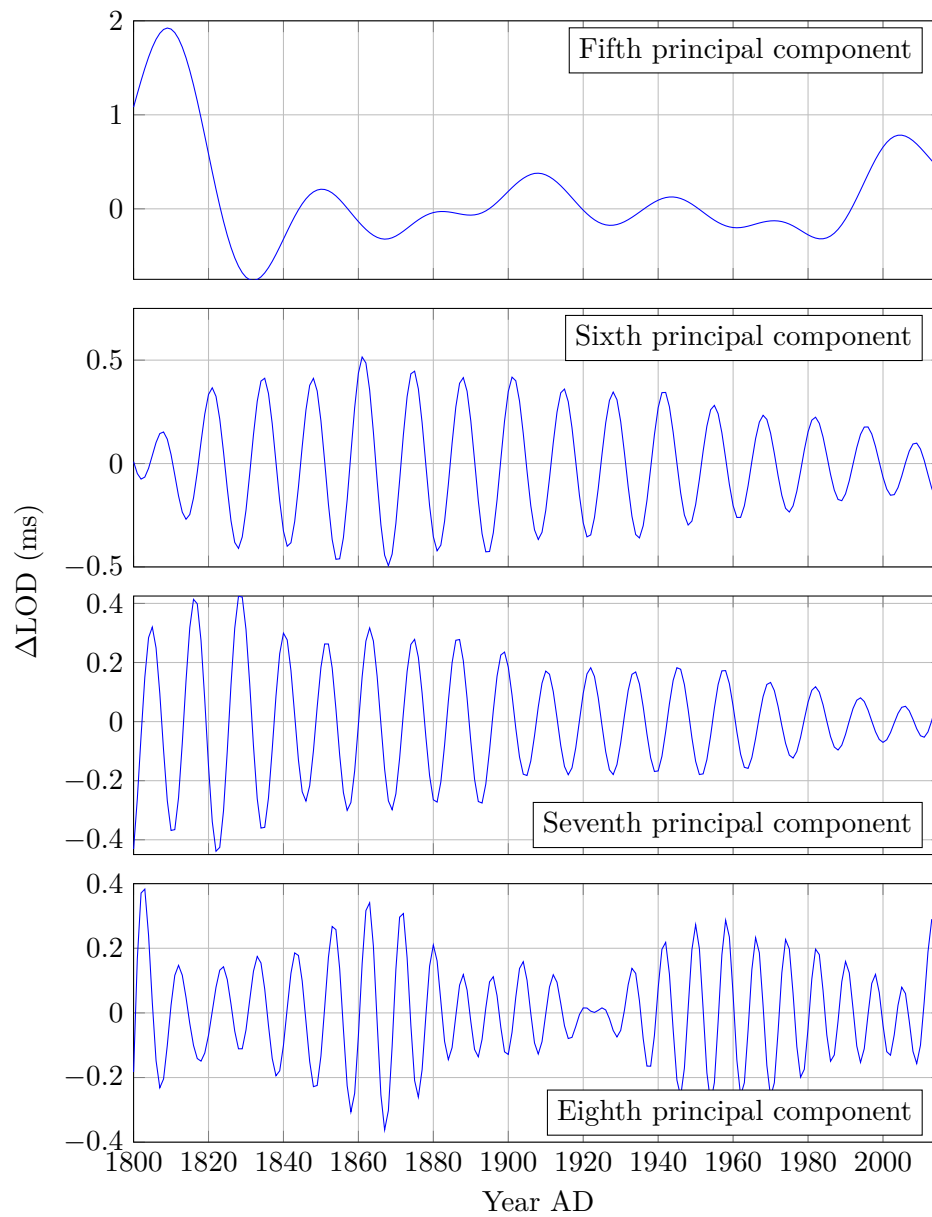


**Figure E.2:** Fifth to eighth principal component obtained in the Singular Spectrum Analysis of the LOD data of Stephenson, Morrison, and Hohenkerk [2016].